

Development of novel particle spectroscopy and investigation of clustering in light neutron-rich nuclei

By

Stuart Hamilton Pirrie

A thesis submitted to
the University of Birmingham
for the degree of
DOCTOR OF PHILOSOPHY

Nuclear Physics Research Group
School of Physics and Astronomy
College of Engineering and Physical Sciences
University of Birmingham
March 2022

UNIVERSITY OF
BIRMINGHAM

University of Birmingham Research Archive

e-theses repository

This unpublished thesis/dissertation is copyright of the author and/or third parties. The intellectual property rights of the author or third parties in respect of this work are as defined by The Copyright Designs and Patents Act 1988 or as modified by any successor legislation.

Any use made of information contained in this thesis/dissertation must be in accordance with that legislation and must be properly acknowledged. Further distribution or reproduction in any format is prohibited without the permission of the copyright holder.

© Copyright by STUART PIRRIE, 2022

All Rights, and indeed all lefts, Reserved

ABSTRACT

Nuclear cluster structures are of great interest to the nuclear physics community, providing good tests of theoretical models and exciting physics beyond the highly-successful shell model. Experiments have been performed in order to attempt to identify cluster structures in ^{18}O, ^{14}C and ^{16}C. The first experiment involved precision measurements of branching ratios for high-energy states in ^{18}O, ranging from 7 $\rightarrow$ 16 MeV. Over 50 states were investigated, with a mixture of previously measured and unmeasured branching ratios — in the case of previously measured branching ratios, typically a very good agreement was seen between this work and literature values. The values of $^{\Gamma_\alpha}/_{\Gamma_{\rm tot}}$, E_x and $\Gamma_{\rm tot}$ were extracted experimentally and used to calculate θ_α^2 using the literature value of J^π, where available. These θ_α^2 values were used to establish the tendency towards clustering for these states, with an emphasis on states that had previously been proposed to be members of rotational bands corresponding to cluster structures $^{14}\mathrm{C} \bigotimes \alpha$ and $^{12}\mathrm{C} \bigotimes 2n \bigotimes \alpha$. No evidence of consistent cluster structure across the proposed bands was observed, casting doubt on the existence of such cluster bands in ^{18}O. However, some states with θ_α^2 values consistent with cluster structure were observed. The second experiment, for which the analysis is ongoing, aimed to provide a proof-of-principle measurement of the ability to produce excitation functions for the compound nuclei ^{14}C and ^{16}C through the thick target inverse kinematics ^{4}He(^{10}Be,^{10}Be)α and ^{4}He(^{12}Be,^{12}Be)α resonant scattering reactions, with the ^{10}Be and ^{12}Be beams produced via fragmentation. The experiment also aimed to identify resonances corresponding to nuclear molecular Hoyle-state configurations, which have long since been theorised.

DEDICATION

Dedicated to Steven Moffat and Mark Gatiss.

Thank you for ensuring that this will not be the worst piece of writing ever produced.

ACKNOWLEDGMENTS

There are many people to whom I owe thanks, for varying reasons. It's difficult to know where to start — I think I will perhaps forgo thanking each individual ancestor, and the work of each scientist whose prior work have made my research possible. As such, I will pick two at random: congratulations Kennedy Bremner (one of my paternal great-great-great grandfathers) and Ludwig Boltzmann (who was chosen by a random scientist generator). To all those of you who missed out, better luck next thesis.

I'd like to start (properly) by thanking my supervisors, Dr. Carl Wheldon and Prof. Tzany Kokalova, for helping me in my nuclear physics understanding, development and analysis as well as career guidance. You have both been excellent supervisors, and I'm sorry that the punishment for that is that I'm sticking around longer. My boi Dr. Neil Curtis, thank you for being an all-around Monte-Carlo behemoth and providing me with many helpful pieces of advice. My nuclear electronics knowledge and capability have increased largely thanks to the efforts and expertise of Dr. Garry Tungate, who to this day is the only person I think I've ever seen actually use the walk adjust on a discriminator. The rest of the nuclear physics staff, and indeed the staff in the department at large, have also been instrumental in developing my skills as a physicist.

To the PhD students in the nuclear physics group, both past and present (and future? Just by reading my thesis in the future you can have like 0.2 thanks), thank you for the great company and aiding me in my life goal to procrastinate as much as humanly possible. You know who you are, but following the trend I will list you all in the order you joined (I think): Sam, Robin, Jack, Nima, Kaeden, Harry, Emzo, Tony, Marianna, Trinder, Pedro, Håkan, Ollie, Jakub, Yiming, Ross, Angus, Italian Simon, Mark, Dawid, Sammy and Stephen. Thanks also to the post-COVID refugees, Suzie and Chris (Oliver), for the straight-up vibing.

A shout-out also to the residents of the second floor of Physics East who adopted me upon my return to a cold and unfeeling campus — Chris (Gill), Ellie (though you were both also pre-COVID refugees up on the 3rd floor as well, so placing you in a paragraph was non-trivial comparatively), Carlton, Aaron, Tabatha, Adam, Jake, Caleb, the Joes (SD, HD and Birmingham) and the Toms (both spin-up and spin-down). I would have never thought that a group of chemists could work their way into my life so easily.

My family and friends from outside work have been, of course, instrumental in the trajectory of my life. Particularly, my mum and dad (sorry, Kennedy Bremner, it couldn't just be you) who have supported and provided for me, and are largely responsible for moulding me into the man (boy) I am today. Kirsten's alright, too. Thanks to the good people of Mumble who have supported this thesis through the watching of thesis streams, moral support and babysitting Jomeroy for me.

A big thanks to my partner, Rachel, who has not only been incredibly patient while I slowly worked my way through my research, but also whose last-minute proofreading was borderline heroic — without you, Rach, I might still be editing my diagrams in Paint so both nuclear structure physics and I owe you a debt of gratitude.

Shoutout to the folks at the UK Science and Technology Facilities Council for all the funding (Grant No. ST/L005751/1) that made this research possible, as well as the European Unions Horizon 2020 research and innovation programme under the Marie Skłodowska-Curie Grant Agreement No. 65F9744. Also, perhaps most importantly, thanks to the current government — you've taught me the importance of never giving up or resigning, even when you obviously should, and how to maintain a good taxpayer-funded work/life balance[1].

[1] https://assets.publishing.service.gov.uk/government/uploads/system/uploads/attachment_data/file/1078404/2022-05-25_FINAL_FINDINGS_OF_SECOND_PERMANENT_SECRETARY_INTO_ALLEGED_GATHERINGS.pdf

LIST OF PUBLICATIONS

FULL PAPERS IN REFEREED JOURNALS

1. Precision branching-ratio measurements in ^{18}O.

   http://dx.doi.org/10.1140/epja/s10050-021-00431-w

   S. Pirrie, C. Wheldon, Tz. Kokalova, J. Bishop, Th. Faestermann, R. Hertenberger, H.-F. Wirth, S. Bailey, N. Curtis, D. Dell'Aquila, D. Mengoni, R. Smith, D. Torresi, and A. Turner,

   Eur. Phys. J. (Topical Issue) **57** *(2021) 150, p1-12 (12 pages).*

2. Undergraduate experiments with a ^{44}Ti source.

   http://dx.doi.org/10.1088/1361-6404/abbca3

   S. Pirrie, G. Tungate, Tz. Kokalova, C. Wheldon, K. Nikolopoulos, P. Santa Rita and A. Turner,

   Eur. J. Phys. **42** (2020) 015805, p1-14 (14 pages).

3. Search for evidence of rotational cluster bands in ^{18}O.

   http://dx.doi.org/10.1103/physrevc.102.064315

   S. Pirrie, C. Wheldon, Tz. Kokalova, J. Bishop, Th. Faestermann, R. Hertenberger, H.-F. Wirth, S. Bailey, N. Curtis, D. Dell'Aquila, D. Mengoni, R. Smith, D. Torresi, and A. Turner,

Phys. Rev. C **102** (2020) 064315, p1-8 (8 pages).

4. Mass measurement of Re-190.

   http://dx.doi.org/10.1088/1361-6471/ab98e3

   M.R. Griffiths, C. Wheldon, Tz. Kokalova, A. Turner, **S. Pirrie**, V. Ziman, N.I. Ashwood, J.D. Malcolm, M. Barr, M. Freer, Th. Faestermann, H.-F. Wirth, R. Hertenberger, R. Gernhäuser and R. Krücken,

   J. Phys. G **47** (2020) 085104 (5 pages).

CONFERENCE PAPERS IN REFEREED JOURNALS

5. Measurement of the structure of potential cluster bands and absolute branching ratios of high-energy states in $^{18}O^{*}$.

   http://dx.doi.org/10.1088/1742-6596/1643/1/012155

   S. Pirrie, C. Wheldon, Tz. Kolalova Wheldon, J. Bishop, R. Hertenberger, H.-F. Wirth, S. Bailey, N. Curtis, D. Dell'Aquila, Th. Faestermann, D. Mengoni, R. Smith, D. Torresi and A. Turner,

   (INPC2019) *J. Phys. Conf.* **1643** (2020) 012155, p1-6 (6 pages).

6. Theragnostics – Alternative production of terbium isotopes at the University of Birmingham using an MC40 cyclotron.

   http://dx.doi.org/10.1088/1742-6596/1643/1/012209

   R.R. Trinder, Tz. Kokalova, D.J. Parker, C. Wheldon, B. Phoenix, P. Ivanov, B. Russel, B. Webster, P. Regan, A. Robinson, D. Cullen, S. Pells, R. Allen, **S. Pirrie**, A. Turner and P. Santa Rita,

   (INPC2019) *J. Phys. Conf.* **1643** (2020) 012201, p1-6 (6 pages).

7. Clustering in ^{18}O – absolute determination of branching ratios via high-resolution particle spectroscopy .

http://dx.doi.org/10.21468/scipostphysproc.3.009

S. Pirrie, C. Wheldon, Tz. Kolalova Wheldon, J. Bishop, R. Hertenberger, H.-F. Wirth, S. Bailey, N. Curtis, D. Dell'Aquila, Th. Faestermann, D. Mengoni, R. Smith, D. Torresi and A. Turner,

(EFB24 2019) *SciPost Phys. Proc.* **3** (2020) 009, p1-10 (10 pages).

8. Investigating artefacts associated with α particle interactions in charge coupled devices.

   http://dx.doi.org/10.1109/nssmic.2017.8533021

   R. Newton, M. J. Scott, J. W. Dickinson, B. Phoenix, D. J. Parker, C. Wheldon, **S. Pirrie**, A. Turner, Tz. Kokalova and M. J. Joyce,

   (IEEE NSS/MIC 2017) *IEEE Nuclear Science Symposium and Medical Imaging Conference Proceedings* (2017) p1-4 (4 pages).

OTHER INTERNATIONAL CONFERENCE PUBLICATIONS

9. A method to determine branching ratios using charged particle detectors for states in ^{18}O.

   http://dx.doi.org/10.1063/1.5078856

   S. Pirrie, Tz. Kokalova, C. Wheldon, S. Bailey, J. Bishop, N. Curtis, R. Smith, D. Torresi, A. Turner, R. Hertenberger, H.-F. Wirth, Th. Faestermann, D. Mengoni and D. Dell'Aquila,

   (SOTANCP4 2018) **2038** (AIP, 2018) 020037, p1-6 (6 pages).

"This PGR's progress to date has been

'At least satisfactory' "

— Carl Wheldon, GRS2 form

Contents

1 Introduction **1**

1.1 Thesis work 2

2 Theoretical overview **4**

2.1 Liquid drop model 4

2.2 Spherical shell-model 6

2.3 Clustering 12

2.3.1 Core + alpha 14

2.3.2 Nuclear molecules 15

2.4 Rotational bands 18

2.5 Alpha widths 19

2.6 Selection rules 20

2.7 Nuclear reaction theory 22

2.7.1 Direct reactions 23

2.7.2 Compound nucleus formation 25

2.7.3 Thick target inverse kinematics 27

2.7.4 R-matrix theory 28

3 Experimental methods for precision measurement of branching ratios in ^{18}O **32**

3.1 Experimental set-up 35

3.1.1 Q3D magnetic spectrograph 36
3.1.1.1 Focal-plane detector 37
3.1.1.2 Particle identification 39
3.1.1.3 Calibration and resolution 39
3.1.1.4 Background 48
3.1.2 Birmingham large-angular-coverage DSSD array 50
3.1.2.1 P-N junctions 50
3.1.2.2 Measuring the position of incident particles 53
3.1.2.3 Detector placement 56
3.1.2.4 Electronics 57
3.1.2.5 Trigger logic 61
3.1.2.6 Energy calibration 63
3.1.2.7 Position calibration 65
3.1.2.8 Resolution 68
3.1.2.9 Determination of kinematic lines 70
3.2 Monte-Carlo simulation 73
3.2.1 Resolution8.1 73
3.2.2 Further smearing effects 78
3.2.3 Simulations performed 84
3.3 Determining the species of decay products 85
3.3.1 Kinematic cones 85
3.3.2 Catania plot 88
3.3.2.1 Determination of γ-decay branching ratios 93
3.3.2.2 Excited levels in daughter nuclei 97

4 Results **103**

4.1 Validation of branching ratios 103

4.2 Precision branching ratio measurements . . . 108
4.2.1 Efficiency-corrected background . . . 110
4.2.2 Non-clustering results . . . 111
4.2.3 7.0 MeV to 9.4 MeV . . . 116
4.2.4 9.6 MeV to 11.9 MeV . . . 118
4.2.5 12.4 MeV to 14.5 MeV . . . 120
4.2.6 14.5 MeV to 16.3 MeV . . . 122
4.2.7 Clustering results . . . 124
4.2.8 The proposed $K^\pi = 0_2^+$ band . . . 126
4.2.9 The proposed $K^\pi = 0_2^-$ band . . . 126
4.2.10 The proposed $K^\pi = 0_4^+$ band . . . 127
4.2.11 The proposed $K^\pi = 0_4^-$ band . . . 130
4.2.12 The proposed $K^\pi = 1^-$ band . . . 131
4.3 Discussion and summary . . . 131

5 Investigations into nuclear molecular structures in ^{14}C and ^{16}C 135
5.1 Motivations . . . 136
5.2 Beam production . . . 138
5.3 Experimental set-up . . . 141
5.3.1 Electronics . . . 146
5.3.2 Degrader thickness . . . 148
5.4 Excitation function determination . . . 150
5.5 Monte-Carlo simulation . . . 152
5.6 Summary . . . 160

6 Conclusions 161
6.1 Future work . . . 163

A Derivation of two-body non-relativistic kinematic solution **165**

References **170**

List of Figures

2.1 A plot of binding energy per nucleon against mass number, for isotopes corresponding to the largest binding energy per nucleon for each mass number between $A = 2$ and $A = 30$. Isotopes labelled in red are nuclei with complete nucleon shell or sub-shell closures. Data taken from Ref. [7]. 7

2.2 A diagram depicting the shells and sub-shells of the nuclear shell model (increasing in energy from the bottom) alongside the number of nucleons that can occupy each sub-shell and the total number of nucleons in a nucleus when a sub-shell is filled (total occupancy). Numbers in bold and underlined represent magic numbers, corresponding to a closed shell and hence increase in stability. The splitting of a shell due to the spin-orbit interaction can be seen to cause other shells to lie between its sub-shells, like with the $1d$ and $2s$ shells — see text for details. 9

2.3 Calculated values of the different potentials in the ^{16}O nuclear system for varying r, using the proton $1d_{5/2}$ orbital. Here, the central potential represents that described in equation 2.2. The total potential can be seen to be attractive only between values of roughly 2-5 fm, mimicking the behaviour of real nucleons in a nucleus. Calculations here were performed using the program WSPOT.FOR, with this figure taken from Ref. [10] as Figure 1.2. . 11

2.4 The Ikeda diagram, showing the alpha thresholds for various even, $N = Z$ nuclei, including the triple alpha threshold of 7.27 MeV for ^{12}C. Taken from Ref. [15] and created by Tz. Kokalova. 15

2.5 The extended Ikeda diagram, showing nuclei with excess neutrons. The lighter nuclei depicted in Figure 2.4 can be seen in the bottom left of the diagram, with neutron number increasing along the vertical axis. Original from Ref. [22], edited figure (used here) from Ref. [26]. 16

2.6 Cluster Shell Model (CSM) calculations performed in Ref. [27] for the ground state of ^{9}Be showing neutron density (top) and matter density (bottom), as well as a depiction of the π-bonding that occurs in this state, are shown in (a). The same is shown in (b) for the 1^{st} excited state, along with a depiction of the σ-bonding that occurs in this state. Antisymmetrized Molecular Dynamics (AMD) calculations, which is a theoretical framework from which properties of nuclei can be derived *ab initio*, for the proton and neutron densities of light Be isotopes from Ref [28] are shown in (c). The neutron density for ^{9}Be shows a structure consistent with π-bonding. 17

2.7 An example of inelastic scattering shown in the laboratory frame, involving a ^{4}He beam (A) incident on a ^{12}C target (B), leaving the ^{12}C in an excited state. The two nuclei do not transfer nucleons, though missing kinetic energy in the final state is used to rearrange the nucleons of the ^{12}C. 24

2.8 A transfer reaction shown in the laboratory frame, in which a ^{7}Li beam transfers a ^{6}He nucleus (shown with a yellow ellipse) to a target ^{12}C nucleus, forming ^{18}O (potentially in an excited state) and p products. There is a Q-value associated with this interaction due to the difference in mass of the initial and final states. 25

2.9 A compound nucleus formation reaction shown in the centre-of-mass frame of the compound nucleus, in which a ^{10}Be nucleus and ^{4}He nucleus (in the entrance channel) fuse to form ^{14}C. This compound nucleus then breaks apart into two fragments in the exit channel, a deuteron and a ^{12}B nucleus. 26

3.1 The rotational bands with potential cluster structure in ^{18}O proposed by von Oertzen et al. [56] are shown in (a), while the excitation energy required for ^{18}O cluster structures to form is shown in (b). 34

3.2 A representation of the experimental set-up used, showing the positions of the Birmingham large-angular-coverage DSSD array and the Q3D magnetic spectrograph in-plane. Angles and distances shown are from the set-up used in 2017, though these are very similar to those used in 2016. Angles and distances across both experimental runs are summarised in table 3.1. Figure adapted from Figure. 1 published in Ref. [57]. 35

3.3 An overview of the Q3D magnetic spectrograph, with the path taken by charged particles due to the magnetic fields highlighted in green [60]. 37

3.4 Depiction of the focal-plane detector, showing the constituent parts. An example trajectory of a charged particle can be seen at the top of the figure, with an example histogram output of charge distribution across the cathode strip foil at the bottom. Figure taken from Ref. [61]. 38

3.5 Particle identification plots from which the species of particles incident on the focal-plane detector can be determined. All plots involve measurement of the energy loss of particles from the signal extracted from the anode wires on the y axis, plotted against energy loss through the first cathode foil (a), position as measured by the cathode strip foil (b) and energy deposited in the scintillator (c). The gates used for the experimental data are shown in red, corresponding to protons. The loci due to deuterons are also labelled. Figure adapted from FIG. 1 published in Ref. [63]. 40

3.6 Q3D spectra obtained for counts as a function of focal-plane position, for the case where all three gates shown in figure 3.5 are utilised (a), the two gates not including the scintillator are utilised (b) and no gates are used to clean up the spectrum (c). 41

3.7 Q3D spectra obtained for the different excitation regions: $-0.5 \rightarrow 2.5$ MeV (a), $7.0 \rightarrow 9.4$ MeV (b), $9.6 \rightarrow 11.9$ MeV (c), $12.4 \rightarrow 14.5$ MeV (d) and $14.5 \rightarrow 16.3$ MeV (e). Energy values given for excitations are taken from Ref. [56] in keV. An increase in the background level for increasing excitation energy is observed, due to various n-body phase spaces that become available above certain energy thresholds. See Sec. 3.1.1.4 for details. 42

3.8 Fitted Q3D spectra for the $-0.5 \rightarrow 2.5$ MeV region, with pure Gaussian fits for both states (a) and with a skewed Gaussian fit for the ground state (b). A visible increase in the fidelity of the fit to the data can be seen for the skewed fit. 44

3.9 Q3D spectra for the $7.0 \rightarrow 9.1$ MeV excitations, rebinned relative to the usual dispersion over 2550 channels for the position of detection in the focal-plane detector (a). Larger bin sizes of $\times 10$ (b), $\times 20$ (c) and $\times 60$ (d) are shown for comparison. Statistics too low for reasonable fitting in many areas can be seen even in the peaks in (a), whereas an obvious loss of features can be observed in (d) relative to the other three. Plots (b) and (c) compromise these two qualities. 46

3.10 Plots of the literature values of energy for excitations in keV against measured centroid value in the focal-plane detector in channels, for $7.0 \rightarrow 9.1$ MeV (a), $7.0 \rightarrow 9.4$ MeV (b), $9.6 \rightarrow 11.9$ MeV (c), $12.4 \rightarrow 14.5$ MeV (d) and $14.5 \rightarrow 16.3$ MeV (e). Fits with the functional form $y = Ax^2 + Bx + C$ were used in all cases and are shown in red, along with the corresponding value of χ^2/dof. Error bars are displayed for each data point, although the error bars are often comparable to the size of the symbol representing a data point. . . 47

3.11 Fitted Q3D spectra for the observed excitation regions, with certain centroid values extracted in this work shown next to the resonances. The regions are 7.0 → 9.4 MeV (a), 9.6 → 11.9 MeV (b), 12.4 → 14.5 MeV (c) and 14.5 → 16.3 MeV (d). The total fit to the data is shown by a solid red line, whereas the individual Gaussian components are indicated using a solid blue line. The dashed pink line represents the background, discussed in the text. Subfigures here have been published in Refs. [57] and [63]. 49

3.12 A P-N junction in equilibrium (a), with the depletion region formed between the two doped semiconductors. The same P-N junction is then put under reverse-bias (b), causing the size of the depletion region to extend across the crystal. Images edited from Ref [71]. 51

3.13 A front strip of the detector (red) is hit by a charged particle in coincidence with a back strip of the detector (blue), resulting in a pixel within which a charged particle can be detected. Image edited in Ref. [71], originally from Ref. [69]. 53

3.14 Depiction of the surface of a DSSD, showing an example of single pile-up (a), multiple-hit (b) and charge-sharing (c). Possible hit positions are shown in purple, with the front strips and back strips corresponding to a hit shown in red and blue, respectively. The relevant inter-strip area in the case of charge-sharing is shown in yellow. 55

3.15 A depiction of the layout of the Birmingham large-angular-coverage DSSD array, with blues dots indicating the centre positions of each pseudopixel. The in-plane and out-of-plane angles are shown on the horizontal and vertical axes respectively. Borders have been placed around each DSSD to enable distinction between the different groups of pixels, with black boxes (representing the pins that are connected to the preamplifier) to indicate the bottom of each detector in the normal orientation as depicted in figures 3.13 and 3.14. . . . 58

3.16 An overview of the electronics set-up used for the DSSDs, showing the processing of the charge signal through to digitisation of the signal by ADCs. Numbers in brackets on each electronics unit refer to the number of inputs. The ×10 multiplicative outputs are the same as the ×1 multiplicative outputs, but amplified by a constant factor of 10. The logic signal from the V895 LEDs is input into the trigger logic, shown in figure 3.18. 59

3.17 A depiction of the common shape of signals output by a detector (top), preamplifier (middle) and amplifier (bottom). Pulses due to three separate detections of charged particles are shown in green, red and blue respectively. The duration of the original charge pulse is shown by the dashed black lines, demonstrating the relationship to the rise time of the preamplifier signal. The width of a Gaussian produced by the amplifier is shown; the width of these pulses can be controlled via the amplifiers. Time axes shown here are not to scale with the real length of pulses in order to compare features. Figure adapted from figures in Refs. [73] and [74]. 60

3.18 An overview of the trigger logic, which was used to gate both the ADCs and the Q3D to provide singles events for both systems. The output logic pulse from the V875 LEDs shown in figure 3.16 is shown in dark green. 62

3.19 An example calibration for a strip of one of the DSSDs, showing the six peaks and the isotopes from which they originate. 63

3.20 Energies measured from a triple-α source in each strip of the DSSD, plotted against electronics channel number, before (a) and after (b) the energy calibration was performed. Three distinct bands (due to the compressed vertical scale) corresponding to the energies from the three isotopes can be seen in the calibrated spectrum. An empty channel can be seen in (b), which was unable to be calibrated due to the lack of a sensible triple α-spectrum — this can be inferred from the corresponding channel in (a). 64

3.21 A Cartesian view of the detector array, showing data taken using a triple-α source with the faces of the detectors covered by the R-masks. A comparison of incorrect mapping of pins to the electronic channels (a) to the correct mapping (b) is given — the Rs can be clearly seen with the correct mapping for each DSSD. 65

3.22 Diagram detailing angle definitions, as well as providing the geometry with which to determine them. The beam travels along the z-axis and interacts with the target, located at the origin, while the product nuclei are detected in the x-y plane shown. Figure adapted from Figure 2 of Ref. [84]. 66

3.23 Energy measured in a front strip of detector 2 against energy measured in a back strip, for silicon singles events obtained during the 9.6 $\rightarrow$ 11.9 MeV excitation region runs. Events ungated except for a low-energy threshold are shown in (a), while an example software gate (the requirement that front and back hits must be within 0.7 MeV of one another for a good event) is shown in (b). 68

3.24 Plots of scattering angle against energy for singles events in the DSSD array, using energy values determined via calibration with the triple-α source (a) and double the energy determined via calibration (b). Calculated kinematic lines for elastic scattering of ^{7}Li on ^{12}C are also plotted for the recoil ^{12}C (red) and the ejectile ^{7}Li (orange) — see text for details. 71

3.25 A diagram showing the likely cause of the energy jump. The amplifier signal, shown in blue, is only partially inside of the 5 µs gate, shown in red. As such, the ADC only registers the height of the signal present in the gate as the gate ends. 72

3.26 Cartesian views of the detector array for events corresponding to excitation energies of 9.6 → 11.9 MeV, for Monte-Carlo data with no position smearing (a), Monte-Carlo data with position smearing as described in the text (b), experimental data coincident with a good Q3D event (c) and all singles DSSD events (d). Subfigures (b) and (c) are published in Ref. [91]. The magenta and green regions in (a) are used to highlight the Gaussian profiles of ^{14}C and ^{17}O detections respectively, while the magenta boundary in (d) highlights the experimental gate placed on data to avoid obscured pseudopixels. 77

3.27 The difference in energy between the front and back strips of a DSSD for events. This was fitted using two Gaussians and a constant background to a good approximation. The width of the relevant fitted Gaussian was 144.5(8) keV. 80

3.28 Histograms showing the measured proton energy for good Q3D events with corresponding ^{18}O excitation energies of 9.6 → 11.9 keV, for the experimental data (a), smeared Monte-Carlo data (b) and unsmeared Monte-Carlo data (c). A much better agreement with the centroids of the states and general features can be seen between (a) and (b). 82

3.29 Catania plots generated for states in the 9.6 → 11.9 keV region, assuming detection of a ^{14}C from a (^{18}O,α) event, using the energy of the highest energy hit per event. Three plots generated using Monte-Carlo simulation are provided, produced with different amounts of experimental smearing: no smearing (a), Resolution8.1 specific smearing (b) and all smearing effects (c). These can be compared to the experimental data (d), with (c) showing the closest agreement. Here, the energy of the undetected α product, as calculated through conservation of momentum, is plotted horizontally, while the energy difference between the beam and detected product nuclei is plotted vertically. The decay paths giving rise to each locus are shown in (a), with the detected particle given in red. 83

3.30 A depiction of the (^{12}C(^{7}Li,p,n)^{17}O) break-up reaction, following the decay of the intermediate ^{18}O (a). The area in which the ejectile ^{17}O can be incident is highlighted by the blue circle. Also shown are plots of the position of ^{17}O ejectiles in the plane of the DSSD array, for a Cartesian co-ordinate system (b) and a polar co-ordinate system (c). See text for details of the various regions shown in subfigure(b). These were produced through Monte-Carlo simulations of three excitations, centred at 8.5 MeV, 10.9 MeV and 20.0 MeV. From these three cases, only events arising from the 20.0 MeV excitation energy can be measured at azimuthal angles larger than 180°. Figure has been published in Ref. [92]. 86

3.31 Catania plots generated assuming detection of a ^{14}C from a ^{14}C+α decay (a) (b), detection of an α-particle from a ^{14}C+α decay (c) (d) and an ^{17}O from a ^{17}O+n (e) (f). Subfigures (a), (c) and (e) were generated using experimental data, while (b), (d) and (f) were generated using Monte-Carlo data, using all hits in each good event. Subfigures (a) and (b) have been published in Ref. [91]. 90

3.32 Catania plots generated assuming detection of a ^{14}C nucleus for the various hit numbers in the DSSD array in a good event. These hits are ordered by energy. The first 6 highest energy hits ((a)→(f) respectively) are given. The events near the top can be seen to persist through to the sixth hit. Subfigure (a) has been published in Ref. [63]. 92

3.33 Catania plots generated assuming detection of a ^{14}C. The regions due to ^{17}O+n decay and ^{14}C+α decay are shown in green and red, respectively. Features arising from γ decays beginning in the 7.117 MeV and 7.969 MeV states are given in magenta and yellow, respectively. Experimental data (a) and Monte-Carlo data (b) are provided for comparison. Figure adapted from Figure 3, published in Ref. [101]. 94

3.34 Cartesian views of the DSSD array for states ranging from 7.0 → 9.1 MeV, for experimental data (a) and Monte-Carlo data (b). The magenta boundary represents the experimental gate over five pseudopixels used to remove γ-event contamination. Also provided are the Monte-Carlo data for just the γ-decay events, showing the population of each pseudopixel by the ejectile ^{18}O. Figure adapted from Figure 4, published in Ref. [101]. 95

3.35 A comparison of experimental data (a) to Monte-Carlo data (b) for events with excitation energy between 14.3 → 14.5 MeV. All available decay paths were simulated, and the corresponding loci identified via Monte-Carlo are labelled. Figure has been published as Figure 4 in Ref. [92]. 97

3.36 Hit patterns on the DSSD array for (^{18}O,n) events with an excitation energy of 11.849 MeV. Monte-Carlo data populating the ground state of ^{17}O (a) and 3.055 MeV state (b) are compared with experimental data (c). Figure has been published as Figure 3 in Ref. [92]. 99

3.37 A Catania plot (generated assuming an (^{18}O,α) reaction) (a) and view of the detector array (b) for Monte-Carlo data. Red regions encapsulate the location of >99.9% 2n-decay events. Subfigure (b) is plotted using only events within the locus to the top left of subfigure (a), containing both (^{18}O,n) and (^{18}O,2n) events. Figure has been published as Figure 5 in Ref. [92]. 100

3.38 Energy distributions of ^{16}O daughters for (^{18}O,2n) events, decaying through an intermediate state in ^{17}O at 4.553 MeV(a) and a state at 6.356 MeV (b). Figure has been published as Figure 6 in Ref. [92]. 102

4.1 The Q3D excitation spectra obtained for the $-0.5 \rightarrow 2.5$ MeV region, gated on events with a corresponding hit in the DSSD array (a) and ungated (b). Note the different vertical scales for subfigures (a) and (b). 104

4.2 Monte-Carlo data generated for events in which a recoil ^{18}O nucleus was detected, produced in either the ground state or first excited state. A beam offset of 3 mm is shown in (a) and (b), matching the geometric efficiency of the experimental data but not the hit pattern, while an offset of 7 mm is shown in (c) and (d) which neither replicates the geometric efficiency nor hit pattern. Subfigures (a) and (c) show events smeared across the widths of the DSSD pseudopixels, while (b) and (d) show the true position of events before smearing. 106

4.3 Monte-Carlo data generated for events in which a recoil ^{18}O nucleus was detected, produced in either the ground state or first excited state. A beam offset of 6 mm is shown in (a) and (b), reproducing the hit pattern of the experimental data (c) well — the geometric efficiency does not. 107

4.4 Efficiency-corrected background profiles for the (a) 7800 keV, (b) 10500 keV, (c) 13200 keV and (d) 15100 keV regions, calculated as the product of the scaled background for each spectrum multiplied by the geometric efficiency profile across the excitation region. The red solid line, dashed magenta line and dotted blue line represent the background profile from the Q3D singles only, α-gated and n-gated events respectively. This demonstrates that the functional form is unchanged by efficiency correction due to uncertainties being larger than efficiency effects. Figure previously published in Ref. [57] as Figure 4. 111

4.5 Q3D spectra obtained for states between 7.0 and 9.4 MeV for Q3D singles data (a), α-decay events (b), n-decay events (c) and γ-decay events (d). The fitted background (dashed magenta line) is constant at just above 0 until the n-decay threshold, at which point the background becomes due to the two-body (^{17}O,n) phase space. 117

4.6 Q3D spectra obtained for states between 9.6 and 11.9 MeV for Q3D singles data (a), α-decay events (b) and n-decay events (c). The fitted background (dashed magenta line) is due to the two-body (^{17}O,n) phase space. 119

4.7 Q3D spectra obtained for states between 12.4 and 14.5 MeV for Q3D singles data (a), α-decay events (b) and n-decay events (c). The fitted background (dashed magenta line) is due to the combination of the two-body ^{17}O+n and three-body (^{16}O,2n) phase spaces. 121

4.8 Q3D spectra obtained for states between 14.5 and 16.3 MeV for Q3D singles data (a), α-decay events (b) and n-decay events (c). The fitted background (dashed magenta line) is due to the combination of the two-body (^{17}O,n) and three-body (^{16}O,2n) phase spaces. 123

4.9 Catania plots generated for the 15825(2) keV excitation in ^{18}O, assuming the decay of $^{18}O^{*}$ into ^{14}C (detected) $+\alpha$ for experimental data (a) and simulated data (b). The different decay paths are labelled and coloured to indicate the different loci. Figure previously published in Ref. [63] as Figure 5. 129

4.10 The proposed states assigned to the tentative cluster bands, with observed excitation energies (given in MeV) from Ref. [56], compared to the results from this work. States determined to display cluster structure are shown within a blue box. Figure originally published in Ref. [57]. 132

5.1 A depiction of a fragmentation reaction, showing the various stages with time progressing from left to right. The overlap region for both the beam and target nuclei are shown in yellow, while the nucleons that go on to produce the prefragment are shown in purple. 136

5.2 An overview of the LISE beam-line, showing the constituent quadrupole and dipole magnets. The ECLAN chamber, which contained the experimental set-up, was situated in the D4 room at the end of the LISE 2K beam-line. Figure taken from Ref. [120]. 138

5.3 Energy of particles plotted against time-of-flight, as measured along the LISE beam-line. Loci due to many different species are labelled, with the locus due to ^{10}Be circled in red. 139

5.4 Energy of particles plotted against time-of-flight, as measured along the LISE beam-line, following beam purification. The region containing ^{10}Be events is shown in a red box; the purification of the beam resulted in a 96% final purity in this instance. Events within the red box, but with higher energy than the obvious energy peak, were mostly likely caused by the high-energy ^{10}Be nuclei causing the production of charged particles within the silicon detector, resulting in an increased amount of charge measured. 140

5.5 Experimental set-up used in the current work. See text for more details. . . 141
5.6 A plot of the active area of the 1000 µm degrader, with horizontal strip number plotted against vertical strip number. The beam-spot is clearly visible in the centre of this active area. 142
5.7 Depiction of a Micron Semiconductor Ltd YY1 detector [123], showing some relevant angles and distances. Figure taken from Ref. [124], published as Fig. 2.143
5.8 Depiction of the two lampshade arrays used in this experiment. Here, the ^{10}Be beam can be seen travelling through the gas volume until it reacts, releasing a product ^{10}Be (measured in lampshade 2) and α (measured in lampshade 1). Figure adapted from figure in Ref. [124], published as Fig. 1. 144
5.9 Cartesian views of the lampshade 1 (a) and lampshade 2 (b) arrays. 144
5.10 The energy loss of particles through a thin detector plotted against kinetic energy measured in a thick detector. These data were collected using the 65 µm degrader detector in conjunction with the E detector described in the text. The loci associated with the detection of ^{10}Be and α nuclei are labelled. These data were taken during a typical experimental run using the experimental set-up shown in Figure 5.5. 145
5.11 A summary of the trigger logic used in the current work to gate the ADCs and TDC. 147
5.12 An example of the particle identification technique using the measured energy of a particle against TOF. Vertical lines can be seen, corresponding to the beam repetition from CSS2. 148
5.13 Measured energy against scattering angle for the telescope (a) and 500 µm DSSD (b). The kinematic lines corresponding to the elastic scattering of ^{4}He on ^{197}Au are plotted, and can be seen to agree well with the data. 149
5.14 A comparison of a typical nuclear reaction ($A + B \rightarrow C + D$) in the lab frame and in the centre-of-mass frame. 151

5.15 The excitation function generated for all hits in the lampshade arrays for the ^{10}Be+α exit channel. Excitation energies at 19 MeV, 20 MeV and 21 MeV were simulated, shown by the green lines — it is clear the reconstructed excitation function does not reproduce these energies accurately. See text for details. 155

5.16 A comparison of the different excitation functions produced using different hit patterns for the ^{10}Be+α exit channel. Details of each subfigure are given in the text. 156

5.17 Kinematic features generated for detected ^{10}Be products. The individual subfigures are described in the text. 157

5.18 Excitation functions generated through two different methods of determining the interaction position: inclusion of an offset based on position of the beam on the degrader (a) and averaged across several interaction positions, detailed in the text (b). The centroids extracted from both methods were reasonable, though the widths of the peaks are visibly larger in (a) relative to (b). 158

A.1 A generic two-body nuclear interaction, in which nuclei C and D are produced at angles ϕ and θ from the beam axis from the reaction of beam A and target B. 165

A.2 Plots for the ^{12}C(^{7}Li,^{7}Li)^{12}C (E_B = 44.0 MeV) case. The energies E_C and E_D are plotted against θ (a), against ϕ (b) and against the corresponding scattering angle for each nucleus (θ for D, ϕ for C) (c). A plot of θ against ϕ is also provided (d). 169

List of Tables

3.1 The centre angles (in-plane) and distances of each constituent DSSD in the Birmingham large-angular-coverage DSSD array, shown for both experimental set-ups (2016 and 2017) during which data were taken. 57

4.1 Branching ratio results for both the 7.0 → 9.1 MeV (2016) and 7.0 → 9.4 MeV (2017) excitation regions in ^{18}O, presented together for comparison. Results shown in green were within one standard deviation of one another, while results shown in yellow were within two standard deviations. 109

4.2 Branching ratio and θ_α^2 values for states not suggested to be members of proposed cluster bands, as published in Ref. [63]. Literature values are from Ref. [64], except where specified by footnotes. Values in red are discussed in section 4.2.7, and shown again in table 4.3 grouped by proposed rotational band. 113

4.3 A table summarizing the results obtained for states in the potential bands, compared with literature values. Errors shown in the table represent statistical errors and, where relevant, the error on geometric efficiency. Results given here were previously published in Ref. [57]. 125

Chapter 1

Introduction

To understand the nature of the Universe has been the fundamental aim of physics since the very beginning. The matter that comprises the Universe, and the way it interacts, in many ways remains a mystery. From as early as the ancient Greek concept of indivisible (ἄτομος) building blocks of nature, the search for a base set of rules that can be applied to all matter has been ubiquitous in the field of science. With the discovery of many chemical elements and the subsequent observations that their properties could be predicted in groups in the 19^{th} century, the first phenomenological clues that these building blocks existed were uncovered. This was particularly clear as the properties of these elements followed a repeating pattern, which seemed to be generally well-ordered by chemical mass [1]. With the discovery of the atomic nucleus by Ernest Rutherford et al. in 1911 [2], and subsequent discovery of the neutron by James Chadwick [3], these building blocks had been thought to be found. By varying the number of protons present in an atomic nucleus, the behaviours and properties of the atom change drastically as the corresponding number of electrons changes — this is, in fact, the underlying ordering that the periodic table produced by Dmitrii Mendeleev had ascertained before the existence of the proton had even been discovered. It is now known that

nucleons are actually composite particles, consisting of three quarks each: two up quarks and a down quark comprise the proton and two down quarks and an up quark comprise the neutron. However, the nuclear system itself presents many mysteries and difficulties in understanding it, even at a nucleon level. Great effort has been taken to elucidate the enigmatic behaviour of this structure, in attempts to develop models that can precisely and accurately predict properties of specific nuclei, such as the existence of energy levels or the deformation of the nucleus (which, in turn, affects the charge distribution and rotational energy).

The focus of this work is in the investigation of α-cluster structures: nuclear systems in which the constituent nucleons coalesce to form α-particle and other sub-structures within the nucleus. This phenomenon provides a good example of nuclear collective excitations that are not well described by the very successful spherical shell-model, and instances in which these structures are found can be very helpful in developing theoretical models. The advantage of these systems is clear in theoretical frameworks in which *ab initio* calculations are attempted — to model a nucleus from first principles, all of the different nucleons (and indeed their constituent quarks and gluons) must be modelled, all of which can interact with one another. Cluster systems reduce the degrees of freedom needed to be considered, greatly diminishing the required processing power. Thus, models can be tested on systems with a larger number of nucleons due to the ability to model cluster structures as few-body systems.

1.1 Thesis work

The work detailed in this thesis relates to two experiments. The first was an experiment performed at the Maier-Leibnitz Laboratory in Munich, populating high-energy states (7.0 $\rightarrow$ 16.0 MeV) in ^{18}O through the transfer reaction ^{12}C(^{7}Li,p)^{18}O* reaction (E_{Li} = 44 MeV).

The Q3D magnetic spectrograph was used to measure the recoil proton, identifying the state populated for each event, while the Birmingham large-angular-coverage DSSD array was utilised to measure products from the decay of the product ^{18}O, determining their species in the process. The aim of this experiment was to establish the α-decay branching ratio for various states proposed to have cluster structure, in order to identify the reality of this claim. The second experiment was performed at the GANIL facility in Caen, France, utilising the fragmentation method to produce beams of ^{10}Be and ^{12}Be. These were incident on a thick α-gas target, populating resonances in the ^{14}C and ^{16}C compound nucleus systems through use of the thick target inverse kinematics method. The aim of this experiment was to identify cluster structures in the two compound nuclei relating to Hoyle-state analogues, while simultaneously providing a proof-of-principle measurement using this novel experimental technique.

Chapter 2

Theoretical overview

This chapter will qualitatively and quantitatively describe some nuclear models, with an emphasis on cluster models of the nucleus. Theoretical concepts are discussed that are later referred to as part of the experimental techniques and analysis performed.

2.1 Liquid drop model

One of the simplest and earliest models for estimating properties of the nuclear system is that of the liquid drop model of the nucleus, first developed by George Gamov in 1929 [4] and later adapted and refined (due in part to the discovery of the neutron) by Bohr, Wheeler, and Weizsaćker [5] [6]. The liquid drop model operates under the assumption that the forces that bind nuclei together are analogous to those that cause the formation of drops in liquids (such as surface tension). This model gives a reasonable approximation for many nuclei, particularly for cases in which the density of nucleons remains approximately constant across a spherical nucleus. Mathematically, this model is often represented by the semi-empirical mass formula,

$$E_B = a_V A - a_S A^{2/3} - a_C \frac{Z(Z-1)}{A^{1/3}} - a_A \frac{(A-2Z)^2}{A} + \delta(A,Z), \tag{2.1}$$

where E_B represents the binding energy of a nucleus with atomic number Z and atomic mass A. The constants specific to each term, represented by a, are determined from experimental data: a_V =15.75 MeV, a_S =17.8 MeV, a_C =0.711 MeV, a_A =23.7 MeV and $\delta(A,Z)$ has a magnitude of ($+\frac{11.18 \text{ MeV}}{A^{1/2}}$ for odd-odd and even-even nuclei, in which the numbers of protons and neutrons are both odd (odd-odd) or both even (even-even), but this term vanishes for even-odd nuclei.

The first term of this expression is known as the volume term, which is linear in terms of A due to its proportionality to the volume. This term represents the attractive strong nuclear force, as well as the incompressibility of nuclear matter due to the very short range repulsion of the nuclear force, which only acts between close nucleons due to its short range. Another problem that arises because of the short range of the nuclear force is that nucleons on the surface experience less force than those further in the nucleus. This is corrected for by the negative surface term (the second term in equation 2.1), which is appropriately proportional to $A^{2/3}$ to represent the surface of the spherical nucleus. The next consideration for investigating the binding energy of a nucleus is the repulsive nature of the electrostatic interactions between constituent protons. This term, referred to as the Coulomb term, approximates the electrostatic potential energy — this is apparent dimensionally, as the Coulomb terms depends both on a distance, $1/A^{1/3}$ (where $A^{1/3}$ is proportional to the radius of the nucleus, R), and the square of the charge, though the relevant factor is $Z(Z-1)$ rather than Z^2 as one proton cannot repel itself.

The fourth term is the asymmetry term, again used for correction — based on the Coulomb term, it is possible to draw the conclusion that systems of zero or one protons, with a large number of neutrons, should be more stable than nuclei close to $A = 2Z$. The reason

this is not observed in nature, and hence what this asymmetry term represents, is that as protons and neutrons are both fermionic particles, they are subject to the Pauli Exclusion Principle (PEP) and thus must fill up energy shells with increasing energy requirements (as with electrons in the atomic system). The spin dependence of the nuclear force also plays a role — this behaviour is exemplified by the two nucleon systems: nn, pp and pn, of which all the singlet states are unbound. The triplet state of the pn system, however, is bound (there exists no triplet state of the two same nucleon systems, as the PEP requires opposing spins).

The final term is known as the pairing term, which again is related to the PEP. This term is 0 when considering even-odd nuclei (A is odd), positive ($+\frac{11.18\ \mathrm{MeV}}{A^{1/2}}$) for even-even nuclei and negative ($-\frac{11.18\mathrm{MeV}}{A^{1/2}}$) for odd-odd nuclei. The existence of this term matches the observed stability of nuclei in nature — even-even nuclei make up the majority of known stable nuclei ($^{146}/_{252}$), vastly outnumbering stable odd-odd nuclei ($^{5}/_{252}$). These final two terms, which are related to a quantum-mechanical treatment of nucleons and are evidently necessary based on observation, hint towards models that are more complex.

2.2 Spherical shell-model

It is apparent that quantum mechanics, in particular the degeneracy of energy levels caused by the PEP, is at work in the nuclear system. By plotting the binding energy per nucleon of different nuclei, like in figure 2.1, obvious peaks are present for the ^{4}He, ^{8}Be, ^{12}C and ^{16}O nuclei. This behaviour hints towards an analogue of the atomic system, in which certain elements (e.g. noble gases, which have their outer electron shells fully occupied) are notably more chemically stable than others. Through solving the Schrödinger equation for the nuclear system, by considering each nucleon to be in a potential well formed by an average of all the interactions with its neighbours (a mean-field approach), a series of quantised energy levels,

or shells, are obtained.

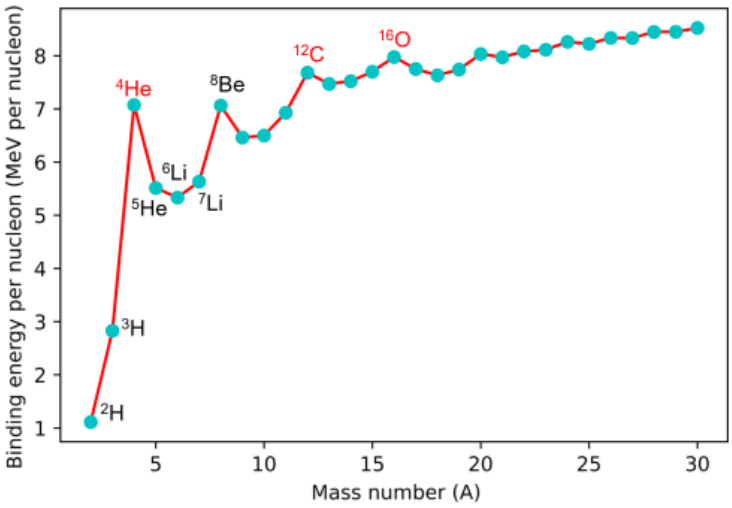


Figure 2.1: A plot of binding energy per nucleon against mass number, for isotopes corresponding to the largest binding energy per nucleon for each mass number between $A = 2$ and $A = 30$. Isotopes labelled in red are nuclei with complete nucleon shell or sub-shell closures. Data taken from Ref. [7].

The form of one such representative potential, known as a Woods-Saxon potential, is given by

$$V(r) = -\frac{V_0}{1 + \exp\left(\frac{r-R}{a}\right)} \tag{2.2}$$

as a function of r, which represents the distance a nucleon has been removed from the centre of a nucleus. In equation 2.2, V_0 represents the energy difference from the top to the bottom of the potential well, R is the mean radius of the nucleus (the radius at which $V(R) = {}^{V_0}/_2$) and a is the diffuseness parameter [8]. The Woods-Saxon potential is easily described phenomenologically, as it is chosen to reproduce the observed nuclear density. This density is a result of the nature of the strong nuclear force, a residual interaction of the strong force that is mediated by π mesons rather than the massless gluons that mediate the

strong force between quarks. From the Heisenberg Uncertainty Principle, one can estimate the range of the nuclear force. Using the π_0 meson as an example, the energy of the exchange particle can be calculated from its mass,

$$\Delta E = mc^2 = 135.0 \text{ MeV}. \tag{2.3}$$

It is then possible to calculate a lifetime, Δt, for this exchange particle, by substituting the value from equation 2.3 into the energy-time form of the Heisenberg Uncertainty Principle, $\Delta E \Delta t \approx \hbar$ (where $\hbar$ is the reduced Planck's constant) and rearranging to get

$$\Delta t \approx \frac{\hbar}{\Delta E} \approx 1.6 \times 10^{-23} \text{ s}, \tag{2.4}$$

which in turn can be used to calculate a range. Assuming the π_0 travels at a speed of c, the range of this force is ≈ 5 fm. The Woods-Saxon potential rapidly drops off to nearly 0 at roughly this range, when sensible parameters for R and a are chosen. It is also attractive at values of r below this value, as nucleons in nuclei are bound together by this potential. The potential given in equation 2.2 is incomplete, however, as the experimentally determined density of nuclei implies that nucleons are not extremely compact (the known incompressibility of nuclear matter, as mentioned previously in section 2.1), and hence the potential cannot be wholly negative for short distances. Further requirements of an appropriate potential can be extracted by comparison of shell model predictions to experimental data.

Nucleons fill up vacancies in shells rather than all collapsing to the lowest energy state because, much like electrons, the proton and neutron are fermions and are thus subject to the Pauli Exclusion Principle. However, as protons and neutrons are distinct from one another due to different quark configurations, each nucleon type fills up shells independently. The lowest energy shell, $1s$ (using spectroscopic notation, where the first number represents the radial quantum number, and s,p,d... represent 0,1,2... units of orbital angular momentum, $\vec{l}$, respectively), has a vacancy for two of each nucleon as by adopting opposing spins, $\vec{s} = +\frac{1}{2}$ or $\vec{s} = -\frac{1}{2}$, they can be distinct from one another. Figure 2.2 shows a basic example of the



Figure 2.2: A diagram depicting the shells and sub-shells of the nuclear shell model (increasing in energy from the bottom) alongside the number of nucleons that can occupy each sub-shell and the total number of nucleons in a nucleus when a sub-shell is filled (total occupancy). Numbers in bold and underlined represent magic numbers, corresponding to a closed shell and hence increase in stability. The splitting of a shell due to the spin-orbit interaction can be seen to cause other shells to lie between its sub-shells, like with the $1d$ and $2s$ shells — see text for details.

lowest-energy shells as described by nuclear shell model, highlighting the different shells and their corresponding occupancies.

Nuclear excitations can hence be described as valence nucleons being "excited" from a

lower shell to a higher shell by having too much energy, and when a nucleon de-excites from a higher shell to a lower shell in the same nucleus, a γ-ray is emitted from the nucleus equal to the energy difference between the two shells. Closed shells result in a much more stable nucleus due to the paired nucleons requiring more energy to excite them into an empty shell, and there are no vacancies for lower shell nucleons to combine with previously unpaired nucleons. Examples of isotopes for which this is the case are shown in red in figure 2.1. Based on the solutions to the Schrödinger equation, peaks at ^{4}He and ^{16}O due to the full shell closure are expected. However, the existence of a peak at ^{12}C suggests there is another factor to consider. The inclusion of a spin-orbit potential causes the theoretical shells to split into sub-shells and thus match the vacancies seen in experiment [9]. Each original shell, defined by the orbital angular momentum, splits into two sub-shells as the spin of a nucleon can either support or oppose the motion of the orbital angular momentum, resulting in different amounts of total angular momentum. The occupancies in a sub-shell, n, can be calculated using the total possible angular momentum of a nucleon in the sub-shell, j, by

$$n = 2|\vec{j}| + 1 = 2(|\vec{l} + \vec{s}|) + 1, \tag{2.5}$$

where $\vec{j} = \vec{l} + \vec{s}$. The total angular momentum must be half-integer, as $\vec{l}$ is integer and $\vec{s}$ is $\pm\frac{1}{2}$, thus n will always be integer. This splitting and corresponding degeneracy matches what is observed with the binding energy per nucleon of ^{12}C, as six nucleons of the same kind results in the closure of the $1p_{3/2}$ shell.

The splitting of these sub-shells, and the energies at which they lie relative to one another, also provides some explanation for the magic numbers that are observed in nature — no magic number exists for the closure of the $2s$ shell, as the splitting of the $1d$ shell creates a situation in which the $1d$ is only partially filled when it becomes energetically favourable for nucleons to occupy the $2s$ level. As the $1d_{3/2}$ is close in energy to the $2s$ shell,

nucleons in the $2s$ shell can be excited with relatively little energy. Thus, there is a reduction in binding energy per nucleon and hence stability — the closure of the $1f_{7/2}$ sub-shell, on the other hand, does result in a noticeable increase in stability due to its distance from the $2p_{3/2}$ sub-shell. These shells, however, do not explain the increase in stability observed in the ^{8}Be nucleus relative to its neighbours.

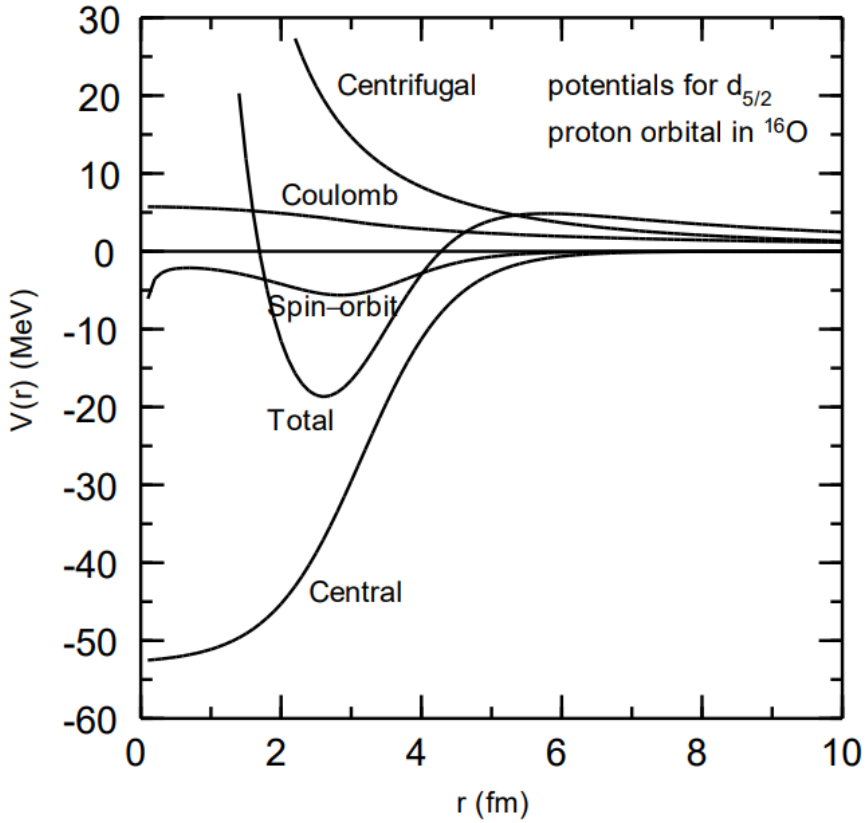


Figure 2.3: Calculated values of the different potentials in the ^{16}O nuclear system for varying r, using the proton $1d_{5/2}$ orbital. Here, the central potential represents that described in equation 2.2. The total potential can be seen to be attractive only between values of roughly 2-5 fm, mimicking the behaviour of real nucleons in a nucleus. Calculations here were performed using the program WSPOT.FOR, with this figure taken from Ref. [10] as Figure 1.2.

The addition of the spin-orbit potential to the Woods-Saxon potential described in

equation 2.2 does not, however, produce a potential well in which nucleons can be bound at an appropriate distance. These potentials can, however, be combined with a Coulomb potential for the repulsive interactions between protons and a centrifugal barrier for nucleons with non-zero values of l. As both of these potentials are positive (repulsive) and their magnitude increases with decreasing r, a potential well can be formed in which bound nucleons can exist, matching measurements of nuclear density. An example of these potentials from Ref. [10] is shown in figure 2.3, calculated for the $1d_{5/2}$ proton orbital in ^{16}O.

2.3 Clustering

The spherical shell-model is very successful, as it is able to accurately predict the decay properties and excitations of many nuclei to a great degree. Issues with this model become apparent, however, when considering the collective excitation of nucleons rather than the excitation of individual valence nucleons. The binding energy per nucleon of ^{8}Be, for example, can be explained when it is known that this nucleus exists not as a spherical collection of protons and neutrons, but rather a two body system formed of a pair of weakly-(un)bound α-particles — the high binding energy per nucleon is due to the high binding energy per nucleon of its constituent α-particles, and this nucleus undergoes α-decay as its primary (and only) decay mode due to the slightly higher binding energy per nucleon of the ^{4}He nucleus (7.074 MeV/A) when compared to that of ^{8}Be(7.062 MeV/A). This interesting structure is an example of nuclear clustering.

Nuclear clustering is a well-established and important phenomenon in nuclear physics, in which the constituent protons and neutrons of a nucleus can condense and hence form substructures. The most common of these substructures is the α-particle, with much theoretical and experimental work supporting its existence as a cluster. One of the earliest

indicators that the α-particle can form inside of a nucleus was α-decay, discovered by Ernest Rutherford and Paul Villard in 1899 [11] and proven to be the emission of a ^{4}He nucleus in 1907 by Rutherford and his colleague, Thomas Royds [12]. Further theoretical evidence is presented by the large binding energy per nucleon of the ^{4}He nucleus relative to similar nuclei (7.074 MeV/A for ^{4}He as opposed to 2.567 MeV/A for ^{3}He and 2.833 MeV/A for ^{3}H) due to its closed $1s_{1/2}$ shells. Suggestions for the existence of α-particle structure in light nuclei came as early as the late 1930s, with predictions from Hafstad and Teller [13] based on binding energy and comparison of the level structure with that obtained for the nuclei using the independent-particle model (the shell-model).

Direct evidence for the existence of α-clustering came in 1954, when astrophysicist Fred Hoyle hypothesised that the contemporary understanding of the triple-α process in stars was insufficient for ^{12}C, and consequently heavier elements, to exist in such a large quantity as was apparent in the Universe [14, 15]. This is due to the unbound nature of ^{8}Be, which has a half-life of $\approx$ 0.6 femtoseconds, and the lack of other stable mass-5 or mass-8 isotopes of any element. Hoyle postulated that this lifetime was too short for a 3rd α-particle to interact and form ^{12}C unless ^{12}C possesses an excited state, slightly above the 3α -threshold of 7.27 MeV [16], which had a 3α-structure. The existence of this resonance would increase the cross-section for this reaction by several orders of magnitude — enough to match the observed amount of ^{12}C, and hence heavier elements, in the Universe. This state, situated at 7.65 MeV, was subsequently measured by experimentalists and confirmed Hoyle's prediction [17, 18], and thus was named the "Hoyle state". That this is the only named state in nuclear physics underlines the unusual nature of the discovery which, rather than being measured directly or explicitly calculated, was inferred from phenomenological observations. In about 1/2500 instances, the Hoyle state can de-excite into the ground state via γ-emission rather than decay back into three distinct α -particles — this too was predicted prior to the measurement of this branching ratio, using observed ^{12}C and ^{16}O abundance ratios relative

to lighter nuclei such as ^{1}H and ^{4}He to fine-tune this prediction.

The Hoyle state represented a failure in the nuclear shell model, as the excitations of individual nucleons was unable to predict the properties of the Hoyle state. This was overcome by the efforts of Haruhiko Morinaga, who could predict the Hoyle state and some of its properties by characterising it as a weakly bound 3α -system [19, 20]. The new physics shown by the Hoyle state began a large amount of theoretical work, notably that of Kiyomi Ikeda et al. The Ikeda diagram (Figure 2.4) is still commonly used to show the threshold excitation energies required for alpha clusters to condense from even-Z, $N = Z$ nuclei that hence could be described as alpha-conjugate [21]. The intrinsic link between the emergence of α-cluster structure and excitation energy is clear from this work.

2.3.1 Core + alpha

The most basic cluster systems that can exist are found just above the ground state nuclei (which occupy the diagonal) in the Ikeda diagram, the core + α system. The model was developed as early as the 1970s, when theoretical calculations predicted that the density of nuclear matter dropping to a third of its normal value inside of a nucleus could result in a phase change; the density of nuclear matter clearly must be continuous but must also be 0 outside of the nucleus, meaning that this phase change (through which an α -particle can condense) would occur at the surface, due to the relatively constant nature of the density inside the nucleus [14]. The condensed α then proceeds to orbit around the remaining core, the latter containing two fewer protons and two fewer neutrons than the original nucleus. As only one α -particle needs to form, these systems can theoretically be found at relatively low excitation energies. A well-studied example of this exists in ^{20}Ne — the ^{16}O + α system [22, 23]. Predictions made using this α-cluster structure are able to accurately reproduce many parts of the known level scheme of the ^{20}Ne nucleus [24, 25].

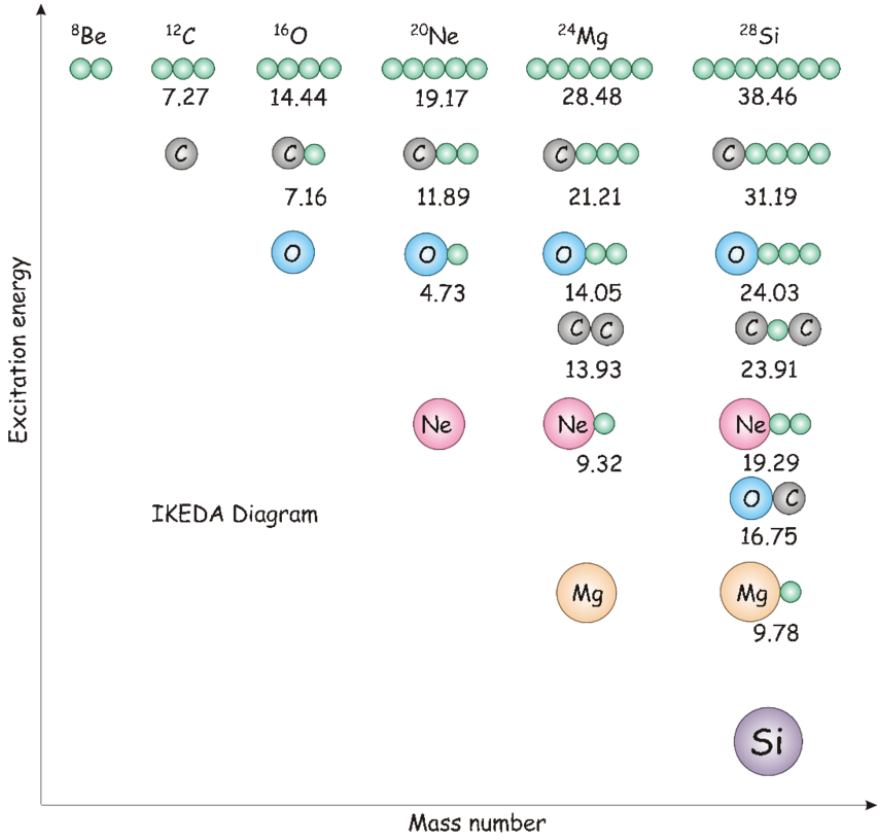


Figure 2.4: The Ikeda diagram, showing the alpha thresholds for various even, $N = Z$ nuclei, including the triple alpha threshold of 7.27 MeV for ^{12}C. Taken from Ref. [15] and created by Tz. Kokalova.

2.3.2 Nuclear molecules

Nuclei that contain valence protons or neutrons are also expected to show evidence of clustering; extended versions of the Ikeda diagram exist, an example of which can be seen in Figure 2.5, demonstrating potential cluster structures in neutron-rich nuclei. A structure that has been predicted to form in some of these instances, such as ^{9}Be, is called a nuclear molecule, as explained below. As stated in Section 2.3, ^{8}Be has a very short half-life and an $\alpha + \alpha$ structure. However, ^{9}Be is stable with the simple addition of a neutron to the system. An explanation for this is found through the description of nuclear molecules: the valence

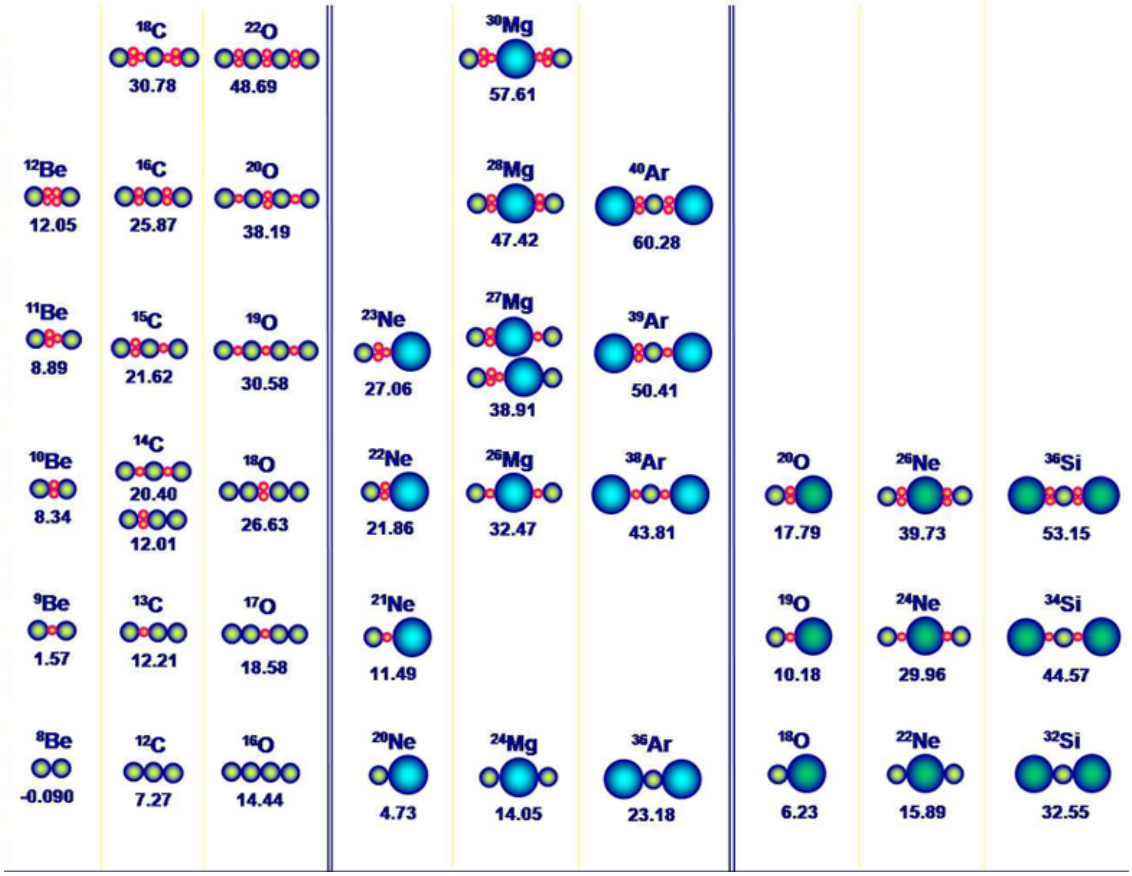


Figure 2.5: The extended Ikeda diagram, showing nuclei with excess neutrons. The lighter nuclei depicted in Figure 2.4 can be seen in the bottom left of the diagram, with neutron number increasing along the vertical axis. Original from Ref. [22], edited figure (used here) from Ref. [26].

neutron acts analogously to an electron in a covalent chemical bond, binding the two alpha particles together through the strong nuclear force, and indeed this model has had success in predicting both the spin-parity of the ground state ($J^\pi = \frac{3}{2}^-$) and the properties of the first excited state ($J^\pi = \frac{1}{2}^+$) [15]. The addition of neutrons to a system is typically more likely to increase stability, particularly in α-cluster candidate nuclei which tend to be close to $N = Z$, due to the lack of Coulomb repulsion between the valence neutron and the α-cores.

Similar to chemical bonds, there are multiple ways in which the neutron orbital can be

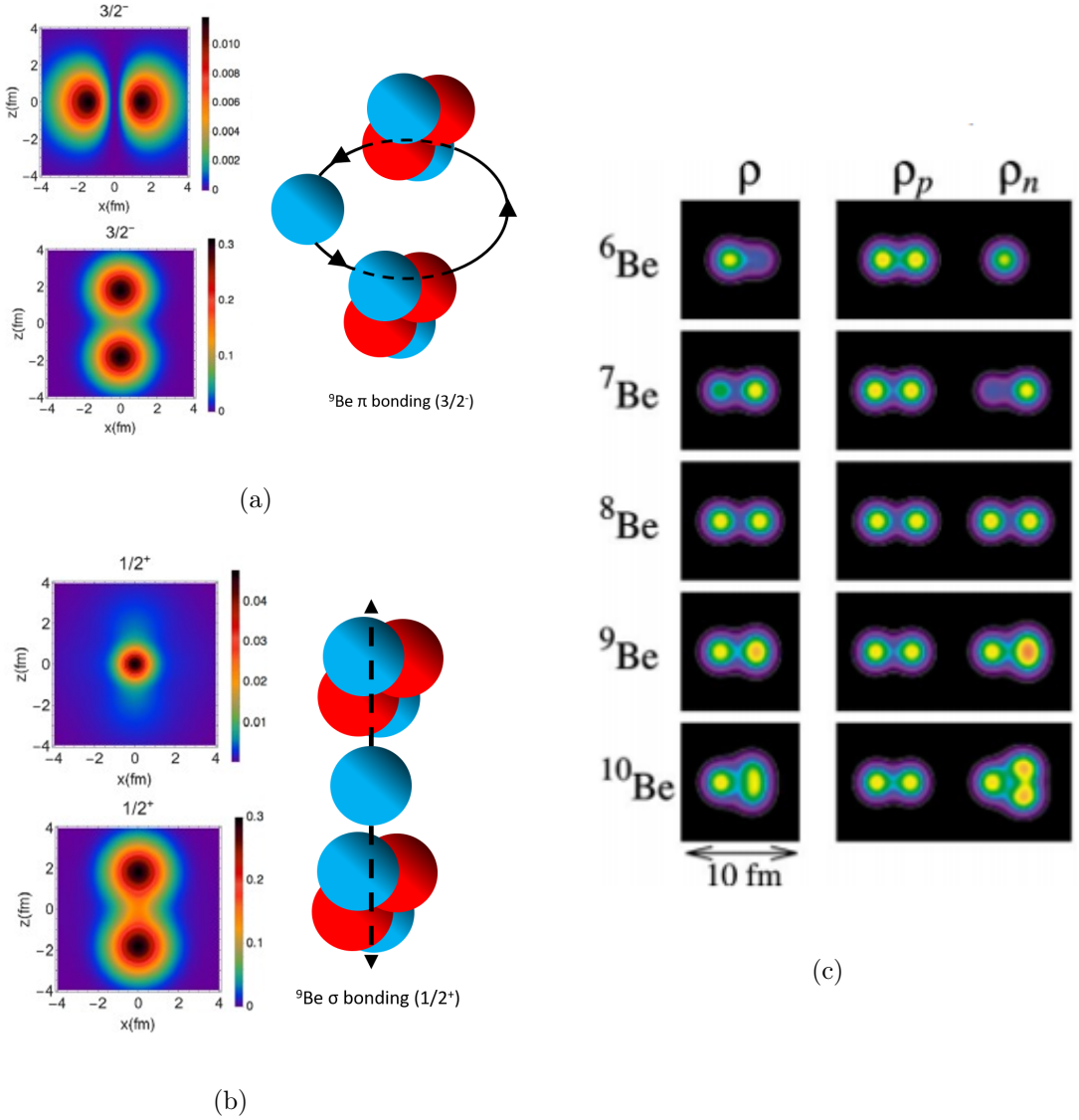


Figure 2.6: Cluster Shell Model (CSM) calculations performed in Ref. [27] for the ground state of ^{9}Be showing neutron density (top) and matter density (bottom), as well as a depiction of the π-bonding that occurs in this state, are shown in (a). The same is shown in (b) for the 1^{st} excited state, along with a depiction of the σ-bonding that occurs in this state. Antisymmetrized Molecular Dynamics (AMD) calculations, which is a theoretical framework from which properties of nuclei can be derived *ab initio*, for the proton and neutron densities of light Be isotopes from Ref [28] are shown in (c). The neutron density for ^{9}Be shows a structure consistent with π-bonding.

positioned in order to bind clusters together. The ground state and first excited state of ^{9}Be both have different bonding properties, caused by different overlaps of the valence neutron $1p_{3/2}$-orbital. In the lower energy ground state system, the movement of the neutron in its orbital is perpendicular to the axis through the centre of the two α -particles, which is known as π-bonding as with chemical bonds. When the movement of the neutron is parallel to the axis through the α -particles, as it is for the 1^{st} excited state, this is known as σ-bonding. Examples of calculations of neutron density done on ^{9}Be are shown in Figure 2.6, as well as depictions of both π-bonding and σ-bonding in the ^{9}Be system.

2.4 Rotational bands

The energy of an excited state in a nucleus, E_x, can be related to its total angular momentum, J, via

$$E_x(J) = \frac{\hbar^2}{2\Theta}(J(J+1)) + E_0, \tag{2.6}$$

where Θ represents the momentum of inertia of the nucleus and E_0 is a constant. If the excitation energy of states is plotted against the corresponding $J(J+1)$ values, it is clear from Equation 2.6 that states with an identical Θ and E_0 would be expected to lie on a straight line, and the members of this line are collectively known as a rotational band. The constant E_0 corresponds to a state that would lie on this line with no total angular momentum, whether one exists or not. As these states share a moment of inertia, it can be inferred that they also share a structure formed by their nucleons. In cluster physics, it is often predicted that cluster states (such as the Hoyle state) should have corresponding excitations for higher values of J^{π} [29, 30].

2.5 Alpha widths

The total decay width, Γ, of a nuclear state is defined as the total rate of decays that occur from that state. If there are multiple decay paths open to the excited state, Γ is simply the sum of all of the individual widths, or decay rates, of each decay path. These individual widths, Γ_i, where i represents a single decay path, are known as the partial widths. The ratio of a partial width to the total width for a particular state gives the branching ratio for a certain decay. From this value, the reduced partial width, γ_i^2, can be calculated by removing barrier penetrability contributions, P_λ, through

$$\gamma_i^2 = \frac{\Gamma_i}{2P_\lambda}. \tag{2.7}$$

This value can then be compared to the Wigner limit, defined as

$$\gamma_W^2 = \frac{3\hbar^2}{2\mu a^2}, \tag{2.8}$$

where μ is the reduced mass and a is the channel radius. The Wigner limit is the partial width of a state that has a uniform wavefunction within the channel radius, and 0 outside of the sphere defined by it [31, 32]. By taking the ratio of the reduced α partial width (looking at the branching ratio for α -decay for a particular state against all other decay modes) to the Wigner limit, the tendency towards clustering for a state can be determined. The range of values this variable, known as the dimensionless reduced width (denoted by θ_α^2), can take is between 0 and 1. Typically, a value of larger than 0.1 is thought to be substantially clustered.

2.6 Selection rules

As the α -particle is an even-even nucleus, it has a ground state spin-parity of 0^+. As the α -particle is bosonic in nature, it can only carry away integer values of angular momentum. If the α -particle carries away an odd value of angular momentum (1,3,5...) then its parity must be negative, based on the relationship $P = (-1)^l$ (the α -particle has even parity), while it must have positive parity if it carries away an even amount (0,2,4...). If an initial nucleus α -decays to a final nucleus with a ground state of 0^+ (for example, in the case where both the initial and final state nuclei are even-even) and this final nucleus has no excitation energy then only natural parity states in the initial nucleus (0^+, 1^-, 2^+, 3^-, 4^+ etc.) can α -decay to the ground state of the final nucleus. This is true of any natural parity state in the final nucleus, while unnatural parity states (0^-, 1^+, 2^- etc.) in the final nucleus could only be populated by the α -decay of an unnatural parity state [33].

As the nucleus consists of protons and neutrons, there is a distribution of the magnetic moments and charge that gives rises to magnetic and electric fields, as well as currents due to the effect of orbiting protons, the most common of which take the form of dipole, quadrupole and octupole, which all vary in intensity with angle. As the distribution of these quantities will vary as nuclei are excited and de-excited between different states, there will be a shift in the associated fields which gives rise to electromagnetic radiation. This is why the de-excitation of a nucleus causes the emission of a γ-ray. This type of decay can fall into two types: electric or magnetic transitions. Electric transitions are defined as those which are ascribed by a change in the charge distribution, while magnetic transitions are those caused by a shift in the current distribution of orbiting protons [34]. The different types of transitions have with them an opposite associated parity shift, each defined by the change in total angular momentum between the two states. As the photon has odd parity, the parity change between these states is defined as $P = (-1)^{l+1}$, and if there is no parity change then

the γ-ray is from an electric transition for an even angular momentum change, and magnetic if the change is odd. The reverse is true for a parity change between the 2 states. There is a suppression of the rate of γ-decay for larger angular momentum changes, characterised by the Weisskopf estimates [35], based on single proton excitations (see [34] for derivation):

$$\begin{aligned} \lambda(E1) &= 1.0 \times 10^{14} A^{\frac{2}{3}} E_\gamma^3, \\ \lambda(E2) &= 7.3 \times 10^{7} A^{\frac{4}{3}} E_\gamma^5, \\ \lambda(E3) &= 3.3 \times 10^{1} A^{2} E_\gamma^7, \end{aligned} \tag{2.9}$$

$$\begin{aligned} \lambda(M1) &= 5.6 \times 10^{13} E_\gamma^3, \\ \lambda(M2) &= 3.5 \times 10^{7} A^{\frac{2}{3}} E_\gamma^5 \quad \text{and} \\ \lambda(M3) &= 4.5 \times 10^{1} A^{\frac{4}{3}} E_\gamma^7, \end{aligned} \tag{2.10}$$

where the electric transition decay rates for a change in angular momentum of 1, 2 and 3 are shown in Equation 2.9 and the magnetic transition decay rates for the same changes are shown in Equation 2.10. Here, E_γ represents the energy difference between the initial and final state and A is the total number of nucleons in the nucleus.

However, these decay probabilities (λ) are larger for electric transitions than magnetic transitions (for the same angular momentum change), approximated by

$$\frac{\lambda(\mathrm{E})}{\lambda(\mathrm{M})} \approx 2A^{\frac{2}{3}}. \tag{2.11}$$

In fact, based on the Weisskopf estimates, the magnetic transitions tend to compete more with the electric transitions corresponding to one order higher. As electric transitions are preferred, it is much more likely for a natural parity state to decay to another natural parity

state than an unnatural parity state of the same angular momentum, and vice-versa for unnatural parity states.

2.7 Nuclear reaction theory

The theory behind nuclear reactions, and the mechanisms by which various nuclei can be produced, is of vital importance both in nuclear structure physics as well as more generally. The nuclear reactions that occur in the cores of fission reactors must be properly modelled and predicted, both for understanding the various energies and amounts of materials needed for a desired energy output, but also in understanding the production of waste products, actinides and radioisotopes made by neutron-activation of reactor materials. Nuclear reactions are also often used to produce medical isotopes, and a detailed understanding of the relevant mechanisms can potentially allow for increased production rates or higher purity.

Nuclear reactions, particularly in the context of nuclear structure physics, involve a beam nucleus incident on a target nucleus — the final state products are dependent on the type of reaction that occurs. The likelihood of a certain kind of reaction taking place between two particles is typically given by the cross-section, σ, which has the dimensions of area, essentially defining the effective area across which a collision would occur. More generally, the cross-section is a measure of the flux for an outgoing particle (of a certain species) as a fraction of the incoming flux from the beam nucleus [36]. A slightly more useful quantity, known as the differential cross-section, is often used due to the angular dependence of cross-section for various reactions. Often the differential cross-section is written as $\frac{d\sigma}{d\Omega}$, where Ω is the solid angle — this value can be integrated across $\Omega = 0, 4\pi$ to give the total, or integrated, cross-section [37].

2.7.1 Direct reactions

Direct reactions refer to interactions in which nuclei interact with one another only as their collective whole, or with a limited number of surface nucleons, such that they can be described by perturbation theory using only first-order corrections [36, 38].

A very simple type of direct reaction is elastic scattering, in which the incident particles scatter off one another and as such change direction. In the case of nuclear elastic scattering, all of the initial kinetic energy of the beam nucleus is transferred to the kinetic energy of the final-state nuclei, so no (or negligible) energy is lost in the process. A common example of this phenomenon is Rutherford scattering, in which two charged nuclei interact with one another via the Coulomb interaction and scatter elastically. This process dominates at low scattering angles, θ, as can be seen by the Rutherford scattering differential cross-section relationship

$$\frac{d\sigma}{d\Omega} = \left(\frac{Z_B Z_T \alpha(\hbar c)}{4E \sin^2 \frac{\theta}{2}} \right)^2 , \tag{2.12}$$

where Z_B and Z_T are the respective charges of the beam and target nuclei, α is the dimensionless fine structure constant, $\hbar$ is the reduced Planck's constant, c is the speed of light in a vacuum and E is the kinetic energy of the beam nucleus.

Inelastic scattering, depicted in figure 2.7, is a similar process — the difference compared to nuclear elastic scattering is that some of the initial kinetic energy of the beam nucleus is used to produce one or more of the product nuclei in an excited state, and hence the kinetic energy of the final-state products is lower than that of the initial-state kinetic energy. In order to do this, the beam nucleus must have sufficient energy to overcome the Coulomb barrier of the target. In the case shown in figure 2.7, of a ^{4}He nucleus incident

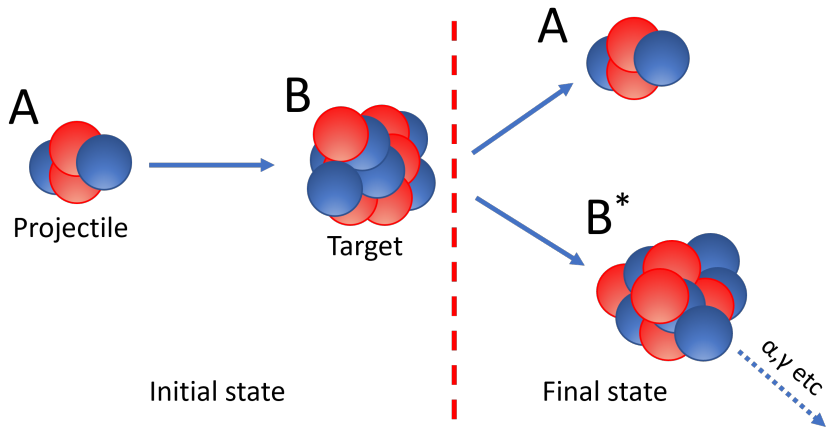


Figure 2.7: An example of inelastic scattering shown in the laboratory frame, involving a ^{4}He beam (A) incident on a ^{12}C target (B), leaving the ^{12}C in an excited state. The two nuclei do not transfer nucleons, though missing kinetic energy in the final state is used to rearrange the nucleons of the ^{12}C.

on a ^{12}C target, the beam must have an energy of at least 3.7 MeV in order to classically overcome this barrier. The ^{12}C is excited into a higher energy level, resulting in a change in the nucleon structure. The excited ^{12}C nucleus will then decay, perhaps by γ-emission to a lower-lying level or, if energetically allowed, by particle emission, such as α-decay into ^{8}Be. The cross-section of inelastic scattering dramatically increases for population of a resonance, so the differential cross-section in terms of both angle and energy $(\frac{d^2\sigma}{d\Omega dE})$ can be measured in order to identify resonances. This is typically measured away from the beam axis, due to contamination at low angles from Rutherford scattering (as well as unscattered beam nuclei).

Other types of direct reaction can involve the transfer of surface nucleons, such as in the case of aptly named transfer reactions. This type of reaction was particularly relevant for the experiment described in chapters 3 and 4, as the ^{12}C(^{7}Li,^{18}O*)p reaction that was utilised is a transfer reaction, in which the beam ^{7}Li transfers a ^{6}He nucleus to the target ^{12}C in order to form ^{18}O, populated in a range of energy levels limited by the initial kinetic

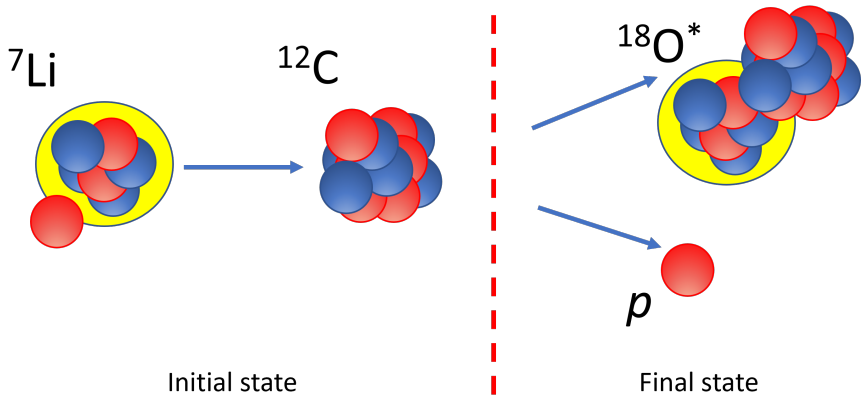


Figure 2.8: A transfer reaction shown in the laboratory frame, in which a ^{7}Li beam transfers a ^{6}He nucleus (shown with a yellow ellipse) to a target ^{12}C nucleus, forming ^{18}O (potentially in an excited state) and p products. There is a Q-value associated with this interaction due to the difference in mass of the initial and final states.

energy of the beam. The excitation energy of the ^{18}O product can then be determined easily through measurement of the kinetic energy and momenta of the recoil p. As transfer reactions have an associated Q-value, due to the difference in the total mass of the inital and final states, it is possible for the final state to either have a greater or smaller amount of kinetic energy than the initial state.

2.7.2 Compound nucleus formation

Compound nucleus formation is a more complicated type of reaction in terms of modelling the behaviour of the nucleons, as all of the nucleons present in the initial state nuclei interact with one another to form an intermediate compound nucleus. This interaction takes longer than those associated with direct reactions as a result, and this is sufficiently long that the constituent nucleons are able to collide, distributing the kinetic energy from the initial state. Thus, the method by which the compound nucleus then breaks apart should be independent of the reaction that formed it — this is known as the independence hypothesis [39, 40].

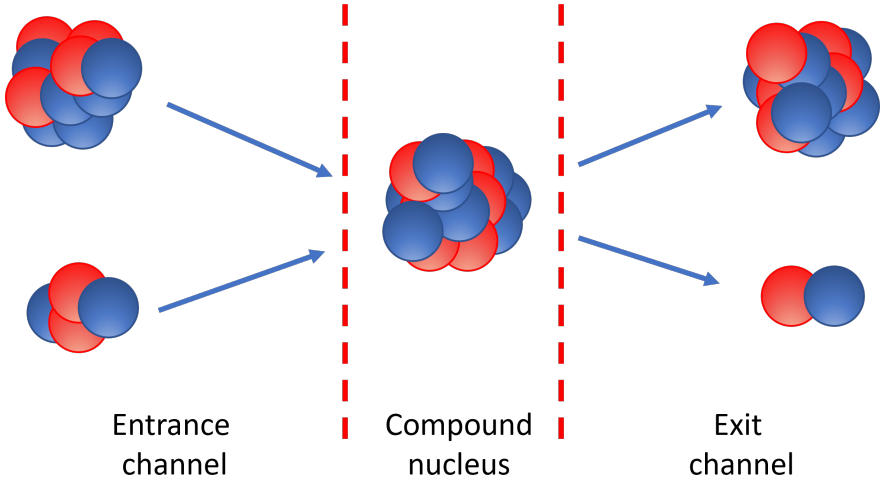


Figure 2.9: A compound nucleus formation reaction shown in the centre-of-mass frame of the compound nucleus, in which a ^{10}Be nucleus and ^{4}He nucleus (in the entrance channel) fuse to form ^{14}C. This compound nucleus then breaks apart into two fragments in the exit channel, a deuteron and a ^{12}B nucleus.

Hence, whether a nucleus is formed via a direct reaction (such as via nucleon transfer) or via compound nucleus formation should not affect the width or excitation energy extracted for a given resonance. Compound nucleus formation is often used to investigate excitation functions for various nuclei, investigating the cross-section for compound nucleus formation as a function of initial beam energy. This type of reaction was utilised in the investigations described in chapter 5 and an example is depicted in figure 2.9.

The decay of a compound nucleus, particularly in regions of low excitation energy where resonances are distinct (i.e. where the average energy difference between the resonances is larger than the average widths of the states), can be well described by R-matrix theory, which can be used to calculate differential cross-sections as a function of energy and angle for a given two-body entrance and exit channel. R-matrix theory is described in more detail in section 2.7.4.

2.7.3 Thick target inverse kinematics

Thick target inverse kinematics, often referred to as TTIK, is an experimental technique first described in Ref. [41] which can be used to extract values of $(\frac{d^2\sigma}{d\Omega dE})$ for given scattering angles and beam energies and thus measure excitation functions. The thick target, commonly a gas target at a chosen pressure, fills the experimental chamber and the beam nucleus is slowed via interactions as it traverses through the gas volume. The advantage over typical thin target measurements is that due to the beam slowing down until it is stopped in the gas, a continuous range of interaction energies can be investigated for a single incident beam energy, removing the requirement for multiple incident beam energies in order to produce an excitation spectrum, as well as avoiding the potential for gaps in the excitation spectrum. Thick target measurements enable the measurement of all scattering angles, including at 180°. This is particularly advantageous, as this minimises unwanted Rutherford scattering events (see equation 2.12). However, unlike in thin target measurements where the interaction position is relatively precisely known (limited to within the target), the interaction point must instead be calculated from the momentum vectors of the product nuclei. This worsens the experimental resolution, and often requires complete measurement of the final state nuclei in order to constrain the interaction position well — the experimental resolution has often been observed to worsen the further away from θ =180° the events are [42]. The requirement for a solid window at the entrance chamber, in order to prevent gas escaping into the beam line, can also result in both angular and energy straggling, thus further increasing position uncertainty.

This technique is performed using inverse kinematics, wherein the beam nucleus is heavier than the target nucleus. Typically in TTIK experiments, the target is chosen to be ^{4}He gas as often this technique is used in investigating α-cluster phenomena. The purpose of using inverse kinematics is to allow both the beam nucleus, as well as any product nuclei

produced following an interaction, to travel a reasonable distance before stopping in the target gas. Inverse kinematics also potentially allows for the investigation of nuclei otherwise unfeasible due to stability, as radioactive beams can be produced at certain facilities (such as GANIL, in Caen, France) which can be sent towards the chamber shortly after production to react. In contrast, regular kinematics measurements require the target to typically be stable or long-lived to avoid interactions with decay product contaminants (which will often have very similar masses to the target nucleus of interest). A high beam current can be used in thin target measurements in an attempt to obtain more data over a short period of time, but this causes other experimental issues (e.g. multiple events occurring at the same time, making analysis more difficult), but even with this, very short-lived nuclei are still unfeasible as a target.

2.7.4 R-matrix theory

R-matrix theory was first utilised in describing resonance data [43, 44, 45], though the uses of this formalism are not limited to resonance data [46, 47]. Values of the differential cross-section are determined from properties of the resonances that make up the excitation function: centroid energy, E, reduced width for a given channel, γ_i^2, and the spin-parity, J^π.

In R-matrix theory, the nuclear system is split into two well-defined regions: an internal region, defined as the volume within the channel radius, a, of the compound nucleus system, and an external region beyond the channel radius. The external region is considered at a distance, r, far enough away that the effect of the residual nuclear interaction is not felt, so only the Coulomb interaction needs to be considered. The Schrödinger equation can be explicitly solved to provide an exact wavefunction in the external region, $\chi_\lambda^{\text{ext}}(r)$. This wavefunction can be approximated by the expression

$$\chi_\lambda^{\text{ext}}(r) = \cos(\delta_\lambda) F_\lambda(\eta, kr) + \sin(\delta_\lambda) G_\lambda(\eta, kr), \tag{2.13}$$

where F_λ and G_λ are the regular and irregular Coulomb functions respectively, δ_λ is the additional phase shift caused by the scattering potential and k is the wavenumber of the system [48]. The Sommerfeld parameter, η, is defined as

$$\eta = \frac{Z_1 Z_2 e^2}{4\pi\epsilon_0 \hbar v}, \tag{2.14}$$

with Z_1 and Z_2 denoting the proton numbers of the two nuclei in the entrance channel and v denoting their relative velocity.

In the internal region, the Schrödinger equation is instead solved numerically, as the nuclear interaction is experienced in this region. The wavefunction and corresponding derivatives that describe this region must equal 0 at the origin and equal $\chi_\lambda^{\text{ext}}(r)$ at $r = a$ for the total wavefunction to be physical. In order to solve the wavefunction in this region, it is expanded over a general basis $\chi_\lambda^{\text{int}}(r) = \sum_{i=1}^{N} c_{\lambda,i}\phi_{\lambda,i}(r)$, where $c_{\lambda,i}$ are coefficients for the functions $\phi_{\lambda,i}$.

With $\chi_\lambda^{\text{int}}(r)$, the matrix elements of the Hamiltonian can be computed. However, due to the finite size of the internal region, the kinetic energy operator is non-Hermitian and thus non-physical as this produces imaginary or complex eigenvalues. To overcome this, the Bloch operator

$$\hat{\mathcal{L}}(L) = \frac{\hbar^2}{2\mu a}\delta(r-a)\left(\frac{d}{dr} - \frac{L}{r}\right) r, \tag{2.15}$$

can be utilised, as the sum of the kinetic energy and Bloch operators is Hermitian. This is because the Bloch operator is only non-zero for $r = a$, enabling it to deal with the issues

of the finite size of the nuclear system. Here, μ is the reduced mass of the two body exit channel and L is an arbitrary constant, typically equal to 0. Hence, the Schrödinger equation is replaced by the Bloch-Schrödinger equation,

$$(\hat{H} - E - \hat{\mathcal{L}})\chi_\lambda^{\text{int}} = \hat{\mathcal{L}}(L)\chi_\lambda^{\text{int}} = \hat{\mathcal{L}}(L)\chi_\lambda^{\text{ext}}, \tag{2.16}$$

from which both the Schrödinger equation and the boundary conditions at $r = a$ are satisfied for an exact solution. Thus, the channel radius a is not needed as a parameter for calculating the wavefunction as an exact solution will have this boundary condition property by nature.

The R-matrix, R_λ, as a function of energy, E, can be related to the wavefunction at the channel radius through the expression

$$R_\lambda(E) = \frac{\chi_\lambda}{a\frac{d}{dr}\chi_\lambda}. \tag{2.17}$$

The size of this matrix depends on the number of entrance and exit channels [48]. From the Coulomb functions F_λ and G_λ, incoming (I_λ) and outgoing (O_λ) functions for the Coulomb potential can be described:

$$\begin{aligned} I_\lambda &= G_\lambda - iF_\lambda, \\ O_\lambda &= G_\lambda + iF_\lambda. \end{aligned} \tag{2.18}$$

These can be related to the shift factor, S_λ, and penetrability, P_λ, via the dimensionless logarithmic derivative [48, 46, 47] of O_λ at $r = a$, L_λ, by

$$L_\lambda = S_\lambda + P_\lambda = ka\frac{\frac{d}{dr}(O_\lambda(ka))}{O_\lambda(ka)}. \tag{2.19}$$

Two different types of R-matrix theory exist: calculable R-matrix, which enables simple determination of solutions for the Schrödinger equation, which is particularly useful for characterisation of the continuum; phenomenological R-matrix allows for the parameterisation of cross-sections for two-body compound nucleus formation interactions, using input parameters for resonances belonging to the system. In phenomenological R-matrix, the expression

$$R_{\lambda,j} = \sum_{j=1}^{N} \frac{\gamma_{\lambda,j}^2}{E_{\lambda,j} - E} \tag{2.20}$$

is used to calculate the R-matrix and hence parameterise the system as a series of poles, each with centroid energy $E_{\lambda,j}$ and reduced width $\gamma_{\lambda,j}^2$. These values can be related to experimental observables via

$$\begin{aligned} E_x &= E_{\lambda,j} - \mathrm{Re}(L_\lambda), \\ \Gamma &= 2\mathrm{Im}(L_\lambda)\gamma_{\lambda,j}^2, \end{aligned} \tag{2.21}$$

where E_x is the resonance centroid energy and Γ is the decay width of a resonance, once the parameters have been optimised to fit experimental differential cross-section data [38]. The latter of these expressions can be related to the penetrability as in equation 2.7.

Chapter 3

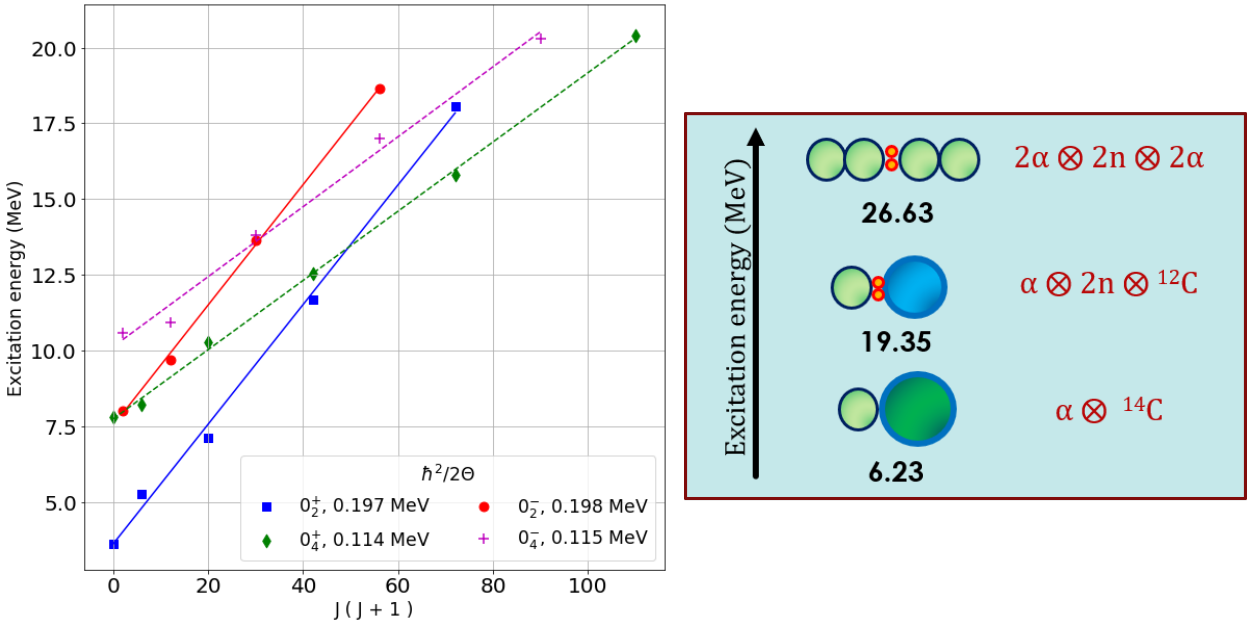
Experimental methods for precision measurement of branching ratios in ^{18}O

The potential for the existence of α-clustered states in ^{18}O has been theorised for many years, as ^{18}O is an excellent candidate for displaying this exotic nucleon arrangement. The full closure of the $1p$ neutron shell and the full closure of the $1p_{3/2}$ proton subshell present in the ^{14}C ground state system provides stability, which suggests that ^{14}C would make a viable core in a "core + α" structure. In fact, the properties of the ^{14}C closely resemble those of ^{16}O, with the latter having both proton and neutron full $1p$ shell closures. Both nuclei have a first excited level energy above 6 MeV — 6.0494(10) MeV for ^{16}O and 6.0938(2) MeV for ^{14}C — and a similar binding energy per nucleon: 7.98 MeV A^{-1} and 7.52 MeV A^{-1} respectively. The comparison of theoretical calculations to experimentally observed states provides evidence of the ^{16}O core, particularly in the ^{20}Ne ($^{16}\mathrm{O}\bigotimes\alpha$) system as demonstrated by the work of Matsuse et al. [25] and Buck et al. [24], and as such the existence of a $^{14}\mathrm{C}\bigotimes\alpha$ structure in excited levels of ^{18}O is in many ways plausible. Evidence of this structure has been reported in the literature, such as in the works of Artemov et al. [49] and Morgan et al. [50].

Nuclear molecular structures, previously mentioned in Section 2.3.2, have also been predicted to present themselves in levels of ^{18}O. One such nuclear molecule is the ^{12}C $\bigotimes$ $2n$ $\bigotimes$ α structure, in which the two valence neutrons bind together the ^{12}C core to the α-particle via the nuclear force, stabilising the system and helping to overcome the substantial Coulomb repulsion. This particular structure has also been suggested based on experiment by Curtis et al. [51], which matches predictions of 6p-4h structures in this nucleus from the field of shape coexistence [52] — there is much evidence linking shape coexistence in light nuclei to cluster phenomena [53, 54, 55].

An experiment by von Oertzen et al. [56] measured an excitation spectrum for ^{18}O, with states populated by the ^{12}C(^{7}Li,p)^{18}O* reaction ($E_{\mathrm{Li}} = 44$ MeV), with the recoil proton incident on the Q3D (named for the constituent one quadrupole and three dipole magnets) magnetic spectrograph. Determining the energy of the proton in this manner provides an excitation spectrum, as the kinetic energy of the proton is dependent on the energy used in exciting the ^{18}O product nucleus. States from $0 \rightarrow 21.2$ MeV were measured, of which ≈ 30 were previously unobserved. The centre of the Q3D was set at several scattering angles (10°, 20° and 39°), which allowed for some indication of angular dependence on population of the states, enabling some estimation of spin and parity. With these states and those observed that had previously been measured in the literature (some of which had known spin-parity properties), rotational bands were tentatively assigned. These proposed rotational bands can be seen in Figure 3.1, alongside the structures proposed to be responsible for them and the excitation energies at which the cluster configurations can form. The $0_2^{+/-}$ band was proposed to have a ^{14}C $\bigotimes$ α structure while the $0_4^{+/-}$ was proposed to have a ^{12}C $\bigotimes$ $2n$ $\bigotimes$ α structure. Both of these bands have an associated positive and negative parity band — this is due to signature splitting, as the structures are asymmetric about the rotation axis (and hence affected by a reflection in this axis). The moment of inertia of both the positive and negative parity bands is the same, but this asymmetry causes a notable difference in

excitation energy for states of different parity.



(a) (b)

Figure 3.1: The rotational bands with potential cluster structure in ^{18}O proposed by von Oertzen et al. [56] are shown in (a), while the excitation energy required for ^{18}O cluster structures to form is shown in (b).

For states in these cluster bands, it would be expected that they would have similar, large values (>0.1) of the dimensionless reduced α-width — this quantity is described in Section 2.5. This value can be calculated with five relevant experimental observables of a specific resonance: the total width, Γ_{tot}, the partial α-width, Γ_α, the excitation energy, E_x, and the spin-parity, J^π. Both E_x and Γ_{tot} can be determined simply by measuring the excitation function of ^{18}O, but Γ_α requires either the measurement of a resonant scattering function (^{14}C + α) or the branching fraction of α-decay for a particular resonance. The spin-parity of the states could be determined by investigating angular distributions, however as these states are proposed to be members of specific rotational bands, they have proposed spins and parities which can be used to calculate the dimensionless reduced α-width.

3.1 Experimental set-up

In order to determine the validity of these bands, a further experiment was performed. This experiment aimed to measure the α-decay branching ratio for states in the proposed bands through the detection of decay products from the compound ^{18}O nucleus. The experiment was performed at the Maier-Leibnitz Laboratory (MLL) in Munich, Germany, with population of states achieved via the ^{12}C(^{7}Li,p)^{18}O* reaction ($E_{\mathrm{Li}} = 44$ MeV), in order to best replicate the excitation functions observed by von Oertzen et al. [56]. The stable ^{7}Li beam was provided by the Van de Graaff Tandem accelerator, with a beam resolution of $\approx$ 5 keV, and was incident on a $^{\mathrm{nat}}$C target. The experiment was run over two years, with a

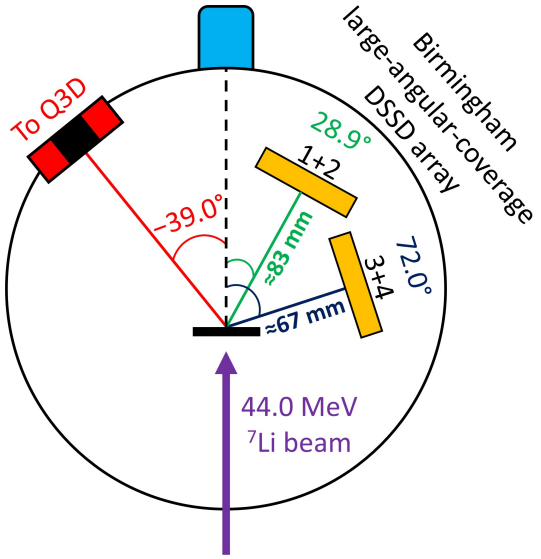


Figure 3.2: A representation of the experimental set-up used, showing the positions of the Birmingham large-angular-coverage DSSD array and the Q3D magnetic spectrograph in-plane. Angles and distances shown are from the set-up used in 2017, though these are very similar to those used in 2016. Angles and distances across both experimental runs are summarised in table 3.1. Figure adapted from Figure. 1 published in Ref. [57].

target thickness of 120 µg/cm^2 the first year and 110 µg/cm^2 the second year. The excitation energy of the ^{18}O recoil was determined through measurement of the corresponding proton in the Maier-Leibnitz spectrograph, set at 39° (with an angular acceptance of ±3°) in-plane and 0° (with an angular acceptance of ±2°) out-of-plane. The ^{18}O recoil, or the corresponding break-up particles, could then be detected by the Birmingham large-angular-coverage double-sided silicon strip detector (DSSD) array, which subtended angular ranges of $14° \rightarrow 92°$ in-plane and $-36° \rightarrow 40°$ out-of-plane. The position of the array was such that the majority of decay products from ^{18}O (in the case where the recoil proton was incident on the aperture of the Q3D) would be detected.

3.1.1 Q3D magnetic spectrograph

The Q3D magnetic spectrograph, as shown in figure 3.3, consists of a quadrupole magnet, a multipole magnet and three dipole magnets. The quadrupole magnet lies just behind the aperture of the Q3D, focusing any incident particles vertically, resulting in a larger range of ejectile solid angles that will result in a measurement in the focal-plane detector. These particles subsequently pass through the fields of the three dipole magnets, causing the path taken by these particles to curve. The multipole element, placed between the first and second dipole magnets, corrects for kinematic broadening and other effects [59, 58].

The Lorentz force for a charged particle in the presence of a magnetic field is given by

$$F = q(\vec{v} \times \vec{B}), \tag{3.1}$$

where $\vec{B}$ is the flux density of the magnetic field, q is the charge of the particle and $\vec{v}$ is the velocity of the particle. As for the same type of particle (e.g. protons) q is constant

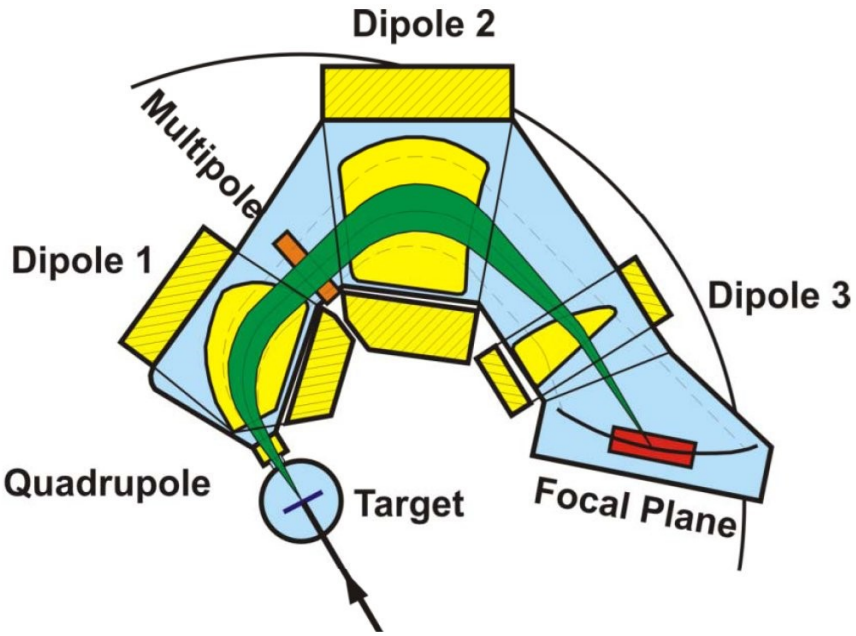


Figure 3.3: An overview of the Q3D magnetic spectrograph, with the path taken by charged particles due to the magnetic fields highlighted in green [60].

(as is $\vec{B}$ for any particle passing through the spectrograph), only the velocity of the particle (proportional to the kinetic energy) impacts the amount of curvature around the path of the Q3D. Thus, the position of the particles as they are detected in the focal-plane detector is thus dependent on the energy of the particles as they are incident on the aperture of the Q3D. Not labelled in figure 3.3 is the electrostatic deflector, placed between Dipole 2 and Dipole 3, which separates particles based on specific mass ($^{m}/_{q}$) value.

3.1.1.1 Focal-plane detector

The focal-plane detector, depicted in figure 3.4, covers 0.89 m — the entire length of the focal-plane is 1.8 m [61, 62]. The focal-plane detector is filled with isobutane gas, at a pressure of 500 mbar, and consists of several stages with which the incident charged particle interacts. The particle first passes through a cathode foil, past two anode wires (parallel

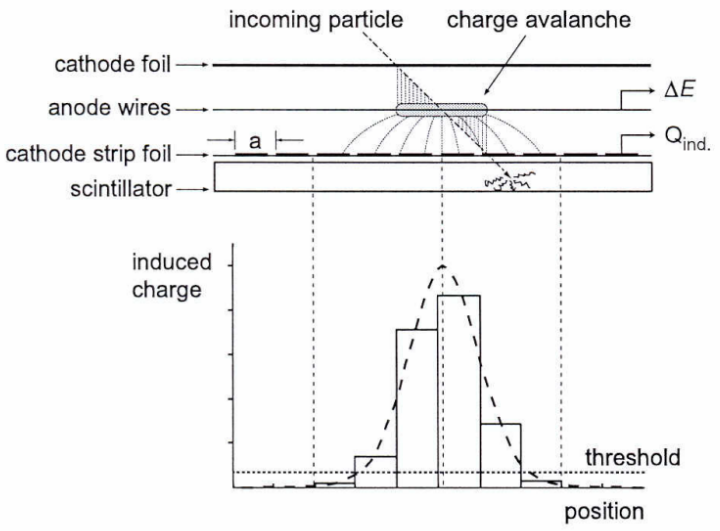


Figure 3.4: Depiction of the focal-plane detector, showing the constituent parts. An example trajectory of a charged particle can be seen at the top of the figure, with an example histogram output of charge distribution across the cathode strip foil at the bottom. Figure taken from Ref. [61].

to one another, in the plane shown by figure 3.4) and then through a second cathode foil, which is segmented into 255 strips, which are each ≈ 3.5 mm in size. Finally, the remaining energy of the particle is deposited and measured in a scintillator detector. The movement of the particle through the electric field generated by the cathode foils and anode wires causes the particle to lose energy, as the charged particle causes ionisation along the path it is travelling. The electrons that are ejected due to the ionisation are accelerated from the first cathode foil towards the anode wires. Once the electrons have reached the anode wire, a charge avalanche occurs, which is detected in strips of the second, segmented cathode foil. There is a distribution of induced charge across strips in this foil, from which the position of the charged particle can be inferred via Gaussian fitting to the charge distribution (an example of which shown in figure 3.4).

3.1.1.2 Particle identification

In order to identify the species of particle measured in the Q3D, the measurements of energy loss and total energy can be used in conjunction with one another. Figure 3.5 shows different particle identification methods, for states in ^{18}O between 9.7 MeV and 11.8 MeV, from which the proton loci can be identified and used to select events for further processing (*aka* gating). In figure 3.5(b), regions of high counts corresponding to the states populated in the product ^{18}O can be seen across the focal-plane detector.

The use of all three of the gates shown allows for a significant reduction in background — in theory, gates using only the energy loss and charge avalanche could be used to filter between species, but in practice the scintillator is needed in many cases to get a reasonably clean spectrum [62]. Figure 3.6 shows a comparison between three spectra using the same data (states in ^{18}O around 7.5 MeV): the spectrum that utilises all three gates (figure 3.6(a)) has a background approximately half of that which does not utilise the anode wire/scintillator particle identification gate (figure 3.6(b)). When no gates are utilised (figure 3.6(c)), the background can be seen to be significantly larger, obscuring all but the most populated excitations.

3.1.1.3 Calibration and resolution

Calibration of the spectra obtained from the Q3D was performed through identification of ^{18}O excited levels, comparing the value of position in channels to previously measured energy values from the literature. Originally, values from Tilley et al. [64] were considered, but due to the large number of previously unmeasured states that required the centroid values measured by von Oertzen et al. [56], the rest of the energy values were extracted similarly for consistency. Labelled spectra from the five energy regions investigated are shown in

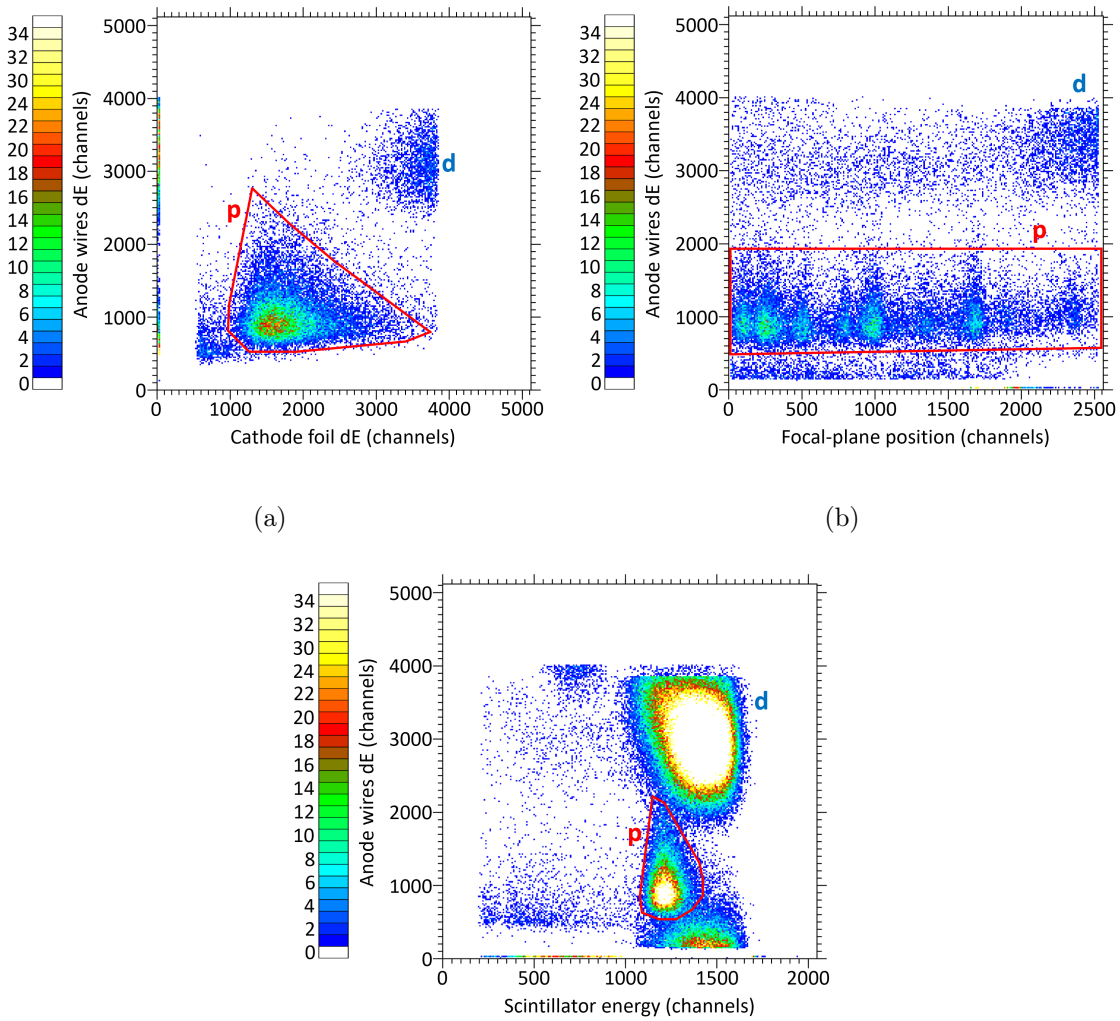


Figure 3.5: Particle identification plots from which the species of particles incident on the focal-plane detector can be determined. All plots involve measurement of the energy loss of particles from the signal extracted from the anode wires on the y axis, plotted against energy loss through the first cathode foil (a), position as measured by the cathode strip foil (b) and energy deposited in the scintillator (c). The gates used for the experimental data are shown in red, corresponding to protons. The loci due to deuterons are also labelled. Figure adapted from FIG. 1 published in Ref. [63].

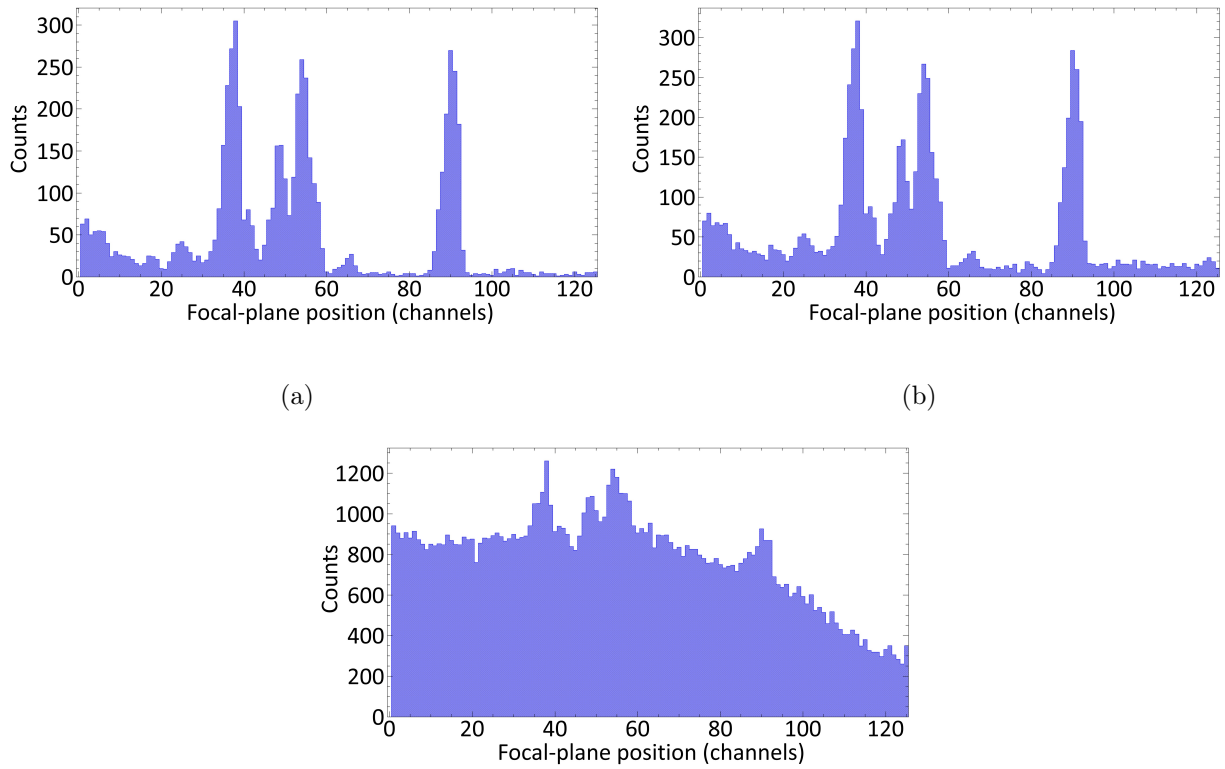


Figure 3.6: Q3D spectra obtained for counts as a function of focal-plane position, for the case where all three gates shown in figure 3.5 are utilised (a), the two gates not including the scintillator are utilised (b) and no gates are used to clean up the spectrum (c).

figure 3.7. In these plots, the focal-plane position corresponds to measured proton energy, which in turn corresponds to decreasing excitation energy in the ^{18}O recoil. It is important to note that the focal-plane detector is curved, resulting in two effects: the first effect is that the energy of a particle as a function of measured position in the focal-plane detector is quadratic, which is reflected in the calibration; the second effect is that states which are distinct and near the edge of the focal-plane can become skewed — this is less noticeable when there is a large density of states as with the higher excitation energy regions.

In order to fit the states reasonably, the resolution of the focal-plane detector had to be determined in order to limit the degrees of freedom of fitting — this is particularly

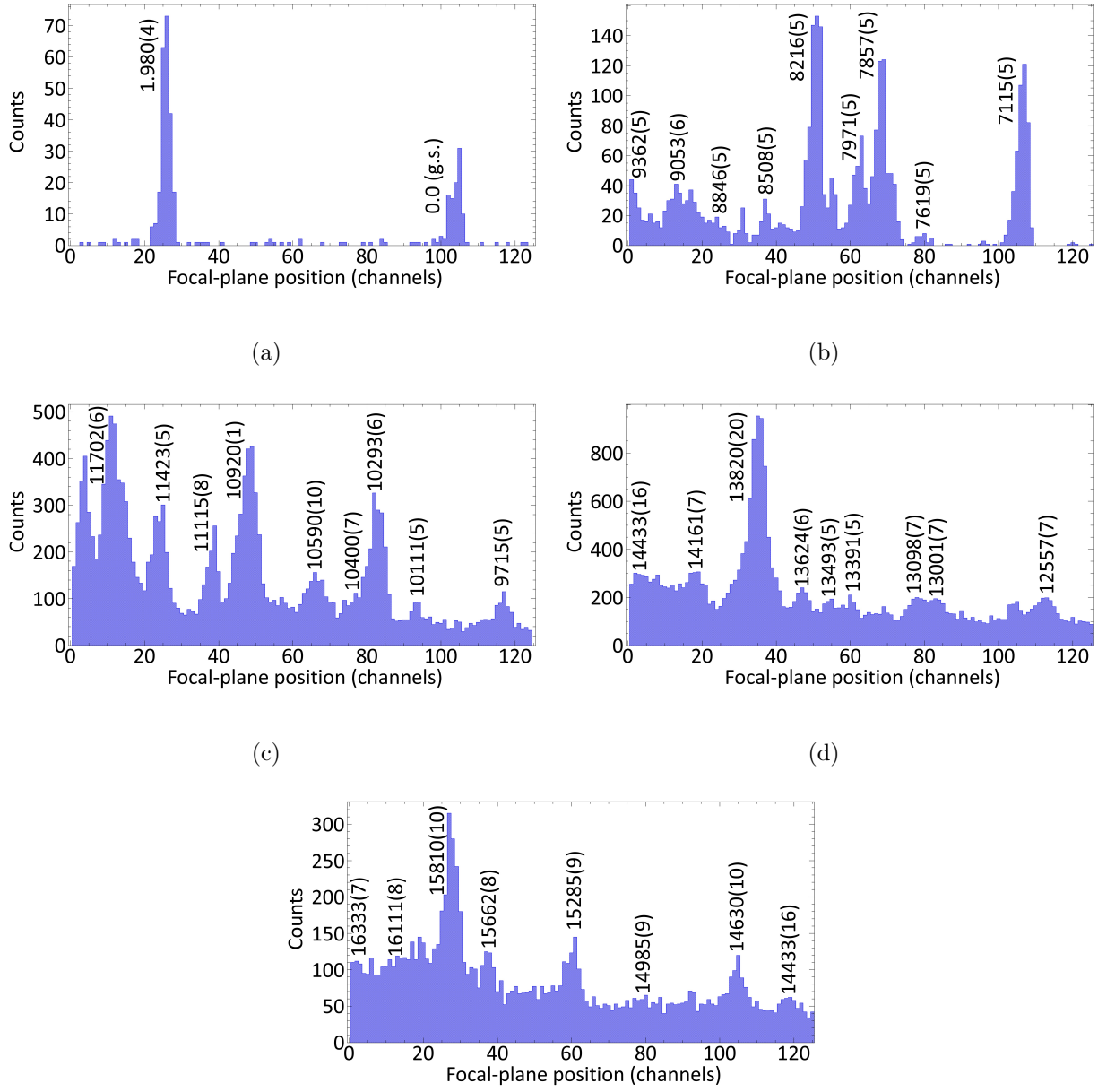


Figure 3.7: Q3D spectra obtained for the different excitation regions: $-0.5 \rightarrow 2.5$ MeV (a), $7.0 \rightarrow 9.4$ MeV (b), $9.6 \rightarrow 11.9$ MeV (c), $12.4 \rightarrow 14.5$ MeV (d) and $14.5 \rightarrow 16.3$ MeV (e). Energy values given for excitations are taken from Ref. [56] in keV. An increase in the background level for increasing excitation energy is observed, due to various n-body phase spaces that become available above certain energy thresholds. See Sec. 3.1.1.4 for details.

important due to the high number of close-lying states in many of the excitation regions. The measured width of an excitation (Γ_{tot}) can be disentangled into the natural linewidth of the state, Γ_{nat}, and the width due to the experimental resolution of the focal-plane, Γ_{res}, through the relationship

$$\Gamma_{\mathrm{tot}} = \sqrt{{\Gamma_{\mathrm{nat}}}^2 + {\Gamma_{\mathrm{res}}}^2}. \tag{3.2}$$

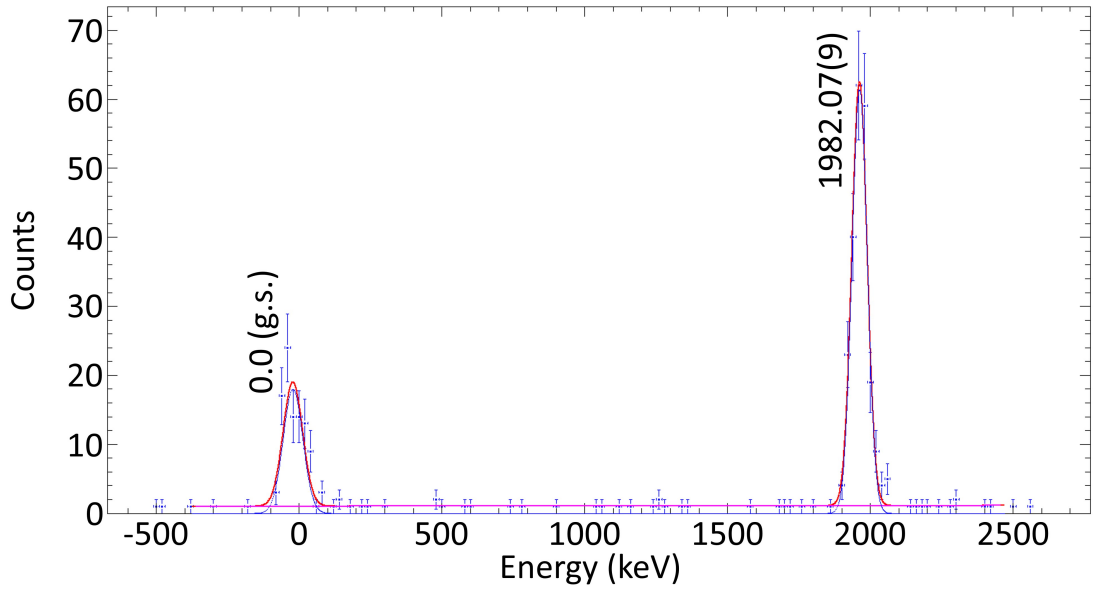
In the case where $\Gamma_{\mathrm{nat}} << \Gamma_{\mathrm{res}}$, the measured width of a state can be approximated to be entirely due to the experimental resolution. Thus, by investigating the lowest excitation region containing only bound states (the ground state and first excited state, shown in figure 3.7(a)), the experimental resolution could be extracted as the natural linewidths of these states are negligible (0 for the stable ground state, and 3.4×10^{-4} eV for the first excited state).

Unfortunately, as can be seen in figure 3.8, the ground state excitation appeared skewed due to the position on the focal-plane. A non-normalised Gaussian distribution, $g(x)$, is defined by

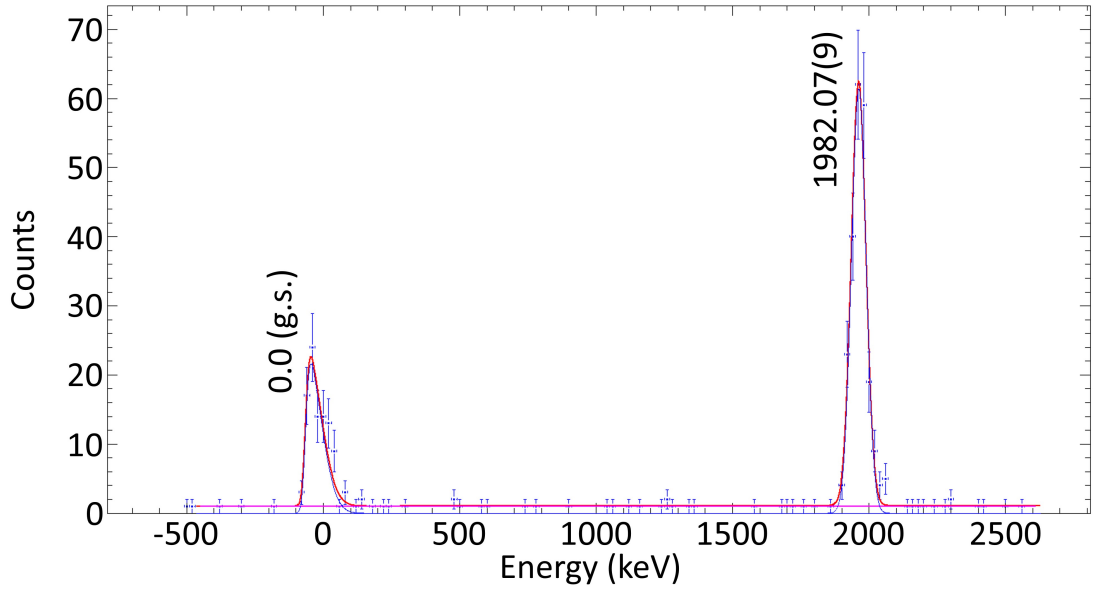
$$g(x) = \frac{A}{\sigma\sqrt{2\pi}} \exp^{-(x-\mu)^2/2\sigma^2}, \tag{3.3}$$

where σ is the standard deviation from the mean value, μ, of the distribution and A is a constant (scaling factor). When fitting a Gaussian, the parameters used are typically the centroid (μ), the full width at half maximum, or FWHM, ($= 2\sqrt{2\ln 2}\ \sigma$) and the counts under the curve ($\propto A$). In order to fit skewed distributions, the function

$$f(x) = g(x) \times (1 + \mathrm{erf}\left[\frac{\alpha(x-\mu)}{\sigma\sqrt{2}}\right]) \tag{3.4}$$



(a)



(b)

Figure 3.8: Fitted Q3D spectra for the $-0.5 \rightarrow 2.5$ MeV region, with pure Gaussian fits for both states (a) and with a skewed Gaussian fit for the ground state (b). A visible increase in the fidelity of the fit to the data can be seen for the skewed fit.

was employed, where α is a parameter that defines the skew of the distribution [65, 66]. A problem arises, however, as the FWHM is not defined for this function and thus cannot be extracted from the fit simply. The FWHM can be estimated analytically, by calculating the difference between the fit values at half of the maximum value for the distribution, though this is less reliable as the corresponding uncertainty is larger. For the fit of the ground state, shown in figure 3.8b, calculating the value of the FWHM using this method gives 69.1 keV, while the extracted width of the first excited state from fitting is 63(4) keV. The resolution of the focal-plane detector is expected to vary over the entire length of the detector, mostly due to the fact that the experimental resolution arises from energy loss from both the beam and product nuclei in the target, which varies with the scattering angle of the proton (which is not uniform with respect to excitation energy in the lab frame) [56].

The values extracted for both of the states shown in figure 3.8 are comparable to the resolution of 60 keV extracted for the same reaction with the Q3D at $-39°$, as determined by T. Dorsch et al. [67]. A resolution of 65 keV was established, based on the extracted values and the knowledge that the target thickness in the current work (110 µg/cm^2 and 120 µg/cm^2) was larger than that of T. Dorsch et al. (70 µg/cm^2). Thus, a lower limit of 65 keV was obtained from these excitations, which prevented issues when fitting weakly-populated states that lay near other, better-populated excitations.

With the resolution of the Q3D established, calibrations of the regions could be performed using Gaussian fitting to establish the centroids of the excitations in units of focal-plane position, estimating the phase space distributions and other background components using a quadratic background. The usual dispersion of events over 2550 channels (corresponding to the number of physical strips multiplied by ten, obtained from the charge fitting procedure) does not provide the necessary statistics for each bin in order to be able to reasonably fit the spectrum, as χ^2 minimisation assumes Gaussian errors and in the low-count limit ($N < 10$) the errors are more Poissonian. Figure 3.9 shows a comparison of different

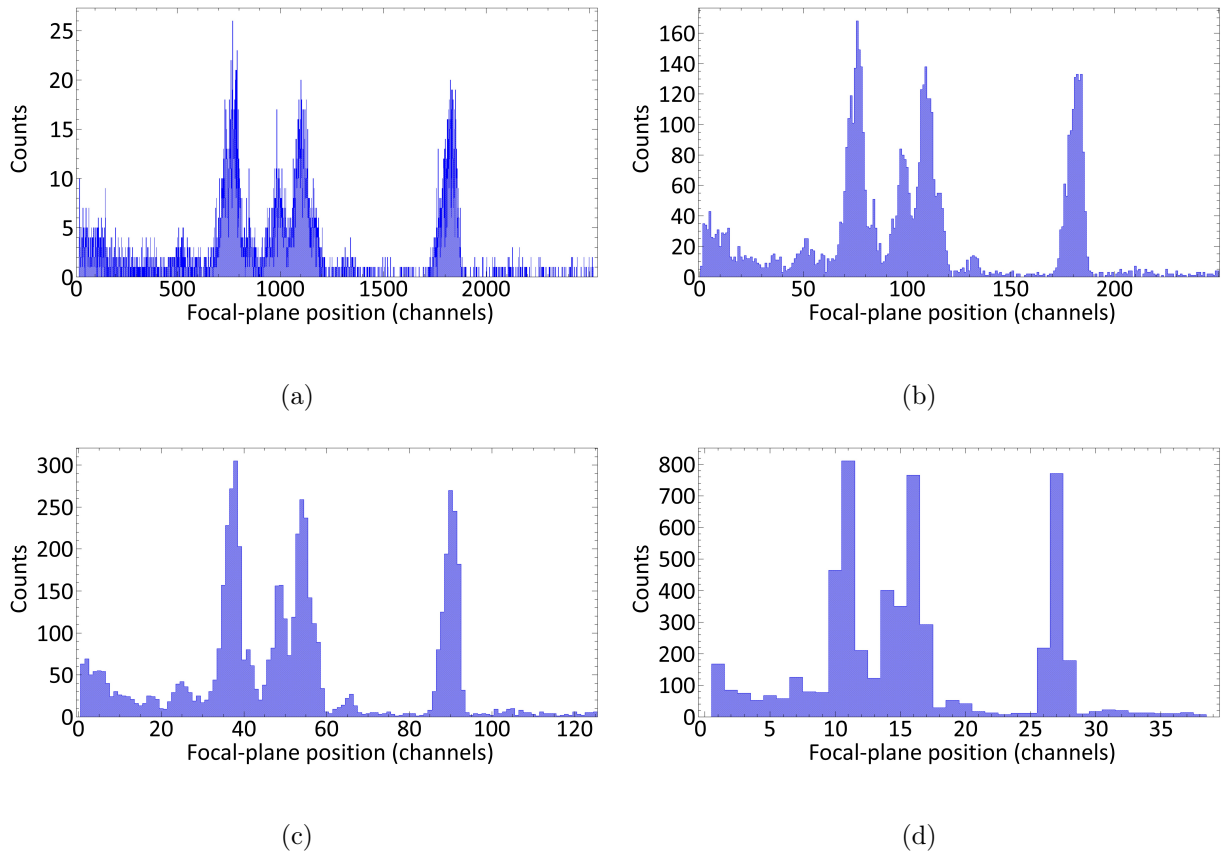


Figure 3.9: Q3D spectra for the 7.0 → 9.1 MeV excitations, rebinned relative to the usual dispersion over 2550 channels for the position of detection in the focal-plane detector (a). Larger bin sizes of ×10 (b), ×20 (c) and ×60 (d) are shown for comparison. Statistics too low for reasonable fitting in many areas can be seen even in the peaks in (a), whereas an obvious loss of features can be observed in (d) relative to the other three. Plots (b) and (c) compromise these two qualities.

binning for the position measurements from the focal-plane detector. The binning chosen for the calibration was typically that of figure 3.9(b) (10 times larger bin size than that of figure 3.9a), as the statistics were appropriate for fitting but did not significantly diminish the ability to distinguish features of the spectrum. In some cases (see figure 3.10) the binning was that of figure 3.9c, in order to aid in the fitting of low-statistics features. Figure 3.10 shows the data used to calibrate the different excitation regions for focal-plane position against the

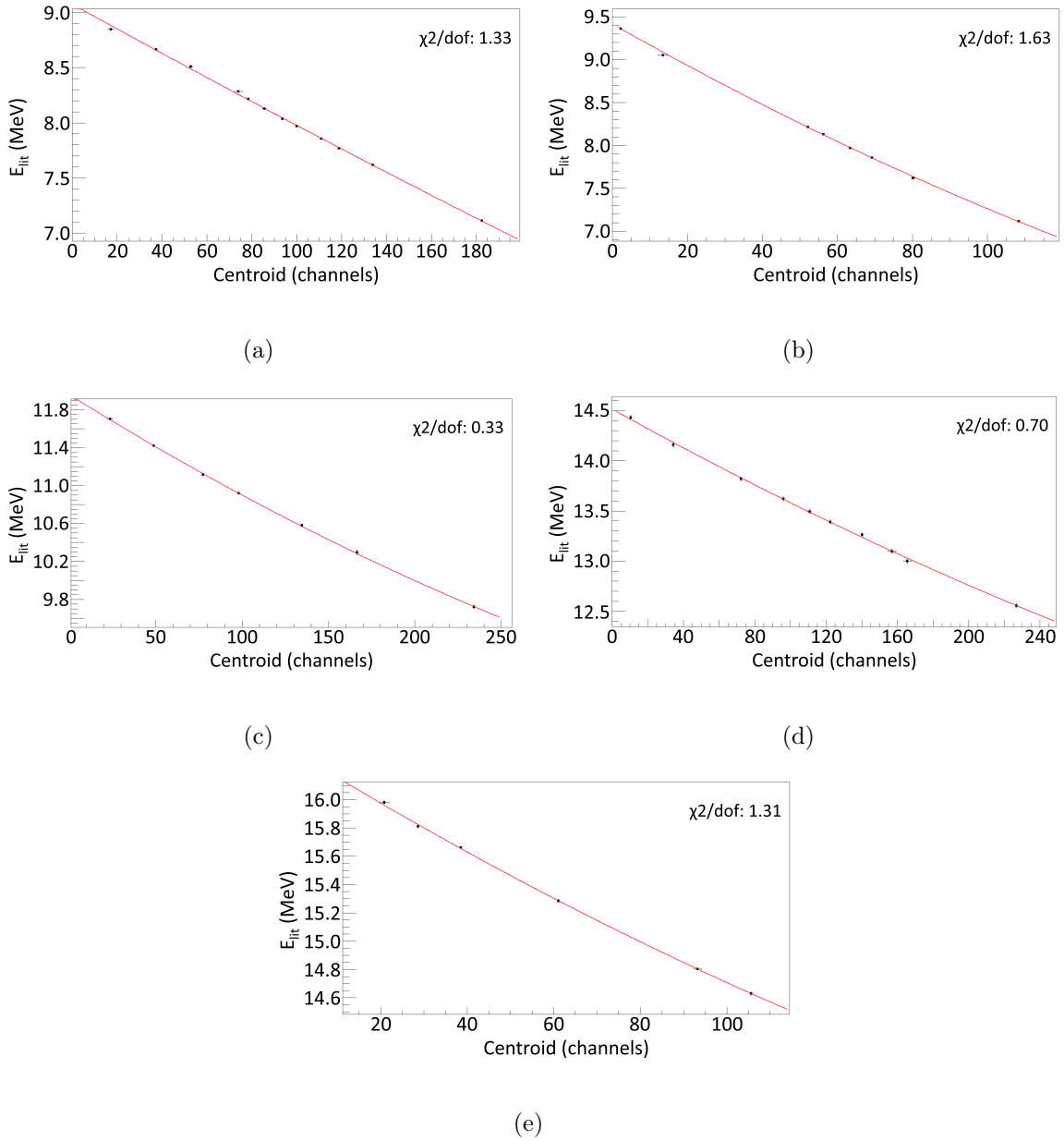


Figure 3.10: Plots of the literature values of energy for excitations in keV against measured centroid value in the focal-plane detector in channels, for 7.0 → 9.1 MeV (a), 7.0 → 9.4 MeV (b), 9.6 → 11.9 MeV (c), 12.4 → 14.5 MeV (d) and 14.5 → 16.3 MeV (e). Fits with the functional form $y = Ax^2 + Bx + C$ were used in all cases and are shown in red, along with the corresponding value of χ^2/dof. Error bars are displayed for each data point, although the error bars are often comparable to the size of the symbol representing a data point.

literature energies from Ref. [56], plotted with the function determined using a least squares regression, with each data point weighted by $1/\sigma^2$, where

$$\sigma = \sqrt{dx^2 + dy^2}, \tag{3.5}$$

dx represents the uncertainty on the measured centroid in channels and dy represents the uncertainty on the literature value for the corresponding energy. A convincing quadratic trend can be observed for the calibrations of all regions. It should be noted that figure 3.10(a) and figure 3.10(b) correspond to calibrations for the same excitation region, but these were done for data sets taken a year apart and thus required separate calibrations.

3.1.1.4 Background

When each region was calibrated, a further fit was performed in order to better establish the centroids and widths for each excitation, and perform a more realistic treatment of the background. These fits can be seen in figure 3.11. The background is represented by a dashed pink line, and can be seen to increase (relative to the data) with excitation energy, E_x. Below E_x = 8045 keV, the neutron-decay threshold for ^{18}O, the background is treated as a constant. Above this value, the background is mostly due to phase-space distributions — from 8045 keV$< E_x <$ 12118 keV the only available phase-space is the three-body phase-space (^{17}O+n+p_{q3d}, where p_{q3d} is the proton detected in the Q3D). The four-body neutron phase-space (^{16}O+n+n+p_{q3d}) becomes available above E_x = 12.118 MeV, which again affects the shape of the background — the introduction of this phase-space to the background occurs between the two regions shown in figure 3.11(b) and figure 3.11(c). There is also the contribution from a further three-body phase space, ^{17}N*+p+p_{q3d}, above E_x = 15942 keV, though the contribution is minimal in the excitation ranges observed due to proximity to the threshold. These phase-space distributions were extracted from Ref. [56],

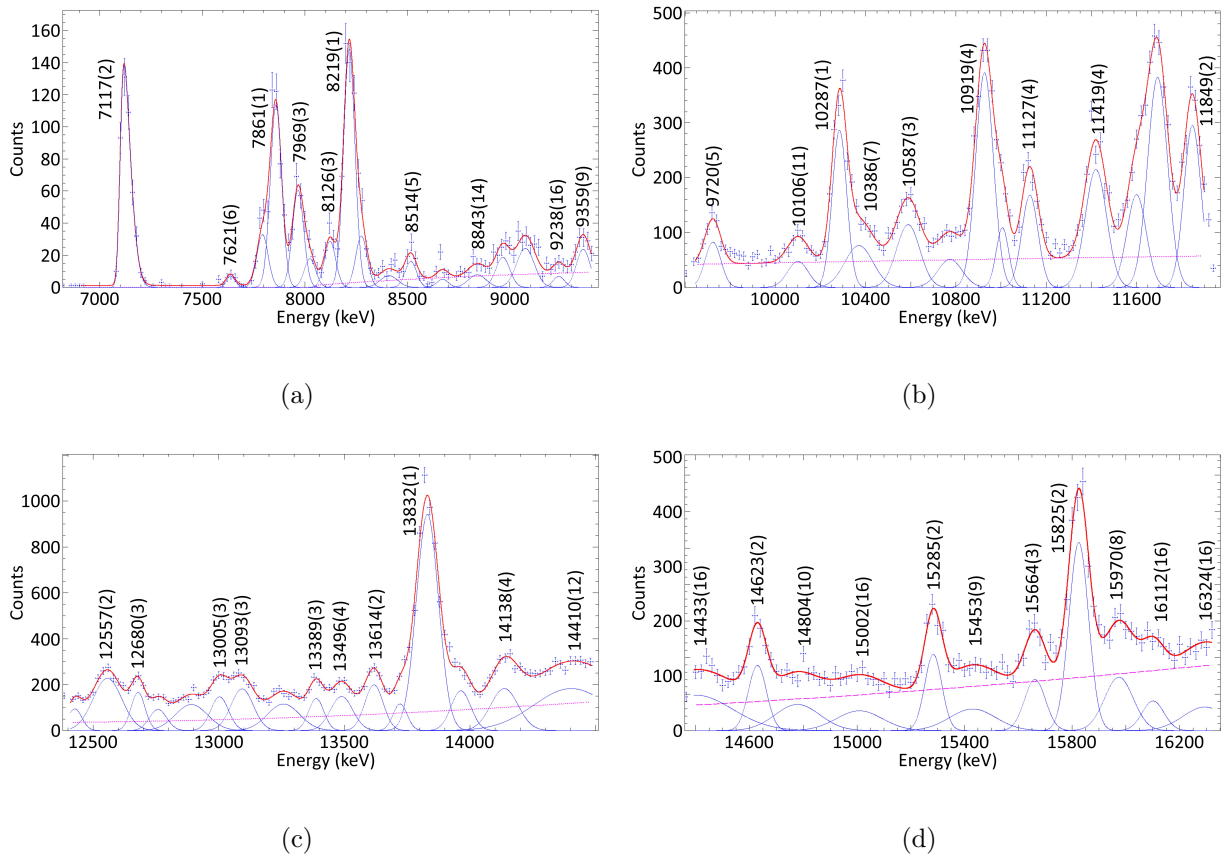


Figure 3.11: Fitted Q3D spectra for the observed excitation regions, with certain centroid values extracted in this work shown next to the resonances. The regions are 7.0 → 9.4 MeV (a), 9.6 → 11.9 MeV (b), 12.4 → 14.5 MeV (c) and 14.5 → 16.3 MeV (d). The total fit to the data is shown by a solid red line, whereas the individual Gaussian components are indicated using a solid blue line. The dashed pink line represents the background, discussed in the text. Subfigures here have been published in Refs. [57] and [63].

where the distributions were calculated using the code SPEC [68]. The backgrounds were then fitted using regression to a quadratic functional form ($R^2 > 0.99$ in all cases, where R^2 is the coefficient of determination), with a scaling factor as a free parameter in order to account for the difference in statistics between the work of Ref. [56] and the current work. The total fit for each region is shown in figure 3.11 with a red solid line, whereas the individual Gaussian components of each state are shown using a solid blue line.

3.1.2 Birmingham large-angular-coverage DSSD array

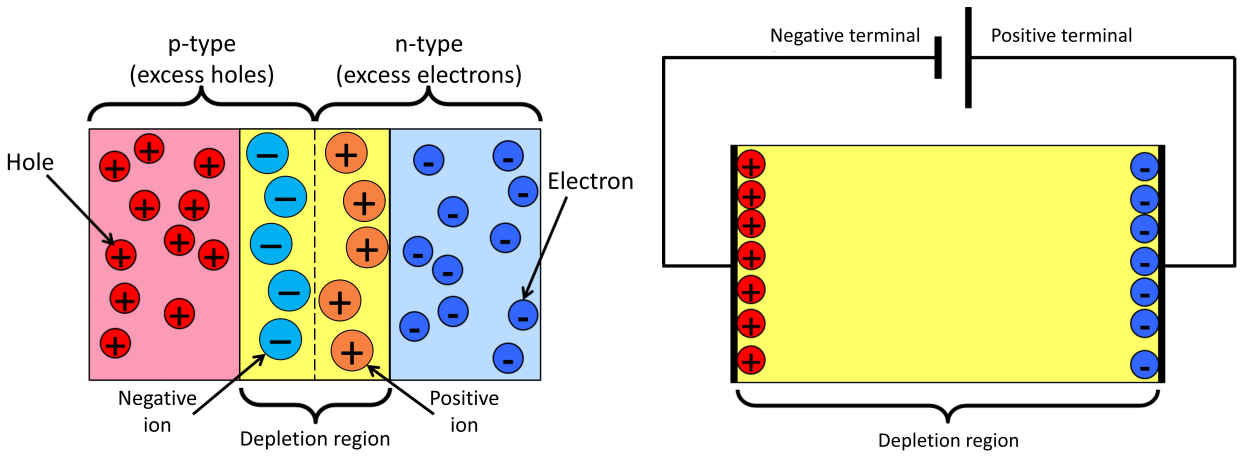
In order to detect the ^{18}O nucleus, or the associated fragments from an ^{18}O* decay, the Birmingham large-angular-coverage DSSD array was utilised. This array consisted of four 500 µm thick, 50×50 mm^2 W1 DSSDs made by Micron Semiconductor Ltd [69]. These detectors are primarily constructed from silicon, which is a Group IV element; silicon forms a crystal, with each (non-surface) silicon atom forming a covalent bond with four neighbouring silicon atoms. Silicon is a semiconductor material, meaning that the conductivity of electricity attempting to pass through it is less than that of a conductor (typically metals) but more than that of an insulator. There are many physical properties of semiconductors that make them useful, such as a decreased resistivity as a function of temperature (the opposite of the phenomenon observed in typical conductors); in the field of semiconductor detector physics, the most vital property is that the resistivity of semiconductors is highly variable with the addition of impurities to the crystal.

3.1.2.1 P-N junctions

The removal of an electron from an atom in the crystal — the movement of an electron to the conduction band from the valence band in band theory — also results in the production of a hole, and hence the creation of an "electron-hole pair". A hole is the name given to the resultant positive charge present in the crystal due to an electron missing from the valence band, and can move through the crystal similarly to electrons promoted to the conduction band. This movement can be understood by considering the movement of an electron from a different atom to the ion — the hole has thus moved in the opposite way through the crystal to that electron. Silicon crystal at 300 K has a band gap, the difference in energy between the valence and conduction bands, of 1.11 eV [70], corresponding to a required temperature of $\approx$ 12.9 kK for electrons to be promoted to the conduction band. Thus, in an intrinsic (pure)

silicon semiconductor, the number of thermal electron-hole pairs produced is relatively small and explains the partial conductivity of this material, as well as the relationship between the resistivity and temperature mentioned previously.

In the case of silicon, the conductivity of the crystal can be affected through the addition of Group III (containing three valence electrons, such as boron) or Group V (containing five valence electrons, such as antimony) atoms. The introduction of these impurities results in a large increase in the number of available charge carriers. For Group V doped silicon, known as an n-type semiconductor, this is easy to conceptualise: the addition of the extra electrons from the doping fills the valence band, as the impurity atoms form four covalent bonds with silicon. The remaining fifth valence electron thus must be present in the conduction band. For p-type semiconductors (Group III impurity), there are fewer electrons available per atom. However, the resulting deficiency of electrons causes a net increase in the number of holes that can travel through the crystal.



(a) (b)

Figure 3.12: A P-N junction in equilibrium (a), with the depletion region formed between the two doped semiconductors. The same P-N junction is then put under reverse-bias (b), causing the size of the depletion region to extend across the crystal. Images edited from Ref [71].

When a p-type semiconductor and an n-type semiconductor are joined together to form a P-N junction, electrons and holes are free to diffuse across the junction. These free charges will migrate across the junction due to the differing potentials of the different regions, producing a diffusion current. The recombination of these holes and electrons near the junction causes ionisation in atoms within this region: a net positive charge within n-type region due to creation of positive ions near the junction, while the p-type region achieves a net negative charge from the creation of negative ions. The region of charge produced by these ions at the boundary of the p-type and n-type semiconductors is known as the depletion region, shown in figure 3.12(a), due to lack of free charges. The electric field established by the movement of free charges across the junction causes a drift current which opposes the diffusion current, and eventually an equilibrium is reached — thus, the depletion region does not grow indefinitely.

A reverse bias can be applied across the semiconductor, with the positive terminal connected to the n-type region and the negative to the p-type. This is depicted in figure 3.12(b). The reverse bias causes an initial current flow which matches the direction of the drift current, opposing the movement of free charges across the junction, so the free charges are swept further out of the depletion region, increasing its size. If a sufficiently large potential difference is applied, the depletion region can extend across the entire crystal. Hence, if any free charges were produced in the crystal, such as if electron-hole pairs were produced through ionisation caused by a charged particle such as an α-particle or photoelectron incident on the crystal, they would be swept up by the field due to the reverse bias and the resulting currents, from both the collection of electrons at the positive terminal and the collection of holes at the negative terminal, could be measured. This is the principle by which the DSSDs measured the energy of incoming charged particles — the number of liberated electron-hole pairs in the crystal is proportional to the energy of the incident particle. Although theoretically there should be no current across the depletion region without

an incident particle to liberate electron-hole pairs, in practice a small leakage current would be observed. This is often due to slight imperfections in the crystal structure of the silicon wafer, and as the detectors age and receive radiation damage, displacing atoms in the crystal structure, the leakage current increases accordingly.

3.1.2.2 Measuring the position of incident particles

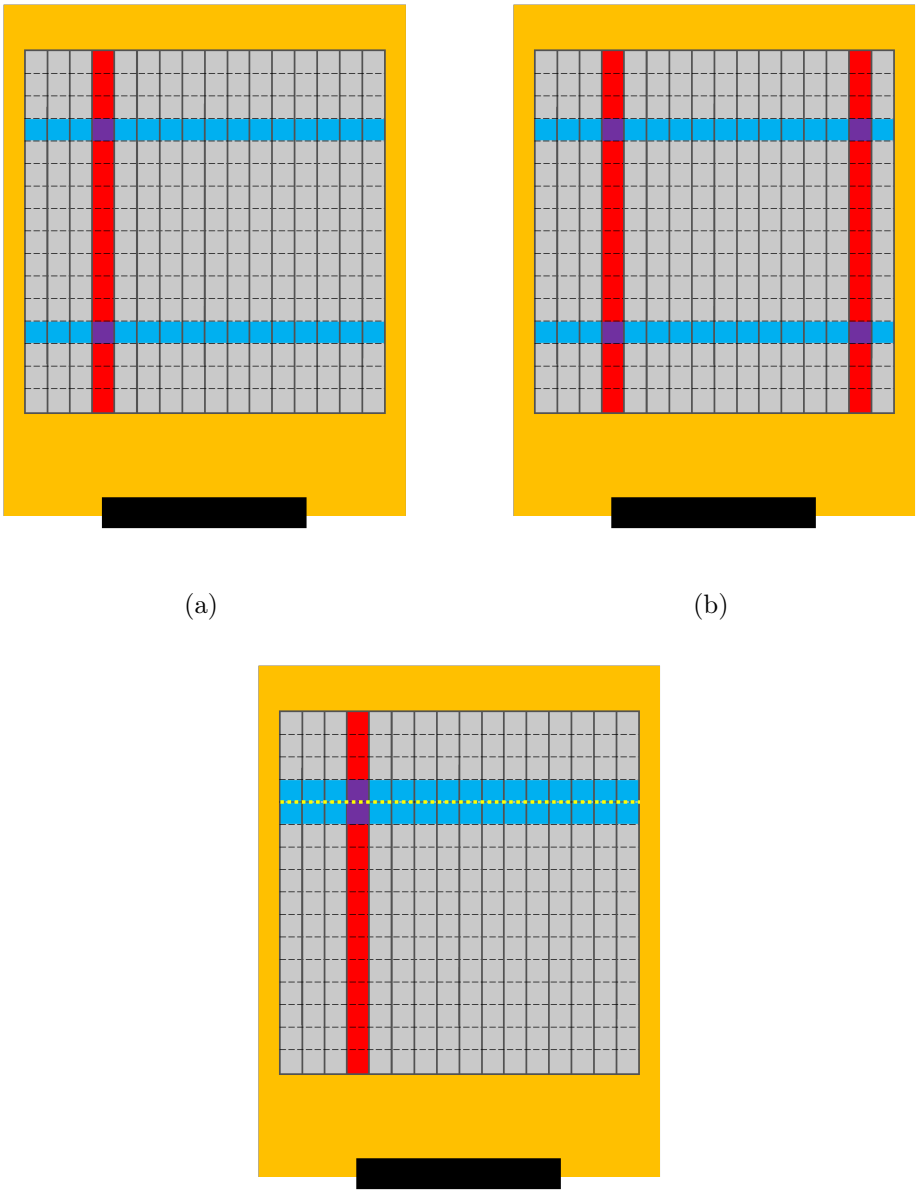
The DSSDs used in this work are segmented into 32 strips, with 16 of those being on the front of the detector and 16 on the back, with the front strips orthogonal to the back strips. The detectors largely consisted of n-type silicon, from which the front (p-type) strips were formed. This was achieved by removing oxidised silicon from the surface of the crystal in vertical strips, and then utilising the ion implantation technique with boron to convert the underlying n-type silicon into p-type silicon. The back strips were n-type, achieved through



Figure 3.13: A front strip of the detector (red) is hit by a charged particle in coincidence with a back strip of the detector (blue), resulting in a pixel within which a charged particle can be detected. Image edited in Ref. [71], originally from Ref. [69].

doping with arsenic. Both sets of strips were covered in a thin layer of aluminium in order to serve as an electrical contact, and were separated from one another through the use of a thin insulator, SiO_2, which was also implanted [72]. The effect of this was the creation of a grid of 256 pseudopixels, enabling measurement of the position of a particle incident on the DSSD, to within an area of ≈ 9 mm^2, by identifying which strips on the front and the back had a particle incident on them within a certain time (in this work, this was about 5 µs). A diagram depicting this is shown in figure 3.13.

Usage of pseudopixels reduces the cost and complexity of experimental set-ups, requiring only 32 channels of nuclear electronics per detector rather than the 256 required if the DSSDs instead had distinct pixels. There is a drawback, however, in the form of uncertainty regarding hit detection. Single pile-up, depicted in figure 3.14(a), occurs when two particles hit the same strip on one side of the detector within 5 µs, resulting in an imbalance in the number of hits in the front and back of the detector. As the front and the back of the detectors measure the energy independently (the front collects the holes, while the back collects the electrons), the events can be reconstructed by taking only the energy from the side of the detector with two hits, and the position of the detections are still known. Double pile-up events, in which two particles hit both the same front and back strip of a detector, are unable to be reconstructed using this method as individual energy measurements for the two particles cannot be extracted. A multiple-hit event, depicted in figure 3.14(b), is similar to the case of single pile-up, but instead the two particles hit entirely different strips on the front and back. This results in four possible detection positions for the two particles, which need to be disentangled in order for the event to be usable. To do this, the energies measured by the front and the back strips can be compared — the true matching of the front strips to the back strips should have very similar energies. In the current work, this was achieved by sorting the hits in the front strips and the hits in the back strips in order of decreasing energy, and grouping the hits based on this ordering. While this method allows for the



(a) (b)

(c)

Figure 3.14: Depiction of the surface of a DSSD, showing an example of single pile-up (a), multiple-hit (b) and charge-sharing (c). Possible hit positions are shown in purple, with the front strips and back strips corresponding to a hit shown in red and blue, respectively. The relevant inter-strip area in the case of charge-sharing is shown in yellow.

reconstruction of the vast number of events, occasionally this could result in the incorrect assignment of positions, particularly in cases of very close particle energies. Figure 3.14(c) depicts the third effect, known as charge-sharing, in which a particle is incident between the strips (shown in yellow) rather than on a strip. This causes the resulting charge in the silicon to be shared between the two neighbouring strips. Reconstructing the hit in this case is very similar to the case of single pile-up, with the only difference being that the position of the singular hit is known to be at the contact wire between the two strips. Distinguishing these events from single pile-up events is not always possible, and as such in the current work any incidents involving detections in two neighbouring strips were assumed to be from a single, charge-sharing event. Events in excess of two hits involving single pile-up were unable to be reconstructed, due to large uncertainty in extracting correct hit patterns — with multiple-hit events, reconstruction is still possible, as long as the hits are all in distinct strips on both the front and back.

3.1.2.3 Detector placement

The four detectors that constitute the Birmingham large-angular-coverage DSSD array were placed in the Q3D reaction chamber (see figure 3.2) such that a total angular coverage of approximately $16° \rightarrow 92°$ in-plane and $-36° \rightarrow 40°$ out-of-plane was achieved. Figure 3.15 shows the layout of the DSSD array, with the centre position of each pseudopixel represented by a blue dot. The four corners that enclose the active area of each detector are also shown by a blue dot. The detectors were mounted sideways to enable less distance between each detector, as otherwise the cabling would prevent this and hence there would be large gaps in the coverage. The positions of the detectors were kept largely consistent across the two years of measurement — the in-plane centre angles and perpendicular distance from the target differed slightly, an overview of which is given in table 3.1. The uncertainties presented for the values in table 3.1 were estimated using comparison to Monte-Carlo data. The

Monte-Carlo data are discussed in detail in section 3.2. The top detectors (1 and 3) and bottom detectors (2 and 4) were offset by 27.5 mm in opposite vertical directions from the centre of the target, though due to an offset of the beam relative to the set-up ($\approx$ 6 mm in 2016, $\approx$ 5.5 mm in 2017), the 0° out-of-plane plane intersected detectors 2 and 4. Each constituent DSSD in the array was set such that the face of each detector lay approximately perpendicular to the vector between the centre of the detector and the target in-plane. It was not possible to achieve this out-of-plane, and as such the effective size difference of the outer (furthest from 0° out-of-plane) strips was larger when compared with the inner strips. This effect, however, was corrected for when considering geometric efficiencies via comparison with Monte-Carlo simulation.

Table 3.1: The centre angles (in-plane) and distances of each constituent DSSD in the Birmingham large-angular-coverage DSSD array, shown for both experimental set-ups (2016 and 2017) during which data were taken.

	2016		2017	
Detector	In-plane centre angle (degrees)	Distance (mm)	In-plane centre angle (degrees)	Distance (mm)
1	27.9(5)	87(1)	28.9(5)	86(1)
2	69.0(5)	80(1)	72.0(5)	80(1)
3	27.9(5)	72(1)	28.9(5)	70(1)
4	69.0(5)	65(1)	72.0(5)	64(1)

3.1.2.4 Electronics

The charge signals output by the DSSDs were processed using a typical nuclear electronics chain, an overview of which is given in figure 3.16. The output of each detector was connected to a Mesytec MPR-32-Series preamplifier [75], with two groups of 16 channels corresponding

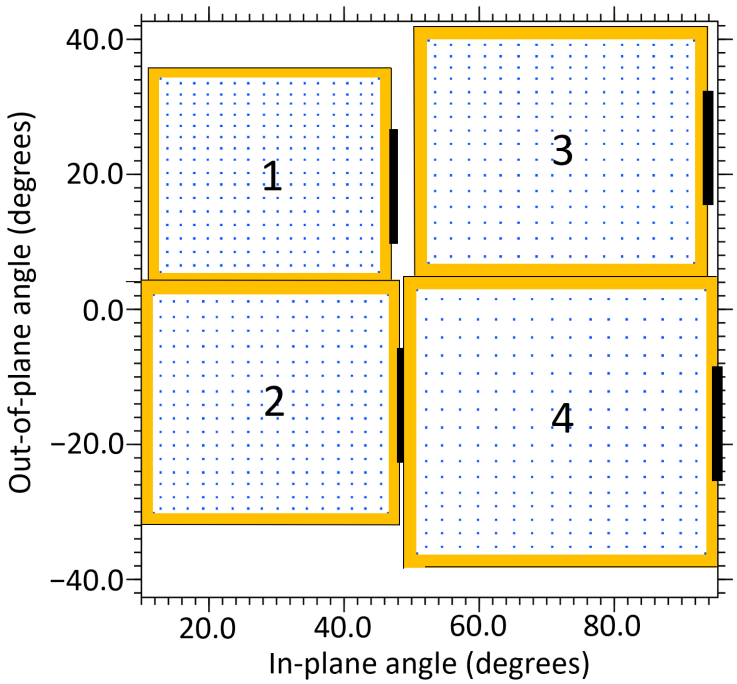


Figure 3.15: A depiction of the layout of the Birmingham large-angular-coverage DSSD array, with blues dots indicating the centre positions of each pseudopixel. The in-plane and out-of-plane angles are shown on the horizontal and vertical axes respectively. Borders have been placed around each DSSD to enable distinction between the different groups of pixels, with black boxes (representing the pins that are connected to the preamplifier) to indicate the bottom of each detector in the normal orientation as depicted in figures 3.13 and 3.14.

to the front and back strips of the detector. The purpose of the preamplifiers was integration and amplification of the small charge pulses before the introduction of large amounts of noise, which increased as the signals travelled. As such, the preamplifiers were placed close to the detectors in order to maximise the signal-to-noise ratio. These preamplifiers were able to output a signal that maintained both the amplitude and timing information of the original charge pulse, through use of a feedback loop containing a capacitor and a resistor in parallel. The output signal demonstrated a sharp rise: the time over which this rise occurred was equal to the charge collection time of the detector. This was followed by a long exponential

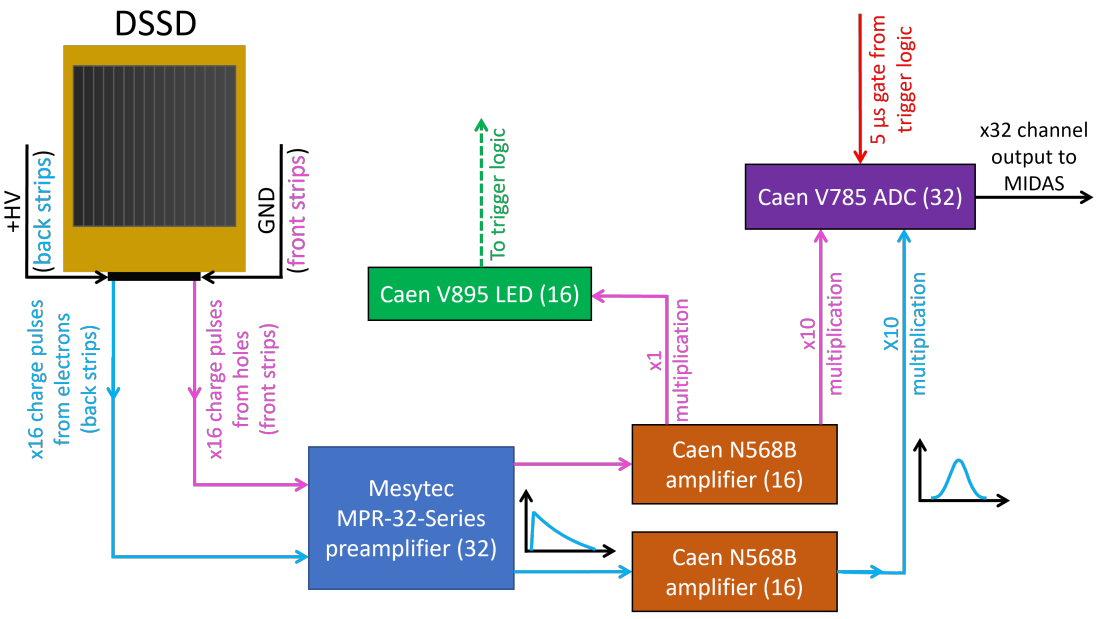


Figure 3.16: An overview of the electronics set-up used for the DSSDs, showing the processing of the charge signal through to digitisation of the signal by ADCs. Numbers in brackets on each electronics unit refer to the number of inputs. The ×10 multiplicative outputs are the same as the ×1 multiplicative outputs, but amplified by a constant factor of 10. The logic signal from the V895 LEDs is input into the trigger logic, shown in figure 3.18.

decay (over $\approx$ 25 µs), a signal shape characteristic of preamplifiers [73]. An example of this signal shape can be seen in figure 3.17. The time constant of the loop, defined as the resistance, 10 MΩ, multiplied by the capacitance, 10 nF, was much larger than the charge collection time, so to a good approximation the amount of charge, Q, present in the charge pulse from the detector was proportional to the output voltage of the preamplifier: in fact, as the capacitance of the preamplifier was constant, the output voltage at the maximum amplitude, V_{out}, was related to the charge by the simple expression $V_{\text{out}} = \frac{Q}{10\ \text{nF}}$.

The signals from the preamplifiers were then processed by CAEN N568B 16 channel spectroscopy amplifiers [76], with two amplifiers required per detector. Amplifiers perform two functions, the most obvious is an increase in the amplitude of the signal, often by

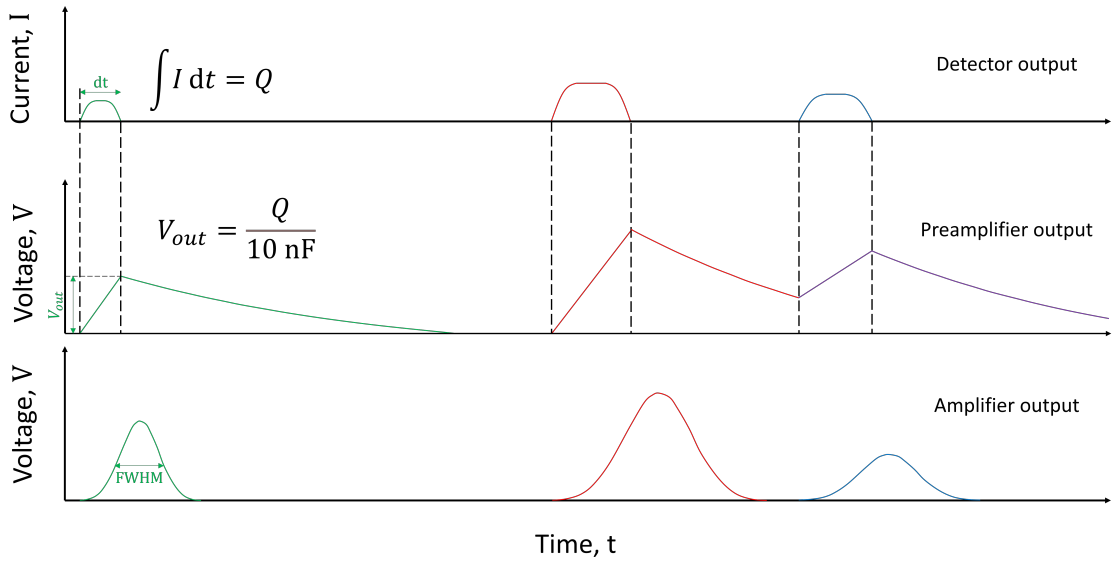


Figure 3.17: A depiction of the common shape of signals output by a detector (top), preamplifier (middle) and amplifier (bottom). Pulses due to three separate detections of charged particles are shown in green, red and blue respectively. The duration of the original charge pulse is shown by the dashed black lines, demonstrating the relationship to the rise time of the preamplifier signal. The width of a Gaussian produced by the amplifier is shown; the width of these pulses can be controlled via the amplifiers. Time axes shown here are not to scale with the real length of pulses in order to compare features. Figure adapted from figures in Refs. [73] and [74].

one or two orders of magnitude. The other function is a reshaping of the signal from the preamplifiers into a Gaussian shape, the width of which can be varied. An advantage of this can be seen in figure 3.17, in which the blue charge pulse has been generated too soon after the red charge pulse, before the capacitor in the preamplifier has fully discharged. This results in signal pile-up, distinct from the DSSD strip pile-up mentioned previously, in which the blue signal is added to the remaining red signal (shown in purple). Thus, there is additional difficulty in extracting a voltage signal proportional to Q for the original blue detection. By shaping the pulses into much narrower Gaussians, the individual pulses can

be extracted and their relevant heights obtained. In this work, the shaping time was chosen to be 1 µs for all DSSD events, which vastly reduced the chance of pile-up.

The DSSDs were biased on the back of the detector using a positive high-voltage supply, while the front was grounded in order to produce the reverse bias. As such, the signal from the back strips was likely to be slightly noisier than that of the front strips — to this end, the ×1 multiplicative outputs from each channel of the amplifiers corresponding to the front strips of the DSSDs were input into CAEN V895 16 channel leading edge discriminators (LED) [77], through which minimum voltage thresholds were set. If a Gaussian signal from the amplifiers had a maximum voltage larger than that of the threshold, a negative logic pulse was output to the trigger logic, discussed below. The ×10 multiplicative outputs of the amplifiers, for both the front and the back strips, were fed into CAEN V785 32 Channel Peak Sensing Analogue-to-Digital Converters (ADCs) [78], with one ADC for each DSSD. The ADCs were also used to set voltage thresholds for incoming pulses — the ADC would only convert an event, even if told to read out by a logic pulse, if the corresponding voltage signal were above this threshold. The ADCs were connected such that if a 5 µs gate were produced by the trigger logic, all of the ADCs would read out the events from all of the DSSD channels measured during that window. The events were processed through use of the Multi Instance Data Acquisition System (MIDAS) software [79] and stored digitally for further analysis. The software SunSort [80] was used for data analysis both during data collection and subsequently offline.

3.1.2.5 Trigger logic

The trigger logic, summarised in figure 3.18, shows the discriminator signal from figure 3.16 input into a LeCroy 429A quad logic fan-in/fan-out (FIFO) [81]. This unit acted as an OR logic gate, outputting a logic pulse whenever a logic pulse from any of the V895 LEDs

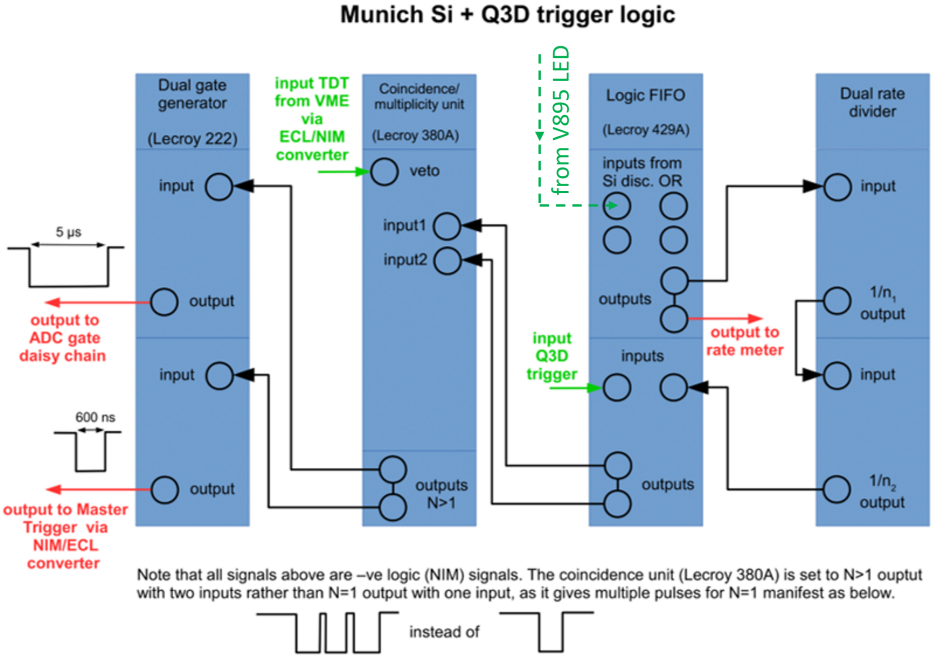


Figure 3.18: An overview of the trigger logic, which was used to gate both the ADCs and the Q3D to provide singles events for both systems. The output logic pulse from the V875 LEDs shown in figure 3.16 is shown in dark green.

was input. The outputted logic pulse was sent to a dual rate divider, through which the occurrence of these signals was scaled down by a factor of 10,000 (through two processes of dividing the rate by 100), due to the high rate of events in the DSSD array. The resultant logic signal was then input to the FIFO unit, this time alongside the trigger from the Q3D. The production of a Q3D trigger signal required a coincidence between a horizontal anode wire and the scintillator detector of the focal-plane detector — due to the relative position of the focal-plane detector elements, this requirement filtered the vast majority of cosmic events out of the trigger. As such, singles events from both the Q3D and the DSSD array were able to trigger a readout of the system. Two OR outputs from the FIFO were then input into a LeCroy 380A multiplicity logic unit [82], and the $N > 1$ outputs of the module were utilised. The $N > 1$ outputs were used rather than the $N = 1$ outputs, as the $N = 1$ outputs exhibited a fault, whereby multiple logic pulses were generated per event rather than

single pulse (see figure 3.18). Thus, in order to generate a signal from the $N > 1$ output, two identical inputs were required. The module was vetoed by the total dead time of the system, which was in the order of 40 µs per event. The outputs from the multiplicity unit were then used to generate gates via a LeCroy 222 dual gate generator [83], with a 5 µs gate used to readout the ADCs and a 600 ns signal used as the master trigger for the whole system.

3.1.2.6 Energy calibration

In order to calibrate the detectors along the electronics chain, a triple-α source containing ^{239}Pu, ^{241}Am and ^{244}Cm was utilised. An example fitted spectrum is shown in figure 3.19, showing the six peaks observed. The fitted states have the vast majority of the α-decay strength for each of their associated isotopes: the 5.106 MeV and 5.154 MeV peaks make up 11.94(7)% and 87.88(20)% of all ^{239}Pu α-decays respectively, while the 5.443 MeV and 5.486 MeV peaks represent 13.1(3)% and 84.8(5)% of ^{241}Am α-decays respectively and the ^{244}Cm peaks at 5.763 MeV and 5.805 MeV provide 23.10(10)% and 76.90(10)% respectively. As such, other α-particle emissions are negligible and hence do not need to be considered

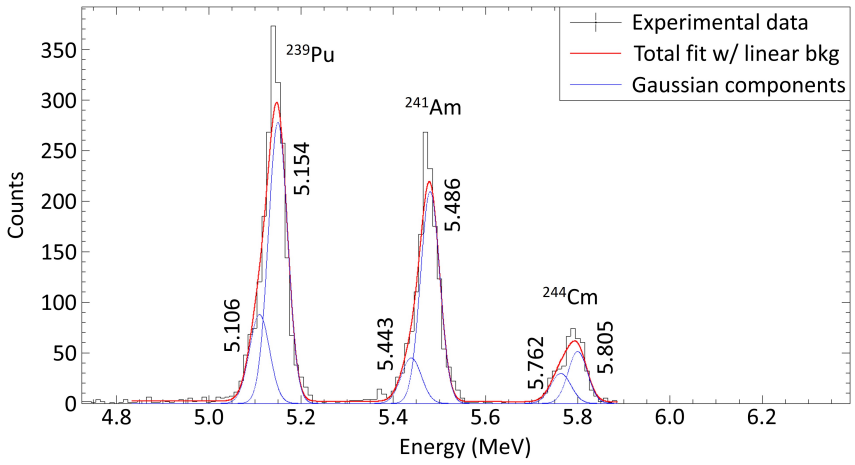
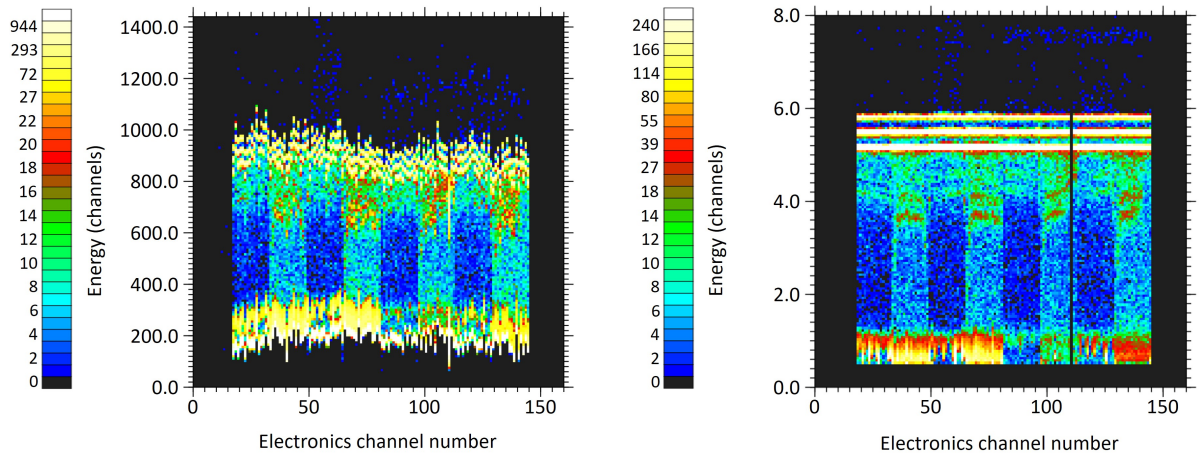


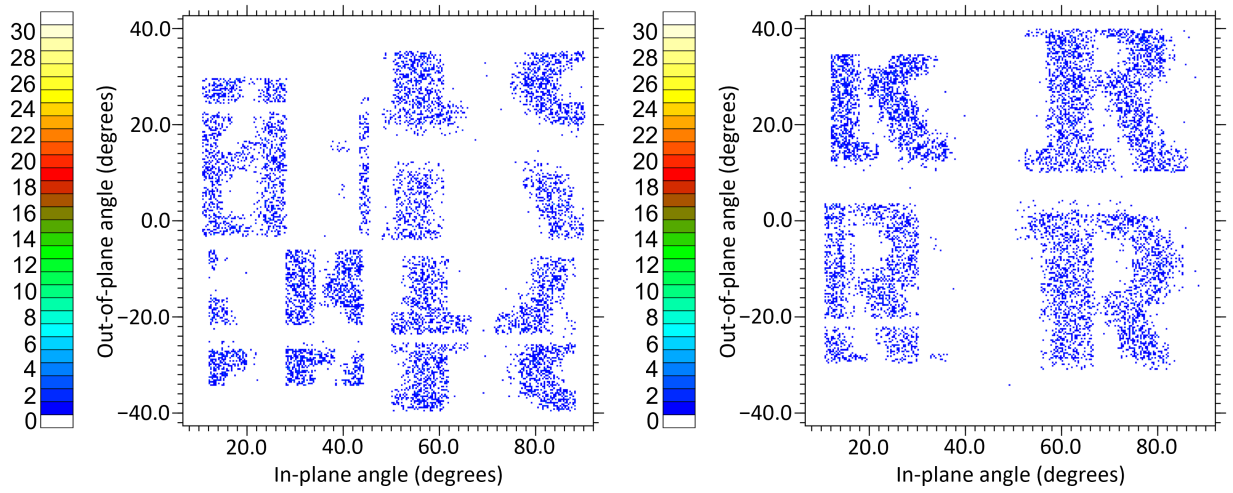
Figure 3.19: An example calibration for a strip of one of the DSSDs, showing the six peaks and the isotopes from which they originate.

during the calibration. The peak seen at 5.154 MeV is actually caused by two distinct α-emissions, at 5.144 MeV and 5.157 MeV — these are much closer together than the resolution of the DSSD array at this energy ($\approx$ 50 keV, which can be determined by the measured width of the α states). Thus, an average of the literature values of the two energies weighted by their intensities was performed in order to obtain the 5.154 MeV value. As each strip on a DSSD had a separate chain of electronics, the calibration was performed for each of the 128 strips. A comparison of the energy spectra obtained for each channel, both before and after calibration, can be seen in figure 3.20.



(a) (b)

Figure 3.20: Energies measured from a triple-α source in each strip of the DSSD, plotted against electronics channel number, before (a) and after (b) the energy calibration was performed. Three distinct bands (due to the compressed vertical scale) corresponding to the energies from the three isotopes can be seen in the calibrated spectrum. An empty channel can be seen in (b), which was unable to be calibrated due to the lack of a sensible triple α-spectrum — this can be inferred from the corresponding channel in (a).



(a) (b)

Figure 3.21: A Cartesian view of the detector array, showing data taken using a triple-α source with the faces of the detectors covered by the R-masks. A comparison of incorrect mapping of pins to the electronic channels (a) to the correct mapping (b) is given — the Rs can be clearly seen with the correct mapping for each DSSD.

3.1.2.7 Position calibration

As well as calibrating the measured energy of particles incident on the DSSDs, the position of interaction in real space had to also be determined. The cabling from the detector to the preamplifier does not necessarily result in a logical channel number for each strip. This is because of space restrictions on the detector printed circuit board (PCB), which results in blocks of 8 strips being reversed on the rear side. Additionally, the wiring of the electronics can lead to detectors being read top-to-bottom or bottom-to-top arbitrarily; the in-plane direction can be read left-to-right or right-to-left. Thus, in most cases assuming that the strips are in order along the electronics chain results in incorrect assignment of position. In order to correct for this, plastic blocks made to fit over the face of the DSSDs were 3D printed. These blocks, known as R-masks, each had a hole in the centre shaped like the letter R. The asymmetry of the letter R across the centre in both axes was ideal, as the

risk of confusing quadrants of the DSSDs is greatly diminished. Thus, incident α-particles from the triple α-source reached the detector through the R-shaped hole, but otherwise were stopped by the plastic block surrounding it. As such, a pattern of hits in an R-shape was observed on the faces of the detectors. Data taken using the triple-α source, with the R-masks placed over the DSSD array, are shown in figure 3.21, highlighting the importance of correct assignment of the strip positions.

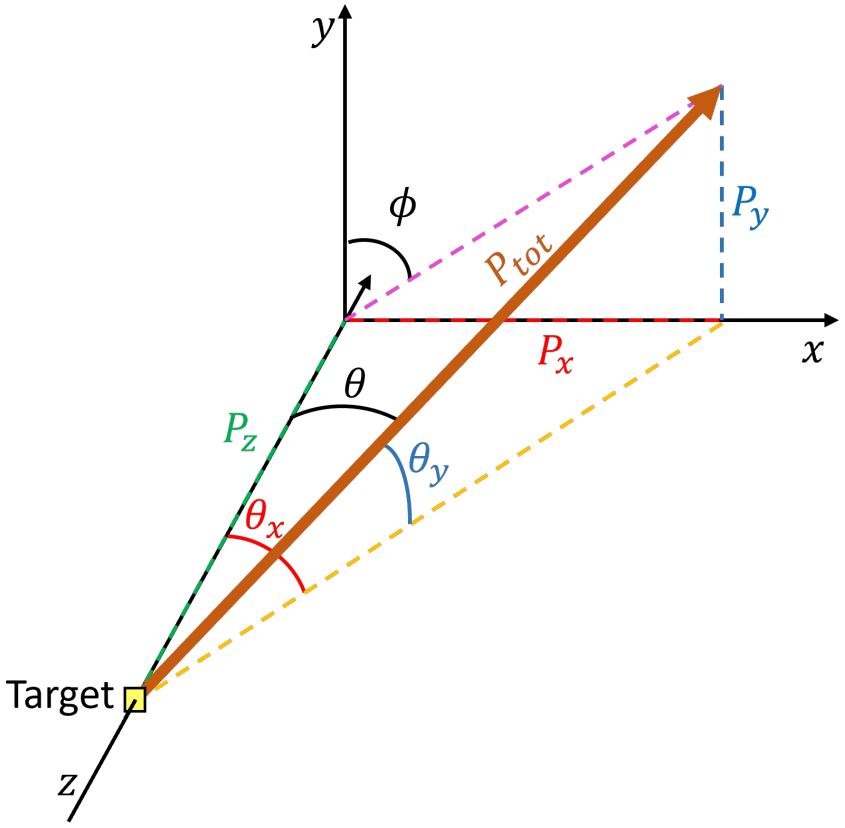


Figure 3.22: Diagram detailing angle definitions, as well as providing the geometry with which to determine them. The beam travels along the z-axis and interacts with the target, located at the origin, while the product nuclei are detected in the x-y plane shown. Figure adapted from Figure 2 of Ref. [84].

From the position of detection on the DSSD array, the in-plane angle, θ_x, and out-of-plane angle, θ_y, can be determined simply through knowledge of the detector position

relative to the target. The beam axis is chosen to be the z-axis by convention, and the detectors are placed in the x-y plane. The position measurement combined with the energy measurement allows for the determination of the momenta of the particle in each Cartesian direction, values that are necessary to identify the species of decay fragments as discussed later in section 3.3.2. The magnitude of the total momentum, P_{tot}, of a non-relativistic particle, with known mass m and energy E as measured by the DSSD array, is simply given by

$$P_{\text{tot}} = \sqrt{2mE}. \tag{3.6}$$

Utilising θ_x and θ_y with the scalar value P_{tot} provides the value of $\vec{P}_{\text{tot}}$, which can be disentangled to provide the Cartesian components P_x, P_y and P_z. From figure 3.22, it can be demonstrated that these components are given by

$$\begin{aligned} \vec{P}_x &= \vec{P}_{\text{tot}} \sin\theta_x \cos\theta_y, \\ \vec{P}_y &= \vec{P}_{\text{tot}} \sin\theta_y \quad \text{and} \\ \vec{P}_z &= \vec{P}_{\text{tot}} \cos\theta_x \cos\theta_y. \end{aligned} \tag{3.7}$$

The scattering angle, θ, and azimuthal angle, ϕ, can also be determined simply. In figure 3.22, the different Cartesian momenta are equal to their corresponding unit position vectors multiplied by the scalar P_{tot}. Hence, the scattering angle is related to the Cartesian in-plane and out-of-plane angles by

$$\theta = \arccos(\cos\theta_x \cos\theta_y), \tag{3.8}$$

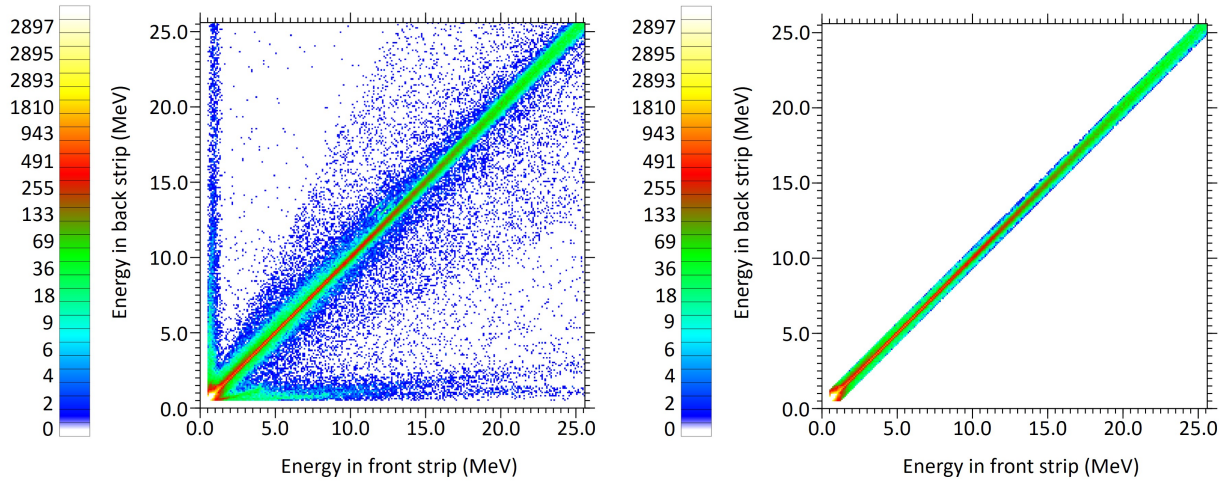
and the azimuthal angle is given by

$$\phi = \arccos(\sin\theta_y), \tag{3.9}$$

enabling a simple conversion between the two co-ordinate systems [84].

3.1.2.8 Resolution

As the DSSDs measure energy from both the front (holes) and back (electrons) strips, logically a reduction in the statistical error of the number of charge carriers, and hence on the measured energy, could be achieved by taking an average of the two values, and this was performed for measurements of energy in the current work. However, this is predicated on the assumption that the measurement of energy from the front and back are always corre-



(a) (b)

Figure 3.23: Energy measured in a front strip of detector 2 against energy measured in a back strip, for silicon singles events obtained during the 9.6 → 11.9 MeV excitation region runs. Events ungated except for a low-energy threshold are shown in (a), while an example software gate (the requirement that front and back hits must be within 0.7 MeV of one another for a good event) is shown in (b).

lated in an event — in the case of pseudopixel pile-up, for example, this may not be the case. Figure 3.23(a) shows the energy measured in a front strip of the detector against the energy measured in the back strip of detector 2 for all silicon-only events above a threshold of 0.5 MeV. This threshold was set across all events in order to eliminate the presence of events due to electronic noise. A clear diagonal line in this plot can be observed, indicating events in which the measured front and back energies are in good agreement. Events with very little energy measured in one of the front or back strips of the detector can be observed near either axis. A region of non-negligible counts either side of the diagonal can also be observed, indicating events where the energies are close but not identical. At high energies, the diagonal line can be seen to disappear into this region, which occurs for two reasons. The first effect is the decrease in resolution, R, of the silicon detectors with increasing energy, E, as defined by the relationship

$$R = 2\sqrt{2\ln 2\frac{Fw}{E}}, \tag{3.10}$$

where F represents the Fano factor, the ratio between the observed variance in the number of charge carriers produced by an interaction in the depletion region of a semiconductor and the variance predicted by Poissonian statistics (for scintillator detectors, this value is 1, whereas for silicon the theoretical and experimental values lie within a range of $0.07 \rightarrow 0.17$ [85, 87, 86]), and w represents the energy required to create an electron-hole pair (in silicon, this value has been measured to be approximately 3.6 eV [90, 89, 88, 86]). Again, this effect can be seen in figure 3.23 to not exceed the 0.7 MeV gate in the region of interest. The second effect is that as the linear energy calibration is performed across $5 \rightarrow 6$ MeV, the fidelity of the calibration at energies far from the calibration region decreases. The fragments from decaying ^{18}O* for the observed states in this work had a maximum energy of ≈ 19 MeV for the case of the ground state of ^{14}C produced via an α-decay from an ^{18}O excitation at around 16.3 MeV. The accuracy of the calibration was hence acceptable for all events of interest,

and a gate requiring a difference of no more than 0.7 MeV between front and back energies measured in 2017 was introduced to remove wrongly constructed events, the effect of which can be seen in figure 3.23(b). For 2016 events, the maximum difference was 0.4 MeV, as for these data lower excitation energies were populated and hence the maximum energy for fragments of interest was correspondingly lower.

3.1.2.9 Determination of kinematic lines

In reactions with a two-body entrance and exit channel, such as in the case of scattering or nucleon transfer reactions, the energy and momentum of the two product nuclei are solvable given knowledge of the masses of all reactants, as well as the energy of the beam nucleus and the excitation energy, if any, of the product nuclei. A derivation for this is provided in Appendix A. As the DSSDs did not require a Q3D trigger to be read out, events not corresponding to the ^{12}C(^{7}Li,p)^{18}O* reaction were able to be observed. As the beam provided by the tandem Van de Graaff accelerator was both stable and pure, and the abundance of ^{12}C in $^{\text{nat.}}$C is 98.9%, elastic scattering of ^{7}Li on ^{12}C was expected to be common, and hence visible in the data. As the energy of the ^{7}Li and ^{12}C after scattering can be calculated for a particular scattering angle, lines can be drawn over an experimental plot of scattering angle against energy, such as in figure 3.24, where the orange and red lines represent the energies of elastically scattered ^{7}Li and ^{12}C as a function of scattering angle, respectively.

During comparison of the experimental data with Monte-Carlo simulation, a substantial difference in spectra produced using energies measured in the DSSD array was noticeable. This issue did not extend to spectra utilising other values, such as comparisons of the shape of the Gaussian profiles for decay species on the face of the detectors (see section 3.3.1 for more detail). This effect was present in all data using both the DSSD array in conjunction with the Q3D taken during both 2016 and 2017. The logical conclusion was that there was

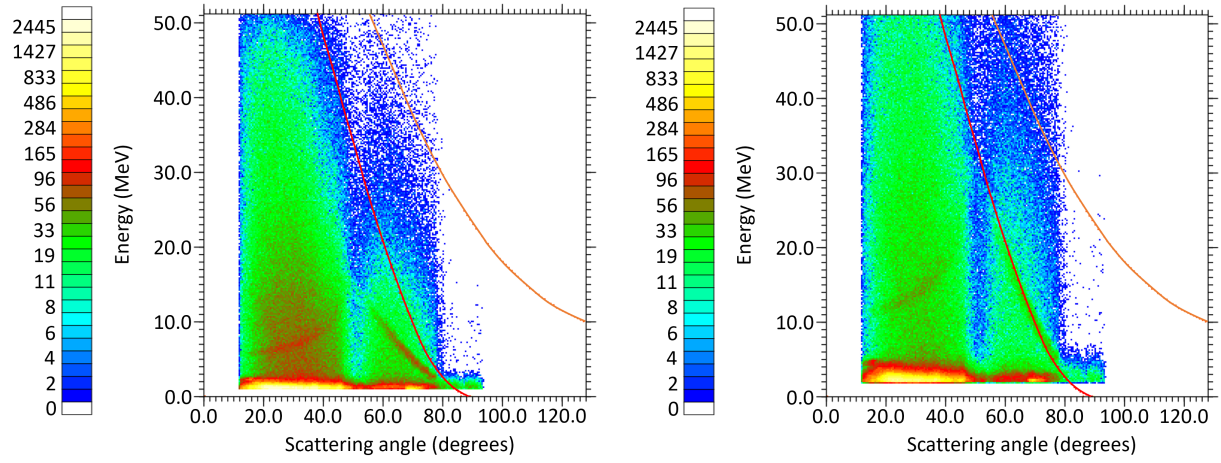


Figure 3.24: Plots of scattering angle against energy for singles events in the DSSD array, using energy values determined via calibration with the triple-α source (a) and double the energy determined via calibration (b). Calculated kinematic lines for elastic scattering of ^{7}Li on ^{12}C are also plotted for the recoil ^{12}C (red) and the ejectile ^{7}Li (orange) — see text for details.

some issue present with the DSSD energy calibrations, but calibrations taken at different times across the experimental runs all agreed with one another precisely. The possibility of the triple-α calibration not holding true for other species of nuclei was considered, perhaps due to energy loss through the thin ($\approx$ 100 nm) dead layer on the surface of the DSSDs — these were ignored during calibration, as the energy loss of the α-particles through this dead layer was 14.4 keV, which is small compared with the intrinsic resolution of the detectors at this energy. However, the discrepancies observed were of the order of MeV, so this was not a sufficiently large effect. Singles events from the silicon were investigated, with the scattering angle (determined through use of equation 3.8) plotted against the measured energy, in order to identify kinematic lines. These data are shown in figure 3.24, with the previously described kinematic lines overlaid in order to match features. Figure 3.24(a) shows the data using the α-calibration as before, and there is a distinct lack of scattering features near the

calculated kinematic lines. However, it was noted that by doubling the energy of the detectors in the DSSD array, as shown in figure 3.24(b), a good agreement was achieved between the scattered ^{7}Li kinematic line and a feature in the experimental data. This doubling of energy measured in the DSSD array was applied to the experimental data across all four detectors (thus, all eight amplifiers/four ADCs). These data were again compared to Monte-Carlo simulation, and a very good agreement was seen in the spectra generated (examples are shown in section 3.3.2), confirming that the kinematic line was identified appropriately. The energies measured in the DSSD array were thus doubled from those calculated via calibration for all data across the experiment.

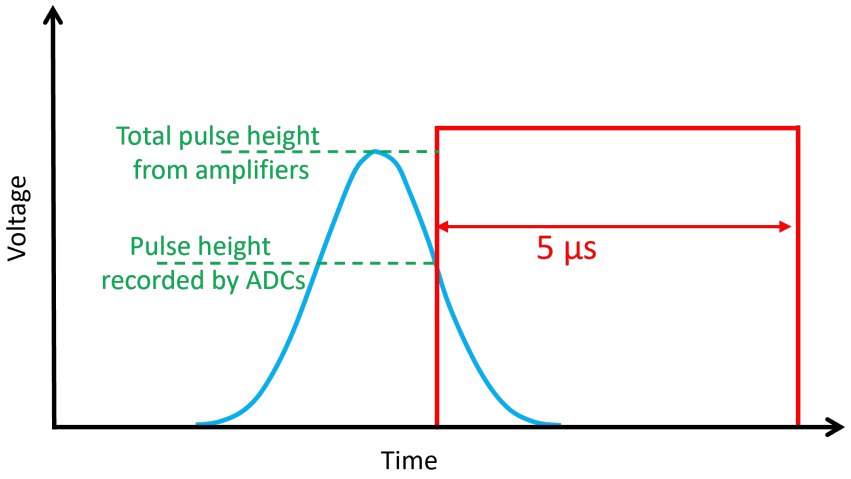


Figure 3.25: A diagram showing the likely cause of the energy jump. The amplifier signal, shown in blue, is only partially inside of the 5 µs gate, shown in red. As such, the ADC only registers the height of the signal present in the gate as the gate ends.

As the actual energy of particles was roughly double that measured from using just the triple-α calibration, it was considered that perhaps the gain across the amplifiers had been changed, but as the effect was present across both years, across all eight amplifiers and not present in any DSSD calibration runs (which were interspersed throughout the experimental campaign), this eventuality was deemed unlikely. The shift in energies for events in the DSSD

array only occurred when Q3D events were also collected (using the trigger logic described previously and shown in figure 3.18), so the likely cause of this shift lay in the timing of the 5 µs gate. As the electronics for readout of events in the Q3D are usually positioned outside of the experimental room, there is usually a sizeable time during which the signal travels. This work necessitated the placement of these electronics closer to the experimental chamber, and as such an artificial delay was added via >20 m of cabling in order to best maintain the usual timing. However, also changed was the output polarity from the amplifiers from previous experiments performed using this set-up, which can have an effect on the delay of the signal [76]. If this timing were slightly off as a result, the 5 µs gate would not allow the ADCs to register the full pulse height of signals from the amplifiers. A depiction of this is shown in figure 3.25, and further effects from this are discussed in section 4.1.

3.2 Monte-Carlo simulation

In order to determine branching ratios for states in ^{18}O, accurately measuring the expected number of events from different decay channels is paramount. As such, Monte-Carlo simulations were produced and used to estimate the geometric efficiency, the fraction of all events from a certain exit channel that would be incident on the DSSD array, including taking into account the gating efficiency, as well as to verify or identify experimental features in the data.

3.2.1 Resolution8.1

Monte-Carlo simulations used in this work were produced using Resolution8.1, an unpublished in-house FORTRAN 77 package written and used by the nuclear structure group at the University of Birmingham, with some details given in Refs. [72, 91, 92, 93, 94, 95]. Thin

target non-relativistic nuclear reactions and decays were simulated through multiple stages of sequential two-body interactions, including direct interactions and compound nucleus formation: scattering (both elastic and inelastic), resonance reactions and nucleon transfer. The nuclei involved in the reaction were each defined via their corresponding mass, m, and charge, q. The mass of a nucleus was approximated to be equal to the total nucleon number. Resolution8.1 would check these values to confirm equal total masses and charge in both the entrance and exit channel, and required that all nuclei involved had $A > 0$. The energy of the beam nucleus was entered, as this was necessary in order to calculate the appropriate kinematics — in this work, the value was 44.0 MeV. Any product nuclei could then be given excitation energy, with a corresponding width, and, if this excitation energy were sufficient, simulated to decay further. The Q-value at each stage of the reaction was required, and thus could be used to check if there were sufficient excitation energy for a decay to proceed. The total number of good events (i.e. events that the simulation would output to file) was also user-specified, though the simulation would terminate if no good events were produced during the first 10^6 simulated events. Only events that had a recoil proton incident within the angular acceptance of the Q3D (-42° to -36° in-plane and -2° to $+2^\circ$ out-of-plane) were simulated, as these were the only events of interest and thus simulating events in which this were not the case was unnecessary, allowing for a significant decrease in computational time required.

Nuclei produced through a nuclear reaction in the simulation travel in a straight line, the direction of which was determined by randomly sampled angles, which were defined relative to the beam axis. Appropriate angular distributions for the decay fragments could be produced using a spherical polar coordinate system (r,θ,ϕ), where ϕ would be generated randomly between user-specified low and high limits. The distribution of θ for the products produced by the initial interaction (in this work, these products were the p recoil and ^{18}O ejectile) could be selected from two user-specified options: these included a uniform distri-

bution in the centre-of-mass frame and a distribution featuring an exponential drop-off in probability from the beam direction. The ability to include a user-defined distribution was also present. A uniform distribution was selected in the present work, in which θ and ϕ of the proton was limited to within the angular acceptance of the spectrometer. The angular distributions of fragments were randomly selected in the lab frame using the in-plane and out-of-plane angles, and so θ and ϕ were instead calculated from these values. The reasoning behind this is discussed in section 3.3.1.

In order to best produce realistic Monte-Carlo data, real-world smearing effects needed to be included. The smearing effects (with the values used in the current work given in brackets, if appropriate) that were applied in Resolution8.1 were:

- Beam energy spread from the Tandem accelerator (0.0004 MeV),
- Divergence of the beam from the entrance of the chamber (0.1°, both in-plane and out-plane),
- The size and shape of the beam spot (1.5 mm, both in-plane and out-plane),
- Energy loss of the beam and fragments in the target,
- Energy straggle of the beam and fragments in the target,
- Angular straggle of the beam and fragments in the target,
- Recoil due to in-flight γ-decay.

Energy loss effects were calculated using the FORTRAN code dedx.f [96], adapted from the code SPAR developed by Armstrong and Chandler, with details of the various energy-loss calculations for the different energy regimes given in Ref. [97]. This code was then also used during analysis to correct for the energy loss of fragments through the target, assuming

the interaction between the beam and target nuclei to have occurred at the centre of the target thickness, through interpolation of a series of energy and range values for the relevant fragment ions in solid ^{12}C.

Resolution8.1 provided a variety of options regarding conditions for the output of simulated data. Only the information pertaining to final state nuclei was output following the simulation, which could be in two forms: the momenta of the nuclei along each Cartesian axis, or the kinetic energy of the particle along with the in-plane and out-of-plane angles. The conversion between the two outputs is simple, utilising equations 3.6 and 3.7. Simulated strip detectors could be placed in the Monte-Carlo simulation, requiring definition of their physical dimensions (area and number of strips) and positions (defined by their angles from the beam axis and distance from the target). Real detector effects, such as an energy threshold, resolution and missing strips (such as in the case of a damaged bond wire in a DSSD), were also able to be simulated. The simulation could then be set to output only final state particles incident on a working strip in the active area of a detector if they had sufficient energy, which would then be smeared according to the energy resolution of the detector. From this, an efficiency could be provided regarding the ratio of events with at least one final-state nucleus incident on a working strip to the total number of events simulated.

In this work, the detectors were not simulated in the Monte-Carlo package and instead were defined in the sort code used to analyse the experimental data, as this guaranteed consistency between the physical positions of the detectors in both the experimental and Monte-Carlo data. As such, the energies and angles of all final state particles, smeared only by the real-world effects listed above, were output for each good event in order to determine geometric efficiencies using the sort code to establish how many events were incident within the solid angle subtended by the DSSD array.

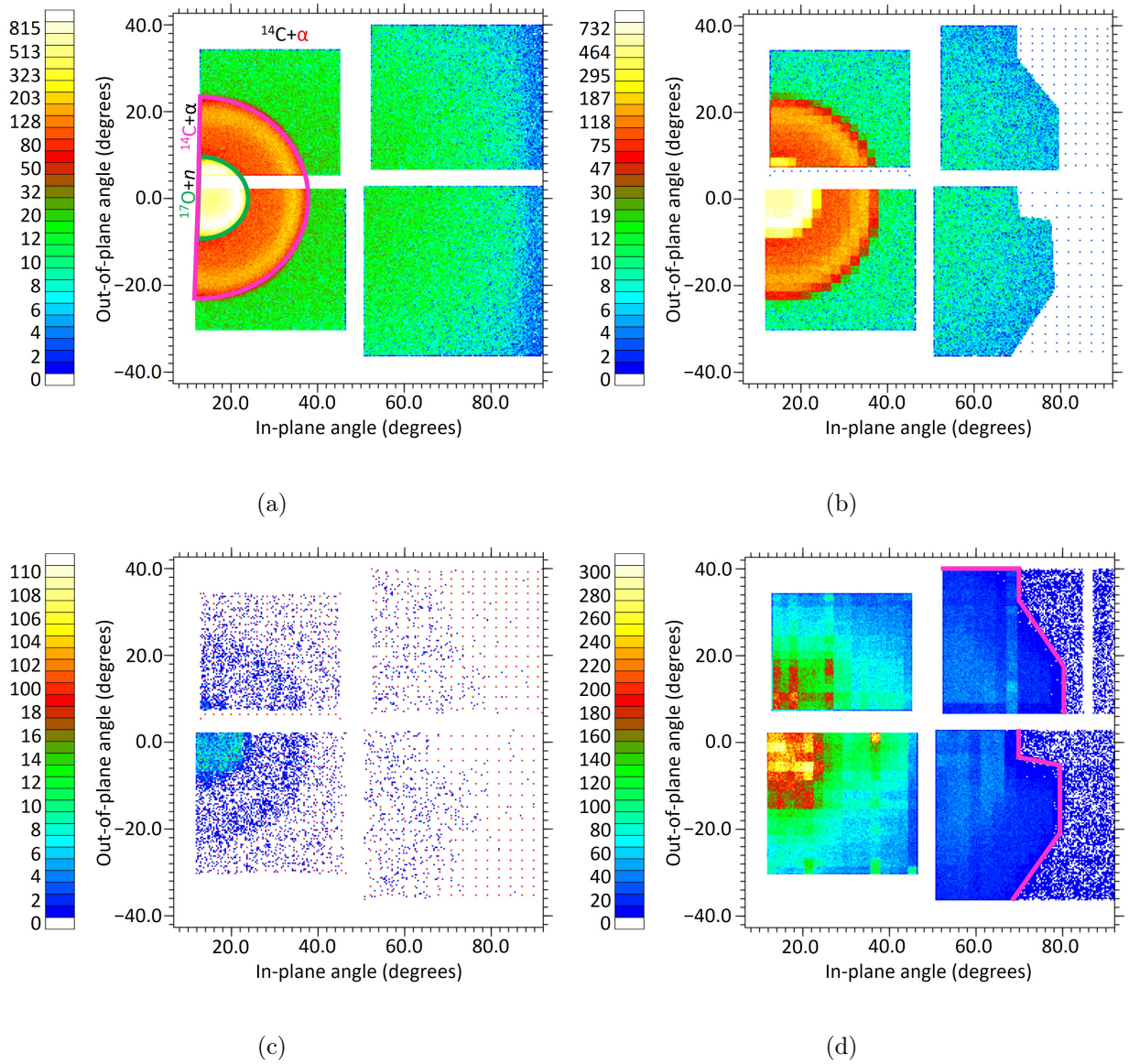


Figure 3.26: Cartesian views of the detector array for events corresponding to excitation energies of 9.6 → 11.9 MeV, for Monte-Carlo data with no position smearing (a), Monte-Carlo data with position smearing as described in the text (b), experimental data coincident with a good Q3D event (c) and all singles DSSD events (d). Subfigures (b) and (c) are published in Ref. [91]. The magenta and green regions in (a) are used to highlight the Gaussian profiles of ^{14}C and ^{17}O detections respectively, while the magenta boundary in (d) highlights the experimental gate placed on data to avoid obscured pseudopixels.

3.2.2 Further smearing effects

As the detectors were defined in the code, other experimental effects needed to be accounted for in order to reproduce the data taken during the experiments. One such example is the uncertainty of position across a DSSD strip. In the experimental data, the position of particles detected by the DSSD array is only known to within an area of ≈ 9 mm^2, a limitation of the size of the strips. In order to aid in analysis of these data, the position of the hit is randomised across the width of a strip, both in the front and the back of the detector, in order to produce a continuous distribution across all of the strips. As the Monte-Carlo data are outputted with the "true" values of energy and angle (after real-world smearing effects), these events need to be smeared across the the widths of the strips to truly recreate the experimental data. Figure 3.26 demonstrates the effect of this, showing the detection position for events arising from the decay of $9.6 \rightarrow 11.9$ MeV excitations in ^{18}O. The events plotted with an unsmeared detection position in figure 3.26(a) can be compared with the same events plotted using a random position across the widths of the corresponding strips shown in figure 3.26(b), with the latter providing a much closer recreation of features present in the real data, shown in figure 3.26(c), gated on good Q3D events. In order to improve the comparison between the Monte-Carlo and experimental data, missing strips (for example, at the bottom of detector 1) are also included. A sharp cut-off for large values of in-plane angle on detectors 3 and 4 can be observed in both figure 3.26(b) and figure 3.26(c) — this was due to the positioning of the target ladder (and in the case of the gap at the top of detector 4, a protruding screw), blocking events from reaching the DSSD array. Figure 3.26(d) shows hits in the DSSD array without the requirement for a good Q3D event, increasing the available statistics in order to better demonstrate this effect, showing the boundary, in magenta, at which events begin to be blocked by the target ladder. This feature needed to be consistent across the Monte-Carlo and experimental data in order to

calculate accurate geometric efficiencies, and hence a software gate was created to exclude angles blocked by the target ladder across all data.

The energy of final-state particles output in the Monte-Carlo data also required further smearing, in order to best match the resolution of the detectors. While the resolution of the detectors from calibration with the triple-α had been established, this only held true for particle energies around $5 \rightarrow 6$ MeV — the range of energies investigated was much larger. Also, the resolution of semiconductor detectors worsens as a function of incident particle rate, as well as incident ion species: the production of delta electrons (electrons with sufficient energy to cause further ionisation of atoms in the crystal, produced in an initial heavy charged particle interaction in a semiconductor crystal) results in a larger fluctuation in the number of charge carriers produced per event [98]. With a lack of excitation peaks with narrow widths measured by the DSSD array in the high-rate experimental runs, the difference in measured energy between the front and back strip for a given event was investigated. Figure 3.27 shows the difference in front and back energies for detector 3 for singles events measured during the $9.6 \rightarrow 11.9$ MeV excitation region runs, displaying a clear peak centred around 0 on top of some much broader feature. Events corresponding to the broader feature belong to events in which there has been an incorrect assignment of hits — detector 3 was selected due to a decreased incident particle rate, reducing the likelihood of pile-up and multiple-hit events. By approximating the broad feature to that of a broad Gaussian on a constant background, a reasonable estimation of the width of the narrow feature (through approximation to a Gaussian) could be established: the value of this width extracted from the fit was 144.5(8) keV ($\chi^2/\text{dof} \approx 5.0$). For singles events taken during the $12.4 \rightarrow 14.5$ MeV excitation runs (these two excitation regions corresponding to the highest available statistics in the DSSD array), the equivalent value was 142.9(7) keV. A Gaussian smearing with a width of 100 keV on the Monte-Carlo energies of final state particles performed twice, once representing the measured front strip energy and once for the measured back strip energy,

was thus appropriate. The resulting Gaussian energy distribution, when these two values were averaged, had a width of $100\sqrt{2}$ keV, comparable to the estimated result from the data.

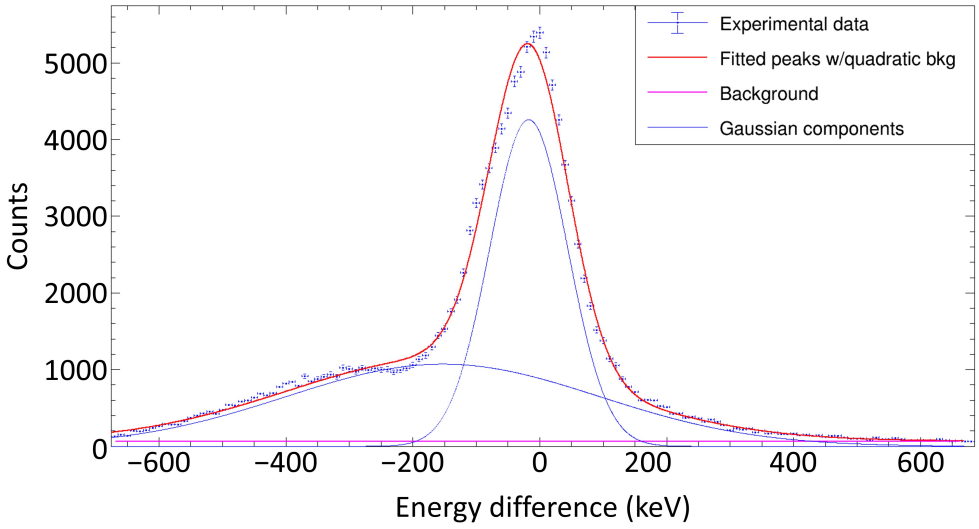


Figure 3.27: The difference in energy between the front and back strips of a DSSD for events. This was fitted using two Gaussians and a constant background to a good approximation. The width of the relevant fitted Gaussian was 144.5(8) keV.

The recoil proton detected by the focal-plane detector also needed significant smearing of both energy and angle in order to match the experiment. As the angle of any proton measurement was unknown, except that it was within the solid angle acceptance of the aperture ($\pm 3.0°$ in-plane and $\pm 2.0°$ out-of-plane), calculating the momentum of the proton resulted in a large uncertainty. Smearing the angle for the Monte-Carlo data was simple, as all Monte-Carlo protons were treated as if they had entered the Q3D at angles of $-39.0°$ in-plane and $0°$ out-of-plane. The energy and momentum of the proton, which needed to be known in order to establish the species of decay products measured in the DSSD array (see section 3.3.2 for more detail), could not be smeared so simply. In the analysis of the experimental data, the Q3D spectra obtained were calibrated to the excitation energy of ^{18}O rather than to the kinetic energy of the proton. Thus, the energy of the proton had to instead be calculated using two-body kinematics (see Appendix A for more detail), using

the centroid angle of the Q3D in conjunction with the known Q-value of 8.401 MeV, the masses of the reactant and product nuclei, the beam energy (44.0 MeV) and the excitation energy as measured by the Q3D. An example for the range of proton energies for states in the $9.6 \rightarrow 11.9$ keV region is shown in figure 3.28(a). In order to produce comparable smearing for the recoil proton in the Monte-Carlo data, the value of excitation energy measured in the Q3D corresponding to an unsmeared proton energy, as output by the Monte-Carlo simulations, was calculated through two-body kinematics using the true angles provided by the Monte-Carlo data. The calculated excitation energy could then be used to calculate a smeared proton energy, again through two-body kinematics, using the centroid values of the Q3D acceptance. The result of this is shown in figure 3.28(b), from a simulation, using states with equal widths (50 keV and equal population (10^5 counts)). The centroids of states in figure 3.28(a) and (b) can be seen to align well, and discrepancies between the features in the two subplots can be explained by the differing widths, differing populations and phase-space background present in the real data. The unsmeared proton energies from the Monte-Carlo are shown in figure 3.28(c), which shows a continuous distribution that does not match that extracted from the real data.

The effect of all the smearing effects on the data together provides a realistic simulation. Figure 3.29 shows simulated Catania plots (discussed in detail in section 3.3.2) produced assuming detection of a ^{14}C nucleus from a (^{18}O,α) event, with varying levels of smearing compared to a Catania plot produced using real data. In figure 3.29(a), no smearing effects of any kind are present, while in figure 3.29(b) only the smearing effects incorporated by Resolution8.1 are present. Figure 3.29(c) shows the case in which all previously described smearing effects are present, and a clear match to the position and widths of the loci to the experimental data (figure 3.29(d)) is observed. The effect is clearest in the locus corresponding to detection of a ^{14}C, labelled in figure 3.29(a), as the other loci are further smeared due to incorrect kinematic assumptions when producing the Catania plots.

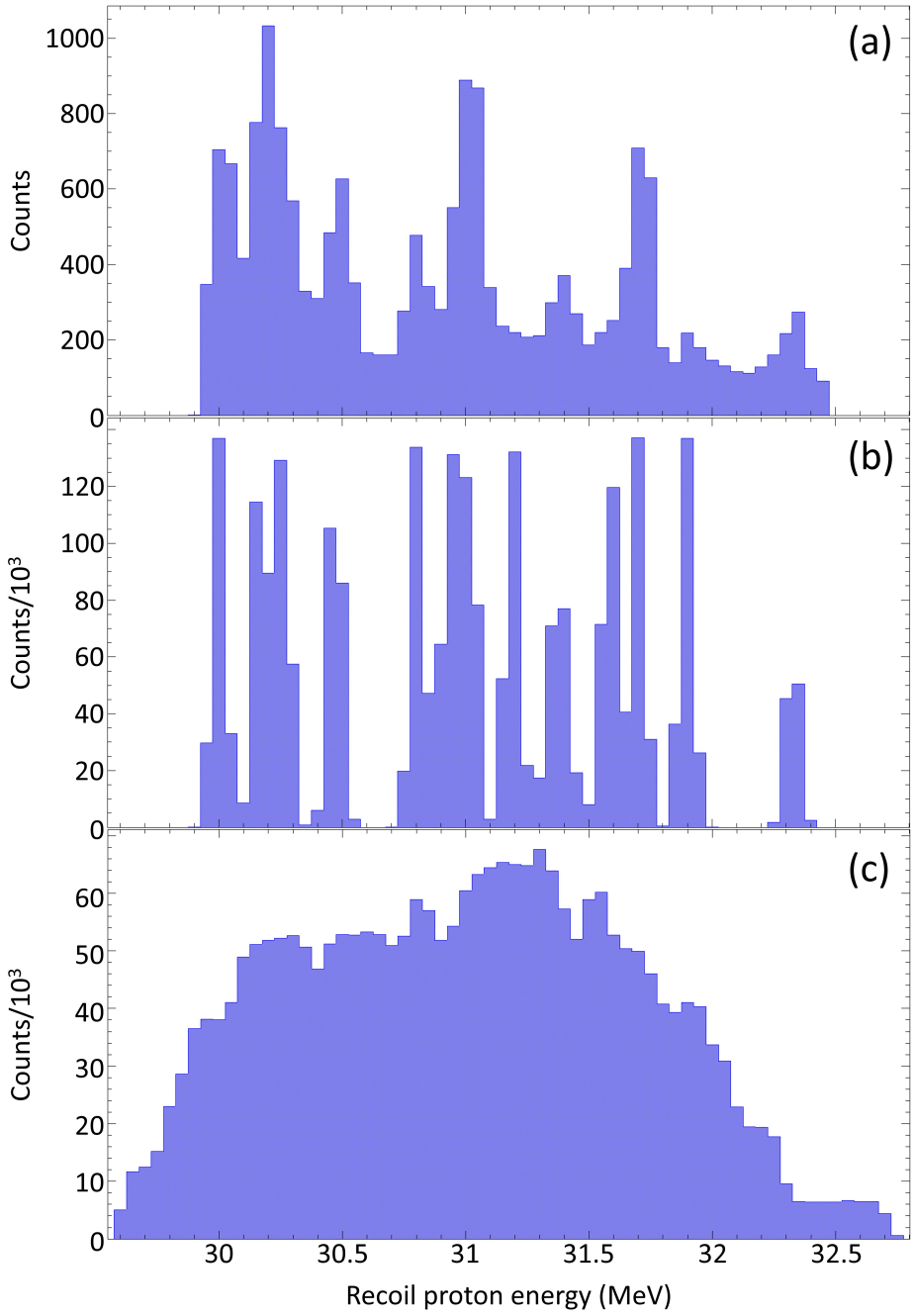


Figure 3.28: Histograms showing the measured proton energy for good Q3D events with corresponding ^{18}O excitation energies of 9.6 $\rightarrow$ 11.9 keV, for the experimental data (a), smeared Monte-Carlo data (b) and unsmeared Monte-Carlo data (c). A much better agreement with the centroids of the states and general features can be seen between (a) and (b).

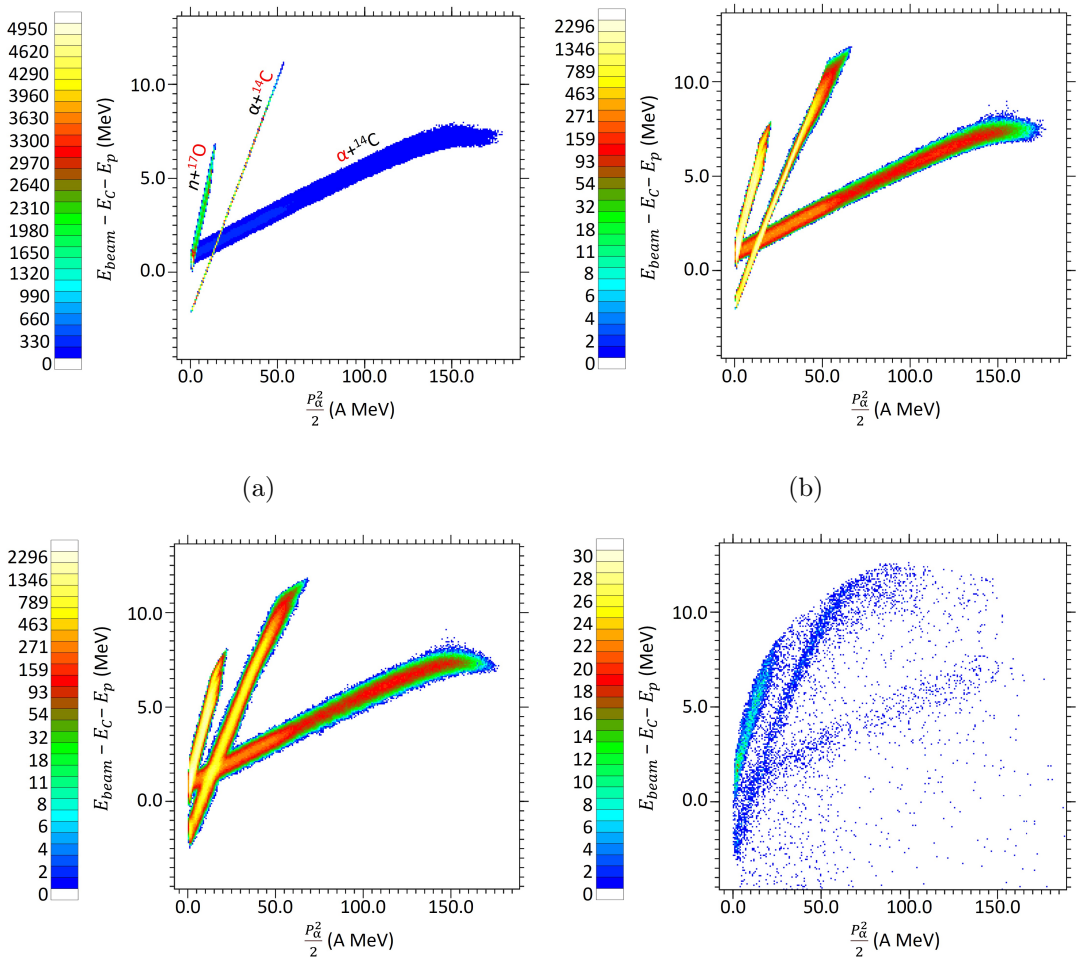


Figure 3.29: Catania plots generated for states in the 9.6 → 11.9 keV region, assuming detection of a ^{14}C from a (^{18}O,α) event, using the energy of the highest energy hit per event. Three plots generated using Monte-Carlo simulation are provided, produced with different amounts of experimental smearing: no smearing (a), Resolution8.1 specific smearing (b) and all smearing effects (c). These can be compared to the experimental data (d), with (c) showing the closest agreement. Here, the energy of the undetected α product, as calculated through conservation of momentum, is plotted horizontally, while the energy difference between the beam and detected product nuclei is plotted vertically. The decay paths giving rise to each locus are shown in (a), with the detected particle given in red.

3.2.3 Simulations performed

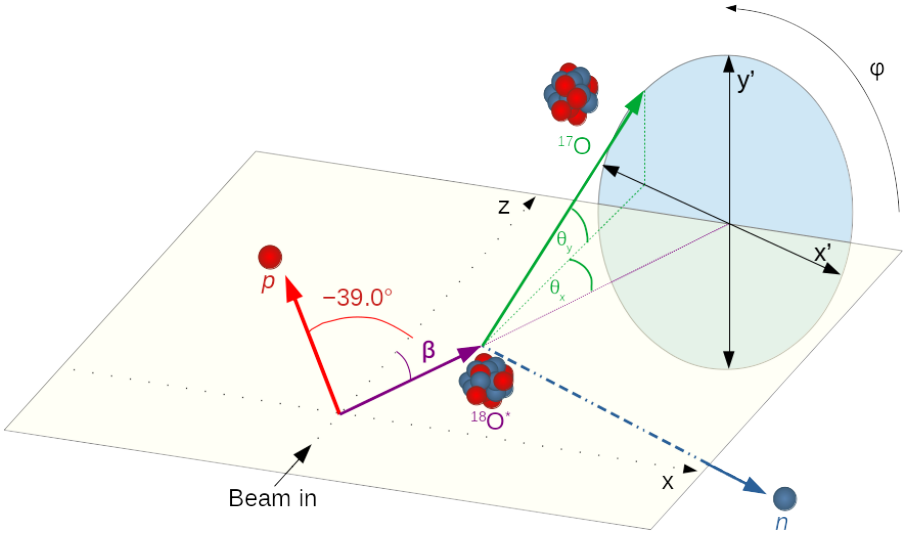
For each of the excitations observed in the various Q3D spectra, Monte-Carlo simulations were performed in order to establish geometric efficiencies and identify kinematic features during analysis. Each observed state was simulated for the different decay paths available to it: for states with $E_x < 6.227$ MeV, the only available decay branch measured in this work was de-excitation via γ-emission; for states within the range 6.227 MeV $\leq E_x <$ 8.045 MeV, only α- and γ-decay were available; ^{18}O* with an excitation energy within 8.045 MeV $\leq E_x <$ 15.942 MeV could also decay via n-emission to ^{17}O; states above 15.942 MeV could also decay via p-emission exclusively to the ground state of ^{17}N. This is because the highest level investigated in ^{18}O* sat at 16.324(16) MeV, so it was not energetically possible to excite the ^{17}N daughter in the current work, the first excited state of which lies at 1.3739(3) MeV [64]. It should be noted that α-decay was not available to states with unnatural parity below 13.129 MeV, as the first unnatural parity state in the daughter ^{14}C nucleus lies at 6.9026(2) MeV (see section 2.6 for details). The population of excited levels in daughter nuclei, where energetically possible, was also simulated, as well as further particle decays that could occur following these excitations. For each decay path, 10^7 events were simulated in order to decrease the relative uncertainty of the associated geometric efficiency. Typically, the widths of states were set to be approximately the average resolution of the focal-plane detector — the effect of smearing on loci due to these widths was negligible when compared to other smearing effects, so these did not need to be simulated again when the widths of each resonance had been extracted from the various Q3D spectra.

3.3 Determining the species of decay products

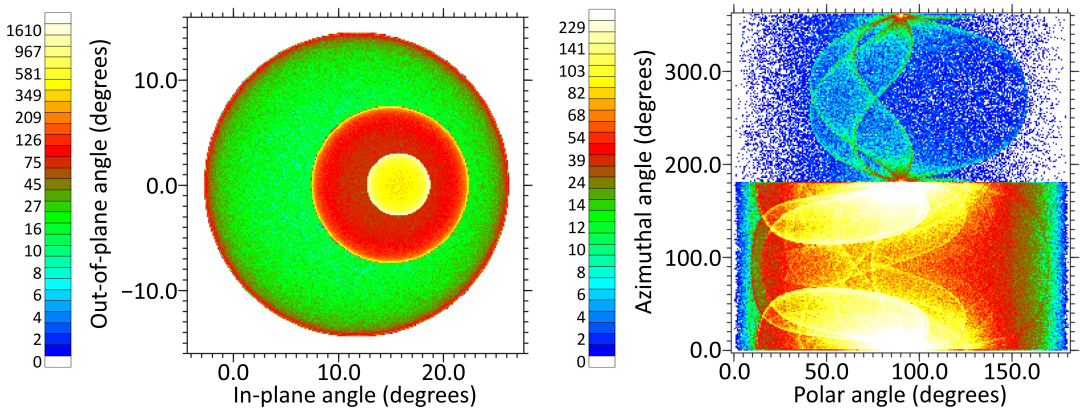
As the species and energy of the recoil proton was measured by the Q3D, measurement of events from the correct reaction (^{12}C(^{7}Li,p)^{18}O*) could be confirmed for DSSD events in coincidence with a good Q3D event. However, determination of the species of products arising from the decay of the ejectile ^{18}O* was also required in order to determine branching ratios. The DSSD array was utilised to determine the species of incident particles, using the known kinematics of the two body exit channels in order to identify features due to distinct daughter nuclei.

3.3.1 Kinematic cones

The reaction of interest, ^{12}C(^{7}Li,p)^{18}O*, has both a two-body entrance and two-body exit channel — therefore, the energies of the recoil and ejectile can be solved for a given scattering angle. As good events measured by the DSSD array require detection of a proton, this highly limits the angles the proton (and hence the ^{18}O, in order to conserve momentum) can travel at during a good event. Thus, any daughter nuclei arising from the decay of an ^{18}O nucleus are constrained to within the volume of a cone, known as a kinematic cone [99], by the path of the proton. A depiction of this is shown in figure 3.30(a), in which the ^{7}Li beam (travelling along z) interacts with the ^{12}C target at the origin, producing the recoil proton and ^{18}O ejectile. The reaction occurs in-plane, with the proton travelling at an angle of -39° and the ^{18}O travelling at a corresponding angle, β. This ^{18}O is excited, and β decreases with increasing excitation energy due to a decrease in the available kinetic energy of the two nuclei and subsequently decays into an ^{17}O nucleus by the emission of a neutron. Again, this is a two-body exit channel and as such the energy/angle relationships of the two product nuclei can be calculated. In the centre-of-mass frame, the total energy the two particles share is



(a)



(b) (c)

Figure 3.30: A depiction of the (^{12}C(^{7}Li,p,n)^{17}O) break-up reaction, following the decay of the intermediate ^{18}O (a). The area in which the ejectile ^{17}O can be incident is highlighted by the blue circle. Also shown are plots of the position of ^{17}O ejectiles in the plane of the DSSD array, for a Cartesian co-ordinate system (b) and a polar co-ordinate system (c). See text for details of the various regions shown in subfigure(b). These were produced through Monte-Carlo simulations of three excitations, centred at 8.5 MeV, 10.9 MeV and 20.0 MeV. From these three cases, only events arising from the 20.0 MeV excitation energy can be measured at azimuthal angles larger than 180°. Figure has been published in Ref. [92].

constrained by the original excitation energy of the ^{18}O nucleus, but the decay can happen in any plane. In the lab frame, the ^{18}O was moving forward relative to the target position and thus the product nuclei are boosted in the lab frame in order to conserve momentum — hence, the paths of the product nuclei are constrained to within the volume of a cone, determined by their masses and available kinetic energy, with a centre along the same vector as the direction of movement of the ^{18}O nucleus, projected from the decay position. In the x-y plane occupied by a DSSD, the result is a circular feature — this is shown by the blue ellipse, representing a plane perpendicular to the path of the ^{18}O nucleus at an arbitrary distance. Figure 3.30(b) shows the kinematic cones (projected onto the x-y detection plane) for three simulated states, of excitation energies 8.5 MeV (the yellow feature, with the smallest diameter), 10.9 MeV (the orange feature, with the median diameter) and 20.0 MeV (the green feature, with the largest diameter) respectively, which can be observed distinctly. The centres of these cones are shifted from one another, due to the decrease in angle β with increasing excitation energy, while the radius of the cones increase with increasing excitation energy. It can also be observed that the surfaces of the cones are the most likely position of detection when no smearing effects are included, a result of kinematic focusing effects. The same data are displayed in figure 3.30(c) as in figure 3.30(b), transformed into spherical polar co-ordinates. The kinematic cones lose the obvious structure displayed in Cartesian co-ordinates, and as such the speed of Monte-Carlo simulation production can be increased when a spectrometer is present by randomly selecting the relevant in-plane and out-of-plane angles, as fewer calculations are required.

Because of these kinematic cones, distinct regions on the DSSD array can be identified as containing all events from a certain decay path — these can be clearly seen in subfigures 3.26(a), (b) and (c), in which events corresponding to the detection of an ^{17}O nucleus from the n+^{17}O (g.s.) exit channel result in the smallest circular feature (enclosed by the green border), due to the limited kinetic energy available to the decay products rel-

ative to the other common exit channel, α+^{14}C (g.s.). The latter decay path gives rise to the other two cones, with detection of the ^{14}C nucleus resulting in the smaller of these two (enclosed by the magenta border) and detection of the α providing the cone with a volume that encapsulates the entire DSSD array. Thus, identifying a region of events due purely to α+^{14}C is simple, but the n+^{17}O (or any decay channel with a smaller kinematic cone) events are contaminated also with other decay paths, meaning that this is an imperfect method of determining the species of incident particles. This method, however, can be used in conjunction with another, as outlined in the section below.

3.3.2 Catania plot

Consider the case where, with the recoil proton measured at the focal-plane detector in the Q3D, the ejectile ^{18}O breaks apart into a ^{14}C (g.s.) nucleus and an α-particle. The total Q-value for the reaction is given by the expression

$$Q = E_C + E_\alpha + E_p - E_{\text{beam}} = 2.173 \text{ MeV}, \tag{3.11}$$

where E_C, E_α, E_p and E_{beam} are the kinetic energies of the ^{14}C, α, recoil proton measured in the Q3D and the beam ^{7}Li nucleus (= 44.0 MeV) respectively. If the ^{14}C nucleus is detected in the DSSD array, then all of these values apart from E_α are known. This value, however, can be determined through calculation of the total momentum of the recoil α. Determining the momenta of the detected ^{14}C and recoil proton via use of equations 3.6 and 3.7 enables calculation of the momentum of the α in each of the Cartesian directions ($i = x, y, z$) via the generic expression

$$P_{\alpha_i} = P_{\text{beam}_i} - P_{C_i} - P_{p_i}, \tag{3.12}$$

though as the beam travels along the z-axis, $P_{\text{beam}_z} = P_{\text{beam}}$ and $P_{\text{beam}_{x,y}} = 0$. The components can be added in quadrature to yield the total momentum of the α-particle, P_α, as

$$P_\alpha^2 = \sum_{i=x,y,z} P_{\alpha_i}^2. \tag{3.13}$$

Again utilising equation 3.6, equation 3.11 can be rearranged to show

$$E_{\text{beam}} - E_C - E_p = \frac{P_\alpha^2}{2m_\alpha} - Q, \tag{3.14}$$

in the form of a linear expression relating the known quantity $E_{\text{beam}} - E_C - E_p$ to the calculated quantity P_α^2. These quantities can be plotted against one another, and the expected result would match a line with a gradient of $1/m_\alpha$ and intercept $-Q$. These momentum calculations are performed assuming that a ^{14}C nucleus is detected, using the appropriate mass to calculate the total momentum in equation 3.6, and as such any events in which the α is detected rather than the ^{14}C, or indeed any products belonging to an entirely different decay path, will be reconstructed incorrectly. Thus, only events that match the assumptions made in the calculations will match the predicted line. Figure 3.31 shows examples of these plots, known as Catania or Romano plots [100], produced using data corresponding to 9.6 $\rightarrow$ 11.9 MeV ^{18}O excitations, with subfigures 3.31(a), (c) and (e) produced using experimental data and subfigures 3.31(b), (d) and (f) produced via Monte-Carlo simulation. In (a) and (b), the line described previously corresponding to a gradient of $1/4$ A^{-1} and intercept -2.173 MeV is also plotted, showing the match between this and the data — events corresponding to the locus that matches this line must thus arise from a ^{14}C+α decay in which the ^{14}C is detected. The other loci that do not match this line must arise from other decays. By performing the above calculations again, either assuming an ^{14}C+α decay but

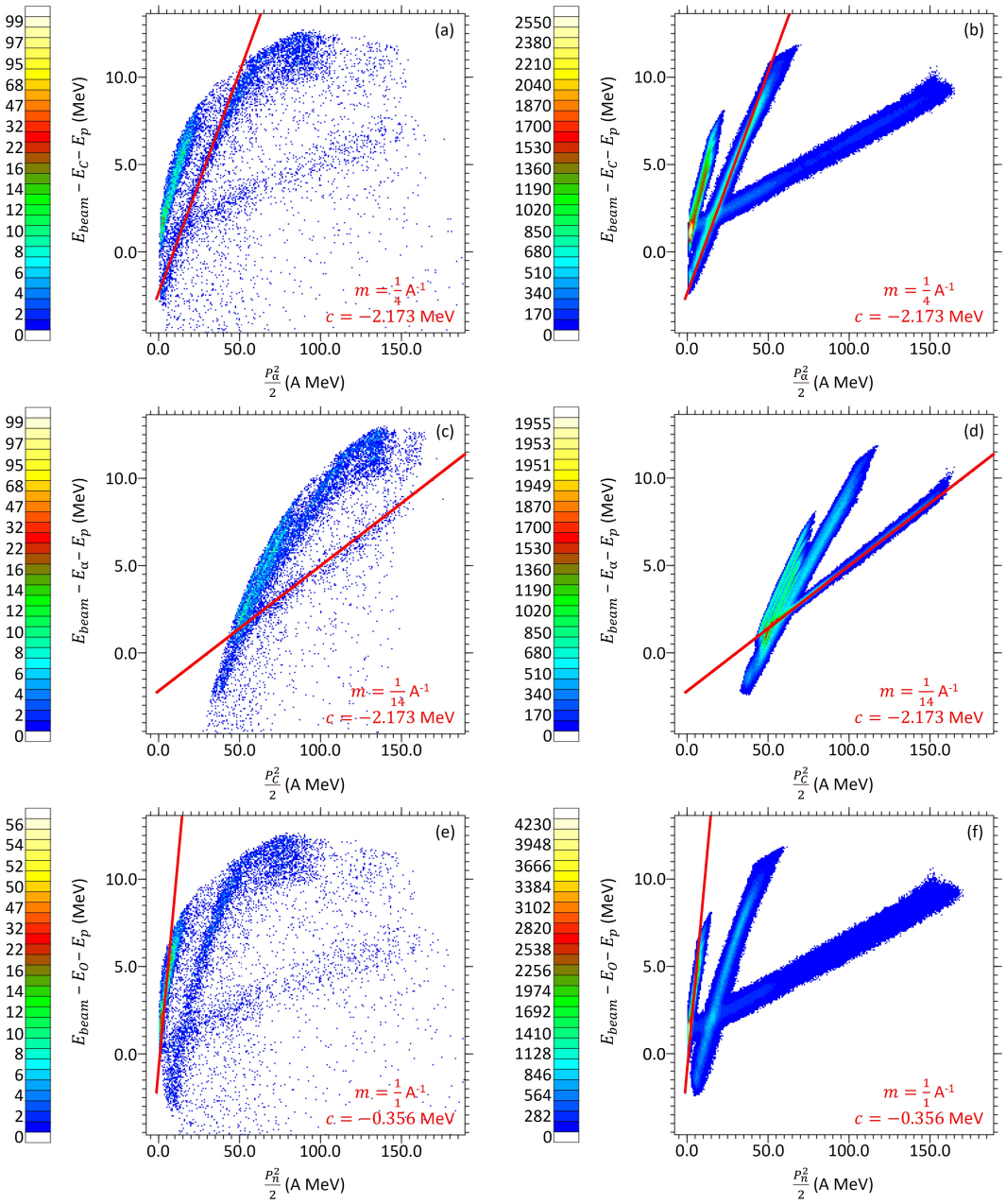


Figure 3.31: Catania plots generated assuming detection of a ^{14}C from a ^{14}C+α decay (a) (b), detection of an α-particle from a ^{14}C+α decay (c) (d) and an ^{17}O from a ^{17}O+n (e) (f). Subfigures (a), (c) and (e) were generated using experimental data, while (b), (d) and (f) were generated using Monte-Carlo data, using all hits in each good event. Subfigures (a) and (b) have been published in Ref. [91].

the α is instead detected (as in (c) and (d)), or a ^{17}O+n decay in which the ^{17}O is detected (as in (e) and (f)), further Catania plots can be produced and the corresponding line with the relevant gradient and intercept plotted. The other loci produced can be seen to match these lines well.

It was not necessarily the case that the highest energy hit, if there were more than one hit across the DSSD array, corresponded to the same reaction that produced the coincident recoil proton measured in the Q3D (though is often the case). As such, all hits were considered when calculating branching ratios, as random coincidences were not simulated in the Monte-Carlo data to take this effect into account. A difference can be seen in figure 3.31(a) and figure 3.29(d), plotted using data from the same excitation range, as the latter is plotted only for the highest energy good hit ($N = 1$) in the DSSD array while the former is plotted for all good hits in the DSSD array ($N > 1$). A feature at the top of the Catania plots (low values of E_C), present in both figures but not in the Monte-Carlo data, that was most prominent in the $N > 1$ case can be seen joined to the locus corresponding to detection of a ^{14}C in a ^{14}C+α event. By plotting the data on a Catania plot for each hit number after energy ordering, this feature can be seen to persist while the others do not: this is shown in figure 3.32, where the Catania plots for all hits corresponding to the same element in the energy-ordered array of hits (i.e. $N = 1$ (a), $N = 2$ (b) etc.) are compared to one another. A likely explanation for this feature was the existence of events due to electronic noise that had sufficient energy to surpass the thresholds set for good events in the DSSD array. The low energy of the hit, alongside the high number of hits in this feature present in many-hit events, leads logically to this conclusion. As these events were commonly paired with a good event, the slight overlap between this feature and the ^{14}C+α locus was not cause for concern — in the case where there were hits that lay at the top of this ^{14}C+α locus and within the ^{17}O+n locus for the same Q3D event, the event was attributed to be due to n-decay in an effort to correct for these rare cases.

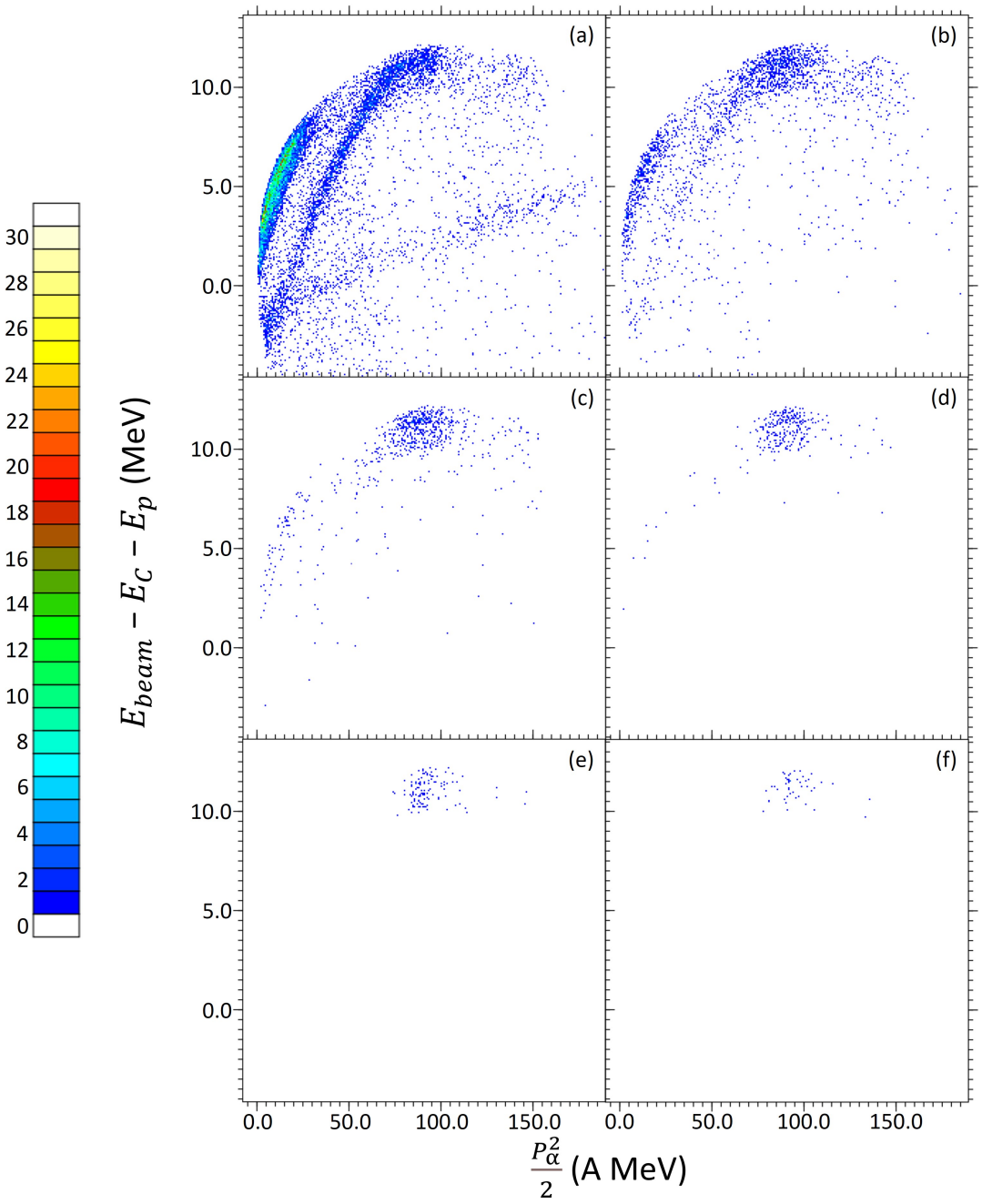


Figure 3.32: Catania plots generated assuming detection of a ^{14}C nucleus for the various hit numbers in the DSSD array in a good event. These hits are ordered by energy. The first 6 highest energy hits ((a)→(f) respectively) are given. The events near the top can be seen to persist through to the sixth hit. Subfigure (a) has been published in Ref. [63].

3.3.2.1 Determination of γ-decay branching ratios

In general, the Catania plot loci are distinct and thus events due to the different decay paths are easy to separate. However, in the excitation ranges investigated there are non-zero γ-decay branches: unnatural parity states below the n-decay threshold for ^{18}O (8.045 MeV) cannot decay via α-emission, and thus were very likely to decay via γ-emission. This would also be true of natural parity states below the α threshold (6.227 MeV), but states meeting these criteria were not investigated due to the interest in α-clustered states. The states that undergo γ-decay presented a problem, as the photons can carry away a large amount of energy while taking comparatively little momentum. This, combined with the fact that there was a large amount of variability on the position of γ-decay loci based on the energy of the associated photon, meant that these features could contaminate the loci corresponding to other decay paths, thus leading to inaccurate branching ratios.

From the excitations investigated below the n-decay threshold, there was obvious potential for high γ-decay branches: the high spins of the 7.117(2) MeV ($J = 4$ [64]) and 7.861(1) MeV ($J = 5$ [64]) states lend themselves to a decreased α-decay probability due to the increased centrifugal barrier, particularly for the 4^+ state due to proximity to the α-decay threshold; the unnatural parity of the 7.7710(5) MeV ($J^\pi = 2^-$, energy and J^π values taken from Ref. [64]) state and suggested unnatural parity of the 7.969 MeV ($J^\pi = (3^+,4^-)$ [64]) state suggest 100% γ-decay branches due to lack of available α-decays, as excited states in the daughter are not energetically available for such low-lying ^{18}O excitations.

Close investigation of the Catania plots produced for events corresponding to ^{18}O excitations between 7.0 $\rightarrow$ 9.4 MeV revealed strong, narrow features that appeared over the α-decay and n-decay loci, which can be observed in figure 3.33(a). Events arising from the γ-decay of states listed above were simulated, with the simulated transitions determined by the strongest γ branches known in the literature [64]. In figure 3.33(b), the transitions from

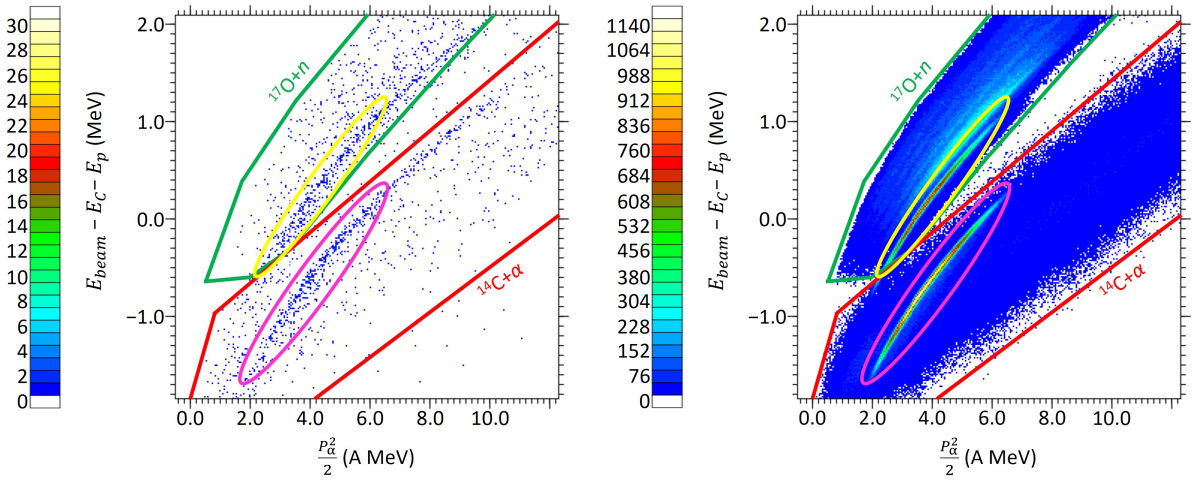


Figure 3.33: Catania plots generated assuming detection of a ^{14}C. The regions due to ^{17}O+n decay and ^{14}C+α decay are shown in green and red, respectively. Features arising from γ decays beginning in the 7.117 MeV and 7.969 MeV states are given in magenta and yellow, respectively. Experimental data (a) and Monte-Carlo data (b) are provided for comparison. Figure adapted from Figure 3, published in Ref. [101].

the 7.117 MeV to the $J^\pi = 4^+$ (M1) state at 3.555 MeV ($I = 69.2(7)\%$) and to the $J^\pi = 2^+$ (E2) states at 1.982 MeV ($I = 27.1(4)\%$) and 3.920 MeV ($I = 2.1(2)\%$) are simulated, with the relevant feature shown in the magenta ellipse. The yellow ellipse shows the feature arising from the transitions starting at the 7.969 MeV to the $J^\pi = 4^+$ state at 3.555 MeV ($I = 67(2)\%$) and to the $J^\pi = 3^+$ state at 5.378 MeV ($I = 21(2)\%$). A good agreement can be seen between the features in the experimental and Monte-Carlo data-sets. The energy of the transition does not affect the kinetic energy available to the ejectile ^{18}O, only causing very small momentum smearing, and as such these features are largely independent of the transition energy (but not of the initial excitation energy). The features that arise due to α-decay (in which a ^{14}C is detected) and n-decay (in which an ^{17}O is detected) are delineated by red and green, respectively.

In order to remove these events from loci associated with branching ratios of other

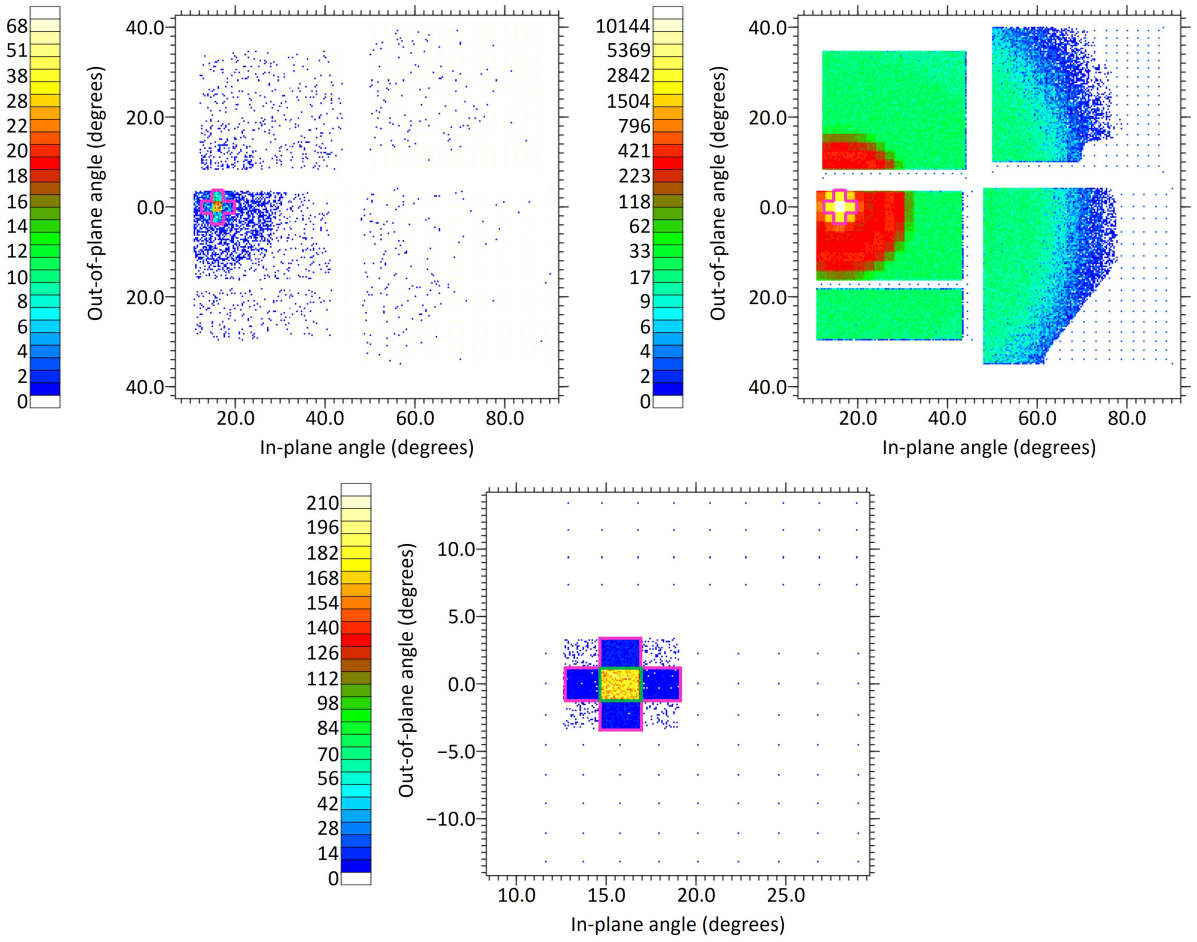


Figure 3.34: Cartesian views of the DSSD array for states ranging from 7.0 → 9.1 MeV, for experimental data (a) and Monte-Carlo data (b). The magenta boundary represents the experimental gate over five pseudopixels used to remove γ-event contamination. Also provided are the Monte-Carlo data for just the γ-decay events, showing the population of each pseudopixel by the ejectile ^{18}O. Figure adapted from Figure 4, published in Ref. [101].

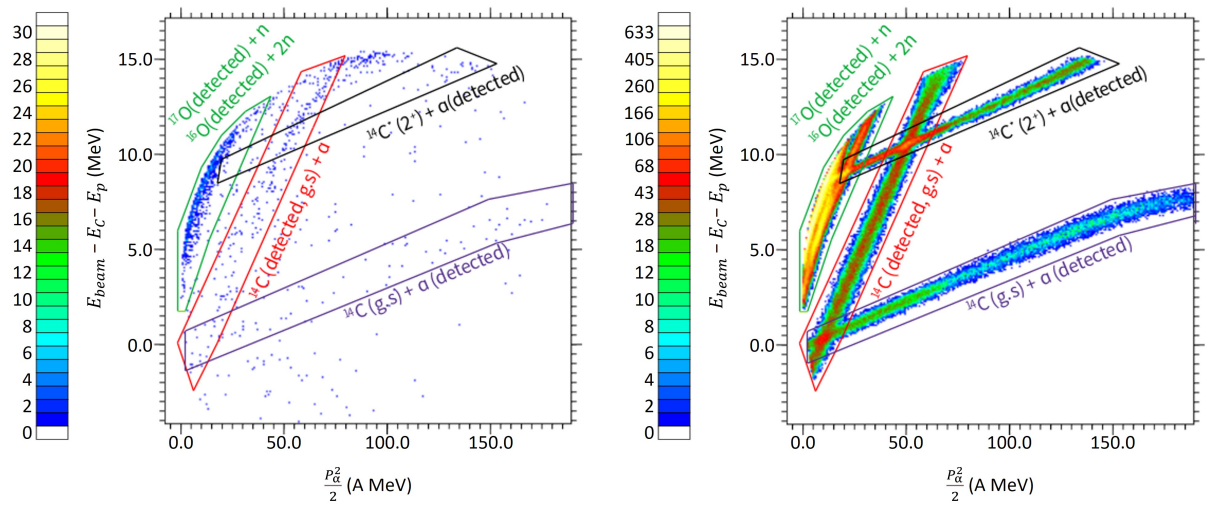
states and channels, the relevant kinematic cones were considered. Due to the small amount of momentum taken away by the photon in a γ-decay, the direction of travel of the detected ^{18}O was almost entirely dependent on the direction of travel of the recoil proton. As such, the solid angle subtended by the associated kinematic cone was very small, due to the large relative mass difference of the two product nuclei and the small angular range of detected

protons. Therefore, the number of pseudopixels which a coincident ^{18}O nucleus could hit was limited. The gate used to select these pseudopixels is shown in magenta in figure 3.34, as shown over both experimental and Monte-Carlo data for states ranging from 7.0 $\rightarrow$ 9.1 MeV. A Monte-Carlo simulation showing only events in which an ^{18}O was detected in the DSSD array following γ-emission, using the transitions listed above, is shown in figure 3.34(c): the magenta boundary around the pseudopixels indicates the region in which $>$ 99.6% of events were found; the green boundary around the central pseudopixel indicates the region containing $>$ 88.7% of events. Events that lay inside of this gate were removed from the Catania plots, and thus these events could be used separately to produce Q3D spectra.

As events from other decay paths also lay within these gates, it was important to consider these events and thus not over-correct for the γ-decay events, which would result in inaccurate branching ratios. In order to do this, the Monte-Carlo simulations were utilised to determine the amount of events from each decay path (for each excitation) that fell outside of the magenta gate shown in figure 3.34 as a fraction of the total number of simulated events. This fraction, f, could then be applied to the experimental data: the remaining number of events in the relevant locus of the Catania plot for each decay path (for each excitation), N_{cat}, could be determined by producing and fitting Q3D spectra gated on the loci. Using this value, the expression

$$N_{\mathrm{gate}} = {}^{N_{\mathrm{cat}}}/_{f} - N_{\mathrm{cat}} \tag{3.15}$$

was employed to establish the number of events incorrectly removed by the gate, N_{gate}, which were then removed from the γ-decay branch and reinstated in the appropriate decay path.



(a) (b)

Figure 3.35: A comparison of experimental data (a) to Monte-Carlo data (b) for events with excitation energy between 14.3 → 14.5 MeV. All available decay paths were simulated, and the corresponding loci identified via Monte-Carlo are labelled. Figure has been published as Figure 4 in Ref. [92].

3.3.2.2 Excited levels in daughter nuclei

Another type of decay path, in which the initial decay of the ^{18}O had sufficient energy to populate excited levels in the daughter nuclei, required careful consideration and treatment as the reduced kinetic energy of the product nuclei greatly affected the geometric efficiency of these events. If any such events were calculated using the geometric efficiency of the corresponding ground state daughter nucleus branch, the relevant branching ratio would thus be inaccurate, lower than the true value. For events with a ^{14}C daughter, the number of levels that needed to be considered and thus Monte-Carlo simulated was relatively low, due to the angular momentum constraints for α-decay discussed previously in Section 2.6. These levels were then simulated and the features on the Catania plots compared with the experimental data. An example of this can be seen in figure 3.35, in which experimental

data are compared to Monte-Carlo data for events corresponding to an excitation energy of around 14.4 MeV as measured in the Q3D. The locus due to population of the first excited state in ^{14}C, with $E_x = 6.0938(2)$ MeV and $J^\pi = 1^-$ [102], is shown in black — no such feature can be seen above background in the experimental data, suggesting that no (or negligible) population of this state had occurred. Events visible on the right of this locus were determined to be due to multiple-hit events, previously shown in figure 3.32, as this clustering of events is not characteristic of the population of an excited level, which would distribute events across the entire area of the locus as determined by Monte-Carlo simulation. In order to avoid misassigning or double counting events that lay within multiple loci, such as with the crossover between the red and black loci in figure 3.35, areas of no crossover for loci arising due to population of excited level, and the number of events within them, could be identified and the likely number of events present in crossover regions determined and corrected for, utilising the Monte-Carlo data to determine the relevant fractions of events — the only instance in which this occurred was for the 15.825(2) MeV state, in which a non-negligible number of events could be observed for decays through a state at approximately 6.9 MeV in ^{14}C. This is further discussed in section 4.2.10.

Events with a ^{17}O daughter (produced via n-decay) had the potential to populate any excited level that was energetically available for a given ^{18}O excitation energy, as n-decay is not subject to the same constraints by selection rules as in the case of α-decay. For events below the $2n$-decay threshold of $S_{2n} = 12.188$ MeV (above which two neutrons are emitted sequentially via the intermediate ^{17}O nucleus, where $S_n = 8.045$ MeV for ^{18}O and $S_n = 4.143$ MeV for ^{17}O), the difference in the hit patterns produced by events corresponding to different ^{17}O daughter levels could be utilised, due to the decrease in available kinetic energy (and hence size of the kinematic cones) for the ^{17}O and n products with increasing excitation energy in the daughter nucleus. The effect of this can be observed in figure 3.36, in which Monte-Carlo data are compared for decays producing ^{17}O in the ground state and

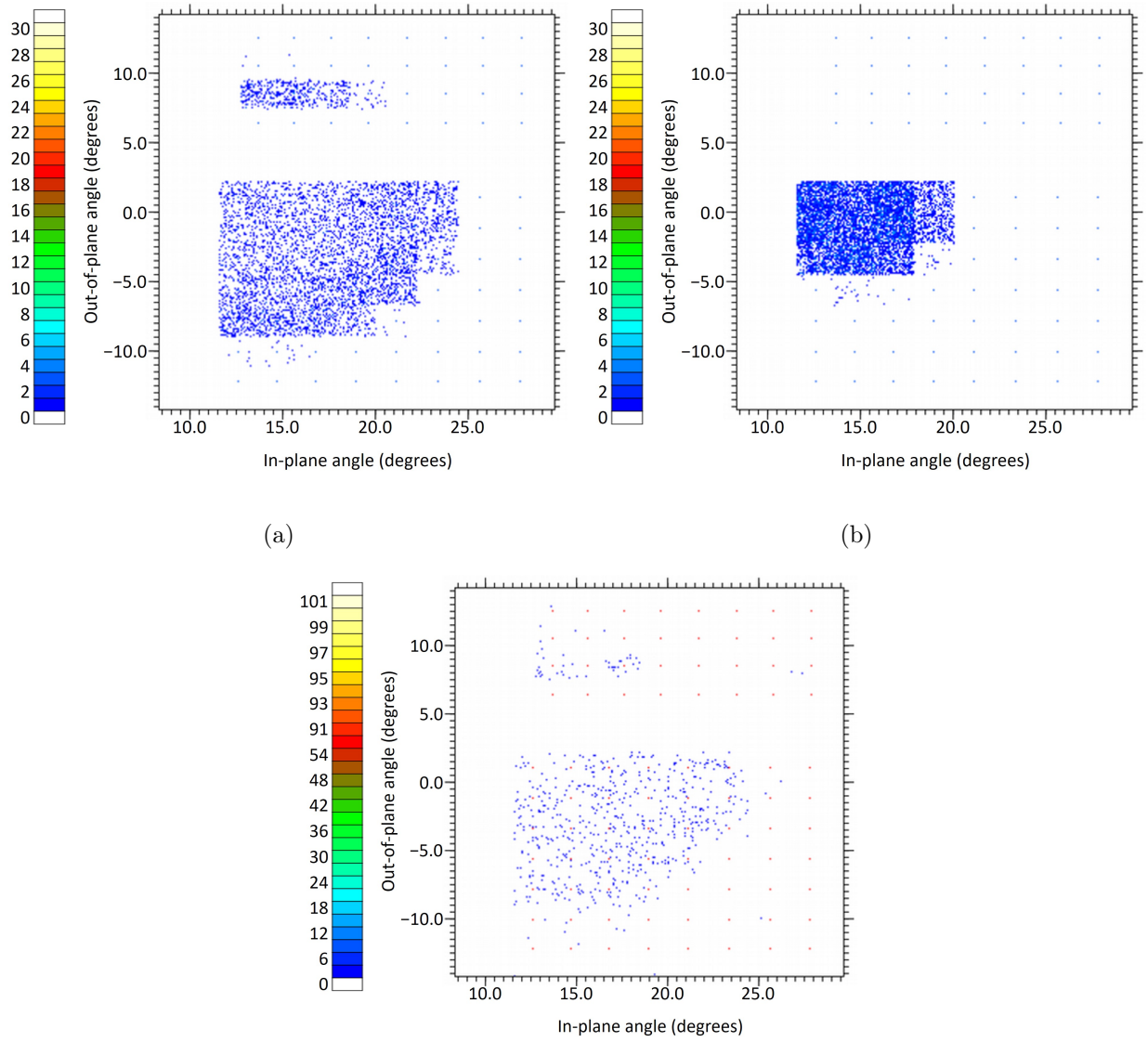
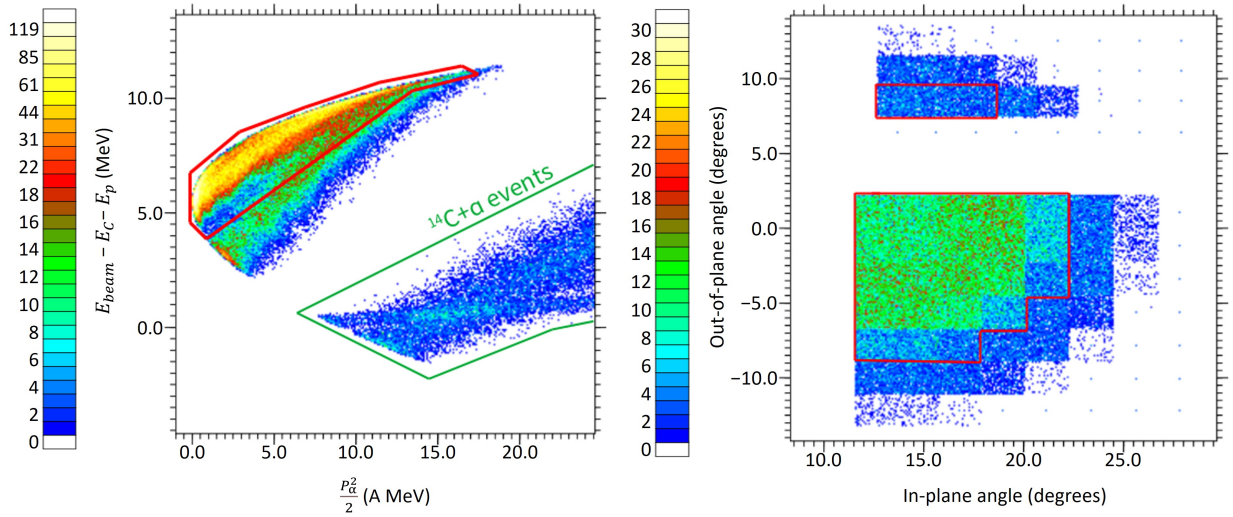


Figure 3.36: Hit patterns on the DSSD array for (^{18}O,n) events with an excitation energy of 11.849 MeV. Monte-Carlo data populating the ground state of ^{17}O (a) and 3.055 MeV state (b) are compared with experimental data (c). Figure has been published as Figure 3 in Ref. [92].

in the second excited (E_x = 3.055 MeV) state, both for reactions proceeding through the 11.849 MeV level in ^{18}O. A large difference in the hit patterns is visible, which was compared to the experimental data in each case in order to establish the tendency towards each level

in the daughter ^{17}O. In figure 3.36, the experimental data can be seen to compare well with the decay through the ground state of ^{17}O rather than through an excited level — the relatively even distribution of events across the pattern established by figure 3.36(a) indicated that most, if not all, of the events in the experimental data populated the ground state of ^{17}O. While careful examination of the experimental data for all states suggested that most of the single n-decay events populated the ground state of ^{17}O, this became harder to establish as excitation energy in the ^{18}O nucleus increased. This relative difference between the kinematic cones decreased — however, the differences in the relevant geometric efficiencies would similarly decrease. Due to these reasons, single neutron decays were assumed to all proceed through the ground state of ^{17}O when considering geometric efficiencies.



(a) (b)

Figure 3.37: A Catania plot (generated assuming an (^{18}O,α) reaction) (a) and view of the detector array (b) for Monte-Carlo data. Red regions encapsulate the location of >99.9% 2n-decay events. Subfigure (b) is plotted using only events within the locus to the top left of subfigure (a), containing both (^{18}O,n) and (^{18}O,2n) events. Figure has been published as Figure 5 in Ref. [92].

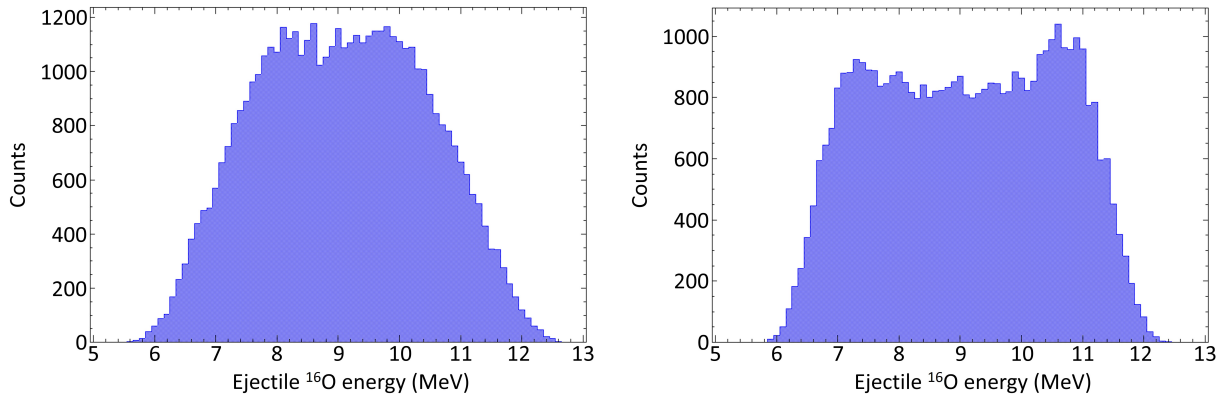
Above the 2n-decay threshold, the daughter ^{17}O had sufficient energy to decay into ^{16}O

by emission of a n. As this decay path resulted in the production of two final state neutrons, both of which were undetected due to their lack of charge, the Catania plot method alone was not sufficient to distinguish these events from other loci — specifically, the single n-decay locus. As the geometric efficiencies of these channels differed greatly, it was important to find some method to distinguish them. In order to do this, both techniques discussed above (using Catania plots and the hit patterns of the detectors) were used in conjunction with one another. Figure 3.37 shows plots created with Monte-Carlo data generated for a state centred around 14.443 MeV, with all available decay paths simulated. Figure 3.37(b) was produced by gating on events in the n-decay locus of the Catania plot in figure 3.37(a) (the locus at the top left), removing the unwanted (^{18}O*,α) events from the hit position plot. Using these Monte-Carlo data, the regions corresponding to $2n$-decay events could be identified and gated around. The regions shown in red contain $> 99.5\%$ of (^{18}O*, $2n$) events, but only 39.0% of (^{18}O*, n) events are found in both gates — this greatly reduces the uncertainty when estimating the total number of (^{18}O*, n) events by extrapolating from the events outside of the red region. A similar method was employed as in section 3.3.2.1 in order to determine the relative branches:

$$N_n = \frac{N_{\text{out}}}{1 - f_n}, \tag{3.16}$$

where N_n is the total number of events from the (^{18}O*, n) channel, f_n is the fraction of (^{18}O*, n) events that lie within the (^{18}O*, $2n$) gated regions determined through Monte-Carlo simulation and N_{out} is the number of (^{18}O*, n) events present outside of the gated regions in the experimental data. Hence, the total number of events due to the (^{18}O*, $2n$) channel, N_{2n}, is given by

$$N_{2n} = N_{\text{gate}} - (N_n \times f_n), \tag{3.17}$$



(a) (b)

Figure 3.38: Energy distributions of ^{16}O daughters for (^{18}O,2n) events, decaying through an intermediate state in ^{17}O at 4.553 MeV(a) and a state at 6.356 MeV (b). Figure has been published as Figure 6 in Ref. [92].

where N_{gate} is the total number of events of any kind present inside of the gated regions. Thus, the only remaining issue was determining the state through which the intermediate ^{17}O nucleus decayed. Unfortunately, due to the lack of information about this intermediate stage due to the uncharged nature of the neutron product, these states were very difficult to distinguish between. One possible method that could be used is via the distribution of the kinetic energies of ^{16}O daughter nuclei. An example of this is displayed in figure 3.38, in which (^{18}O*, 2n) events are simulated through the decays of the 4.553 MeV and 6.356 MeV states; a clear difference in the distributions can be seen. Unfortunately, the statistics were not high enough in the current work to investigate this further. The geometric efficiency of the (^{18}O*, 2n) channel for each ^{18}O excitation was thus determined by averaging across the associated geometric efficiencies found via Monte-Carlo for each possible ^{17}O daughter nuclei level. The uncertainty associated with the averaging of the geometric efficiency for this branch was propagated when calculating the relevant branching ratio uncertainties.

Chapter 4

Results

Using the experimental techniques described in the previous chapters, branching ratios were established for various decay paths. This was done for states in all of the measured excitation region, a range of 7.0 $\rightarrow$ 16.0 MeV, with the results presented and discussed in this chapter.

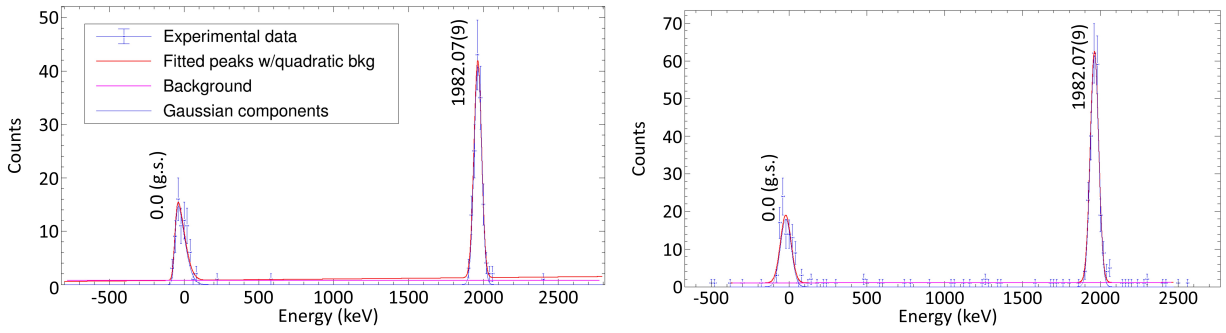
The results discussed in this chapter have been published across two papers: S. Pirrie et al. "Search for evidence of rotational cluster bands in ^{18}O", published in *Phys. Rev. C* 102 (2020), p. 064315 [57], and S. Pirrie et al. "Precision branching-ratio measurements in ^{18}O", published in *Eur. Phys. J. A* 57.4 (2021), p. 150 [63]. Much of the text in this chapter was originally published in these papers, specifically in sections 4.2.2 and 4.2.7, where this is again stated.

4.1 Validation of branching ratios

The total number of decays of a particular path that were expected, calculated using Monte-Carlo data in conjunction with the decays measured in the geometric acceptance of the

DSSD array, could have been used in principle to determine absolute branching ratios. In an attempt to validate this, the results gathered for the bound state excitation region ($-0.5 \rightarrow 2.5$ MeV) were utilised as the recoil ^{18}O produced was expected to have a geometric efficiency of ≈100% due to the limited radius of the associated kinematic cone (kinematic cones are described in detail in Section 3.3.1). The fraction of good Q3D events with a corresponding hit in the DSSD array for this excitation region was found to be 80.1% (372 good Q3D events, of which 298 had a corresponding good DSSD event), much lower than expected based on the geometric efficiency established from the Monte-Carlo data. One possible explanation for this was that background events in the Q3D excitation spectrum, events which did not correspond to a population of either the ground or first excited states, could be affecting this fraction and causing a systematic shift downwards. This was investigated by plotting the Q3D excitation spectrum for any events with at least a single detection in the DSSD array, in order to identify if the counts in each resonance remained the same as for the ungated Q3D spectrum.

As can be seen from Figure 4.1, there was a notable decrease in the fraction of counts



(a) (b)

Figure 4.1: The Q3D excitation spectra obtained for the $-0.5 \rightarrow 2.5$ MeV region, gated on events with a corresponding hit in the DSSD array (a) and ungated (b). Note the different vertical scales for subfigures (a) and (b).

in both peaks for the events gated using the DSSD array relative to the ungated spectrum: 75±17% for the ground state and 61±8% for the first excited state. This demonstrated that it was not possible for all good Q3D events to have had a corresponding DSSD hit for these states, despite the predictions of the Monte-Carlo simulations. Due to the proximity of the kinematic cone to the region between detectors 1 and 2 in which events could not be detected, the possibility that the detector placement was inaccurate in the simulations was considered.

This was explored, and the results are shown in Figures 4.2 and 4.3. In these figures, the Monte-Carlo data are presented both unsmeared as well as smeared across the relevant pseudopixels of the DSSD array, in order to better visualise the number of events based on the geometric efficiency. The red boxes shown highlight the pseudopixels in which the vast majority (>99.9%) of Monte-Carlo events lay. The ratio of events between the top and bottom central pseudopixels for the experimental data, shown in Figure 4.2, was 0.74±0.07, with 90 and 121 events in the top and bottom pseudopixel respectively. The uncertainty on the ratio was determined through propagation of the standard error on each count, $\sigma_N = \sqrt{N}$. The beam offset (the vertical position of the beam relative to the experimental set-up) was varied in the Monte-Carlo simulations in order to establish whether or not such an offset occurred that both decreased the geometric efficiency of the ^{18}O detections while maintaining the general distribution of the events across the pseudopixels. Unfortunately, it was determined that the geometric efficiency would only begin to significantly decrease after the events were distributed almost entirely across the top strip of detector 2, as shown in figures 4.2(a) and (b), which did not match the experimental data. The beam spot size was also varied in order to investigate the effect this would have on the data, but the position distribution of ^{18}O nuclei, displayed in figures 4.2(b), (d) and 4.3(b), were instead found to be limited by the acceptance window of the Q3D rather than by the shape of the beam. In fact, due to the small size of pseudopixels, a slight beam shift of 1 mm (as is the difference

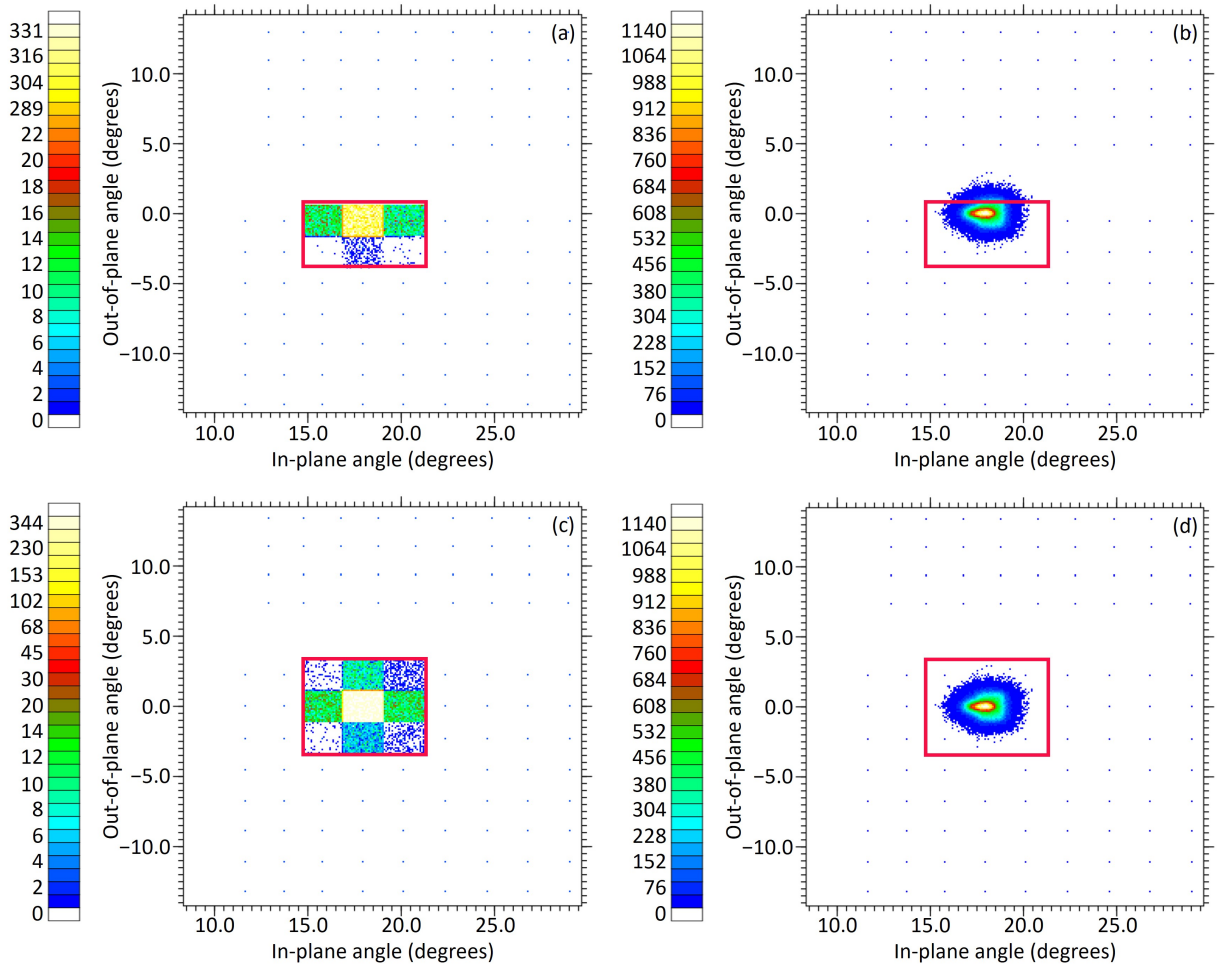


Figure 4.2: Monte-Carlo data generated for events in which a recoil ^{18}O nucleus was detected, produced in either the ground state or first excited state. A beam offset of 3 mm is shown in (a) and (b), matching the geometric efficiency of the experimental data but not the hit pattern, while an offset of 7 mm is shown in (c) and (d) which neither replicates the geometric efficiency nor hit pattern. Subfigures (a) and (c) show events smeared across the widths of the DSSD pseudopixels, while (b) and (d) show the true position of events before smearing.

between figures 4.2(c) and (d) compared with figures 4.2(a) and (b)) results in a large change in the hit distribution across the DSSD pseudopixels. For these data taken in 2016, the beam offset was found to be ≈6 mm based on matching the Monte-Carlo hit distribution to the experimental data (as shown in figure 4.3).

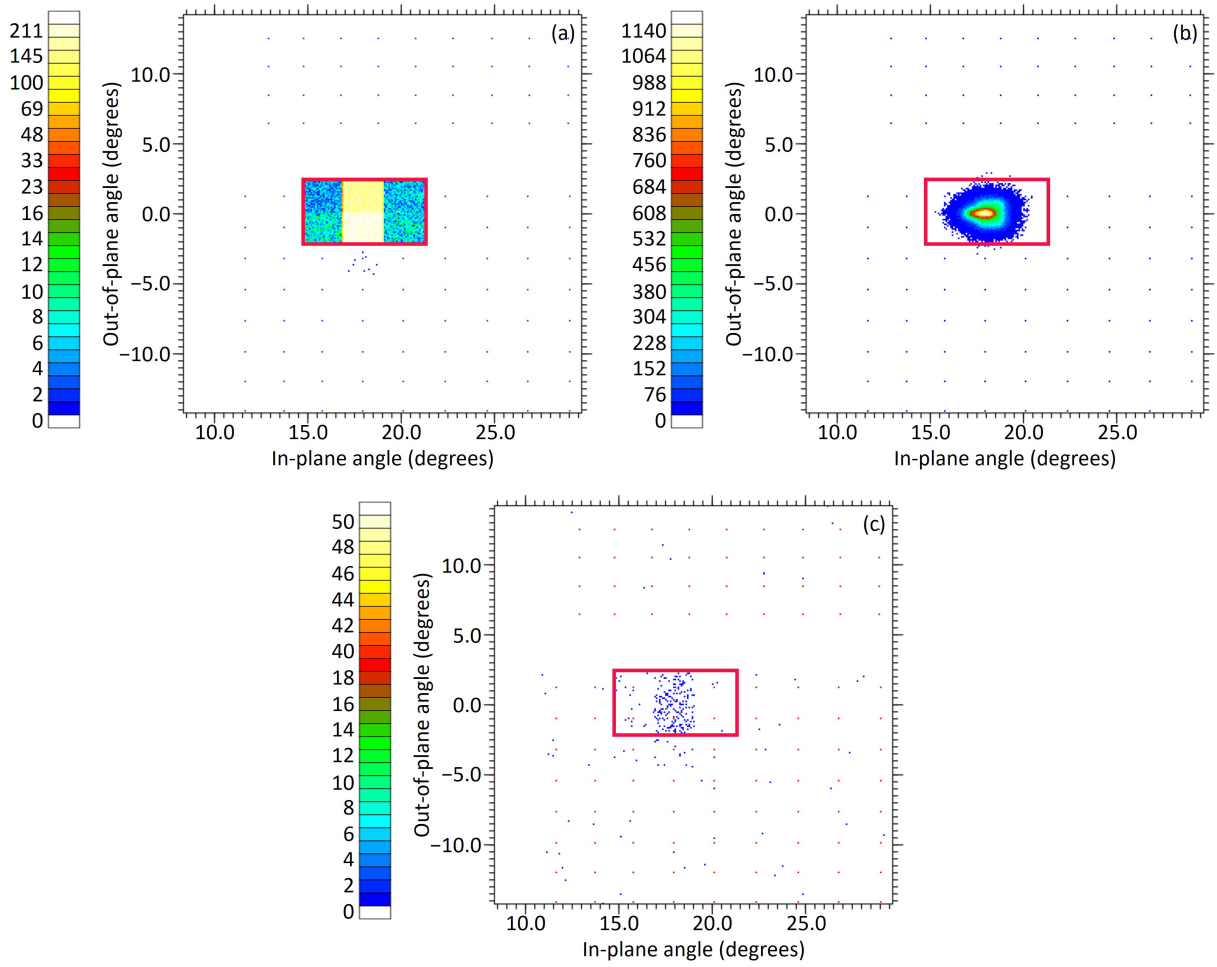


Figure 4.3: Monte-Carlo data generated for events in which a recoil ^{18}O nucleus was detected, produced in either the ground state or first excited state. A beam offset of 6 mm is shown in (a) and (b), reproducing the hit pattern of the experimental data (c) well — the geometric efficiency does not.

Thus, in order to explain the missing events, the issues with timing described in section 3.1.2.9 were revisited. As events output via the amplifier had a decreased voltage, it was probable that good events from the DSSD array would be rejected due to being below the threshold of the peak-sensing ADCs, and would hence result in an artificially decreased number of events. As there were only data for two states from which the amount of events lost could be determined due to known branching ratios, the ground state and

the first excited state, it was not viable to infer the number of missing events for higher-lying states to a reasonable certainty. As such, the decision was made to normalise the measured branching ratios to each other rather than calculate the absolute branching ratios. This normalisation involved establishing the available decay paths (with the exception of β-decay and electron capture), calculating the total number of events from each branch (using the geometric efficiencies and measured events) and normalising each branch over the total calculated number of events from all branches.

In an attempt to validate this method, the 7.0 $\rightarrow$ 9.1 MeV data collected in 2016 and the 7.0 $\rightarrow$ 9.4 MeV data collected in 2017 were compared in order to establish consistency between the two experimental runs, due to the large overlap of the two data sets. The calculated branching ratios for each year and their associated uncertainties are given in table 4.1. From these results, it can be seen that 11 of the 15 states had branching ratios that lay within one standard deviation of one another (shown in green) while 4 of the states lay within two standard deviations (shown in yellow). Typically, the results shown in tables 4.2 and 4.3 for these states were calculated using the weighted average of these two results: two notable exceptions are the 7969(3) keV and 8037(5) keV states, for which the fits to the 2016 data were difficult to constrain — hence, only the 2017 values are used. The uncertainty for these states in the 2016 data is underestimated, as in order to fit the data very stringent conditions on centroid and width had to be placed.

4.2 Precision branching ratio measurements

Branching ratio values were obtained for most of the observed states — these, along with discussion of the results, were split across two papers: Ref. [57] (S. Pirrie et al. *Search for evidence of rotational cluster bands in* ^{18}O, Phys. Rev. C 102 p. 064315), focused on the

E_{level} (keV)	$\Gamma_\alpha/\Gamma_{\text{tot}}$	$\Gamma_{\gamma/n}/\Gamma_{\text{tot}}$	$\Gamma_\alpha/\Gamma_{\text{tot}}$	$\Gamma_{\gamma/n}/\Gamma_{\text{tot}}$
	2016		2017	
7117(2)	0.49(2)	0.51(2)	0.48(4)	0.52(3)
7621(6)	1.05(10)	-0.05(10)	0.97(16)	0.03(15)
7794(2)	0.66(7)	0.34(7)	0.62(8)	0.38(8)
7861(1)	0.93(1)	0.07(1)	0.94(4)	0.06(2)
7969(3)	0.10(1)	0.90(1)	0.03(3)	0.97(3)
8037(5)	0.50(20)	0.50(20)	0.34(9)	0.66(9)
8126(1)	0.90(3)	0.10(3)	0.90(4)	0.10(4)
8219(1)	0.85(2)	0.15(2)	0.89(2)	0.11(2)
8280(1)	0.50(4)	0.50(4)	0.40(11)	0.60(11)
8409(11)	0.22(12)	0.77(12)	0.04(4)	0.96(4)
8514(5)	0.19(6)	0.81(6)	0.18(10)	0.82(10)
8675(4)	0.28(14)	0.72(14)	0.11(12)	0.89(12)
8843(14)	0.29(14)	0.71(14)	0.34(14)	0.66(14)
8963(5)	0.33(8)	0.67(8)	0.16(8)	0.84(8)
9076(8)	0.13(4)	0.87(4)	0.24(6)	0.76(6)

Table 4.1: Branching ratio results for both the 7.0 → 9.1 MeV (2016) and 7.0 → 9.4 MeV (2017) excitation regions in ^{18}O, presented together for comparison. Results shown in green were within one standard deviation of one another, while results shown in yellow were within two standard deviations.

states that were tentatively assigned to the proposed rotational bands discussed in Ref. [56], and Ref. [63] (S. Pirrie et al. *Precision branching-ratio measurements in* ^{18}O, Eur. Phys. J. A 57.4 p. 150), a more general paper detailing the branching ratios obtained for states that were not involved in the proposed rotational bands. Discussion of the results from these publications as published is presented below, along with the tables (Table 1 in both publications) containing all the experimental results. Figures 4.5, 4.6, 4.7, 4.8 and 4.9 are taken from Ref. [63], while figure 4.4 is taken from Ref. [57].

4.2.1 Efficiency-corrected background

The following text and figure were previously published in Ref. [57].

The background for fitted states, shown by dashed magenta lines in Figures 4.5, 4.6, 4.7, 4.8, represents the different n phase space distributions: the two-body ^{17}O,n distribution between 8.045 MeV and 12.188 MeV, and the combination of the two-body and three-body ^{16}O,2n distributions above 12.188 MeV. Below S_n, a constant background was fitted. The functional form of the background was extracted from Ref. [56] and scaled to match the spectra obtained - this was done for all decay channel spectra. The chosen scaling of the background results in a non-negligible systematic shift in measured branching ratios for wide states in the n-decay channel, where the background was expected and seen to be largest, resulting in a larger relative uncertainty than for other states. Figure 4.4 shows the efficiency-corrected backgrounds for each region, for the α- and n-decay channels, demonstrating very similar functional forms to the ungated Q3D singles profile. This is due to the change in detection efficiency over a given excitation region being negligible when compared with the experimental uncertainty.

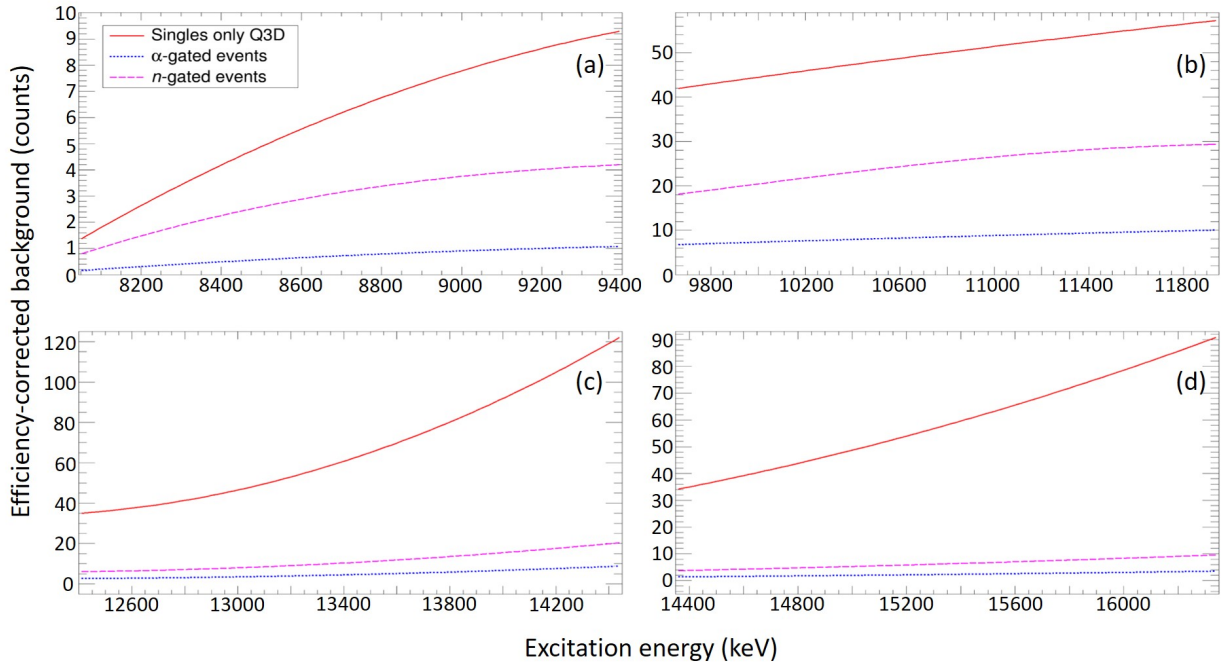


Figure 4.4: Efficiency-corrected background profiles for the (a) 7800 keV, (b) 10500 keV, (c) 13200 keV and (d) 15100 keV regions, calculated as the product of the scaled background for each spectrum multiplied by the geometric efficiency profile across the excitation region. The red solid line, dashed magenta line and dotted blue line represent the background profile from the Q3D singles only, α-gated and n-gated events respectively. This demonstrates that the functional form is unchanged by efficiency correction due to uncertainties being larger than efficiency effects. Figure previously published in Ref. [57] as Figure 4.

4.2.2 Non-clustering results

The results from Ref. [63] are presented first, along with the fits to the data referred to in the text. The text is edited slightly to relate to relevant sections in this work, but is largely left untouched from the published version.

Previous measurements in which excitations in ^{18}O were measured along with values of Γ_α and, in some cases, Γ_n have been performed using various techniques. Notable examples,

which are compared to the results obtained in the current work in the text and tables 4.2 and 4.3, include the work of Avila et al. [103], Yang et al. [104], Goldberg et al. [105] and Johnson et al. [106]. Avila et al., Goldberg et al. and Johnson et al. populated states in ^{18}O using the Thick Target Inverse Kinematics (TTIK) technique through ^{14}C+α elastic scattering, investigating $\Gamma_\alpha/\Gamma_{\rm tot}$ via resonant scattering and an R-Matrix approach for energies of 8.0 $\rightarrow$ 15.0 MeV, 9.0 $\rightarrow$ 21.3 MeV and 8.0 $\rightarrow$ 11.0 MeV, respectively. Yang et al. populated states via the ^{9}Be(^{13}C,^{18}O)α reaction and measured lower limits for branching ratios of several states ranging between 10.3 $\rightarrow$ 15.9 MeV.

Table 4.2: Branching ratio and θ_α^2 values for states not suggested to be members of proposed cluster bands, as published in Ref. [63]. Literature values are from Ref. [64], except where specified by footnotes. Values in red are discussed in section 4.2.7, and shown again in table 4.3 grouped by proposed rotational band.

Current work					Literature				
E_{level} (keV)	Γ_{tot} (keV)	$\Gamma_\alpha/\Gamma_{tot}$	$\Gamma_\gamma/\Gamma_{tot}$	θ_α^2	E_{level} (keV)	Γ_{tot} (keV)	$\Gamma_\alpha/\Gamma_{tot}$ (lit.)	$\Gamma_\gamma/\Gamma_{tot}$	J^π
7117(2)	<16	0.49(2)	0.51(2)	>0.007*	7116.9(12)	<0.00024	—	—	4^+
7621(6)	<35	1.02(9)	<0.07	<0.07*	7615.9(7)	<2.5	—	—	1^-
7794(2)	<16	>0.63(5)	0.37(5)	0.07	7796(5)	<50*	—	—	0^+
7861(1)	<11	0.93(1)	0.07(1)	<170	7864(5)	—	—	—	5^-
7969(3)	<12	<0.06	0.97(3)	<0.5	7977(4)	—	—	—	$(3^+,4^-)$
8037(5)	<33	0.34(9)	0.66(9)	<0.004*	8037.8(7)	<2.5	1^2	—	1^-
$S_n = 8045$ keV			Γ_n/Γ_{tot}					Γ_n/Γ_{tot}	
8126(3)	<15	0.90(3)	0.10(3)	<50	8125(2)	—	—	—	5^-
8219(1)	<13	0.88(2)	0.12(2)	0.01*	8213(4)	1(8)	$0.89(11)^2$	$0.11(5)^2$	2^+
8280(1)	<28	0.48(4)	0.52(4)	0.1*	8282(3)	8(1)	$0.34(4)^2$	$0.66(10)^2$	3^-
8409(11)	<56	<0.10	0.94(4)	0.004*	8410(8)	8(6)	—	—	(2^-)
8514(5)	<22	0.19(5)	0.81(5)	0.08*	8521(6)	5	—	—	(4^-)
8675(4)	<16	<0.27	0.82(9)	—	8660(6)	8	—	—	—
8843(14)	80(30)	0.32(10)	0.68(10)	0.03	8817(12)	70(12)	$<0.01^2$	1^2	(1^+)
8963(5)	<33	0.24(5)	0.76(6)	—	8955(4)	43(3)	$0.07(3)^2$	$0.9(6)^2$	—
9076(8)	90(20)	0.16(3)	0.84(3)	—	9053(6)	100^1	—	—	—

9238(16)	<14	0.9(3)	<0.39		<0.009	9270(20)	—	—	—	$(0,1,2)^-$
9359(9)	50(20)	0.44(8)	0.56(8)		0.02	9361(6)	27(15)	—	—	2^+
9720(5)	<20	0.26(7)	0.74(7)		<0.007	9713(7)	15^1	$0.27(5)^4$	—	(5^-)
10106(11)	<14	0.55(10)	0.45(10)		<0.008	10118(10)	16(4)	$0.44(18)^2$, $0.35(7)^4$	$0.6(3)^2$	3^-
10287(1)	40(6)	0.60(4)	0.40(4)		0.05	10295(14)	<50	$0.66(11)^2$, $>0.37(3)^3$	$0.34(8)^2$	4^+
10386(7)	70(15)	0.39(7)	0.61(7)		0.02	10396(9)	30^1	$0.7(2)^2$	$0.7(4)^2$	3^-
10587(3)	96(10)	<0.12	0.94(6)		<0.003	10595(15)	70^1	—	—	—
10774(9)	100(30)	<0.32	0.80(12)		—	$10762(8)^1$	10^1	$0.45(15)^4$	—	—
10919(4)	30(20)	0.18(4)	0.82(4)		0.003	10910(20)	30^1	—	—	—
10997(16)	<37	<0.11	0.94(5)		<0.001	10990(20)	<50	$<0.12^2$	$0.9(6)^2$	(2^-)
11127(4)	43(8)	0.68(6)	0.32(6)		—	11130(20)	5^1	$>0.65(3)^3$, 0.80^4	—	—
11419(4)	84(5)	0.74(6)	0.26(6)		0.05	11410(20)	35^1	$0.8(3)^2$, $>0.23(1)^3$, $0.90(10)^4$	$0.25(14)^2$	(4^+)
11604(9)	76(2)	0.50(10)	0.50(10)		0.07	11620(20)	25^1	$0.75(12)^2$, $0.90(10)^4$	$0.25(8)^2$	5^-
11696(1)	74(3)	0.73(6)	0.27(6)		0.4	11690(20)	27^1	$0.52(6)^2$, $>0.89(3)^3$	$0.48(6)^2$	6^+
11849(2)	60(5)	0.17(3)	0.83(3)		0.004	11820(20)	19^1	—	—	(3^-)
$S_{2n} = 12188$ keV			Γ_n/Γ_{tot}	Γ_{2n}/Γ_{tot}						
12427(5)	<51	0.29(9)	0.59(9)	<0.21	0.002*	12410(20)	24^1	—	—	(3^-)
12557(2)	107(8)	0.63(5)	0.31(5)	<0.11	0.2	12530(20)	24^1	$0.7(2)^2$, $>0.79(3)^3$	0.29(16)	6^+
12680(3)	<17	0.53(7)	0.37(7)	<0.17	—	$12711(8)^1$	10^1	$0.40(5)^2$	$0.60(12)^2$	—
12764(3)	55(20)	0.51(8)	0.36(8)	<0.21	—	$12777(8)^1$	20^1	—	—	—
12893(7)	134(6)	0.39(8)	0.45(8)	<0.23	—	$12903(7)^1$	73^1	—	—	—
13005(3)	49(16)	0.48(11)	0.38(11)	<0.26	0.009	12990(20)	68(18)	$0.74(18)^2$	$0.26(10)^2$	(4^-)
13093(3)	81(11)	0.26(7)	0.57(7)	0.16(7)	0.004	$13098(7)^1$	40^1	—	—	1^-

13258(10)	122(10)	0.39(7)	0.32(7)	0.30(7)	—	13262(8)[1]	90[1]	—	—	—
13389(3)	<53	0.09(4)	0.48(4)	0.42(4)	<0.001	13400(20)	108(20)	—	—	(2^-)
13496(4)	<38	0.21(8)	0.40(8)	0.39(8)	—	13493(5)*	10[1]	—	—	—
13614(2)	<23	0.15(3)	0.40(3)	0.45(3)	<0.002	13624(6)[1]	22[1]	>0.07(1)[3]	—	—
13726(6)	33(1)	0.23(9)	0.31(9)	0.47(9)	—	13742(7)[1]	3[1]	—	—	—
13832(1)	73(3)	0.38(3)	0.23(3)	0.39(3)	0.01	13820(20)[1]	28[1]	$0.12(5)^2$, >0.32(2)[3]	$0.9(3)^2$	1^-
13972(8)	50(12)	0.35(8)	0.31(8)	0.34(8)	—	13937(6)[1]	17[1]	$0.53(19)^2$	$0.5(4)^2$	—
14138(4)	105(12)	0.46(8)	0.22(8)	0.32(8)	0.05	14170(40)	140(50)	>0.16(1)[3]	—	(6^-)
14410(12)	350(30)	0.21(4)	0.37(4)	0.42(4)	—	14450(50)	≈1070	$0.4(2)^2$	$0.6(2)^2$	—
14623(2)	50(30)	0.13(3)	0.32(3)	0.55(3)	—	14630(10)[1]	27[1]	—	—	—
14804(10)	110(40)	<0.13	0.50(9)	0.47(9)	—	14803(7)[1]	53[1]	—	—	—
15002(16)	120(40)	0.15(6)	0.49(6)	0.37(6)	—	14985(9)	88[1]	—	—	—
15285(2)	50(5)	0.09(3)	0.53(3)	0.38(3)	—	15230(40)	≈300	—	—	—
15453(9)	>116	<0.18	0.54(6)	0.34(6)	—	15471(9)	127	—	—	—
15664(3)	53(19)	<0.24	0.51(8)	0.32(8)	—	15662(8)	40	—	—	—
15825(2)	56(7)	0.89(10)	<0.21		0.08	15810(10)[1]	20[1]	>0.57(2)[3]	—	—

[1]Value from Ref. [56].
[2]Value from Ref. [103].
[3]Value from Ref. [104].
[4]Value from Ref. [105].

4.2.3 7.0 MeV to 9.4 MeV

The first region (Q3D setting) investigated lay between 7.0 MeV and 9.4 MeV, above the α-decay threshold of 6.227 MeV. During this excitation region, the n-decay channel becomes possible (S_n = 8.045 MeV). States below this energy are given a value of $\Gamma_\gamma/\Gamma_{tot}$ using the method detailed in section 3.3.2.1 and Ref. [101]. There has been little work done in determining particle-decay branches relative to γ-decay branches for states in ^{18}O, so these values represent a first measurement of both $\Gamma_\gamma/\Gamma_{tot}$ and $\Gamma_\alpha/\Gamma_{tot}$ for these resonances. The value of $\Gamma_\alpha/\Gamma_{tot}$ for the 7969(3) keV state is consistent with 0, supporting the tentative unnatural parity 3^+ or 4^- assignments. The value of $\theta_\alpha^2 < 0.5$ in Table 4.2 was calculated assuming $J = 4$, but it should be noted that $\theta_\alpha^2 < 0.07$ assuming $J = 3$. The excitation spectra acquired while gating on the different decay paths are shown in Figure 4.5.

Above the n-decay threshold, several states have been observed with no prior measurement of $\Gamma_\alpha/\Gamma_{tot}$ and Γ_n/Γ_{tot}. The $J^\pi = 3^-$ state at 8280(1) keV has been previously measured in Ref. [103] to have values of 0.34(4) and 0.66(10) for $\Gamma_\alpha/\Gamma_{tot}$ and Γ_n/Γ_{tot} respectively. This value of Γ_n/Γ_{tot} is in agreement with the value of 0.52(4) obtained here, while the value of $\Gamma_\alpha/\Gamma_{tot}$, 0.48(4), lies a little over 2σ away. This state has a calculated value of $\theta_\alpha^2 = 0.1$ using the literature value of $\Gamma_{tot} = 8(1)$ keV from Ref. [64], which is often the typical boundary at which excitations might be considered clustered.

The state at 8843(14) keV has a similar energy to that measured by Avila et al. [103] of 8.82(3) MeV, but the value of Γ_n/Γ_{tot} obtained is $\approx$100%, significantly different to the value of 0.68(10) measured in the current work. This could imply that a different state has been observed in this work.

The 9238(16) keV state is proposed in the literature [64] to have possible spin assignments of 0^-, 1^- and 2^-. Based on the value $\Gamma_\alpha/\Gamma_{tot} = 0.9(3)$ obtained in the current work, the

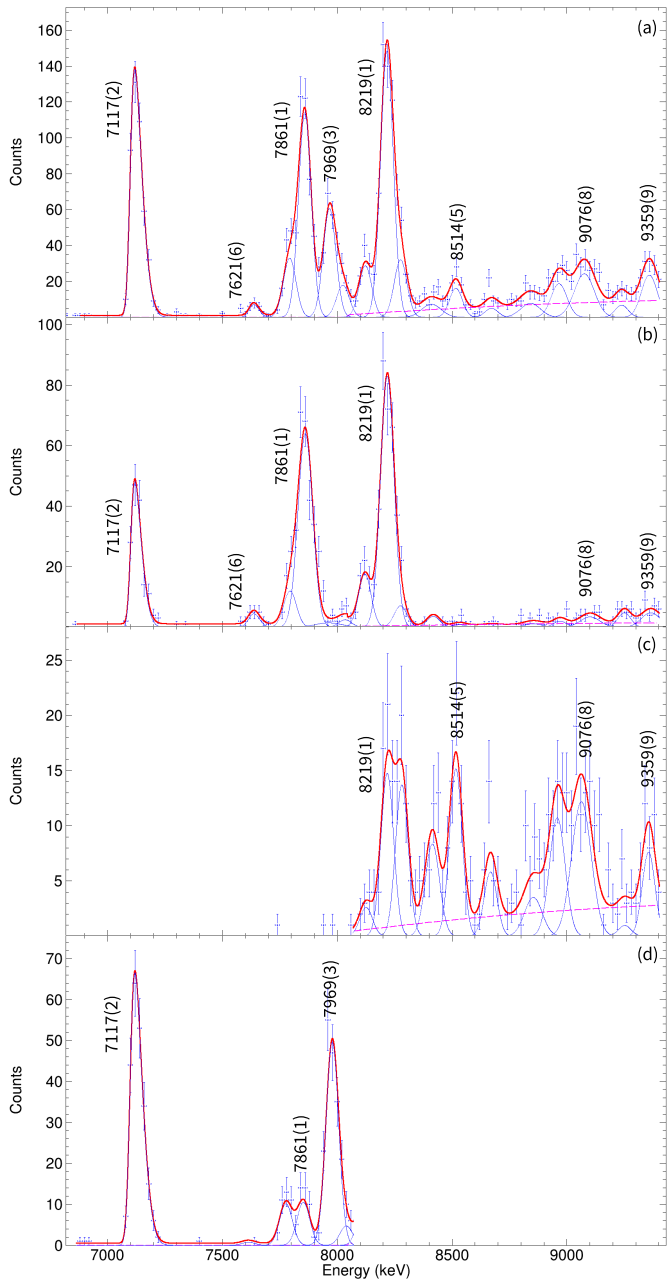


Figure 4.5: Q3D spectra obtained for states between 7.0 and 9.4 MeV for Q3D singles data (a), α-decay events (b), n-decay events (c) and γ-decay events (d). The fitted background (dashed magenta line) is constant at just above 0 until the n-decay threshold, at which point the background becomes due to the two-body (^{17}O,n) phase space.

only possible assignment of these three is the natural parity 1^-, due to angular momentum selection rules for α-decay. The large error on this value is due to the weak population of the state.

The tentative assignment of $J^\pi = 2^-$ (unnatural parity) for the 8409(11) keV state [64] is consistent with the results obtained in this work, as the value of $\Gamma_\alpha/\Gamma_{tot}$ is within 2σ of 0. For the state at 8514(5) keV, the non-zero value of $\Gamma_\alpha/\Gamma_{tot} = 19(5)$ contradicts the tentative $J^\pi = 4^-$ assignment in Ref. [64].

The states at 7861(1) keV and 8126(3) keV have upper limit values of θ_α^2 presented in Table 4.2 of < 170 and < 50 respectively, which gives potential for these states to display cluster structure. This largely depends on their widths, which are too narrow to be measured in the current work - in the case of the 7861(1) keV state, this could be as narrow as 10 eV and still be above the typical cluster threshold of θ_α^2 =0.1. Other than these two states and the 8280(1) keV state, the values of θ_α^2 obtained do not suggest α-cluster structure in the measured states in this excitation region.

4.2.4 9.6 MeV to 11.9 MeV

The states in the excitation range of 9.6 MeV to 11.9 MeV are shown in Figure 4.6, along with the spectra obtained when the available decay paths in the Catania plot are gated on.

The $J^\pi = 3^-$ state at 10106(11) keV has been measured to have $\Gamma_\alpha/\Gamma_{tot} = 0.44(18)$ by Avila et al. [103], within 1σ of the value 0.55(10) obtained in the current work, and $\Gamma_\alpha/\Gamma_{tot} = 0.35(7)$ by Goldberg et al. [105], within 2σ. The value of Γ_n/Γ_{tot} obtained in this work, 0.45(10), is also in agreement with that of Avila et al. [103] of 0.6(3).

Regarding the $J^\pi = 3^-$ 10386(7) keV state, the value of $\Gamma_n/\Gamma_{tot} = 0.61(7)$ is in agreement with that obtained by Avila et al. [103] of 0.7(4), while the value of $\Gamma_\alpha/\Gamma_{tot} = 0.39(7)$ is

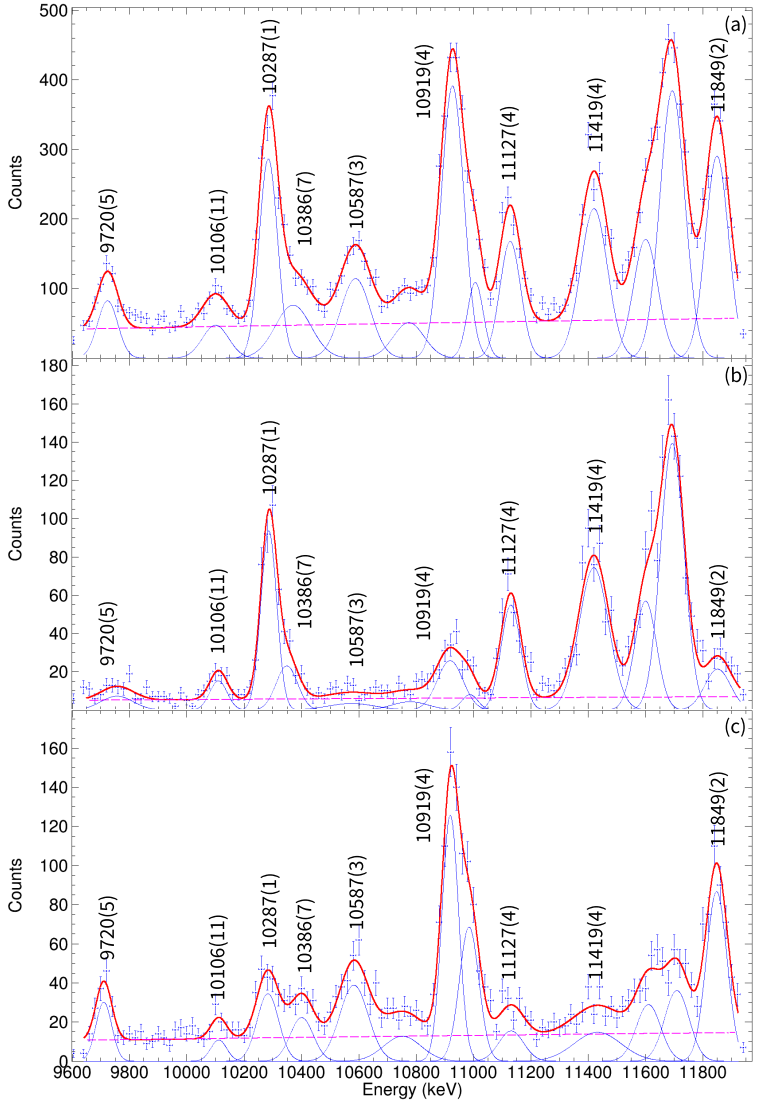


Figure 4.6: Q3D spectra obtained for states between 9.6 and 11.9 MeV for Q3D singles data (a), α-decay events (b) and n-decay events (c). The fitted background (dashed magenta line) is due to the two-body (^{17}O,n) phase space.

within 2σ agreement of the previous value of 0.7(2).

A previous measurement by Goldberg et al. [105] of the 10774(9) keV state produced a value of $\Gamma_\alpha/\Gamma_{tot} = 0.45(15)$, in agreement with the value of $\Gamma_\alpha/\Gamma_{tot} < 0.32$ obtained in the current work.

Measurement of the 10997(16) keV state yielded values of $^{\Gamma_\alpha}/_{\Gamma_{tot}} < 0.11$ and $^{\Gamma_n}/_{\Gamma_{tot}} = 0.94(5)$, in excellent agreement with the values of < 0.12 and 0.9(6) obtained by Avila et al. These values are also consistent with the tentative assignment of this state as a $J^\pi = 2^-$ [64].

The value of $^{\Gamma_\alpha}/_{\Gamma_{tot}} = 0.68(6)$ measured for the 11127(4) state is in good agreement with that measured by Yang et al. [104] of $> 0.65(3)$, and is within 2σ of the value of 0.80 published by Goldberg et al. [105] without an uncertainty.

The tentatively assigned $J^\pi = 4^+$ [64] 11419(4) state was measured to have a value of $^{\Gamma_\alpha}/_{\Gamma_{tot}} = 0.74(6)$, in excellent agreement with the results of Avila et al. (0.8(3)), Yang et al. (>0.23(1)) and Goldberg et al. (0.90(10)), while improving upon the uncertainty provided by the other absolute measurements. The value of $^{\Gamma_n}/_{\Gamma_{tot}} = 0.26(6)$ is likewise in good agreement with the value of 0.25(14) measured by Avila et al. [103].

Aside from the 11696(1) keV state discussed in Ref. [57], there is no evidence of cluster structure for any states in this region with prior spin-parity information. All calculated θ_α^2 values are significantly under 0.1, suggesting typical shell-model behaviour of states in this region.

4.2.5 12.4 MeV to 14.5 MeV

The Q3D excitation spectra for energies ranging from 12.4 MeV to 14.5 MeV are shown in Figure 4.7, with the Q3D singles spectrum as well as spectra arising from α-decay and n-decay events.

At 12188 keV, the $2n$-decay channel opens and excited ^{18}O nuclei have enough energy to decay sequentially to ^{16}O. As described previously in section 3.3.2.2, this can have a significant effect on the geometric efficiency and as such must be taken into account to

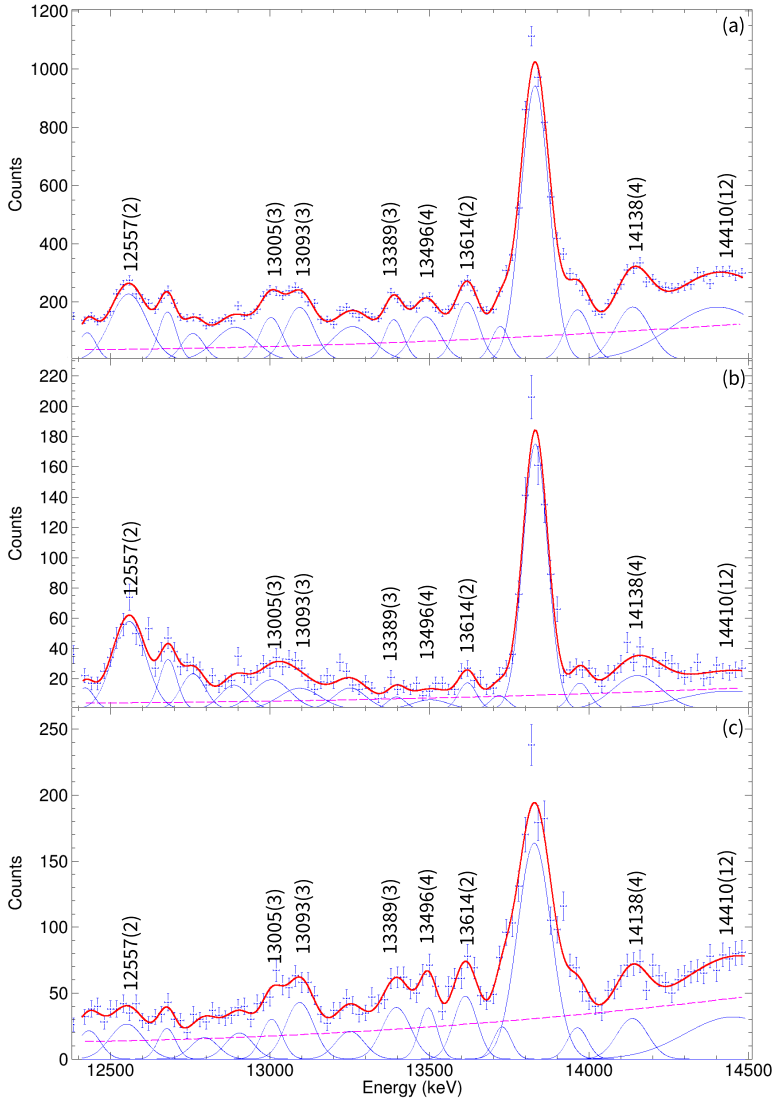


Figure 4.7: Q3D spectra obtained for states between 12.4 and 14.5 MeV for Q3D singles data (a), α-decay events (b) and n-decay events (c). The fitted background (dashed magenta line) is due to the combination of the two-body ^{17}O+n and three-body (^{16}O,2n) phase spaces.

produce accurate branching ratios. Results in this region have the total n-decay branch split into decays that proceed via single n-emission and double n-emission.

The levels at 12680(3) keV and 12764(3) keV provide a challenge to fit, especially as there is evidence of wide, α-decaying states around this region [103, 105]. Despite this, the

value of $\Gamma_\alpha/\Gamma_{tot} = 0.53(7)$ for the 12680(3) keV state is in good agreement with the value obtained by Avila et al. [103] of 0.40(5), perhaps being slightly higher due to the presence of these wide states.

The 13005(3) keV state has a measured $\Gamma_\alpha/\Gamma_{tot}$ of 0.49(16), over 3σ from 0. This suggests that the tentative $J^\pi = 4^-$ assignment is incorrect, as no evidence is seen of decays through an excited state of ^{14}C for α-decays from this level.

The value of $\Gamma_\alpha/\Gamma_{tot} = 0.18(4)$ for the 13614(2) keV state is consistent with that measured by Yang et al. [104] of >0.07(1). Consistency is also seen for the states at 13972(8) keV, 14138(4) keV and 14410(12) keV, all lying within 1σ of the results from Avila et al. [103], or consistent with the lower limits measured by Yang et al. [104]. The 14138(4) keV state is also seen to be inconsistent with the tentative $J^\pi = 6^-$ spin-parity assignment.

No states in this region, aside from the $J^\pi = 6^+$ state at 12557(2) keV, display cluster structure based on the values of θ_α^2. This again suggests population of mostly shell-model states in this region, though there is potential for cluster structure in the states at 12764(3) keV and 12893(7) keV if these states were determined to have sufficiently-high spin ($J \geq 6$).

4.2.6 14.5 MeV to 16.3 MeV

The Q3D excitation spectra for singles, α-decay-gated and n-decay-gated events is shown in Figure 4.8. The 14410(12) keV state is seen on the far left of the spectra, though with considerably lower statistics than in Figure 4.7. The width for this state is fixed to that measured in the previous excitation region when fitting this excitation region, as lower statistics in this region and a possible artificial decrease in counts at the edge of the focal plane acceptance can cause fitting difficulties. The value of Γ_{tot} given in Table 4.2 for this state is thus that

measured in Figure 4.7. The branching ratios extracted using the data in this region are $\Gamma_\alpha/\Gamma_{tot} = 0.17(7)$, $\Gamma_n/\Gamma_{tot} = 0.38(7)$ and $\Gamma_{2n}/\Gamma_{tot} = 0.45(7)$, which all lie within 1σ of the same results from the lower excitation range measurement.

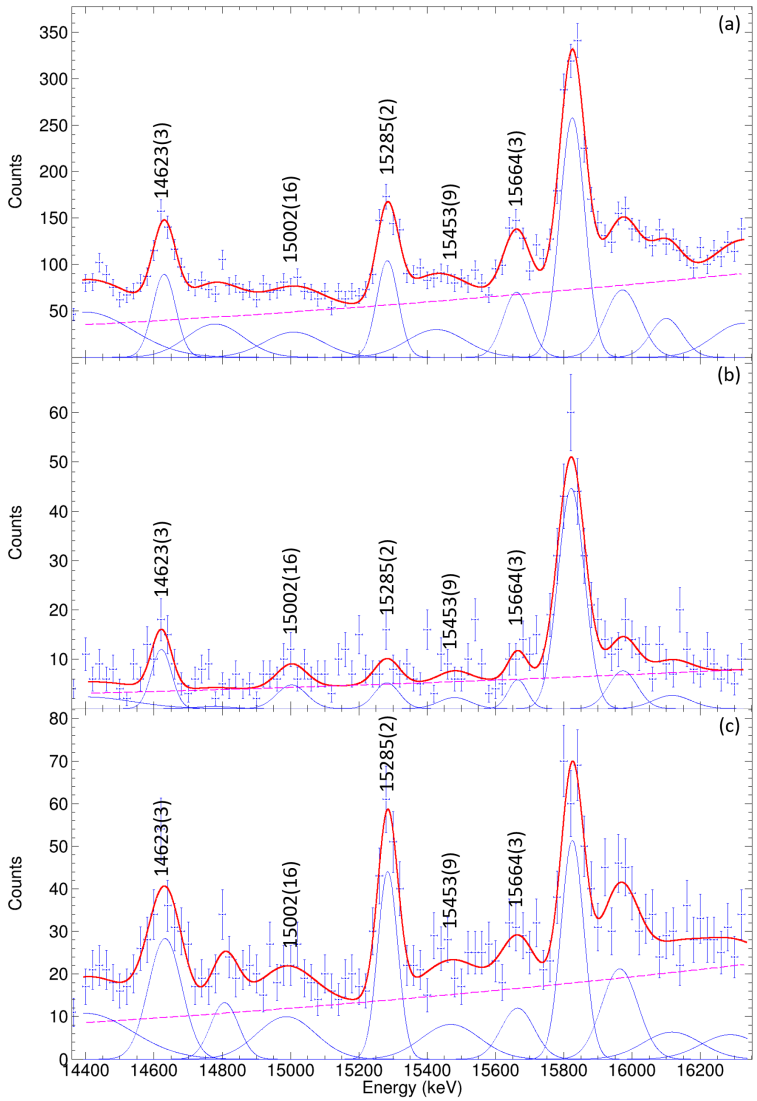


Figure 4.8: Q3D spectra obtained for states between 14.5 and 16.3 MeV for Q3D singles data (a), α-decay events (b) and n-decay events (c). The fitted background (dashed magenta line) is due to the combination of the two-body (^{17}O,n) and three-body (^{16}O,2n) phase spaces.

There is literature information on values of Γ_i/Γ_{tot} for states in the range of 14.5

to 15.0 MeV from Avila et al. [103], though the largely different widths and values of Γ_i/Γ_{tot} compared with states measured in the current work suggest that different states are observed across both works, which is likely due to the typical increase of level density as a function of excitation energy.

Three further states at 15970(8) keV (Γ_{tot}=90(30) keV), 16112(16) keV (Γ_{tot}=90(40) keV) and 16324(16) keV (Γ_{tot} >126 keV) are observed, which have previously been seen in the work of von Oertzen et al. [56] at energies of 15981(9) keV, 16111(8) keV and 16333(7) keV respectively. These centroid energies lie above the p-decay threshold, S_p = 15.942 MeV, the branching ratio for which was unable to be determined in the current work due to contamination of this locus. The contamination arises from pile-up events — events in which there are multiple hits in a DSSD detector, of which some are random (do not originate from the reaction which produced the recoil proton incident on the Q3D). Reconstruction of the unrelated hits causes a region on the Catania plot that lies across the p-decay locus. As such, values of branching ratios for these states have not been presented.

The results from the current work represent the first comprehensive branching-ratio measurements of ^{18}O below 16 MeV. Where previous results exist, these are generally in good agreement to the current work. In some instances, the branching ratios have provided additional constraints and allow unnatural spin-parity assignments to be ruled out.

4.2.7 Clustering results

The results from Ref. [57] are presented below, detailing the tendency towards clustering of the states suggested to be members of the proposed rotational bands in Ref. [56]. The text below is again largely unchanged from the published version. The fits used to extract experimental values were those shown in figures 4.5, 4.6, 4.7 and 4.8.

Table 4.3: A table summarizing the results obtained for states in the potential bands, compared with literature values. Errors shown in the table represent statistical errors and, where relevant, the error on geometric efficiency. Results given here were previously published in Ref. [57].

J^π (lit.) (from rot. bands)	E_{level} (MeV)	Γ_{tot} (keV)	$\Gamma_\alpha/\Gamma_{\text{tot}}$	Barrier penet.	θ_α^2	E_{level} (lit.)[1] (MeV)	Γ_{tot} (lit.)[1] (keV)	$\Gamma_\alpha/\Gamma_{\text{tot}}$ (lit.)[2]
				$K^\pi = 0_2^+$				
4^+	7.117(2)	< 16	0.49(2)	$5.2(1)\times10^{-7}$	> 0.007[3]	7.115(5)	< 0.0004[4]	—
6^+	11.696(1)	74(3)	0.73(6)	0.02120(2)	0.4	11.702(6)	19(7)	0.52(6), > 0.89(3)
				$K^\pi = 0_2^+$				
1^-	8.037(5)	< 33	0.34(9)	0.0528(7)	< 0.004[3]	8.035(5)	< 2.5[5]	1
(3^-)	9.720(5)	< 20	0.26(7)	0.1301(6)	< 0.007	9.715(5)	15(4)	0.27(5)
(5^-)	13.614(3)	< 23	0.15(3)	0.2350(2)	< 0.002	13.624(6)	22(7)	> 0.07(1)
				$K^\pi = 0_4^+$				
0^+	7.794(2)	< 16	> 0.63(5)	0.0422(3)	0.07[6]	7.796(5)	< 10	—
2^+	8.219(1)	< 13	0.88(2)	0.03258(9)	0.01[3]	8.216(5)	1.9(2)[7]	0.89(11)
4^+	10.287(1)	40(6)	0.60(4)	0.07951(8)	0.05	10.293(6)	23(8)	0.66(11)
6^+	12.557(2)	107(8)	0.63(5)	0.04726(8)	0.2	12.557(7)	22(8)	0.7(2), > 0.79(3)
(8^+)	15.824(2)	55(7)	α_0: 0.38(10)	0.02882(3)	0.08[8]	15.810(10)	20(8)	> 0.57(2)
				$K^\pi = 0_4^-$				
(1^-)	10.587(3)	96(10)	< 0.12	< 0.12	< 0.003	10.59(1)	70(16)	—
(3^-)	10.919(4)	30(20)	0.18(4)	0.18(4)	0.003	10.92(1)	30(9)	—
(5^-)	13.832(1)	73(3)	0.38(3)	0.38(3)	0.01	13.82(1)	27(8)	0.12(5), > 0.32(2)

[1]Values from Ref. [56], except in certain cases denoted by extra footnotes.

[2]See text for details.

[3]Value of θ_α^2 calculated using literature width, due to limits of experimental resolution.

[4]Width from Ref. [107].

[5]Width from Ref. [64].

[6]Value of θ_α^2 presented without limit, due to conflicting limits on Γ_{tot} and $\Gamma_\alpha/\Gamma_{\text{tot}}$.

[7]Width from Ref. [103].

[8]Calculated using α_0 value.

4.2.8 The proposed $K^\pi = 0_2^+$ band

The states observed in the potential $K^\pi = 0_2^+$ band were the 4^+ 7.117 MeV and the 6^+ 11.696 MeV states. Due to the 7.117 MeV state lying below the neutron threshold, γ-decay had to be taken into account using the method detailed in section 3.3.2.1. The value of $^{\Gamma_\alpha}/_{\Gamma_{\rm tot}}$ obtained was 0.49(2), representing the first-such measurement for this state. Using this value gave θ_α^2 >0.007 when calculated using the upper limit of $\Gamma_{\rm tot}$ of <25 fs (>2.63×10^{-2} eV) [107], as due to the resolution of the Q3D, the fitting performed was not sensitive to the width of this state. It is therefore concluded that the 4^+ state is not a member of a cluster band, limited by the narrow $\Gamma_{\rm tot}$. It should, however, be noted that the value of $\Gamma_{\rm tot}$ was not established from direct measurement, and if the width of the state were determined accurately and found to be an order of magnitude larger than the limit presented in Ref. [107], the value of θ_α^2 would increase to above 0.1.

The 11.696 MeV 6^+ state was measured to have $^{\Gamma_\alpha}/_{\Gamma_{\rm tot}} = 0.73(6)$, a value that lies between that measured by Avila et al. [103] via resonant scattering of 0.52(6) and the lower limit determined by Yang et al. [104] of >0.89(3). The mean of these two values gives $^{\Gamma_\alpha}/_{\Gamma_{\rm tot}} = 0.82(15)$, which lies within 1σ of the value from the current work. Using $\Gamma_{\rm tot} = 74(3)$ keV from the fit of the excitation spectrum, a value of $\theta_\alpha^2 = 0.39$ is obtained, suggesting that this state does indeed possess a cluster structure.

4.2.9 The proposed $K^\pi = 0_2^-$ band

The observed states from the proposed $K^\pi = 0_2^-$ band were the 1^- 8.037 MeV, (3^-) 9.720 MeV and (5^-) 13.614 MeV resonances. For 8.037 MeV, the value of $^{\Gamma_\alpha}/_{\Gamma_{\rm tot}}$ measured was 0.34(9). While this is not in agreement with the result from Avila et al.

[103], which measured 100% of the strength of this resonance belonging to the α-branch, this

current measurement is sensitive to the γ-branch, to which the majority of decays for this state belong. Using the upper limit of $\Gamma_{\rm tot}$ <2.5 keV [64], a value of θ_α^2 <0.004 is obtained, which suggests that this state does not represent a clustered band head.

The 9.720 MeV state appears to be a combination of two closely-separated states, as the centroid of the resonance changes from 9.711(4) MeV when gated by n-decay events to 9.760(12) MeV when gated by α-decay events. The existence of a further, weakly-populated majority α-decaying state is in good agreement with previous measurements [105, 103, 106] in this region. The value ${}^{\Gamma_\alpha}/_{\Gamma_{\rm tot}} = 0.26(7)$ for this combined part is consistent with the value of 0.27(5) measured by Goldberg et al. [105], and produces $\theta_\alpha^2 < 0.007$ from the upper limit $\Gamma_{\rm tot}$ <20 keV.

The 13.614 MeV state is measured to have ${}^{\Gamma_\alpha}/_{\Gamma_{\rm tot}} = 0.15(3)$ here, in agreement with the upper limit measurement of Ref. [104], ${}^{\Gamma_\alpha}/_{\Gamma_{\rm tot}}$ >0.07(1). Together with the measured width, $<$ 23 keV, a value of $\theta_\alpha^2 < 0.002$ is obtained. It can clearly be seen that none of these states display cluster structure, and thus the cluster band does not exist.

4.2.10 The proposed $K^\pi = 0_4^+$ band

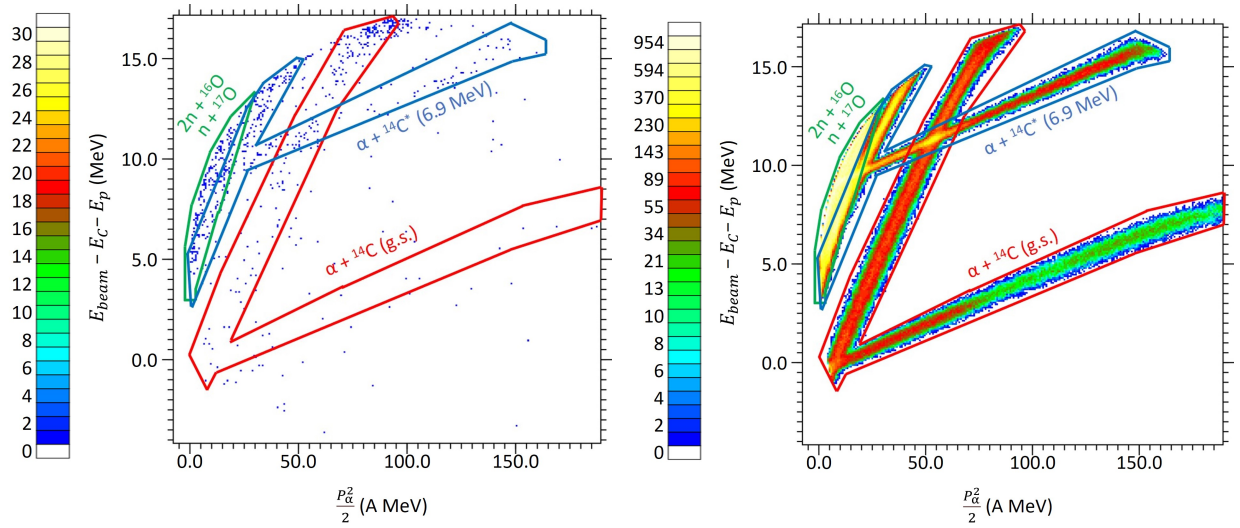
The band head of this proposed band lies at 7.794 MeV and has $J^\pi = 0^+$, determined by angular distributions [56]. There is difficulty in resolving this state, as there also exists a 2^- state at 7.770 MeV which lies well within the experimental resolution of the 0^+ level. By presenting both states summated, the value of ${}^{\Gamma_\alpha}/_{\Gamma_{\rm tot}}$ represents a lower limit for the 7.794 MeV state due to the inability of the 7.770 MeV state to α-decay. Taking ${}^{\Gamma_\alpha}/_{\Gamma_{\rm tot}} = 0.63(5)$ and, using the measured width of <16 keV, a value of $\theta_\alpha^2 = 0.07$ is obtained — this could increase depending on the true α-branch of the state, but it is likely this state does not display cluster structure as the true width of the state may be much lower, while the corresponding ${}^{\Gamma_\alpha}/_{\Gamma_{\rm tot}}$ cannot be >1.

The 8.219 MeV 2^+ state lies above the n-decay threshold, and for this excitation energy the n-decay and γ-decay events are indistinguishable due to overlapping loci on the Catania plot, as well as the extremely similar geometric efficiencies of the n- and γ-branches just above the n-threshold. As the geometric efficiencies are so similar, assuming all of these non-α events arise from n-decay has no effect on the measured value of the α-branch. The effect on the n-branch decreases as excitation energy increases and the γ-branch is suppressed. The value of ${}^{\Gamma_\alpha}/_{\Gamma_{\rm tot}} = 0.88(2)$ measured in the current work agrees with that measured in Ref. [103] of 0.89(11) to within 1σ, while reducing the uncertainty by an order of magnitude. Together with the measured width from Ref. [103], a value of $\theta_\alpha^2 = 0.01$ is obtained, suggesting that this state does not display cluster structure.

The 10.287 MeV 4^+ state is well-populated, with ${}^{\Gamma_\alpha}/_{\Gamma_{\rm tot}} = 0.60(4)$. This value is consistent with previous measurements, 0.66(0.11) [103] and $> 0.37(3)$ [104]. The width measured in this work is 40(6) keV, resulting in $\theta_\alpha^2 = 0.05$.

The 6^+ state lies at 12.557 MeV, with a measured width of 107(8) keV. The measured value of ${}^{\Gamma_\alpha}/_{\Gamma_{\rm tot}} = 0.63(5)$ is consistent with the value obtained by Ref. [103] of 0.7(2), but lower than that measured by Ref. [104] of >0.79(3). The large discrepancy in width with literature values may suggest an overlap of states in this region in the current work, unable to be clearly separated due to the experimental resolution.

A state at 15.824 MeV, predicted to have $J^\pi = 8^+$ based on being a member of the proposed band, was observed in the current work. The measured value of ${}^{\Gamma_{\alpha 0}}/_{\Gamma_{\rm tot}} = 0.38(10)$ is within two standard deviations of the result measured in Ref. [104] of >0.57(2). However, there is also a large α-branch that passes through an excited state in ^{14}C (7.012 MeV, $J^\pi = 2^+$), suggested, through comparison to Monte-Carlo simulation and the requirement that the excited level be natural parity due to selection rules made evident by the existence of decays to the ground state of ^{14}C, to be ${}^{\Gamma_{\alpha 5}}/_{\Gamma_{\rm tot}} = 0.51(10)$. However, a notable centroid



(a) (b)

Figure 4.9: Catania plots generated for the 15825(2) keV excitation in ^{18}O, assuming the decay of ^{18}O* into ^{14}C (detected) $+\alpha$ for experimental data (a) and simulated data (b). The different decay paths are labelled and coloured to indicate the different loci. Figure previously published in Ref. [63] as Figure 5.

shift occurs ($\approx$ 20 keV, to 15.841(4) MeV) when looking at events passing though the excited level of ^{14}C. It is therefore possible that this region contains the overlap of a natural and unnatural parity state which have a separation much less than the experimental resolution of this work, and these decays pass through the 6.903 MeV $J^\pi = 0^-$ state, the lowest-lying determined unnatural parity state in ^{14}C, as the comparison to Monte-Carlo data is not sensitive to a 100 keV shift in the excitation energy of the daughter nucleus. This state is the only state to suggest decay through an excited level in the daughter ^{14}C in the experimental data. Figure 4.9 shows the Catania plot generated using experimental data for this excitation, compared with Monte-Carlo simulation. A clear number of events in the blue locus (corresponding to decay through an excited state in ^{14}C) distinct from other loci can be seen in the experimental data.

4.2.11 The proposed $K^\pi = 0^-_4$ band

There are three observed states in this proposed negative-parity rotational band, lying at measured energies of 10.587(3) MeV (1^-), 10.919(4) MeV (3^-) and 13.832(1) MeV (5^-). These spin-parities are all tentative, arising in-part from rotational fitting [56].

The 10.587 MeV state was observed to have ${}^{\Gamma_\alpha}/_{\Gamma_{\rm tot}} < 0.12$, much lower than expected for a cluster state with a low spin. This represents the first measurement of this value by any method, and using the measured width of 96(10) keV gives $\theta^2_\alpha < 0.003$, indicating a lack of cluster structure for this state.

The 10.919 MeV state was strongly-populated, overlapping with a weakly-populated state at 10.985(6) MeV. The current work measures ${}^{\Gamma_\alpha}/_{\Gamma_{\rm tot}} = 0.18(4)$ for the 10.919 MeV state, again representing a first measurement of this value. Due to the overlap of the peaks, there was a reasonable uncertainty on the value of the width, measured here to be 30(20) keV. This gives $\theta^2_\alpha = 0.003$, again indicating that this state does not belong to a cluster band.

The highest energy state observed in this proposed rotational band was the 5^- 13.832 MeV state. This state was well-populated, overlapping with two smaller states (one either side) of energies 13727(5) keV and 13965(1) keV; as the centroids of these states were at least 100 keV away from each other, resolving them was possible. The value of ${}^{\Gamma_\alpha}/_{\Gamma_{\rm tot}}$ was measured to be 0.38(3), in agreement with the value of >0.32(2) from Ref. [104]. A value of 0.12(5) is reported in Ref. [103], measured through resonant scattering, though this discrepancy may be due to the high level-density in this region. The width of this state was determined to be 73(3) keV, which results in $\theta^2_\alpha = 0.01$, suggesting an absence of α-clustering in the structure of this excitation.

4.2.12 The proposed $K^\pi = 1^-$ band

The proposed $K^\pi = 1^-$ band had potential members within the observed excitation regions. One state of interest is at 11.127(2) MeV, suggested to be the 4^- member of this band. The value $\Gamma_{\alpha 0}/\Gamma_{\rm tot} = 0.68(6)$ was extracted, disproving this state assignment as unnatural parity α-decays are forbidden to decay to the ground-state of ^{14}C, and this excitation energy is too low to populate the first excited state. This result is in good agreement with the value from Ref. [104] of >0.65(3) and within two standard deviations of 0.8, presented without error in Ref. [105].

4.3 Discussion and summary

Branching ratios for the states proposed to be members of the tentative rotational bands suggested in Ref. [56] were determined, as well as for other states that lay within the observed excitation region, with a total of > 50 states investigated. For members of the proposed negative-parity bands, $K^\pi = 0_2^-$ and $K^\pi = 0_4^+$, no cluster structure was observed based on values of θ_α^2, with the largest of these belonging to the $J^\pi = 5^-$ state at 13.832(1) MeV with a value of $\theta_\alpha^2 = 0.01$, an order of magnitude below the threshold at which a nuclear state could be considered clustered.

By itself, the lack of evidence towards the existence of these negative-parity bands also casts doubt on the existence of the positive-parity bands, as these exist with the corresponding negative parity bands due to the intrinsic reflection asymmetry of the associated structures (^{14}C $\bigotimes$ α and ^{12}C $\bigotimes$ $2n$ $\bigotimes$ α). Supporting this, the majority of members across the positive-parity bands were also determined to have values of θ_α^2 that were not consistent with cluster structure. Two notable exceptions are the $J^\pi = 6^+$ members of both proposed

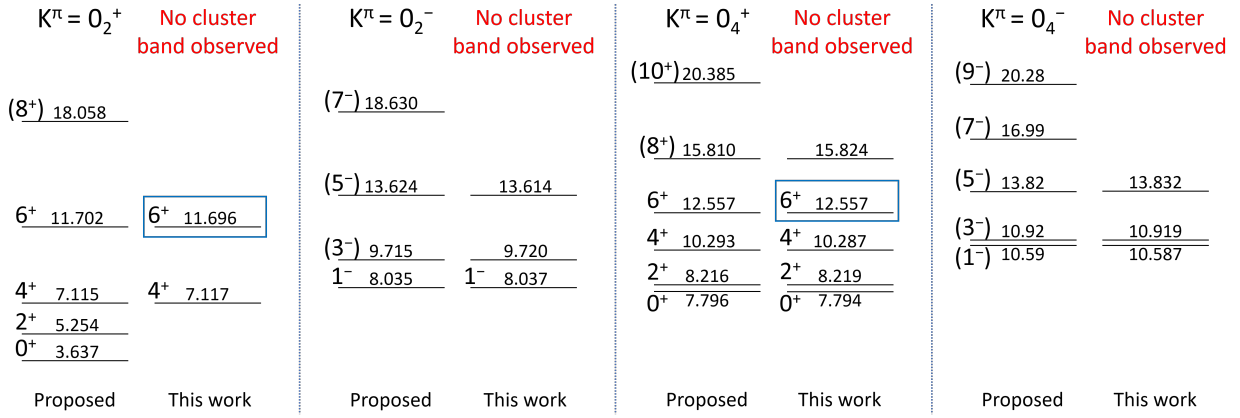


Figure 4.10: The proposed states assigned to the tentative cluster bands, with observed excitation energies (given in MeV) from Ref. [56], compared to the results from this work. States determined to display cluster structure are shown within a blue box. Figure originally published in Ref. [57].

bands: the 11.696(1) MeV state with $\theta_\alpha^2 = 0.4$ and the 12.557(2) MeV state with $\theta_\alpha^2 = 0.2$. The $J^\pi = 4^+$ state at 7.117(2) MeV in the proposed $K^\pi = 0_2^+$ band was not found to be consistent with cluster structure, and due to the lack of other potential 4^+ band members observed in this energy regime this suggests that the proposed $K^\pi = 0_2^+$ band does not exist. However, the value of θ_α^2 obtained for this state is limited by the width of the state. The width extracted from the literature [107] was not measured directly, and as such measurement of this width could, in principle, result in a value of θ_α^2 consistent with cluster structure — however, this would require the measured width to be an order of magnitude higher than the lower limit established from Ref. [107]. The lack of other measured states consistent with cluster structure in the proposed $K^\pi = 0_4^+$ band indicates that this band does not exist with the members proposed. As such, none of the proposed bands investigated were found to contain members with consistent cluster structure — these results are summarised in figure 4.10. While no clear cluster bands were observed, the existence of two states displaying significant cluster structure, both with $J^\pi = 6^+$, hints at the potential existence of fragmented clustering in ^{18}O, a phenomenon that has been observed in mid-mass nuclei

[108].

Due to the lack of conclusive spin assignments for many of the states investigated, there is difficulty in establishing whether or not there is sufficient cluster strength fragmented across many states of the same spin-parity. In the work of Avila et al. [103], Cluster Nucleon Configuration Interaction Model (CNCIM) [109] calculations were performed to model states displaying the cluster configuration $^{14}\mathrm{C}\bigotimes\alpha$. From these calculations, several states with low values of θ_α^2 (< 0.1) were predicted, with the cluster strength in each J^π split across the states, which were then compared with states observed experimentally, populated through ^{14}C+α resonant elastic scattering. There was some overlap between the states observed in the current work and those in Ref. [103], with around 20 comparable states — this potentially signals a lower likelihood of populating $^{14}\mathrm{C}\bigotimes\alpha$ states via the ^{12}C(^{7}Li,p)^{18}O* ^{6}He transfer reaction. Of the states measured, some similarities between predictions made by this model and the current work are observed.

The predicted $J^\pi = 3^-$ states at 9.990 MeV, 10.655 MeV and 10.789 MeV with θ_α^2 values of 0.01, 0.02 and 0.04 respectively can be compared with the known $J^\pi = 3^-$ states, measured in the current work with excitation energies 10.106 MeV and 10.386 MeV, and the state at 10.774 MeV with unknown parity. These states were determined here to have θ_α^2 values of < 0.008, 0.02 and 0.02 (assuming the latter state was indeed a $J^\pi = 3^-$ excitation) respectively, comparable with those predicted by the CNCIM calculations — in the case of the upper limit < 0.008, this value was limited by the experimentally measured width (in this work determined to be < 14 keV), which in the literature is given to be 16(4) keV [64], implying the width of this state likely lies close to the < 14 keV value and hence the true value of θ_α^2 is close to 0.008.

Two previously assigned $J^\pi = 4^+$ states that were measured in the current work, at 10.287 MeV and 11.419 MeV, were found to have θ_α^2 values comparable to those determined

by Avila et al.: the former was found to be 0.05 in the current work (rather than 0.09 found by Avila et al.); the latter was found to be 0.05, the same as the value determined by Avila et al. Only in the latter case does this state match the prediction made by the CNCIM calculations regarding the α-strength of the state. However, the unassigned state at 8.963 MeV was found to have a value of $\theta_\alpha^2 < 0.17$ if a spin of $J = 4$ was chosen, similar to both the value predicted by calculation, $\theta_\alpha^2 = 0.26$, and experimentally, $\theta_\alpha^2 \approx 0.2$ [103]. Again, the upper bound in the current work arises from the experimentally measured Γ_{tot}, which, based on previous literature values, is likely a limit close to the true value.

The two states displaying significant cluster structure (as measured in this work), the $J^\pi = 6^+$ states at 11.696 MeV and 12.557 MeV, yield values of θ_α^2 of 0.4 and 0.2 respectively, which are not entirely consistent with those predicted by the CNCIM calculations for states at energies of 11.112 MeV and 13.035 MeV, predicted with θ_α^2 values of 0.2 and 0.28 respectively, though the suggestion of strong cluster states in the region is supported by these states measured experimentally. A state between these two, with energy at 11.991 MeV and with $\theta_\alpha^2 = 0.07$, is predicted by the calculations: if the previously tentative assignment of $J^\pi = 3^-$ for the state at 11.849 MeV were incorrect, and this state were instead a 6^+, the value of θ_α^2 obtained in the current work is 0.06, matching well this prediction.

It can therefore be concluded that the possibility for fragmented clustering in this nucleus is present, though further spin assignment information for the states measured here would be required to provide a more definitive answer, as the density of states measured in this work was relatively high and thus comparison between measured unassigned states and those predicted by calculation is tenuous. The lack of strong cluster states measured in this work as compared with that of Avila et al. [103] perhaps hints at a lower propensity for population of $^{14}\text{C} \bigotimes \alpha$ structure states using the ^{6}He transfer reaction utilised in the current work, perhaps instead favouring states that display a $^{12}\text{C} \bigotimes 2n \bigotimes \alpha$ structure.

Chapter 5

Investigations into nuclear molecular structures in ^{14}C and ^{16}C

An experiment was performed utilising the LISE (Ligne d'Ions Super Epluchés) [110, 111] beam-line at the Grand Accélérateur National d'Ions Lourds (GANIL) facility in Caen, France. Beams of ^{10}Be and ^{12}Be were produced using the fragmentation method [112, 113, 114], a beam production technique in which a high-energy beam is incident on a target nucleus. This collision, typically peripheral, results in a system of the participant nucleons within the overlap region of the interaction, and a system of the remaining nucleons in the beam nucleus, known as a prefragment. Not all of the nucleons from the two nuclei are involved in the process, and hence the system is not in thermal equilibrium. Several spectator nucleons are lost due to this lack of thermalisation, with other nucleons lost through evaporation from the prefragment (the abrasion-ablation model of fragmentation [115]), but the remaining nucleons are able to produce an intermediate compound nucleus with a high excitation energy. This nucleus proceeds to decay into secondary fragments, the species of which depend on multiple conditions, such as the distribution of excitation energy within in

the spectator nucleons [114]. A depiction of this multi-step process is shown in figure 5.1.

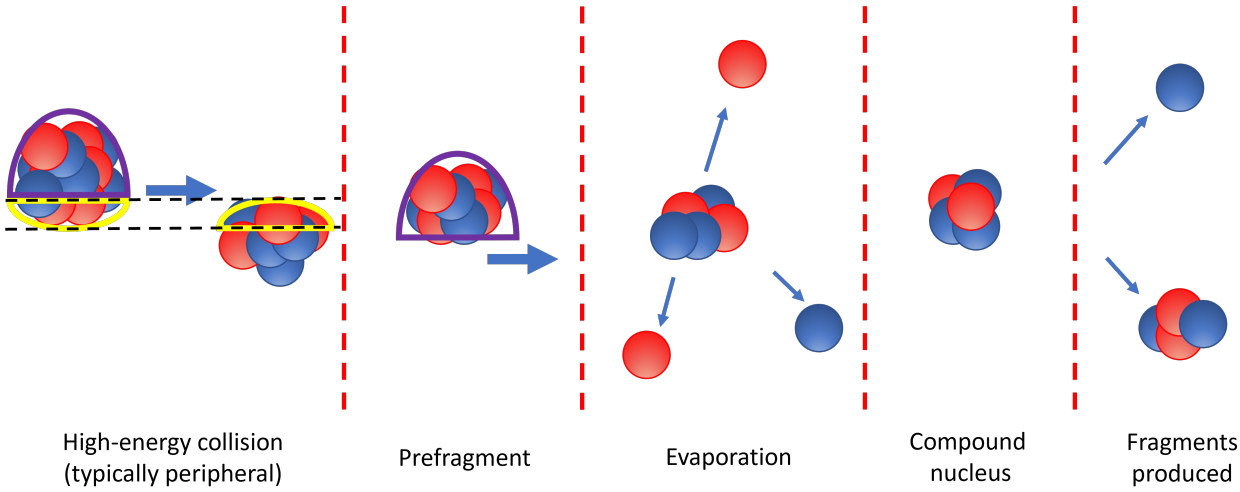


Figure 5.1: A depiction of a fragmentation reaction, showing the various stages with time progressing from left to right. The overlap region for both the beam and target nuclei are shown in yellow, while the nucleons that go on to produce the prefragment are shown in purple.

The ^{10}Be and ^{12}Be were incident on a thick ^{4}He gas target in order to produce ^{14}C and ^{16}C nuclei respectively. A series of silicon detectors were used in order to detect fragments from the decays of the compound nuclei, enabling the generation of corresponding excitation functions. Analysis of these data is ongoing, with the current status presented in this chapter.

5.1 Motivations

In order to develop complete models of nucleon-nucleon interactions, data are needed from a wide variety of nuclear systems. The available data that can be obtained are often limited by ease of measurement: in many cases, production of a desired nucleus can be the limiting factor, due either to low cross-sections or the short lifetime of possible reactants. The latter can be overcome by the use of radioactive ion beam facilities, producing short-lived isotopes

through methods such as fragmentation. These isotopes can then travel further along a beam-line and hence be used in further reactions. Utilising this method in conjunction with thick target inverse kinematics (TTIK), detailed in section 2.7.3, could theoretically enable the investigation of exotic nuclei considered implausible via more common techniques. The current work represents the first use of high-energy fragmentation beams used to populate resonances through the TTIK method. A possible hurdle in this method is the anticipated decrease in the experimental resolution provided utilising the TTIK method.

The ^{14}C and ^{16}C nuclei were investigated due to the potential for the existence of nuclear molecular structures in these nuclei; nuclear molecules are excitations in the form of nuclear clusters, commonly α-particles, typically in a chain formation, and bound by valence nucleons which are often neutrons due to the lack of Coulomb repulsion. Similar structures have been observed in isotopes of beryllium [15, 116, 117], which were discussed in section 2.3.2. Theoretical calculations performed by Itagaki et al. [118] have suggested that these structures may in fact by more stable than corresponding α-conjugate structures found in even-even, $N = Z$ nuclei, such as the Hoyle state in ^{12}C. As the ^{14}C system has previously been studied using similar methods, such as in the work of Freer et al. [119], measurement of this nucleus through the fragmentation and TTIK method described previously allows for a validation of results obtained. The ^{14}C is in particular of interest due to the potential for Hoyle-state analogues, though many of the findings relating to these structures are contradictory: thus, the use of a novel approach may shed some light on the proposed existence of these analogues.

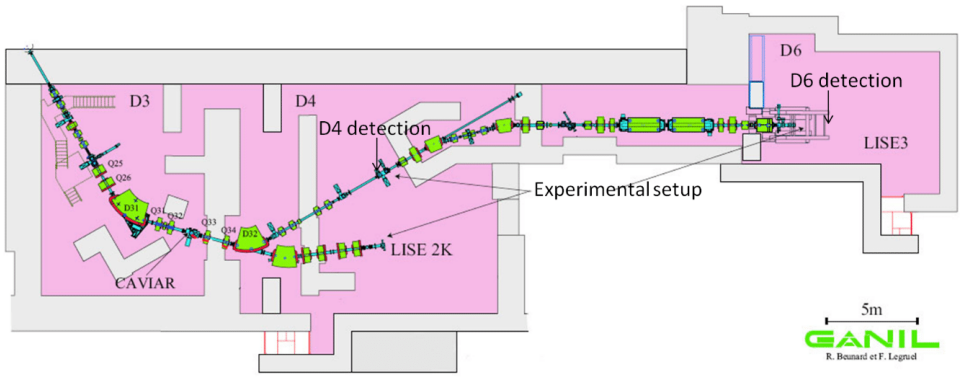


Figure 5.2: An overview of the LISE beam-line, showing the constituent quadrupole and dipole magnets. The ECLAN chamber, which contained the experimental set-up, was situated in the D4 room at the end of the LISE 2K beam-line. Figure taken from Ref. [120].

5.2 Beam production

A beam of ^{18}O at 900 MeV, with a current of ≈3 eμA, was produced by CSS2 [121] — a separated sector cyclotron at the GANIL facility — which was then sent through the LISE beam-line, an overview of which is shown in figure 5.2. Within the beam-line, the ^{18}O beam nuclei were focused onto a natural Be target, of thickness 1.9995 mm and at an angle of 45°, by a series of quadrupole magnets in the D3 room. A fragmentation reaction then occurred, producing a variety of fragments of different nuclear species in the final state. Measurement of the values of magnetic rigidity, B_ρ, kinetic energy, E, energy loss through a known distance and material, ΔE, and time-of-flight (TOF), T, could be utilised to determine the species of each final state nucleus. The total kinetic energy of a nucleus travelling along the beam-line is related to the magnetic rigidity via the expression

$$E = \frac{q^2 B_\rho^2}{2A}, \tag{5.1}$$

where q is the charge state of the nucleus and A is the nuclear mass [110]. Thus, the kinetic energy of a beam nucleus could be determined simply from the magnetic rigidity. The TOF was determined between the target and the final focusing element, a total distance of 43 m [111], in order to reduce the relative uncertainty. An example of species identification is shown in figure 5.3, with energy plotted on the vertical axis and TOF plotted on the horizontal axis. The species that correspond to each feature are labelled — once one species had been identified, it was trivial to identify the rest. Species with a value of $A/q = 2$ can be seen grouped at the right-hand side of the plot, and the feature corresponding to the relevant beam in this instance, ^{10}Be, is circled — it is clear from figure 5.3 that many species were produced, with creation of ^{10}Be relatively uncommon when compared with other isotopes, hence necessitating good beam purification.

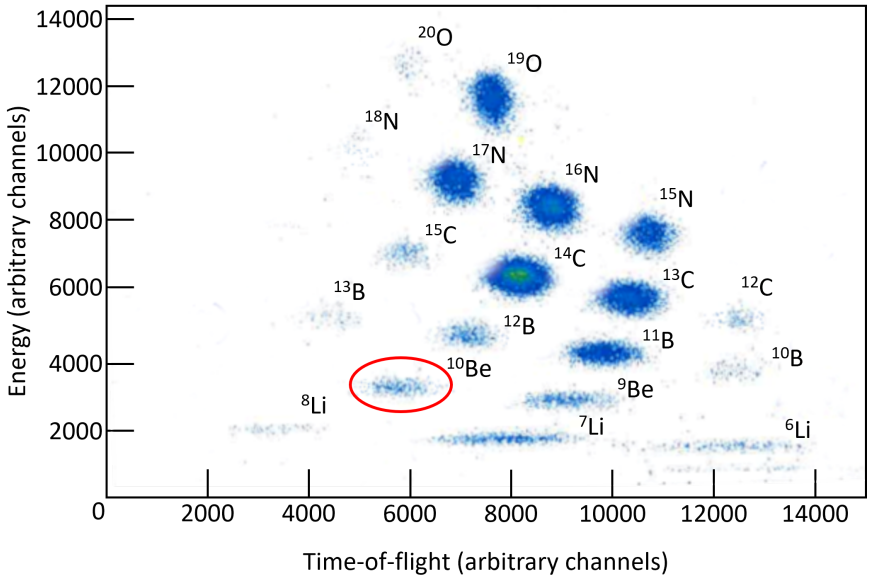


Figure 5.3: Energy of particles plotted against time-of-flight, as measured along the LISE beam-line. Loci due to many different species are labelled, with the locus due to ^{10}Be circled in red.

To achieve high secondary-beam purity, several techniques were employed. The LISE beam-line incorporates a three-step process, selecting events using ΔE and B_ρ values to

remove unwanted species from the beam. A Wien filter, in which an electrostatic and magnetic field are used in conjunction to select species based on velocity, is also contained within the beam-line in order to improve purification [111]. As well as these, a 2.252 mm thick Be wedge was placed downstream of the Be target to further increase the purity of the Be beams, through separation of different beam species due to different amounts of energy-loss through the wedge. Figure 5.4 shows an example of the effect of the purification techniques, with a 96% total purity for ^{10}Be events and limited features that could potentially be due to other species.

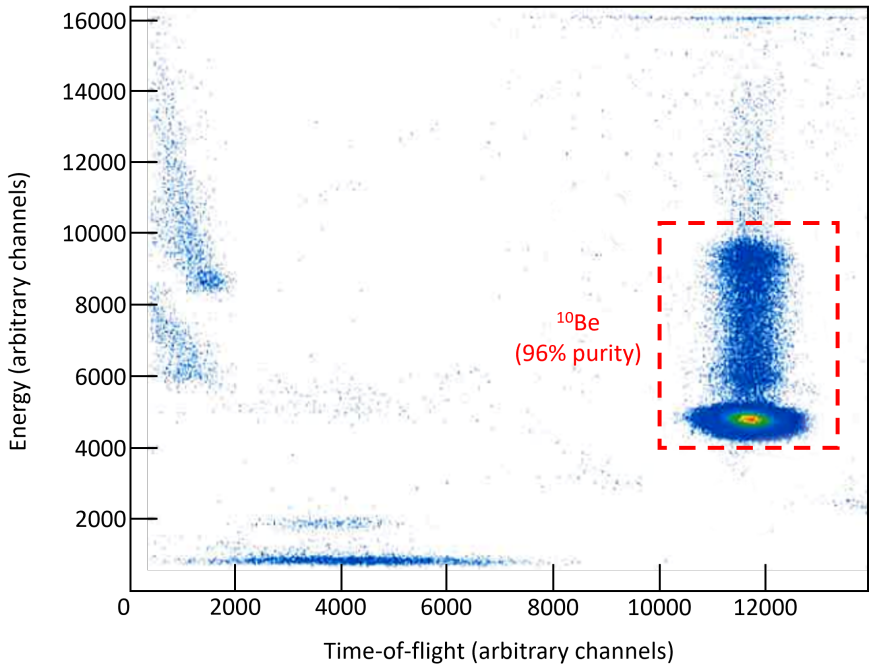


Figure 5.4: Energy of particles plotted against time-of-flight, as measured along the LISE beam-line, following beam purification. The region containing ^{10}Be events is shown in a red box; the purification of the beam resulted in a 96% final purity in this instance. Events within the red box, but with higher energy than the obvious energy peak, were mostly likely caused by the high-energy ^{10}Be nuclei causing the production of charged particles within the silicon detector, resulting in an increased amount of charge measured.

5.3 Experimental set-up

An overview of the experimental set-up used with the ^{10}Be beam, showing the positions of the various detectors based on perpendicular distances defined by the beam axis, is shown in figure 5.5.

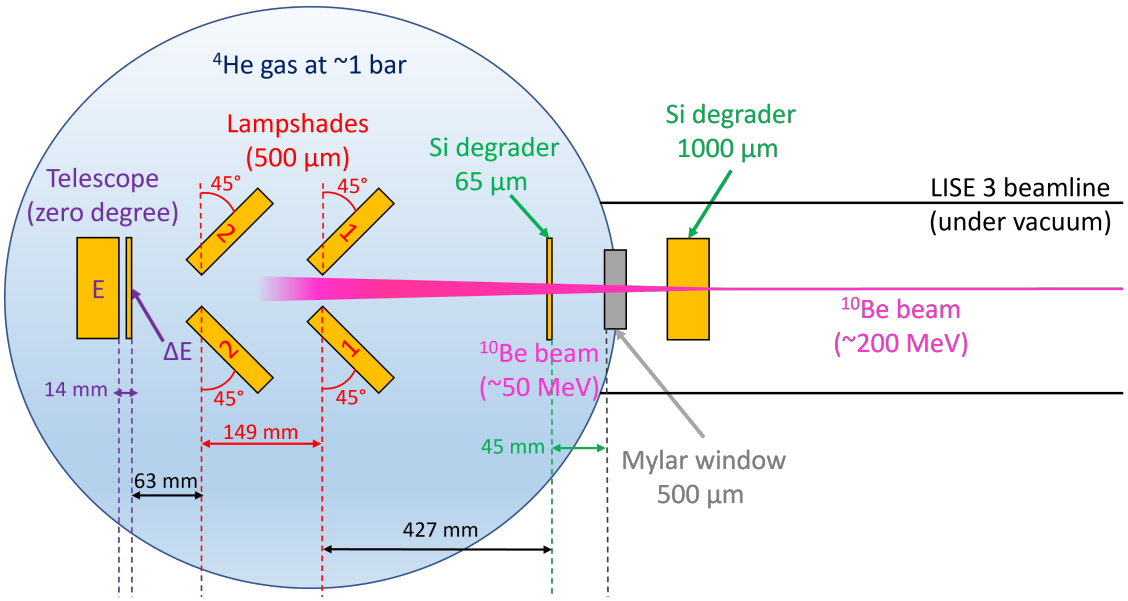


Figure 5.5: Experimental set-up used in the current work. See text for more details.

In order to reduce the energy of the beam to roughly 50 MeV, two silicon degraders were utilised. These were both W1 Micron Semiconductor Ltd double-sided silicon strip detectors (DSSDs) [69], one with thickness 65 µm and the other 1000 µm. The 1000 µm detector was placed in the beam-line, and could be tilted with respect to the beam in order to change the effective degrader thickness. This was located outside of the ECLAN (Experimental Chamber with Low Attenuation for Neutrons) [122] reaction chamber depicted in figure 5.5. The 65 µm degrader was placed inside the reaction chamber, 45 mm behind a 500 µm Mylar window. The purpose behind placing this detector in the chamber was in order to be able to better identify the beam energy following energy straggling through both the 1000 µm degrader and the Mylar window, as well as enabling some indication of

the amount of angular straggling on an event-by-event basis. These active degraders also enabled measurement of the beam spot size, through identification of the area of high event rate. An example of this is shown in figure 5.6.

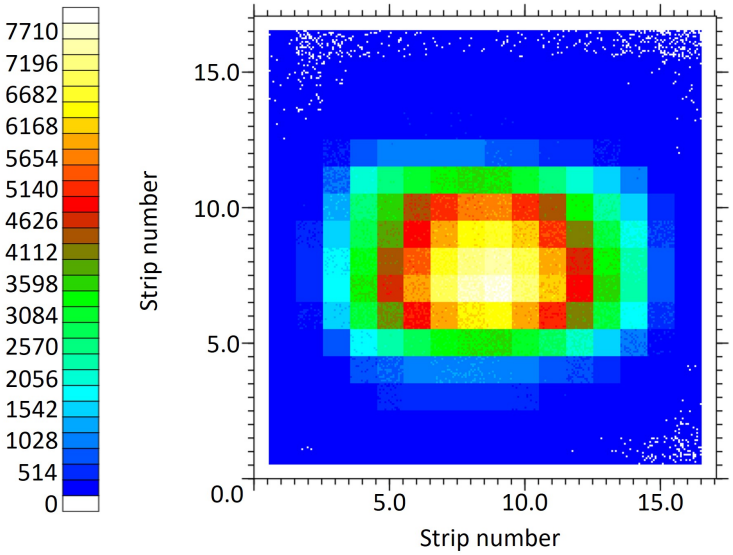


Figure 5.6: A plot of the active area of the 1000 µm degrader, with horizontal strip number plotted against vertical strip number. The beam-spot is clearly visible in the centre of this active area.

The reaction chamber was filled with ^{4}He gas at a pressure of approximately 1 bar, contained by the Mylar window in order to prevent gas leaking into the beam-line. Twelve Micron Semiconductor Ltd 500 µm YY1 single-sided non-resistive silicon strip detectors [123] were placed in the chamber in order to detect products from reactions of the beam with the gas. Each YY1 detector consisted of sixteen strips, enabling detection of charged particles (see section 3.1.2.1 for more information on the function of semiconductor detectors) across a total coverage of 42°. The geometry of these detectors can be seen in figure 5.7, showing the positions of the strips and printed circuit board (PCB).

The detectors were placed into two lampshade configurations, depicted in figure 5.8, in which six YY1 detectors are mounted at an angle of 45° from the beam axis in order

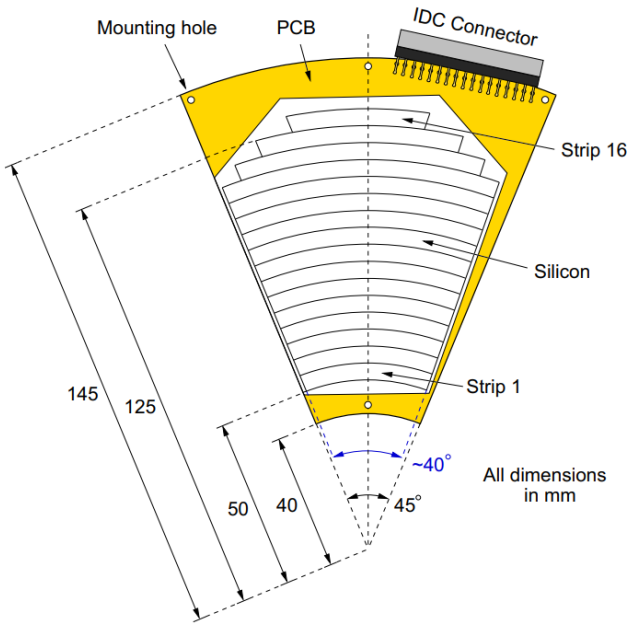


Figure 5.7: Depiction of a Micron Semiconductor Ltd YY1 detector [123], showing some relevant angles and distances. Figure taken from Ref. [124], published as Fig. 2.

to provide total azimuthal coverage. Adjacent YY1 detectors were mounted 60° apart, as measured from the centre of each detector, in order to subtend the entire azimuthal space — the centres of the detectors were placed at azimuthal angles of 30°, 90°, 150°, 210°, 270° and 330° respectively. There was a gap in the centre of the lampshades such that zero degree unscattered beam travelled through the centre of the array without interacting with a YY1 detector. The positions of the lampshade detectors was determined through measurement of the perpendicular distance between the front of the lampshade mount and the Mylar window. The perpendicular distance between the mount and the inner edge of the YY1 detectors was known to be 9 mm, though this was verified through use of Vernier Calipers. The distances given in figure 5.5 are relative to the inner edge of the YY1 detectors: the distance from the window to lampshade 1 was determined to be 472 mm and the distance from the window to lampshade 2 was determined to be 621 mm. Figure 5.9 shows the positions of the active areas of the strips in Cartesian space — data shown here were collected with the ^{10}Be beam incident

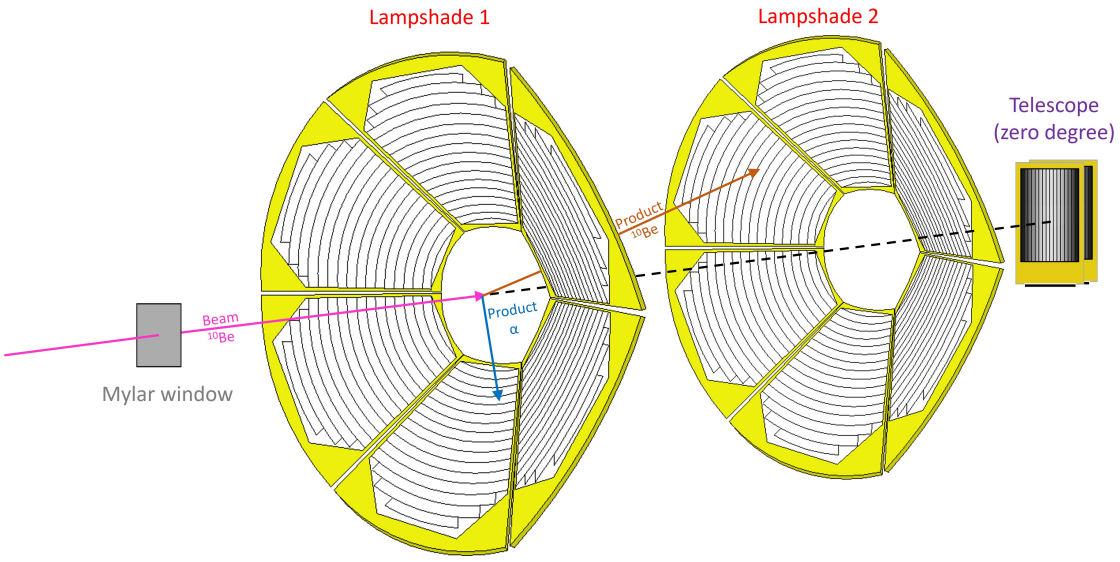


Figure 5.8: Depiction of the two lampshade arrays used in this experiment. Here, the ^{10}Be beam can be seen travelling through the gas volume until it reacts, releasing a product ^{10}Be (measured in lampshade 2) and α (measured in lampshade 1). Figure adapted from figure in Ref. [124], published as Fig. 1.

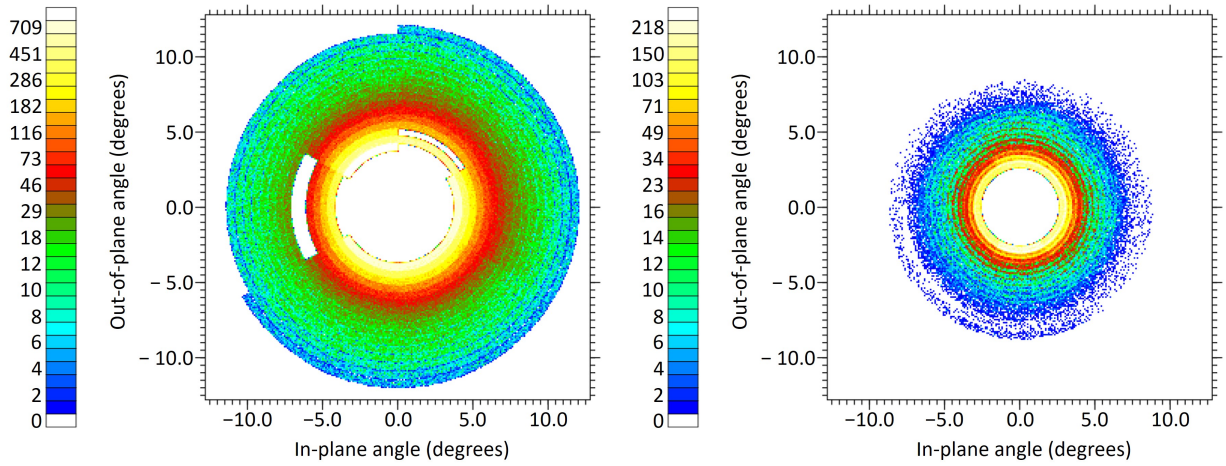


Figure 5.9: Cartesian views of the lampshade 1 (a) and lampshade 2 (b) arrays.

on the ^{4}He gas target, with the number of events in each strip of the detectors decreasing radially from the beam axis. Several missing strips can be observed in the detectors that constitute lampshade 1.

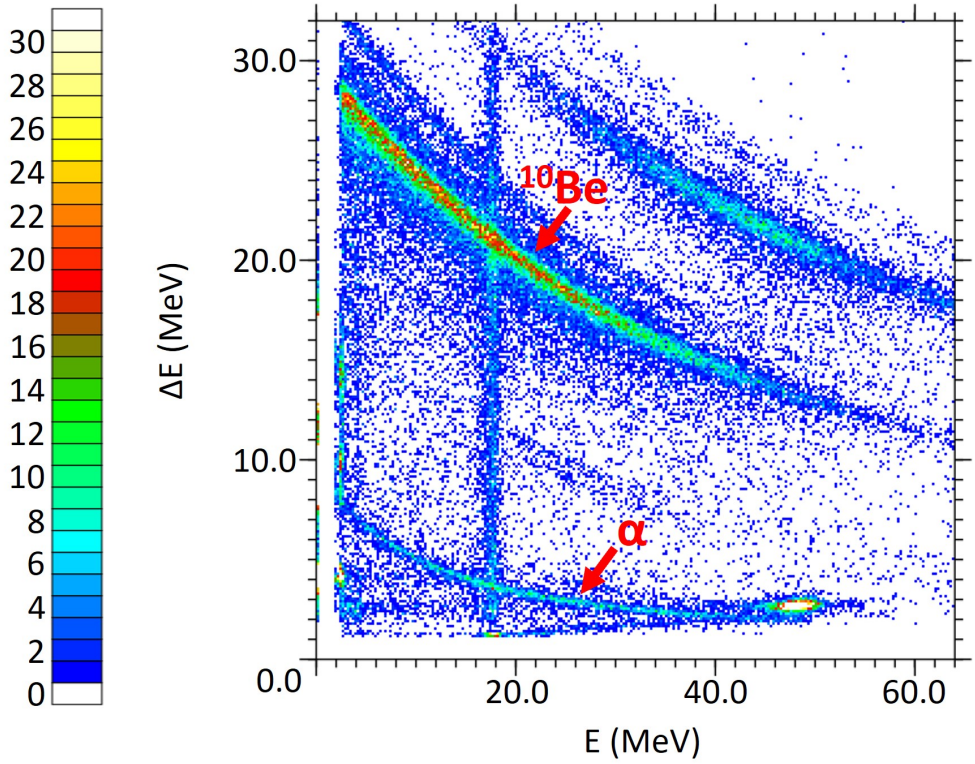


Figure 5.10: The energy loss of particles through a thin detector plotted against kinetic energy measured in a thick detector. These data were collected using the 65 µm degrader detector in conjunction with the E detector described in the text. The loci associated with the detection of ^{10}Be and α nuclei are labelled. These data were taken during a typical experimental run using the experimental set-up shown in Figure 5.5.

At a distance of 702 mm from the window, a zero-degree telescope consisting of a thin 20 µm (ΔE) and a 1000 µm (E) W1 Micron Semiconductor Ltd DSSD was positioned. The E detector was mounted 14 mm behind the ΔE, determined by measurement of the mounts and the PCB thickness using Vernier Calipers. As a charged particle travels through the ΔE detector, the kinetic energy of the particle decreases as ionisation occurs in the semiconductor crystal — for a sufficiently thin detector, the energy change per unit distance, $\frac{dE}{dx}$, can be well approximated by the mean stopping power for ions in silicon, $\langle\frac{dE}{dx}\rangle_{\mathrm{Si}}$, given by the non-relativistic Bethe formula

$$-\left\langle \frac{dE}{dx} \right\rangle_{\mathrm{Si}} = \frac{n_{\mathrm{Si}} z^2}{m_e v^2} \times \frac{e^4}{4\pi\epsilon_0^2} \times \ln\left(\frac{2m_e v^2}{I_{\mathrm{Si}}}\right). \tag{5.2}$$

Here, m_e is the electron mass, n_{Si} is the electron number density of silicon and I_{Si} is the mean ionisation potential of silicon. Thus, the only values that vary based on the properties of the incoming particle are z and v, the charge and velocity of the incident particle, respectively. As equation 5.2 is proportional to the reciprocal of v^2, the energy loss for a particle (for a given mass, m) is inversely proportional to the kinetic energy as, in the non-relativistic limit, $E = \frac{1}{2}mv^2$. Typically, the particle will have sufficient remaining kinetic energy to pass through the volume of the ΔE detector and pass into the E detector, hence the kinetic energy of the particle can be measured. Thus, by plotting the energy loss of the particle as a function of the total kinetic energy, species can be distinguished due to the mass and charge dependence of this relationship. An example of this form of particle identification is shown in figure 5.10.

5.3.1 Electronics

The signals from these detectors were output along a typical nuclear electronics chain. The charge pulses from the detectors were each input into a Mesytec MPR-32-Series preamplifier [75] followed by a CAEN N568B 16 channel spectroscopy amplifier [76]. These analogue signals were digitised through use of CAEN V785 32 Channel Peak Sensing ADCs [78], allowing the data to be processed by the software MIDAS [79]. For more detail on the function of these modules, see section 3.1.2.4. The ADCs were gated through use of trigger logic, summarised in figure 5.11, the result of which was a 5 µs gate output.

The detectors were calibrated using a triple α source, with an example spectrum shown previously in figure 3.19. The resolution of the detectors varied drastically, and thus

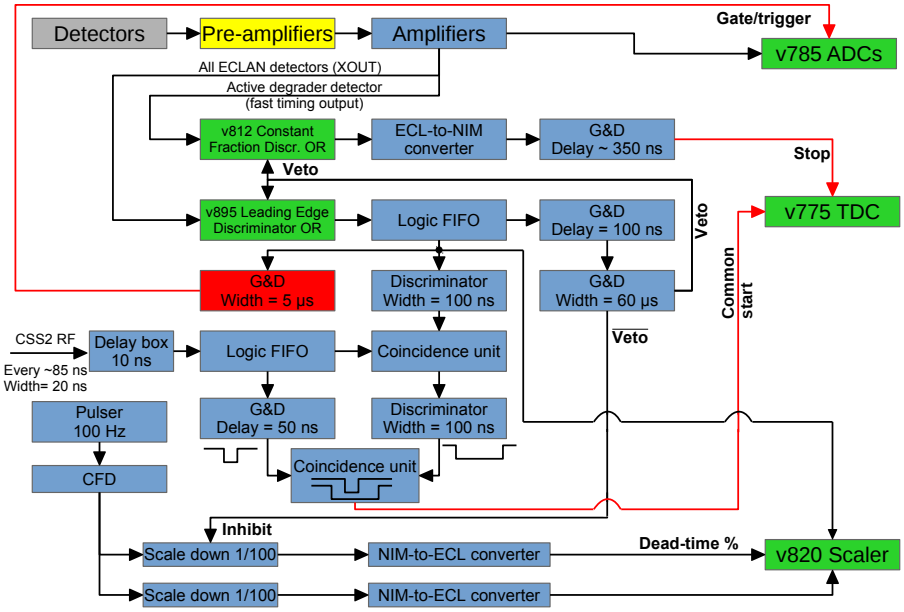


Figure 5.11: A summary of the trigger logic used in the current work to gate the ADCs and TDC.

a mixture of three and six peaks (the latter including the strongest fine-structure features of the α-particle peaks) were fitted to the data. The 20 µm ΔE detector posed a problem, however, as even at around 5 MeV the α-particles are able to pass through the crystal without stopping, thus preventing a total measurement of the kinetic energy. As such, the thickness profile for the ΔE detector was obtained in order to calculate the expected energy loss of α-particles through the detector. This calculation was done using the code DEDX [96].

Time-of-flight measurements were possible through use of a CAEN V775 16 channel Time-to-Digital Converter (TDC) [125], which was started by the RF from CSS2 and stopped by the output signal from the front strips of the 1000 µm degrader. The stop signal was passed through the fast timing output of the amplifier into a CAEN V812 16 channel Constant Fraction Discriminator (CFD), from which a gate was produced through use of a Lecroy 222

dual gate generator [83] with a delay of approximately 350 ns. By plotting the Energy of a detection in the degrader against time elapsed between the start and stop signals input into the TDC, another form of particle identification was possible. An example of this is shown in figure 5.12.

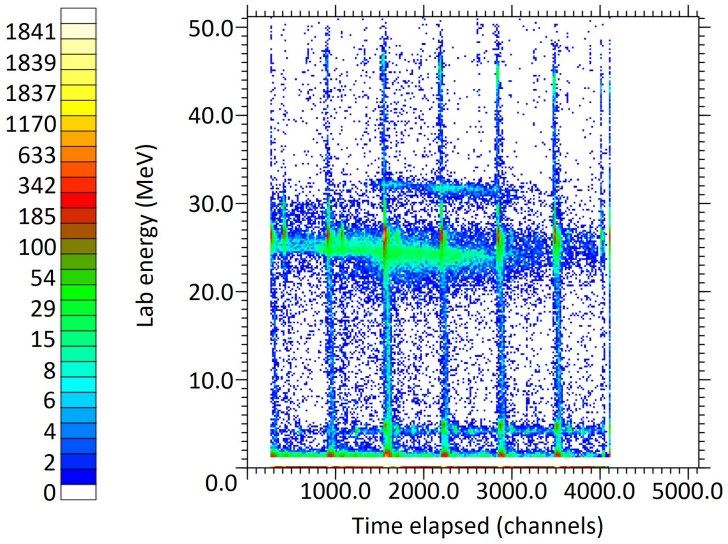


Figure 5.12: An example of the particle identification technique using the measured energy of a particle against TOF. Vertical lines can be seen, corresponding to the beam repetition from CSS2.

5.3.2 Degrader thickness

As the 65 µm active degrader was required to measure the beam energy in order to improve experimental resolution, a thickness profile was needed in order to accurately establish the relationship between energy loss through this degrader and incident beam energy. In order to do this, a measurement was performed at the Birmingham MC40 cyclotron [126] in which a ^{4}He beam of ≈12.3 MeV was incident on a 90 µg/cm^{2} natural gold (^{197}Au) foil. By measuring elastic scattering of the beam off the the foil, for which the product energy at a given angle is well-known, the amount of energy loss through a strip in the 65 µm DSSD could be utilised to

determine the thickness of the strip. The 65 µm DSSD was placed in a telescope orientation in conjunction with a 1000 µm DSSD, in-plane at an angle of $-32.5°$ relative to the beam direction, with the thin and thick detectors placed at distances of 138 mm and 153 mm from the foil respectively. Additionally, a 500 µm DSSD was placed at an angle of 32.5°, slightly further away (at a distance of 170 mm) i.e. on the opposite side of the beam to the telescope. The purpose of this detector was to enable a better measurement of the beam energy — though all of the detectors used were calibrated using a triple α source, the total energy of the beam deposited in the telescope was subject to the resolution of both the thin and thick detector thus producing a less clear result. Particles detected by the telescope also had to travel through three dead layers (two from the thin detector, one from the thick detector) as opposed to one dead layer for detection by the 500 µm DSSD.

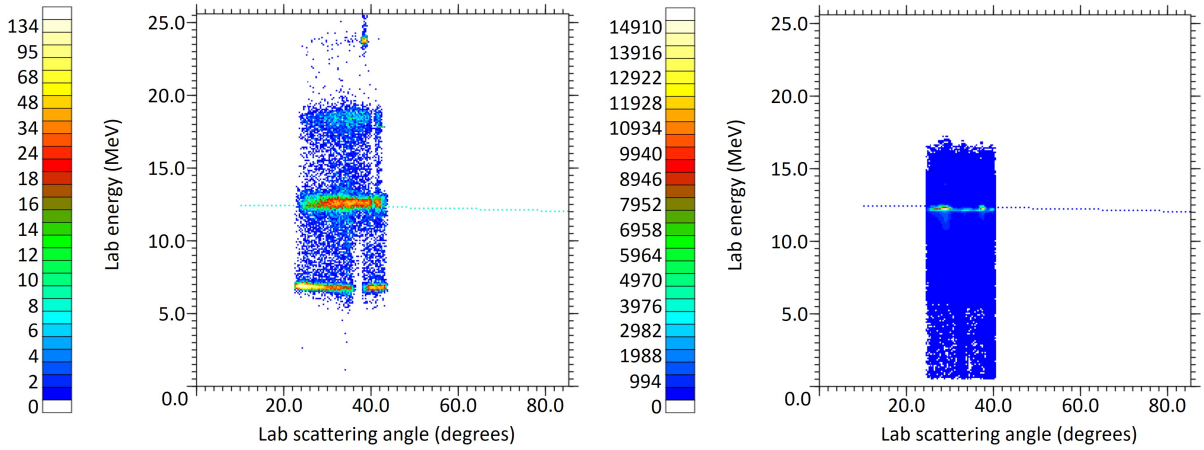


Figure 5.13: Measured energy against scattering angle for the telescope (a) and 500 µm DSSD (b). The kinematic lines corresponding to the elastic scattering of ^{4}He on ^{197}Au are plotted, and can be seen to agree well with the data.

Figure 5.13 shows a plot of measured lab energy for detected particles against scattering angle in the lab frame: figure 5.13(a) contains the energy-angle data for the telescope, in which the energy plotted is the sum of the energies measured by both stages of the telescope; figure 5.13(b) shows the data obtained for the 500 µm detector. Also plotted in both fig-

ures 5.13(a) and (b) is the kinematic line associated with an α particle scattered from ^{197}Au. This can be seen to agree well with the observable features in the data — however, the feature present in (a) can be seen to be much wider than that in (b) as predicted. Thus, the line in figures 5.13(b) was used to establish the beam energy. The energies of nuclei detected by the detectors were corrected for energy-loss through the gold foil, through use of the code DEDX [96], assuming the average interaction occurred at the centre of the thickness of the target. Once this had been achieved, the thickness profile of the detector was determined by calculation, again using DEDX.

5.4 Excitation function determination

In order to produce an excitation function for the compound nucleus from the detected energies and positions of charged particles incident on the various detectors described in section 5.3, a conversion between the lab frame (in which the particles are measured) and the centre-of-mass (COM) frame can be used. Figure 5.14 shows a generic interaction between a beam nucleus, B, and a target nucleus, A, to produce two product nuclei, C and D, for both the lab frame and the COM frame. In the lab frame, A travels towards B (which is at rest) with energy and mass E_A and m_A, and the two product nuclei are focused in the beam direction due to conservation of momentum. In the COM frame, A and B travel towards each other with kinetic energies E'_B and E'_A — the product nuclei instead travel at angles of α and β respectively, where $\alpha + \beta = 180°$.

In the reaction of interest, an intermediate compound nucleus is formed between these initial and final states. The excitation energy of this compound nucleus, E_x, can be calculated through the expression

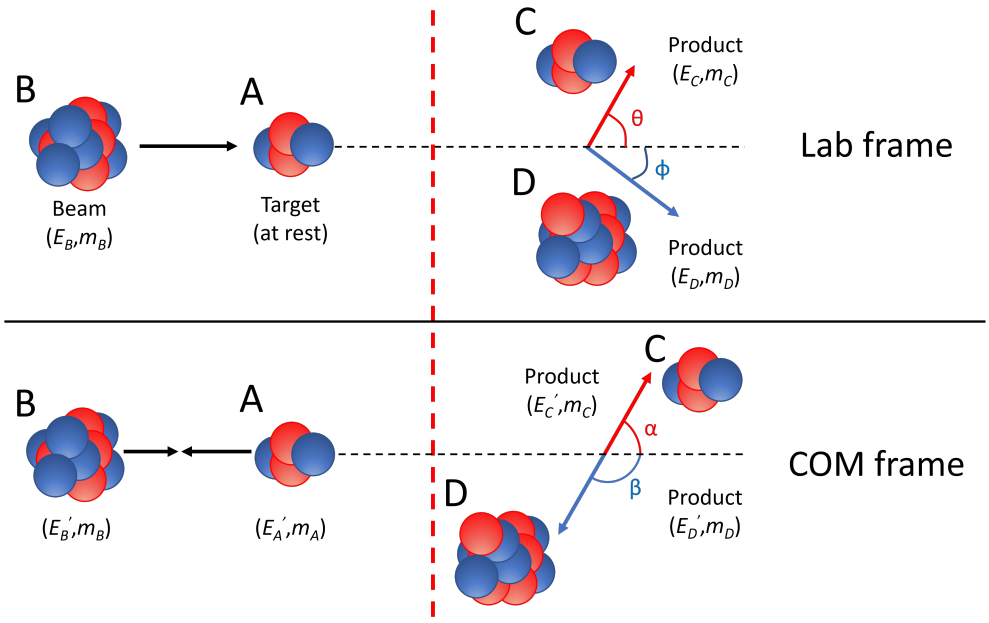


Figure 5.14: A comparison of a typical nuclear reaction ($A + B \rightarrow C + D$) in the lab frame and in the centre-of-mass frame.

$$E_x = \frac{m_A}{m_A + m_B} E_B + Q_{\text{compound}}, \tag{5.3}$$

where Q_{compound} is the Q-value associated with the formation of the compound nucleus. Using D as an example, the energy of a product nucleus in the lab frame, E_D, can also be related to its corresponding velocity in the COM frame, $v_D' = \sqrt{\frac{2E_D'}{m_D}}$, and the velocity of the COM, $V_{\text{COM}} = \frac{m_C v_C + m_D v_D}{m_C + m_D}$ [42], by

$$E_D = E_B \frac{m_B m_D}{(m_A + m_B)^2} \left(\left(\frac{V_{\text{COM}}}{v_D'} \right)^4 + 2 \left(\frac{V_{\text{COM}}}{v_D'} \right)^3 \cos\alpha + \left(\frac{V_{\text{COM}}}{v_D'} \right)^2 \right). \tag{5.4}$$

In order to determine the value of α, the initial interaction position must be determined. This can be done by calculating different values of α and β for given interaction positions and determining which position corresponds closest to $\alpha + \beta = 180°$.

5.5 Monte-Carlo simulation

Monte-Carlo simulations were performed using REX (Resonant EXcitation simulation), an in-house package used by the nuclear structure group at the University of Birmingham. A previous version of this code (REX 6) is described in detail in Ref. [124], while the Monte-Carlo simulations described here were produced using REX 8. The changes from REX 6 to REX 8, some of which are mentioned later in the text, including the addition of

- an excitation function option, defined by a Rutherford scattering energy dependence,
- the ability to simulate compound gas targets, in which the average mass and charge of the constituent elements are used for energy loss, angular straggling and energy straggling,
- calculation of time-of-flight for the beam and product nuclei, which can be output following each event,
- solid target options (previously only gas targets were able to be simulated),
- the ability to simulate break-up reactions following a two-body interaction,
- the option for active degraders (detectors that double as degraders),
- the ability to calculate energy-loss using a user-inputted file (of energy in MeV against energy-loss in MeVcm^2/mg), rather than the default DEDX code.

REX requires a number of user inputs in order to generate Monte-Carlo data, which can be split into two following categories: inputs defining the reaction of interest and inputs defining the experimental set-up.

The reaction of interest is defined by the masses and charges of the reactants and products, as well as the total Q-value for the reaction. Products can be defined to undergo break-up reactions, again defined by the masses and charges of the fragments and Q-value of the break-up reaction. Compound nucleus formation reactions also require the Q-value for the compound nucleus formation stage as well as for the total reaction. Population of excited levels, particularly in the case of compound nucleus formation, is an important consideration. As well as allowing for individual levels to be defined in the simulation, with a Gaussian distribution defined by centroid, FWHM and intensity for each state, the option for a uniform distribution of excitation energies is also available; useful for examining continuum effects as well as investigating ranges of excitation energy that could be expected to be seen for a given experimental set-up. The effect of the background from Rutherford scattering, inversely proportional to the square of the beam energy as previously shown in equation 2.12, can also be simulated. Angular distributions for each excitation can also be defined, returning the distribution of the relevant Legendre polynomial for a given user-defined value of angular momentum. Excitation energies, defined by centroid energy and width, can also be assigned to product nuclei.

The experimental set-up parameters require definition of a target, either solid or gas. The material is then defined by the density (at standard temperature and pressure for a gas target), as well as the relative amounts of different atoms in the material (defined by mass and charge). For gas targets, the pressure must also be provided. A user-defined step-size for particles travelling through the gas is used to calculate kinematics during generation of the data. A circular window for gas target experiments can be simulated, defined by radius, material and thickness.

Beam degraders, either active (in the form of a DSSD) or inactive, can be simulated both inside and outside of the reaction chamber. All DSSDs (including active degraders) are able to be simulated with a range of thicknesses, active areas, energy thresholds and

energy resolutions. Degrader detectors, unlike DSSDs positioned in the chamber to detect fragments, only require the distance from the window, as these sit along the beam-axis; DSSDs positioned in the chamber are also defined by the relevant polar and azimuthal angles. Lampshade arrays, defined with the same geometry described in section 5.3, can be placed within the simulation. Much like the degrader detectors, these arrays sit centrally along the beam axis (albeit inside the chamber) and hence only the position relative to the window is needed.

Once all of the inputs have been entered, REX generates a scattering event with a random excitation energy (bound by the input parameters). The position relative to the window, direction of travel from the beam axis and energy of the beam nucleus are then calculated as the beam travels through the degraders and gas volume for each step (the frequency of which is defined by the inputted step-size). In order to do this accurately, energy-loss through the various materials is calculated through use of DEDX. Energy and angular straggling effects are also calculated, smearing both the energy and direction of the beam randomly (based on the parameters of the material the beam is travelling through) for each event. Once the kinetic energy of the beam has dropped to that of the initially selected excitation energy, the previously defined input two-body reaction (or reactions, in the case of break-up events) occurs. As REX simulates reactions as a series of two-body interactions, the energies and angles of these product nuclei are randomly selected as confined by non-relativistic two-body kinematics (see Appendix A for more details), though this may be weighted by a corresponding Legendre polynomial if relevant. The resulting product nuclei are then tracked similarly to the beam at each step, until they are either incident upon an area defined as an active detector (detected), or stopped in the gas (undetected). Product nuclei can also be considered undetected if they reach the edge of the defined simulation volume, if they are incident on the inactive region of a detector (e.g. the PCB around the detectors), if they do not have sufficient energy upon reaching the active area of a detector

to be considered an event (below the set energy threshold, once energy resolution effects have been calculated), or if they have sufficient energy to pass through the detector (such as in the case of a ΔE detector). Each detector can also be specified to detect only species of certain types (for looking at specific kinematic features), so events can also be rejected based on this condition. Once a certain number of good events (defined by the number of required detections) have been generated, the simulation ceases. The 'good' events are output with the energy and position at detection (defined by the Cartesian in-plane and out-of-plane angles), enabling equivalent analysis as performed on experimental data. Also included in the output are the mass and particle ID of the particle, enabling more specific Monte-Carlo analysis not possible within the real data.

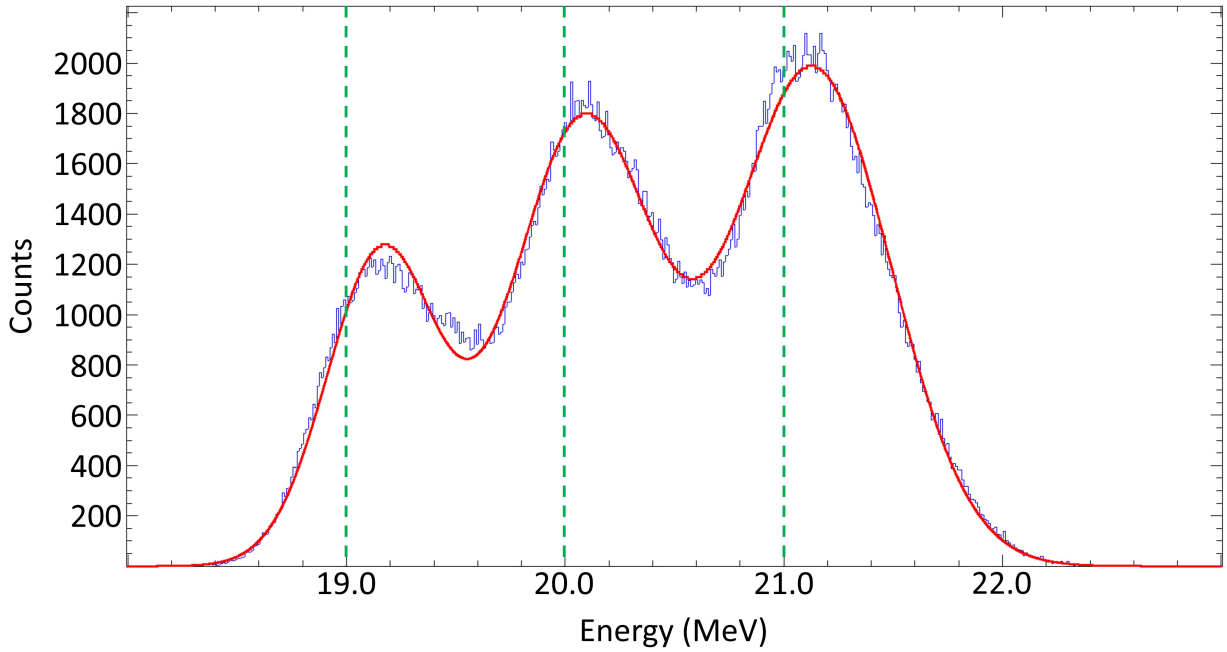


Figure 5.15: The excitation function generated for all hits in the lampshade arrays for the ^{10}Be+α exit channel. Excitation energies at 19 MeV, 20 MeV and 21 MeV were simulated, shown by the green lines — it is clear the reconstructed excitation function does not reproduce these energies accurately. See text for details.

Monte-Carlo events were generated in which ^{10}Be and α events were produced follow-

ing the formation of a ^{14}C nucleus, in order to establish the resolution and accuracy with which excitation energies could be reconstructed. Three excitation energies, delta functions situated at 19 MeV, 10 MeV and 21 MeV, were simulated to this end. Reconstruction of these excitation energies utilising detection of both products in any of the lampshade detectors is shown in figure 5.15. The green vertical lines denote the positions of the various excitation energies, while the red line overlaid on the data shows a fit using three Gaussian distributions. It is clear from comparison of the fit to the green lines that the centroid energies are incorrectly reconstructed in this case, with the reconstructed excitation energy between 100 $\rightarrow$ 200 keV too large.

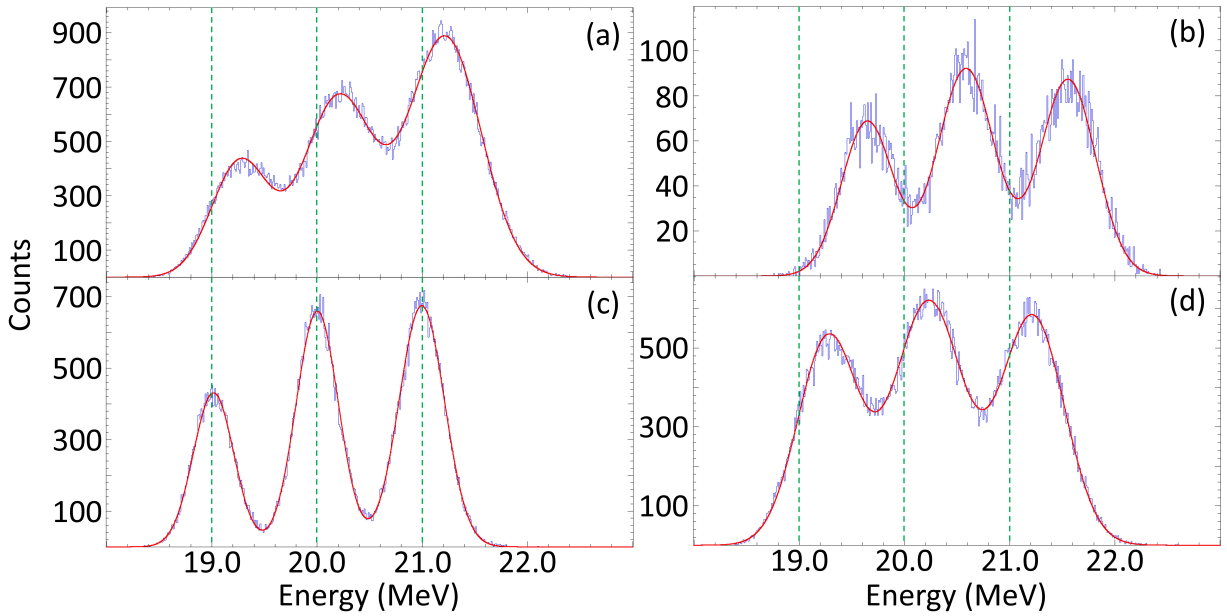


Figure 5.16: A comparison of the different excitation functions produced using different hit patterns for the ^{10}Be+α exit channel. Details of each subfigure are given in the text.

In order to investigate this, the individual hit patterns for each lampshade were investigated. Figure 5.16 shows the results of this investigation, with the hit patterns as follows: figure 5.16(a) shows events in which both the ^{10}Be and α were detected in lampshade 1; figure 5.16(b) shows events in which the ^{10}Be nucleus was detected in lampshade 1 and the

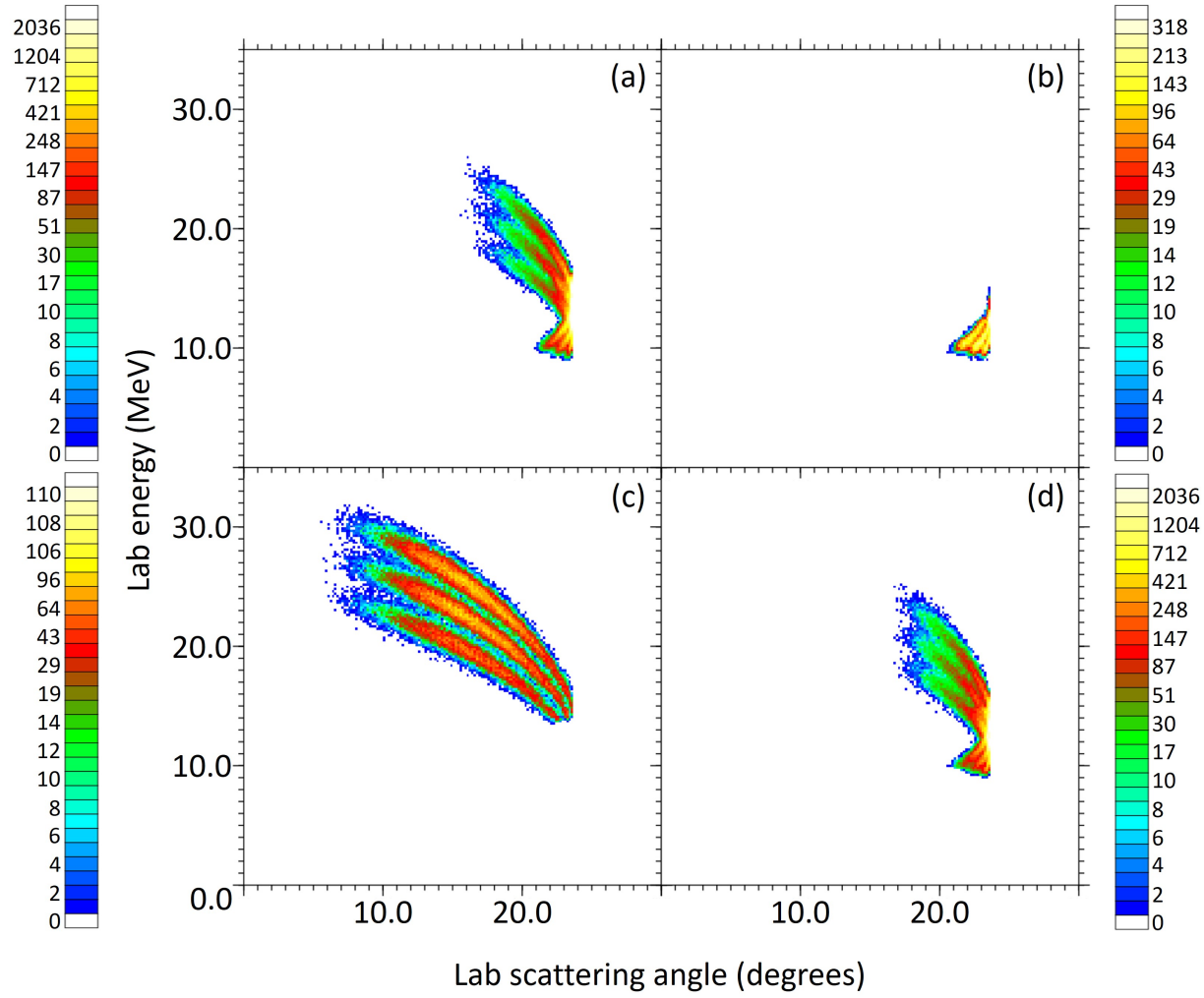
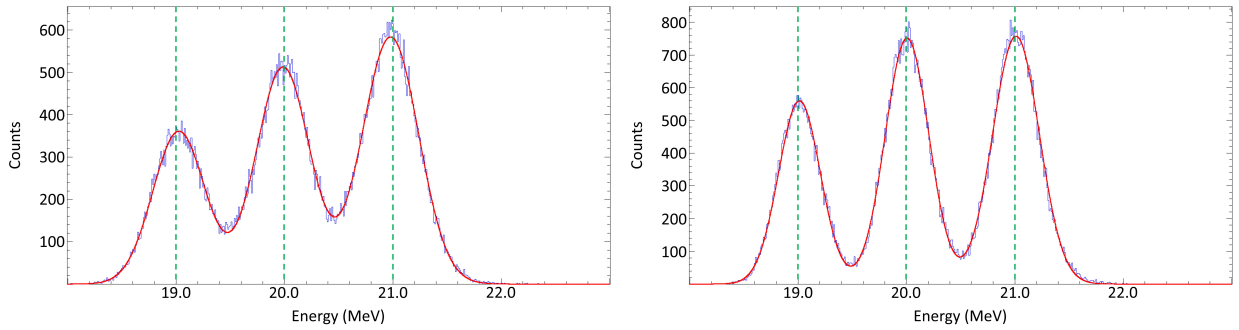


Figure 5.17: Kinematic features generated for detected ^{10}Be products. The individual sub-figures are described in the text.

α-particle was detected in lampshade 2; figure 5.16(c) shows events in which the ^{10}Be nucleus was detected in lampshade 2 and the α-particle was detected in lampshade 1; figure 5.16(d) shows events in which both the ^{10}Be and α were detected in lampshade 2. In all but figure 5.16(c), it is clear that the excitation energies are reconstructed too high to varying degrees. However, the reconstructed excitation energies in figure 5.16(c) match well to the input excitation energies. This was explained through the kinematic distributions for each case, shown in figure 5.17.

Figure 5.17 shows the kinematic features (including experimental resolution effects) for the ^{10}Be product for cases in which the particle is detected. Here, subfigures (a) $\rightarrow$ (d) are using the same data as described for the subfigures in figure 5.16. Due to the nature of inverse kinematics, multiple energy solutions exist for a given angle — this, however, results in a crossover point in the energy-angle distributions for which a large change in energy is experienced for small change in angle, leading to a relatively large uncertainty in angle (resulting in a large uncertainty on the position of the interaction). As can be seen from figure 5.17, this crossing over point was visible in all distributions other than that in figure 5.17(c) (in which the ^{10}Be is detected in lampshade 2 and the α is detected in lampshade 1), providing an explanation for why this particular hit configuration provided accurate excitation reconstruction.



(a) (b)

Figure 5.18: Excitation functions generated through two different methods of determining the interaction position: inclusion of an offset based on position of the beam on the degrader (a) and averaged across several interaction positions, detailed in the text (b). The centroids extracted from both methods were reasonable, though the widths of the peaks are visibly larger in (a) relative to (b).

While only using data in which the ^{10}Be and α were detected in this specific configuration is possible, this would severely limit the available statistics and thus increase the uncertainties on extracted quantities. In reconstruction of these excitation energies, the an-

gles α and β (as shown in figure 5.14) were calculated for various positions along the beam axis. The corresponding position for which $\alpha + \beta$ was closest to 180° could then be assumed to be the interaction position of the beam and target. However, this method was the one used to produce figure 5.15 and hence did not work at the crossover point. As such, an offset in the beam axis for an interaction (done on a case-by-case basis, due to the large beam-spot size observed on the degraders, in order to correct from the distance from the centre of the degrader) was included, as if the interaction did not occur along the beam-axis as a result of the beam-spot size then the reconstructed excitation energies could potentially be smeared out. While this succeeded in increasing the fidelity of the reconstruction in terms of centroid, the resolution of the reconstruction observed was still larger than ideal (567(4) keV, 579(5) keV and 610(3) keV for the widths of the three reconstructed excitation energy peaks, respectively). The data and corresponding fit are shown in figure 5.18(a). Thus, some more stringent conditions were placed on the data in order to identify the correct interaction position. Any gas steps in which the difference between the expected value and the calculated/measured value for several different experimental observables was below a certain threshold tolerance (weighted for each value, depending on the magnitude) were determined. Thus, the interaction position was taken as the average of these possible positions and the excitation energy thus calculated, an example spectrum of which is shown in figure 5.18(b). The observables used were

- the difference between $\alpha + \beta$ and 180°,
- the difference between the predicted energy of each product (α and ^{10}Be) and the measured value,
- the difference between the predicted scattering angle of each product and the measured value.

By calculating the average possible interaction position in this way, the resolution consid-

erably improved, with the widths of the excitation features determined to be 455(2) keV, 475(2) keV and 508(2) keV respectively, a decrease of around 100 keV from the features in figure 5.18(a). The fidelity of the fitted excitation energies to the known centroid values was also good, with values of 19.013(1) MeV, 20.006(1) MeV and 21.011(1) MeV respectively, where the uncertainties provided are simply those associated with the fitting.

5.6 Summary

The motivations and a description of the experimental technique have been discussed for the ongoing analysis of the ^{14}C and ^{16}C nuclei using fragmentation and TTIK techniques to measure excitation functions. At present, the data have been calibrated through use of the triple-α data and analysis code has been prepared in order to attempt to reconstruct events, utilising the method of determining the interaction position of the beam and target (via the average position along the beam-axis for a series of acceptable possible positions) as described with the Monte-Carlo data. Initial investigation of the experimental data suggests that an excitation function will be able to be produced with reasonable resolution, once cleaning of events using the telescope and degraders have been fully implemented.

Chapter 6

Conclusions

Investigations into potential cluster bands in ^{18}O were performed, utilising high-resolution particle spectroscopy, through both the Q3D magnetic spectrograph at the Maier-Leibnitz Laboratory and the Birmingham large-angular-coverage DSSD array, in conjunction with extensive Monte-Carlo simulations to determine branching ratios for a number of decay paths. The decay paths investigated were γ-decay, α-decay, n-decay and $2n$-decay, with consideration of the population of excited states in the daughter nuclei in order to provide more accurate branching ratios — the only energetically available decay paths to which the employed method was not sensitive were those of β-decay and electron capture, though these are typically suppressed well above particle-decay thresholds due to the comparatively long half-lives of these decay modes. Methods to determine branching ratios for γ-decay and n-decay were discussed and employed without the use of γ- or n-spectroscopy.

States between 7 $\rightarrow$ 16 MeV were populated through use of the ^{12}C(^{7}Li,p)^{18}O* reaction ($E_{\mathrm{Li}} = 44$ MeV) reaction, and the values for the individual branches were mostly in good agreement with previous literature values, such as those presented in Refs. [103], [104], [105] and [106]. Many of the branching ratios determined here were previously unmeasured,

though the agreement of previously measured branching ratios with the literature for other states gives confidence in these values. The value of θ_α^2 was calculated, using the measured excitation energy and widths, for states with known or proposed values of J^π in the literature. For cases in which the measured width of the state was too small to be determined due to the experimental resolution, an upper limit was calculated based on the uncertainty of the fit — an upper limit of θ_α^2 was then determined, unless an appropriate literature value of the width was available.

For states in the tentative cluster bands, only two were found to be consistent with cluster structure: the 11.696(1) MeV proposed $J^\pi = 6^+$ member of the $K^\pi = 0_2^+$ band and the 12.557(2) proposed $J^\pi = 6^+$ member of the $K^\pi = 0_4^+$ band. All other values of θ_α^2 were found to be inconsistent with cluster structure, thus refuting the existence of these bands with the tentatively assigned members.

Another investigation, exploring potential nuclear molecular structures in the ^{14}C and ^{16}C systems, has been performed. This was done utilising resonant scattering through the thick target inverse kinematics approach, with ^{10}Be and ^{12}Be secondary beams produced through high-energy fragmentation of a 900 MeV ^{18}O primary beam incident on a $\approx$2 mm thick natural Be target. These secondary beams were incident on a thick α-gas target, causing interactions along the beam axis. The products of these interactions could subsequently be detected by a variety of silicon strip detectors placed in the reaction chamber. Monte-Carlo simulations have been performed, investigating the effect of various methods of reconstructing the interaction position between the beam and target nuclei on the measured excitation centroid energy and experimental resolution, allowing analysis to progress to the next stage.

6.1 Future work

States that lie just above the α-decay threshold in ^{18}O ($S_\alpha = 6.227$ MeV) are typically relatively long-lived, partly due to the lack of energetically available decay paths. This increase in lifetime corresponds directly to a decrease in the natural linewidth, Γ, of the state. In order to better identify the tendency towards clustering for several of the states investigated in the current work, measurement of these natural line-widths could be performed. In the case of the 7.117 MeV state, the magnitude of this value is potentially too small to measure as a width, though lifetime measurements for the γ-decay, β-decay (if present) and α-decay branches could be performed with more ease to determine each of Γ_γ, Γ_β and Γ_α through the Heisenberg Uncertainty Principle relationship. These could then be used to evaluate Γ for the system, enabling a more certain evaluation on the tendency towards cluster structure in this state.

As mentioned previously in section 4.3, the existence of two clustered states with the same J^π (with no other clustered states observed) is reminiscent of the fragmented α-clustering phenomenon, in which coupling of a cluster state to a non-cluster state causes a series of excitations to form nearby to the original cluster state, each with the same J^π as one another. This has been well observed in light-to-medium mass nuclei [108, 127, 128]. Further fragmented states from this coupling could exist nearby, which could aid in extracting information about the original cluster state (if such a state existed). The most probable region for these to sit is between 11.9 $\rightarrow$ 12.4 MeV, where several states have previously been measured by von Oertzen et al. [56] utilising the same reaction as the current work. An experiment similar to the current work in which the values of $\Gamma_\alpha/\Gamma_{\text{tot}}$ and Γ_{tot} for states in the region could be determined may yield a clue to whether any potential fragmented structure exists. Definitive spin assignments for many states in the excitation region investigated would also allow comparison between states with similar J^π

values, enabling a more conclusive determination of whether fragmented clustering is present in this nucleus.

With regards to the analysis of the ^{14}C and ^{16}C data, excitation functions must be generated through identification of events in which a ^{10}Be and α product are detected from the same interaction. The data can be cleaned up to provide this, using vetoes provided by the zero degree telescope and better determination of the inital beam energy and position through use of the degrader detectors. The excitation functions generated will be efficiency corrected, compensating for effects caused by detector positioning. These can then be fully normalised, providing a value for the differential cross-section as a function of energy for different scattering angles. Using the R-matrix code AZURE2 [129], observables such as centroid, width and J^π for the resonances populated will be determined and compared with previous data to check for consistency and legitimacy in the measurement, particularly for the previously studied ^{14}C system. The tendency towards clustering for these resonances can then be determined, calculating θ_α^2 in each case — from these values, cluster states with appropriate values of J^π to form a rotational band may or may not be observed, in an effort to identify structures that could be nuclear-molecule Hoyle-state analogues.

Appendix A

Derivation of two-body non-relativistic kinematic solution

Consider the non-relativistic two-body case, displayed in figure A.1, in which a beam nucleus, B, of known energy, E_B, interacts with a target nucleus, A, which is at rest, to produce two product nuclei, C and D. The product nuclei have energies E_C and E_D respectively, and the masses of the the nuclei are known. The nucleus C is left in an excited state, with an

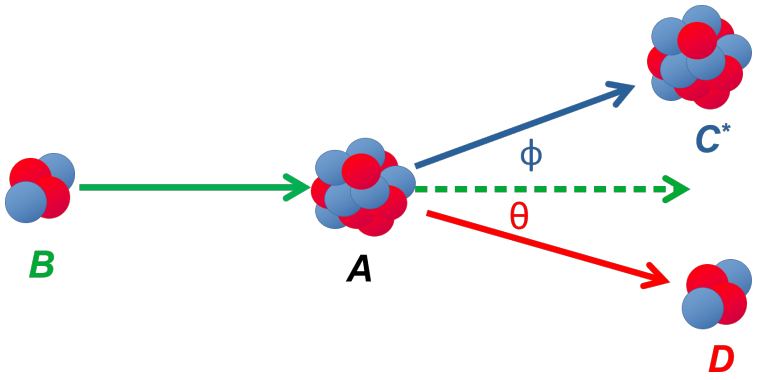


Figure A.1: A generic two-body nuclear interaction, in which nuclei C and D are produced at angles ϕ and θ from the beam axis from the reaction of beam A and target B.

excitation energy, E_x. Choosing the plane in which the reaction occurs, C and D travel at angles ϕ and θ from the beam axis respectively. The Q-value of the reaction is determined by the difference in nuclear masses, m, before and after the reaction, as described by

$$Q = (\sum_{i=A,B} m_i - \sum_{f=C,D} m_f)c^2, \tag{A.1}$$

where c is the speed of light. Conservation of momentum, P, along the beam axis, momentum along the in-plane axis perpendicular to the beam axis, and energy can be employed to yield the expressions

$$E_B + Q = E_C + E_D + E_x, \tag{A.2}$$

$$P_B = P_D \cos\theta + P_C \cos\phi \quad \text{and} \tag{A.3}$$

$$P_C \sin\phi = P_D \sin\theta. \tag{A.4}$$

Rearranging and squaring equation A.3 leads to equation A.5,

$$P_C^2 \cos^2\phi = (P_B - P_D \cos\theta)^2. \tag{A.5}$$

Squaring equation A.4 gives

$$P_C^2 \sin^2\phi = P_D^2 \sin^2\theta, \tag{A.6}$$

which, through use of the trigonometric identity $\sin^2\theta = 1 - \cos^2\theta$, yields

$$P_C^2 \cos^2\phi = P_C^2 - P_D^2 \sin^2\theta. \tag{A.7}$$

Both equation A.5 and equation A.7 can be equated and rearranged, to produce the expression

$$P_C^2 = P_B^2 + P_D^2 \cos^2\theta + P_D^2 \sin^2\theta - 2P_B P_D \cos\theta, \tag{A.8}$$

which can again be simplified using the identity $P_D \sin^2\theta + P_D^2 \cos^2\theta = P_D^2$. The momentum of a non-relativistic particle can be related to its mass and energy by $\sqrt{2mE}$, transforming equation A.8 into

$$2m_C E_C = 2m_B E_B + 2m_D E_D - 4\sqrt{m_B m_D E_B E_D}\cos\theta, \tag{A.9}$$

which can be further manipulated by substituting in equation A.2. Thus,

$$\frac{m_C}{m_B}(E_B + Q - E_D - E_x) = E_B + \frac{m_D}{m_B}E_D - 2\sqrt{\frac{m_D}{m_B}E_B E_D}\cos\theta \tag{A.10}$$

by dividing through by $2m_B$. This can be expressed in the form $Ax^2 + Bx + C = 0$, as

$$E_D\left(\frac{m_C}{m_B} + \frac{m_D}{m_B}\right) - 2\sqrt{\frac{m_D}{m_B}E_B}\cos\theta\sqrt{E_D} + E_B\left(1 - \frac{m_C}{m_B}\right) - \frac{m_C}{m_B}(Q - E_x) = 0, \tag{A.11}$$

where $x = \sqrt{E_D}$, as all the other values are known. Hence, through solving the quadratic, the energy of particle D, as a function of the angle θ, can be shown to be given by

$$E_D = \left(\frac{-2\sqrt{\frac{m_D}{m_B}E_B}\cos\theta \pm \sqrt{4\frac{m_D}{m_B}E_B\cos^2\theta - 4\left(\frac{m_C}{m_B} + \frac{m_D}{m_B}\right)\left(E_B\left(1 - \frac{m_C}{m_B}\right) - \frac{m_C}{m_B}(Q - E_x)\right)}}{2\left(\frac{m_C}{m_B} + \frac{m_D}{m_B}\right)}\right)^2, \tag{A.12}$$

where the positive and negative roots provide the first and second kinematic solutions. If there is no second kinematic solution, the negative root yields the positive root, offset by a phase difference of 180°. The energy of particle C can be determined through rearrangement of equation A.2, though this will be in terms of θ rather than ϕ, the angle of scattering for particle C. To convert from θ to ϕ, equation A.4 can be rearranged to provide the expression

$$\phi = \arcsin\left(\sqrt{\frac{2m_D E_D}{2m_C E_C}}\sin\theta\right), \tag{A.13}$$

from which it is trivial to calculate ϕ, as E_C and E_D are known. Figure A.2 shows the example for a 44.0 MeV ^{7}Li beam nucleus (B and D) incident on a ^{12}C target nucleus (A and C), scattering elastically — only the first kinematic solution is shown, as there is no second kinematic solution for this case. In figure A.2(a) and figure A.2(b), the energies E_C and E_D sum to 44.0 MeV for a given angle, as expected. The range of ϕ is $-90° < \phi < 90°$, again as expected, as it is not kinematically possible for the product ^{12}C to back-scatter. Figure A.2(d) shows that if the ^{7}Li were to perfectly back-scatter ($\theta = 180°$), then the corresponding ^{12}C would move in the opposite direction along the beam axis ($\phi = 0°$), which is logical in order to conserve momentum. The opposite case, in which $\theta = 0°$, results in ϕ being undefined, as the ^{7}Li would have to have not interacted with the ^{12}C nucleus and passed straight through it — the two-body non-relativistic kinematics calculated here sadly do not have the scope to predict quantum tunnelling, as the corresponding energy of the ^{7}Li in this case remains at the beam energy, 44.0 MeV.

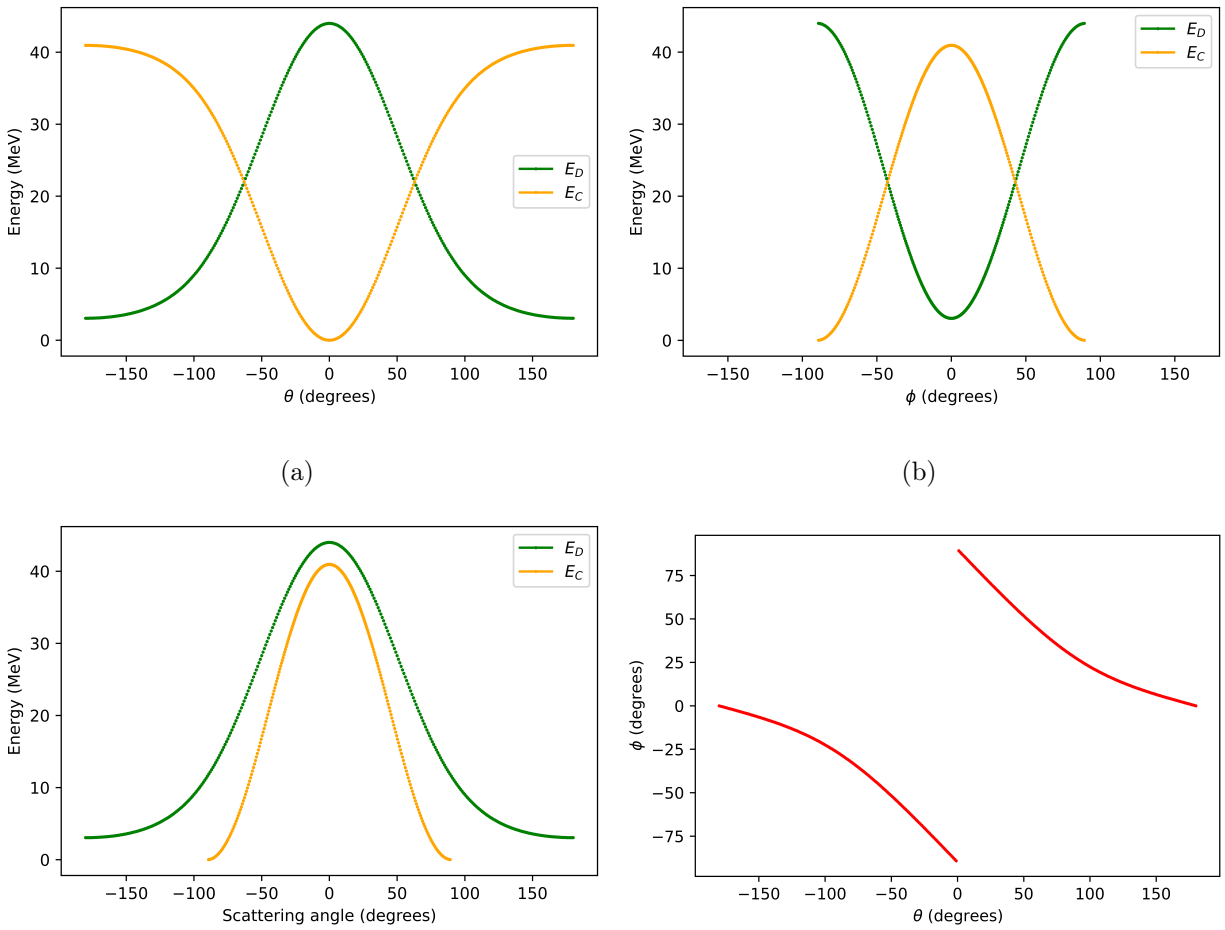


Figure A.2: Plots for the ^{12}C(^{7}Li,^{7}Li)^{12}C ($E_B = 44.0$ MeV) case. The energies E_C and E_D are plotted against θ (a), against ϕ (b) and against the corresponding scattering angle for each nucleus (θ for D, ϕ for C) (c). A plot of θ against ϕ is also provided (d).

References

[1] D. Mendeleev. "Über die Beziehungen der Eigenschaften zu den Atomgewichten der Elemente". In: *Zeitschrift für Chemie* 12 (1869), pp. 405–406.

[2] E. Rutherford. "The scattering of α and β particles by matter and the structure of the atom". In: *The London, Edinburgh, and Dublin Philosophical Magazine and Journal of Science* 21.125 (1911), pp. 669–688. DOI: 10.1080/14786440508637080.

[3] J. Chadwick. "The existence of a neutron". In: *Proceedings of the Royal Society of London A* 136 (1932), pp. 692–708. DOI: 10.1098/rspa.1932.0112.

[4] G. Gamow. "Mass defect curve and nuclear constitution". In: *Proceedings of the Royal Society of London A* 126.803 (1930), pp. 632–644. DOI: https://doi.org/10.1098/rspa.1930.0032.

[5] N. Bohr and J. A. Wheeler. "The Mechanism of Nuclear Fission". In: *Physical Review* 56 (5 Sept. 1939), pp. 426–450. DOI: 10.1103/PhysRev.56.426.

[6] C. F. von Weizsäcker. "Zur Theorie der Kernmassen". In: *Zeitschrift für Physik* 96 (1935), pp. 431–458. DOI: https://doi.org/10.1007/BF01337700.

[7] W.J. Huang et al. "The AME 2020 atomic mass evaluation (I). Evaluation of input data, and adjustment procedures". In: *Chinese Physics C* 45.3 (Mar. 2021), p. 030002. DOI: 10.1088/1674-1137/abddb0.

[8] K.S. Krane. *Introductory Nuclear Physics*. John Wiley & Sons, 1987. Chap. 3,11. ISBN: 0-471-80553-X.

[9] M. G. Mayer. "On Closed Shells in Nuclei. II". In: *Physical Review* 75 (12 June 1949), pp. 1969–1970. DOI: 10.1103/PhysRev.75.1969.

[10] B. A. Brown. Lecture Notes in Nuclear Structure Physics, National Superconducting Cyclotron Laboratory and Department of Physics and Astronomy, Michigan State University. 2011. URL: https://people.nscl.msu.edu/~brown/reaction-codes/wspot/wspot-brown.pdf.

[11] E. Rutherford. "Uranium radiation and the electrical conduction produced by it". In: *The London, Edinburgh, and Dublin Philosophical Magazine and Journal of Science* 47.284 (1899), pp. 109–163. DOI: 10.1080/14786449908621245.

[12] E. Rutherford and T. Royds. "Spectrum of the Radium Emanation". In: *Nature* 78.2019 (July 1908), pp. 220–221. ISSN: 1476-4687. DOI: 10.1038/078220c0.

[13] L. R. Hafstad and E. Teller. "The Alpha-Particle Model of the Nucleus". In: *Physical Review* 54 (9 Nov. 1938), pp. 681–692. DOI: 10.1103/PhysRev.54.681.

[14] B.R. Fulton. "Clustering in nuclei: Nuclear chains, nuclear molecules and other exotic states of nuclear matter". In: *Contemporary Physics* 40.5 (1999), pp. 299–311. DOI: 10.1080/001075199181378.

[15] W. von Oertzen, M. Freer, and Y. Kanada-En'yo. "Nuclear clusters and nuclear molecules". In: *Physics Reports* 432.2 (2006), pp. 43–113. DOI: 10.1016/j.physrep.2006.07.001.

[16] F. Hoyle. "On Nuclear Reactions Occuring in Very Hot STARS. I. the Synthesis of Elements from Carbon to Nickel." In: *Astrophysical Journal Supplement* (1954).

[17] C. W. Cook et al. "^{12}B, ^{12}C, and the Red Giants". In: *Physical Review* 107 (2 July 1957), pp. 508–515. DOI: 10.1103/PhysRev.107.508.

[18] F. Hoyle et al. "A state in C-12 predicted from astrophysical evidence". In: *Physical Review* 92 (1095c 1953).

[19] O. Kirsebom. "Viewpoint: Watching the Hoyle State Fall Apart". In: *Physics* 10.103 (2017).

[20] H. Morinaga. "Interpretation of Some of the Excited States of $4n$ Self-Conjugate Nuclei". In: *Physical Review* 101 (1 Jan. 1956), pp. 254–258. DOI: 10.1103/PhysRev.101.254.

[21] K. Ikeda, N. Takigawa, and H. Horiuchi. "The Systematic Structure-Change into the Molecule-like Structures in the Self-Conjugate $4n$ Nuclei". In: *Progress of Theoretical Physics* E68: 464-475 (1968). DOI: 10.1143/PTPS.E68.464.

[22] W. von Oertzen. "Covalently bound molecular structures in the α + ^{16}O system". In: *The European Physical Journal A* 11.4 (Nov. 2001), pp. 403–411. DOI: 10.1007/s100500170052.

[23] J. Hiura et al. "Alpha-Cluster plus ^{16}O-Core Model for ^{20}Ne and Neighboring Nuclei". In: *Progress of Theoretical Physics* 42.3 (Sept. 1969), pp. 555–580. DOI: 10.1143/PTP.42.555.

[24] B. Buck, C. B. Dover, and J. P. Vary. "Simple potential model for cluster states in light nuclei". In: *Physical Review C* 11 (1975), pp. 1803–1821. DOI: 10.1103/PhysRevC.11.1803.

[25] T. Matsuse, M. Kamimura, and Y. Fukushima. " Study of the Alpha-Clustering Structure of ^{20}Ne Based on the Resonating Group Method for ^{16}O+α : Analysis of Alpha-Decay Widths and the Exchange Kernel". In: *Progress of Theoretical Physics* 53.3 (Feb. 1975), pp. 706–724. DOI: 10.1143/PTP.53.706.

[26] C. Beck. "Recent Experimental Results on Nuclear Cluster Physics". In: *Journal of Physics: Conference Series* 863 (June 2017), p. 012002. DOI: 10.1088/1742-6596/863/1/012002.

[27] V. Della Rocca and F. Iachello. "Cluster shell model: I. Structure of ^{9}Be, ^{9}B". In: *Nuclear Physics A* 973 (2018), pp. 1–32. DOI: https://doi.org/10.1016/j.nuclphysa.2018.02.003.

[28] Y. Kanada-En'yo, M. Kimura, and H. Horiuchi. "Antisymmetrized Molecular Dynamics: a new insight into the structure of nuclei". In: *Comptes Rendus Physique* 4.4 (2003), pp. 497–520. DOI: https://doi.org/10.1016/S1631-0705(03)00062-8.

[29] W. R. Zimmerman et al. "Unambiguous Identification of the Second 2^{+} State in ^{12}**C** and the Structure of the Hoyle State". In: *Physical Review Letters* 110 (15 Apr. 2013), p. 152502. DOI: 10.1103/PhysRevLett.110.152502.

[30] W. Bauhoff, H. Schultheis, and R. Schultheis. "Alpha cluster model and the spectrum of ^{16}O". In: *Physical Review C* 29 (3 Mar. 1984), pp. 1046–1055. DOI: 10.1103/PhysRevC.29.1046.

[31] Y. Suzuki et al. *Structure and reactions of light exotic nuclei*. CRC Press, 2003. DOI: 10.4324/9780203168271.

[32] C. Wheldon et al. "High-resolution measurement of absolute α-decay widths in ^{16}O". In: *Physical Review C* 83 (6 June 2011), p. 064324. DOI: 10.1103/PhysRevC.83.064324.

[33] K.S. Krane. *Introductory Nuclear Physics*. John Wiley & Sons, 1987. Chap. 8. ISBN: 0-471-80553-X.

[34] K.S. Krane. *Introductory Nuclear Physics*. John Wiley & Sons, 1987. Chap. 10. ISBN: 0-471-80553-X.

[35] V. F. Weisskopf. "Radiative Transition Probabilities in Nuclei". In: *Physical Review* 83 (5 Sept. 1951), pp. 1073–1073. DOI: 10.1103/PhysRev.83.1073.

[36] I. J. Thompson and F. M. Nunes. *Nuclear Reactions for Astrophysics: Principles, Calculation and Applications of Low-Energy Reactions*. Cambridge University Press, 2009. DOI: 10.1017/CBO9781139152150.

[37] *The Differential Cross Section*. [Online; accessed 2022-01-12]. Jan. 2021. URL: https://phys.libretexts.org/Bookshelves/@go/page/29500.

[38] J. E. Bishop. "Experimental investigation of alpha-gas states using high-multiplicity particle spectroscopy". PhD thesis. UK: University of Birmingham, 2018.

[39] N. Bohr. "Neutron Capture and Nuclear Constitution". In: *Nature* 137.3461 (Feb. 1936), pp. 344–348. DOI: 10.1038/137344a0.

[40] S. N. Ghoshal. "An Experimental Verification of the Theory of Compound Nucleus". In: *Physical Review* 80 (6 Dec. 1950), pp. 939–942. DOI: 10.1103/PhysRev.80.939.

[41] K. P. Artemov et al. "Effective Method of Study of α-cluster states". In: *Soviet Journal of Nuclear Physics* 52 (1990), pp. 408–411.

[42] S. Bailey. "New Analytical Techniques for the Investigation of Alpha Clustering in Nuclei". PhD thesis. UK: University of Birmingham, 2016.

[43] E. P. Wigner. "Resonance Reactions". In: *Phys. Rev.* 70 (9-10 Nov. 1946), pp. 606–618. DOI: 10.1103/PhysRev.70.606.

[44] Kapur P. L. and Peierls R. "The dispersion formula for nuclear reactions". In: *Proceedings of the Royal Society of London A* 166 (), pp. 277–295. DOI: https://doi.org/10.1098/rspa.1938.0093.

[45] A. M. Lane and R. G. Thomas. "R-Matrix Theory of Nuclear Reactions". In: *Reviews of Modern Physics* 30 (2 Apr. 1958), pp. 257–353. DOI: 10.1103/RevModPhys.30.257.

[46] P. Descouvemont. *The R-matrix Method*. Presentation performed at the *R*-matrix training school in Orsay. Sept. 2017.

[47] P. Descouvemont and D. Baye. "The R-matrix theory". In: *Reports on Progress in Physics* 73.3 (Feb. 2010), p. 036301. DOI: 10.1088/0034-4885/73/3/036301.

[48] D. Baye. *An introduction to the R-matrix method*. Delivered at the 2010 ECT Trento, Doctoral Training Programme. 2010.

[49] K. P. Artemov et al. "Study of the α-cluster structure of ^{18}O in the reaction ^{14}C(^{6}Li,d)^{18}O(α)^{14}C". In: *Soviet Journal of Nuclear Physics* 37.6 (1983), pp. 805–808. URL: http://inis.iaea.org/search/search.aspx?orig_q=RN:15058062.

[50] G. L. Morgan et al. "Study of ^{18}O through ^{14}C+α reactions". In: *Nuclear Physics A* 148 (1970), pp. 480–491. DOI: 10.1016/0375-9474(70)90641-X.

[51] N. Curtis et al. "Evidence for a molecular rotational band in the $^{14}\mathrm{C}+\alpha$ decay of ^{18}O and the α decay of ^{22}Ne". In: *Physical Review C* 66 (2 Aug. 2002), p. 024315. DOI: 10.1103/PhysRevC.66.024315.

[52] H. T. Fortune. "Probable 6p-4h states in ^{18}O". In: *Physical Review C* 18 (2 Aug. 1978), pp. 1053–1055. DOI: 10.1103/PhysRevC.18.1053.

[53] M. Kimura and H. Horiuchi. "Coexistence of cluster structure and superdeformation in 44Ti". In: *Nuclear Physics A* 767 (2006), pp. 58–80. ISSN: 0375-9474. DOI: https://doi.org/10.1016/j.nuclphysa.2005.12.006.

[54] D. Jenkins. "Alpha clustering in nuclei: another form of shape coexistence?" In: 43.2 (Jan. 2016), p. 024003. DOI: 10.1088/0954-3899/43/2/024003.

[55] A. Bisoi et al. "Superdeformation and α-cluster structure in ^{35}Cl". In: *Physical Review C* 88 (3 Sept. 2013), p. 034303. DOI: 10.1103/PhysRevC.88.034303.

[56] W. von Oertzen et al. "Molecular and cluster structures in ^{18}O". In: *European Physical Journal A* 43 (2010), pp. 17–33. DOI: 10.1140/epja/i2009-10894-2.

[57] S. Pirrie et al. "Search for evidence of rotational cluster bands in ^{18}O". In: *Physical Review C* 102 (6 Dec. 2020), p. 064315. DOI: 10.1103/PhysRevC.102.064315.

[58] M. Löffler, H. J. Scheerer, and H. Vonach. "The ion optical properties of the Munich Q3D-spectrograph investigated by means of a special experimental ray tracing method". In: *Nuclear Instruments and Methods* 111.1 (1973), pp. 1–12. DOI: https://doi.org/10.1016/0029-554X(73)90090-6.

[59] C. A. Wiedner et al. "Performance of a QDDD spectrograph". In: *Nuclear Instruments and Methods* 105.2 (1972), pp. 205–210. DOI: https://doi.org/10.1016/0029-554X(72)90559-9.

[60] R. Krücken. Private communication.

[61] H.-F. Wirth et al. "A position sensitive cathode strip detector with single strip readout for the Munich Q3D magnetic spectrograph". Unpublished.

[62] H.-F. Wirth. "Bau eines hochauflösenden Fokalebenendetektors für den Münchner Q3D-Magnetspektrographen". PhD thesis. München: Technische Universität München, 2001.

[63] S. Pirrie et al. "Precision branching-ratio measurements in ^{18}O". In: *The European Physical Journal A* 57.4 (Apr. 2021), p. 150. ISSN: 1434-601X. DOI: 10.1140/epja/s10050-021-00431-w.

[64] D. R. Tilley et al. "Energy levels of light nuclei $A = 18$–19". In: *Nuclear Physics A* 595.1 (1995), pp. 1–170. DOI: https://doi.org/10.1016/0375-9474(95)00338-1.

[65] A. O'Hagan and T. Leonard. "Bayes estimation subject to uncertainty about parameter constraints". In: *Biometrika* 63.1 (Apr. 1976), pp. 201–203. DOI: 10.1093/biomet/63.1.201.

[66] S. K. Ashour and M. A. Abdel-Hameed. "Approximate skew normal distribution". In: *Journal of Advanced Research* 1.4 (2010), pp. 341–350. ISSN: 2090-1232. DOI: https://doi.org/10.1016/j.jare.2010.06.004.

[67] T. Dorsch. "Untersuchung von Cluster-Strukturen der neutronenreichen Sauerstoff-Isotope ^{18}O, ^{19}O und ^{20}O mit der (^{7}Li,p)-Reaktion". PhD thesis. München: Technische Universität München, 2008.

[68] H. G. Bohlen. *Spectra Analysis code SPEC (version F)*. HMI Berlin (2003).

[69] Micron Semiconductor Ltd. accessed on 2017-03-14. URL: http://www.micronsemiconductor.co.uk/pdf/w1.pdf.

[70] C. Kittel. *Introduction to solid state physics.* 6^{th} *ed.* John Wiley & Sons, 1986. ISBN: 9780471415268.

[71] S. Pirrie. *Investigating the clustered structure of* ^{6}*Li using an MC40 cyclotron.* 4th year report, School of Physics and Astronomy, University of Birmingham. 2017.

[72] R. Smith. "Experimental measurements of break-up reactions to study alpha clustering in carbon-12 and beryllium-9". PhD thesis. UK: University of Birmingham, 2017.

[73] G. F. Knoll. *Radiation Detection and Measurement*. John Wiley & Sons, 2000. Chap. 4. ISBN: 0-471-07338-5.

[74] *Electronic Instrumentation for Radiation Detection Systems*. 2016, accessed on 2018-09-02. URL: http://radiologykey.com/electronic-instrumentation-for-radiation-detection-systems/.

[75] mesytec GmbH & Co. accessed on 2021-07-22. URL: https://www.mesytec.com/products/datasheets/MPR-16.pdf.

[76] CAEN. *Mod. N568B/LC 16 Ch Spectroscopy Amplifiers*. Version 4. Jan. 26, 2007.

[77] CAEN. *Mod. V895 16 Channel Leading Edge Discriminator*. Version 3. Mar. 19, 2009.

[78] CAEN. *Mod. V785, 16/32 Channel Peak Sensing ADC*. Version 11. Nov. 11, 2005.

[79] C. Unsworth and V. Pucknell. *Multi Instance Data Acquisition System*. accessed on 2021-07-09. URL: http://npg.dl.ac.uk/MIDAS/.

[80] S. M. Singer. *Sunsort reference manual*. 1999-09-29, accessed on 2021-07-09. URL: http://npg.dl.ac.uk/MIDAS/manual/SunSort/.

[81] LeCroy Corporation. 1995, accessed on 2021-07-22. URL: https://teledynelecroy.com/lrs/dsheets/428.htm.

[82] LeCroy Corporation. accessed on 2021-07-22. URL: https://www.star.bnl.gov/public/tof/operations/modules/LC_380A.htm.

[83] LeCroy Corporation. 1995, accessed on 2021-07-22. URL: https://teledynelecroy.com/lrs/dsheets/222.htm.

[84] C. Wheldon. *Derivations for two-body kinematics (both relativistic and non-relativistic)*. June 13, 2019. URL: http://www.np.ph.bham.ac.uk/research_resources/programs/ckin/kinematics.pdf.

[85] R. C. Alig, S. Bloom, and C. W. Struck. "Scattering by ionization and phonon emission in semiconductors". In: *Physical Review B* 22 (12 Dec. 1980), pp. 5565–5582. DOI: 10.1103/PhysRevB.22.5565.

[86] I. V. Kotov, H. Neal, and P. O'Connor. "Pair creation energy and Fano factor of silicon measured at 185 K using ^{55}Fe X-rays". In: *Nuclear Instruments and Methods in Physics Research Section A: Accelerators, Spectrometers, Detectors and Associated Equipment* 901 (2018), pp. 126–132. DOI: https://doi.org/10.1016/j.nima.2018.06.022.

[87] G. W. Fraser et al. "The X-ray energy response of silicon Part A. Theory". In: *Nuclear Instruments and Methods in Physics Research Section A: Accelerators, Spectrometers, Detectors and Associated Equipment* 350.1 (1994), pp. 368–378. DOI: https://doi.org/10.1016/0168-9002(94)91185-1.

[88] F. Scholze, H. Rabus, and G. Ulm. "Mean energy required to produce an electron-hole pair in silicon for photons of energies between 50 and 1500 eV". In: *Journal of Applied Physics* 84.5 (1998), pp. 2926–2939. DOI: 10.1063/1.368398.

[89] R. D. Ryan. "Precision measurements of the ionization energy and its temperature variation in high purity silicon radiation detectors". In: *Institute of Electrical and Electronics Engineers, Transactions on Nuclear Science* NS-20.1 (Feb. 1973), pp. 473–480. DOI: 10.1109/TNS.1973.4326950.

[90] R. H. Pehl et al. "Accurate determination of the ionization energy in semiconductor detectors". In: *Nuclear Instruments and Methods* 59.1 (1968), pp. 45–55. DOI: https://doi.org/10.1016/0029-554X(68)90342-X.

[91] S. Pirrie et al. "Measurement of the structure of potential cluster bands and absolute branching ratios of high-energy states in ^{18}O*". In: 1643 (Dec. 2020), p. 012155. DOI: 10.1088/1742-6596/1643/1/012155.

[92] S. Pirrie et al. "Clustering in ^{18}O - absolute determination of branching ratios via high-resolution particle spectroscopy". In: *SciPost Physics Proceedings* (3 2020), p. 9. DOI: 10.21468/SciPostPhysProc.3.009.

[93] N. Curtis et al. "Evidence for a highly deformed band in ^{16}O+^{16}O breakup of ^{32}S". In: *Physical Review C* 53 (4 Apr. 1996), pp. 1804–1810. DOI: 10.1103/PhysRevC.53.1804.

[94] N. Curtis et al. "Association of the ^{12}C+^{12}C breakup states in ^{24}Mg with the quasi-molecular resonances". In: *Physical Review C* 51 (3 Mar. 1995), pp. 1554–1557. DOI: 10.1103/PhysRevC.51.1554.

[95] N. Curtis. "^{12}C and ^{16}O breakup of ^{24}Mg, ^{28}Si and ^{32}S." PhD thesis. UK: University of Birmingham, 1995.

[96] Private communication, dedx.f, Nuclear physics research group, University of Birmingham (unpublished).

[97] T. W. Armstrong and K. C. Chandler. "SPAR, a FORTRAN program for computing stopping powers and ranges for muons, charged pions, protons, and heavy ions". In: (May 1973). DOI: 10.2172/4477546.

[98] G. F. Knoll. *Radiation Detection and Measurement*. John Wiley & Sons, 2000. Chap. 2. ISBN: 0-471-07338-5.

[99] D. Robson. "Nuclear reactions with resonant-particle production". In: *Nuclear Physics A* 204.3 (1973), pp. 523–528. ISSN: 0375-9474. DOI: https://doi.org/10.1016/0375-9474(73)90392-8. URL: https://www.sciencedirect.com/science/article/pii/0375947473903928.

[100] E. Costanzo et al. In: *Nuclear Instrumentation and Methods in Physics* 295.3 (1990), pp. 373–376. DOI: https://doi.org/10.1016/0168-9002(90)90715-I.

[101] S. Pirrie et al. "A method to determine γ branching ratios using charged particle detectors for states in ^{18}O". In: *AIP Conference Proceedings* 2038.1 (2018), p. 020037. DOI: 10.1063/1.5078856.

[102] F. Ajzenberg-Selove. "Energy levels of light nuclei A =13–15". In: *Nuclear Physics A* 523.1 (1991), pp. 1–196. ISSN: 0375-9474. DOI: https://doi.org/10.1016/0375-9474(91)90446-D.

[103] M. L. Avila et al. "α-Cluster Structure of ^{18}O". In: *Physical Review C* 90.2 (2014), p. 024327. DOI: 10.1103/PhysRevC.90.024327.

[104] B. Yang et al. "Investigation of the ^{14}C+α molecular configuration in ^{18}O by means of transfer and sequential decay reaction". In: *Physical Review C* 99 (6 June 2019), p. 064315. DOI: 10.1103/PhysRevC.99.064315.

[105] V. Z. Goldberg et al. "Alpha-cluster states in ^{18}O". In: *Physics of Atomic Nuclei* 68.7 (2005), pp. 1079–1086. DOI: https://doi.org/10.1134/1.1992561.

[106] E. D. Johnson et al. In: *European Physical Journal A* 42 (June 2009), p. 135. DOI: 10.1140/epja/i2009-10887-1.

[107] J. W. Olness, E. K. Warburton, and J. A. Becker. "^{18}O Excitation Energies and Lifetimes from Ge(Li) Measurements in the ^{19}F(t, $\alpha\gamma$)^{18}O Reaction". In: *Physical Review C* 7 (6 June 1973), pp. 2239–2251. DOI: 10.1103/PhysRevC.7.2239.

[108] S. Bailey et al. "Extracting the spectral signature of α clustering in ^{44,48,52}Ti using a continuous wavelet transform". In: *Physical Review C* 100 (5 Nov. 2019), p. 051302. DOI: 10.1103/PhysRevC.100.051302.

[109] A. Volya and Y. M. Tchuvil'sky. "Nuclear clustering using a modern shell model approach". In: *Physical Review C* 91 (4 Apr. 2015), p. 044319. DOI: 10.1103/PhysRevC.91.044319.

[110] R. Anne et al. "The achromatic spectrometer LISE at GANIL". In: *Nuclear Instruments and Methods in Physics Research Section A: Accelerators, Spectrometers, Detectors and Associated Equipment* 257.2 (1987), pp. 215–232. ISSN: 0168-9002. DOI: https://doi.org/10.1016/0168-9002(87)90741-8.

[111] R. Anne and A. C. Mueller. "LISE 3: a magnetic spectrometer—Wien filter combination for secondary radioactive beam production". In: *Nuclear Instruments and Methods in Physics Research Section B: Beam Interactions with Materials and Atoms* 70.1 (1992), pp. 276–285. DOI: https://doi.org/10.1016/0168-583X(92)95943-L.

[112] J. P. Bondorf. "Statistical Multifragmentation of Nuclei". In: *The Response of Nuclei under Extreme Conditions*. Ed. by R. A. Broglia and G. F. Bertsch. Boston, MA: Springer US, 1988, pp. 279–293. ISBN: 978-1-4613-0895-9. DOI: 10.1007/978-1-4613-0895-9_13.

[113] B. Jakobsson et al. *The Disintegration of Nuclei in Violent Heavy Ion Interactions at 55A MeV - 110A MeV*. Tech. rep. LUIP–8205. Sweden, 1982, p. 45. URL: http://inis.iaea.org/search/search.aspx?orig_q=RN:13704016.

[114] X. Campi and J. Hüfner. "Nuclear spallation-fragmentation reactions induced by high-energy projectiles". In: *Physical Review C* 24 (5 Nov. 1981), pp. 2199–2209. DOI: 10.1103/PhysRevC.24.2199.

[115] J. W. Wilson, L. W. Townsend, and F. F. Badavi. "A semiempirical nuclear fragmentation model". In: *Nuclear Instruments and Methods in Physics Research Section B: Beam Interactions with Materials and Atoms* 18.1 (1986), pp. 225–231. DOI: https://doi.org/10.1016/S0168-583X(86)80035-0.

[116] M. Freer. "The clustered nucleus — cluster structures in stable and unstable nuclei". In: *Reports on Progress in Physics* 70.12 (2007), pp. 2149–2210. DOI: 10.1088/0034-4885/70/12/r03.

[117] M. Freer et al. "$\alpha : 2n : \alpha$ Molecular Band in ^{10}Be". In: *Physical Review Letters* 96 (4 Jan. 2006), p. 042501. DOI: 10.1103/PhysRevLett.96.042501.

[118] N. Itagaki et al. "Molecular-orbital structure in neutron-rich C isotopes". In: *Physical Review C* 64 (1 May 2001), p. 014301. DOI: 10.1103/PhysRevC.64.014301.

[119] M. Freer et al. "Resonances in ^{14}C observed in the ^{4}He(^{10}Be, α)^{10}Be reaction". In: *Physical Review C* 90 (5 Nov. 2014), p. 054324. DOI: 10.1103/PhysRevC.90.054324.

[120] Grand Accélérateur National d'Ions Lourds (GANIL). accessed on 2021-09-25. URL: https://www.ganil-spiral2.eu/scientists/ganil-spiral-2-facilities/experimental-areas/d3-d6/.

[121] Grand Accélérateur National d'Ions Lourds (GANIL). accessed on 2021-09-25. URL: https://www.ganil-spiral2.eu/scientists/ganil-spiral-2-facilities/accelerators/.

[122] R. Lemmon. accessed on 2022-01-22. URL: https://www.technologysi.stfc.ac.uk/Pages/ECLAN.aspx.

[123] Micron Semiconductor Ltd. accessed on 2022-01-14. URL: http://www.micronsemiconductor.co.uk/product/yy1/.

[124] N. Curtis and J. Walshe. "REX: A Monte Carlo simulation of thick gas target resonant scattering reactions". In: *Nuclear Instruments and Methods in Physics Research Section A: Accelerators, Spectrometers, Detectors and Associated Equipment* 797 (2015), pp. 44–56. DOI: https://doi.org/10.1016/j.nima.2015.06.027.

[125] CAEN. *Mod. V775 16/32 Channel Multievent TDC*. Version 14. Dec. 12, 2012.

[126] University of Birmingham and Cyclotron Facility. Accessed on 2022-02-22. URL: https://www.birmingham.ac.uk/research/activity/nuclear/about-us/facilities/mc40-cyclotron-facility.aspx.

[127] M. Norrby. "Alpha-Cluster Structures in Medium Light Nuclei". PhD thesis. Åbo: Åbo Akademi University, 2011.

[128] M. Kimura and H. Horiuchi. "Coexistence of cluster structure and superdeformation in ^{44}Ti". In: *Nuclear Physics A* 767 (Mar. 2006), pp. 58–80. DOI: 10.1016/j.nuclphysa.2005.12.006.

[129] R. E. Azuma et al. "AZURE: An R-matrix code for nuclear astrophysics". In: *Physical Review C* 81 (4 Apr. 2010), p. 045805. DOI: 10.1103/PhysRevC.81.045805.